

Investigation of Bubble Hydrodynamics in Gas-Solid Fluidized Beds Containing Immersed Horizontal Tube Banks for Lignite Drying Application

Von der Fakultät für Maschinenbau, Elektrotechnik und
Wirtschaftsingenieurwesen der Brandenburgischen Technischen
Universität Cottbus zur Erlangung des akademischen Grades eines
Doktor-Ingenieurs genehmigte Dissertation

vorgelegt von

Teklay Weldeabzgi Asegehegn, MSc.

Geboren am 20.10.1979 in Adwa, Äthiopien

Vorsitzender: Prof. Dr.-Ing. Harald Schwarz

Gutachter: Prof. Dr.-Ing. Hans Joachim Krautz

Gutachter: Prof. Dr.-Ing. Heinz Peter Berg

Tag der mündlichen Prüfung: 16. Dezember 2011

Rechtliche Bedingungen / Copyright

Investigation of Bubble Hydrodynamics in Gas-Solid Fluidized Beds Containing Immersed Horizontal Tube Banks for Lignite Drying Application von Teklay Weldeabzgi Asegehegn steht unter einer Creative Commons Namensnennung-NichtKommerziell-KeineBearbeitung 3.0 Deutschland Lizenz.

Sämtliche Rechte am Inhalt dieser Arbeit verbleiben beim Autor. Der Autor überträgt der Brandenburgischen Technischen Universität Cottbus das einfache Verbreitungsrecht, also das Recht, im Rahmen der gesetzlichen Aufgaben der Hochschulbibliotheken weitere Kopien dieser Dissertation herzustellen und zu verbreiten bzw. in Datennetzen zur Verfügung zu stellen.

Diese Arbeit darf heruntergeladen und frei verwendet werden, wenn sie entsprechend zitiert wird. Eine Bearbeitung von Inhalten dieser Arbeit (zum Beispiel von Abbildungen, Tabellen, Text, usw.) bedarf der Erlaubnis des Autors. Eine kommerzielle Nutzung der Dissertation und die Vervielfältigung aus kommerziellen Zwecken sind ausgeschlossen.

Acknowledgements

I would like to express my deep gratitude to my research supervisor Prof. Dr.-Ing. Hans Joachim Krautz, for giving me the opportunity to work at his chair and providing me with the optimum working conditions. His guidance, enthusiastic encouragement and patience have been a source of inspiration throughout the course of this work. I would also like to thank Prof. H. P. Berg for being my second reviewer and critically reviewing my dissertation. I would also like to thank Prof. H. Schwarz for being the head of the committee for my dissertation examination board. My grateful thanks are also extended to Dr.-Ing. Matthias Klatt for his advice and assistance during my research work.

It is a pleasure to thank those all of my colleagues at the Chair for Power Plant Technology, Brandenburg University of Technology in Cottbus (BTU Cottbus) who supported me during my time at the chair. They provided me with a very friendly atmosphere and ensured that working at the department was always fun. Of the most, I would like to thank Dipl.-Wi.-Ing. (FH) Matthias Schreiber with whom I have had and still have a wonderful time. He has been a continuous support for me during my research work as well as private matters. I am sure it would have not been possible without his help. I would also like to thank Dipl.-Ing. Alexander Findeisen for his support and encouragement when I just came to the chair.

I would like to thank to the International Graduate School supported by the BTU Cottbus and the Brandenburg Ministry of Higher Education, Research and Culture, and to the COORETEC-Initiative from the Federal Ministry of Economics and Technology for their financial support of this research project.

Last, but not the least, I would like to thank my family and friends for their firm support and patience in the most important period of my life. My special gratitude is directed to my lovely wife, Rafi, for her never-ending love, prayer, patience, faith, understanding and support that kept me holding on even in the most difficult time. My two kids Yididya and Rimna you are the precious gift God has given to me. I love you so much.

Summary

In recent years, the interest in gas-solid fluidized beds in power generations is becoming unabated, due to the development of circulating fluidized bed combustion chambers and steam drying of lignite. Fluidized beds are characterized by their excellent heat and mass transfer properties, intense gas-solid mixing, and possibility of continuous and large-scale operations. However, they have several drawbacks that provide a strong motivation for further studies and developments. These include erosion of vessel and internals, formation of agglomerates, non-uniform products and high particle entrainment. These drawbacks are bottlenecks for practitioners to reliably design and scale-up industrial fluidized bed reactors. The main reason is that the complex gas-particle two-phase flow that occur in these systems is not yet fully understood.

In bubbling fluidized beds, bubble characteristics such as size, shape and velocity have a vital influence on the hydrodynamics of the bed and hence on its performance as a chemical reactor and/or a heat exchange unit. In many industrial applications such as lignite dryer heat transfer tubes are usually inserted to enhance the rate of heat and mass transfer and chemical conversion. However, their presence strongly influences the bubbling behavior of the beds. Therefore, reliable design and scale-up of these systems come only after fundamental understanding of the bubbling behavior is achieved. Therefore, the main objective of this research work is to investigate the bubble hydrodynamics of fluidized beds with immersed horizontal tubes in order to improve the understanding of the bed hydrodynamics. The influence of tube bank geometries and particle size on bubble characteristics as well as pressure drop and bed expansion was investigated. For this purpose, both numerical and experimental studies were employed.

For the experimental measurements, a new nonintrusive digital image analysis technique was developed. The technique allowed for the simultaneous measurements of bed expansion and various bubble properties. An in-house software was developed to fully automate the image acquisition and data processing procedure. Results obtained by the technique were validated by comparing with relevant correlations available in the literature as well as manual calculations and were in very good agreement. Based on the experimental results obtained by this technique, new theoretical correlations for bed expansion ratio as well as bubble growth and rise velocity were proposed. The models were in very good agreement with the experimental data for wide range of superficial velocities and particle sizes.

For the numerical studies, the Eulerian-Eulerian two-fluid model based on the kinetic theory of granular flow was used. This CFD model has been considered as a fundamental tool for modeling gas-solid fluidized beds and has been extensively used for the last couple of decades. However, its quantitative validation remains insufficient for a wide range of reactor geometries and operating conditions. In this work validation of the model using experimental measurements of bed expansion and bubble properties obtained from a pseudo-two-dimensional fluidized bed was

performed. The influence of grid size, two-dimensional simulations, and different modeling parameters such as the friction packing limit, drag model and solid-wall boundary conditions were investigated. The results showed no major influence of the grid size on the macroscopic bed hydrodynamics at least for the grid sizes studied in this work. The mean bubble properties predicted by two-dimensional simulations were in reasonable agreement with experiments at lower superficial velocities. They deviated at higher bed height and this was more pronounced at higher gas superficial velocities. Though results from three-dimensional simulations were in better agreement with the experimental measurements, the computational effort need was very high making them impractical for parametric studies and sensitivity analyses.

The two-fluid model generally showed reasonable agreement with the experimental measurements of pressure drop, bed expansion and bubble properties in bubbling regime. It was also showed that the choice of friction packing limits, drag laws and specular coefficients have little influence on the bubble properties. However, as the gas superficial velocity is increased and the bed moved towards slugging and turbulent regimes a big deviation arose and the two-fluid model failed to predict reasonably the fluidized bed hydrodynamics for the freely bubbling bed.

For a bubbling bed, both experimental measurements and numerical simulations showed that inserting horizontal tube banks had either no or marginal influence on the static bed pressure drop and bed expansion. On the other hand, bubble hydrodynamics were strongly influenced and controlled by the geometry of the immersed tubes. In freely bubbling fluidized beds bubble size as well as rise velocity increased with bed height and superficial velocity. In beds with immersed tubes, such general trends were completely disturbed. Tubes appeared to restrict rapidly growing bubbles. As a result the mean bubble diameter and rise velocity were lower in the vicinity of the tube banks than in the freely bubbling bed. Results from different particle sizes showed that in a freely bubbling bed increasing the mean particle size increased the bubble diameter and rise velocity as well as bed expansion. In fluidized beds with dense horizontal tubes on the other hand, the mean bubble properties were almost independent of the particle sizes.

Zusammenfassung

In den letzten Jahren hielt das Interesse an Gas-Feststoff-Wirbelschichten aufgrund der Entwicklung von Brennkammern mit zirkulierender Wirbelschicht und der Dampftrocknung von Braunkohle unvermindert an. Wirbelschichten zeichnen sich durch ihr exzellentes Wärmeübertragungs- und Massentransportverhalten, der intensiven Vermischung von Gas und Partikeln und der Möglichkeit von kontinuierlichem und großskaligem Betrieb aus. Dennoch besitzen sie einzelne Nachteile, die eine große Motivation für weitere Untersuchungen und Entwicklungen liefern. Diese beinhalten die Erosion von Behälter und Einbauten, die Entstehung von Agglomeraten, ungleichmäßige Produkteigenschaften aufgrund ungleichmäßiger Partikelverweilzeiten während des kontinuierlichen Betriebs und hoher Partikelaustrag. Diese Nachteile stellen für Fachleute Flaschenhälse für die zuverlässige Auslegung und maßstabsgerechte Vergrößerung industrieller Wirbelschichtreaktoren dar. Der Hauptgrund dafür ist, dass die in diesen Systemen auftretenden komplexen Gas-Partikel-Zweiphasenströmungen noch nicht vollständig verstanden sind.

In blasenbildenden Wirbelschichten haben die Eigenschaften der Blasen wie Größe, Form und Geschwindigkeit einen grundlegenden Einfluss auf die Hydrodynamik der Wirbelschicht und damit auf die Leistungsfähigkeit als verfahrenstechnischer Reaktor und/oder Wärmeübertragungseinheit. In vielen industriellen Anwendungen, wie der Trocknung von Braunkohle, werden Rohre eingebracht, um die Wärme- und Stoffübertragung sowie chemische Umwandlungen zu verbessern. Ihre Anwesenheit beeinflusst das Verhalten der Blasen stark. Daher kann eine zuverlässige Auslegung und ein Scale-up dieser Systeme nur mit einem grundlegenden Verständnis des Blasenverhaltens erreicht werden. Das Ziel dieser wissenschaftlichen Arbeit ist es, die Blasenhydrodynamik von Wirbelschichten mit dicht gepackten horizontalen Rohren zu untersuchen, um diese besser zu verstehen. Es wurde der Einfluss der Rohranordnungen und Partikelgröße auf die Blaseigenschaften sowie den Druckverlust und die Wirbelschichtausdehnung untersucht. Zu diesem Zweck wurden sowohl numerische als auch experimentelle Untersuchungen durchgeführt.

Für die experimentellen Messungen wurde eine neuartige, nicht-intrusive Bildanalysetechnik entwickelt. Sie erlaubt eine simultane Messung der Wirbelschichtausdehnung und verschiedener Blaseigenschaften. Um die Bildverarbeitung und -analyse vollständig zu automatisieren, wurde eigens eine Software entwickelt. Die erzielten Ergebnisse wurden mittels relevanter Korrelationen aus der Literatur sowie manueller Berechnungen validiert und zeigten eine sehr gute Übereinstimmung. Basierend auf den experimentellen Ergebnissen konnten neue Korrelationen für die Wirbelschichtausdehnung sowie Blasengröße und -aufstiegsgeschwindigkeit vorgeschlagen werden. Diese zeigten eine sehr gute Übereinstimmung mit experimentellen Daten für einen weiten Bereich von Leerrohrgeschwindigkeiten und Partikelgrößen.

Für die numerischen Untersuchungen wurde das Euler-Euler Two-Fluid Model basierend auf der Kinetic Theory of Granular Flow angewendet. Dieses CFD-Modell wird als grundlegendes Hilfsmittel zur Modellierung von Gas-Feststoff-Wirbelschichten angesehen und wurde in den letzten Jahrzehnten intensiv angewendet. Dennoch ist seine Validierung für einen weiten Bereich von Reaktorgeometrien und Betriebsbedingungen unzureichend. In dieser Arbeit wurde die Validierung des Modells mittels experimenteller Messungen von Wirbelschichtausdehnung und Blaseneigenschaften in einer quasi-2D Wirbelschicht durchgeführt. Der Einfluss von Gittergröße, zweidimensionaler Simulation und verschiedener Parameter wie dem Reibungspackungslimit, dem Widerstandsmodell und der Partikel-Wand-Randbedingungen wurde untersucht. Die Ergebnisse zeigten keine wesentlichen Einflüsse der Gittergröße auf die makroskopische Wirbelschichthydrodynamik zumindest in den untersuchten Größenordnungen. Die von den zweidimensionalen Simulationen erhaltenen, gemittelten Blaseneigenschaften waren für niedrigere Leerrohrgeschwindigkeiten in guter Übereinstimmung mit dem Experiment. Sie wichen in größerer Höhe und insbesondere bei höheren Geschwindigkeiten zunehmend davon ab. Obwohl die Ergebnisse dreidimensionaler Simulationen besser mit den experimentellen Messungen übereinstimmten, machte der extrem hohe Rechenaufwand diese für parametrische Studien und Sensitivitätsanalysen unmöglich.

Das Two-Fluid Model zeigt im Allgemeinen eine gute Übereinstimmung mit den experimentellen Messungen von Druckverlust, Wirbelschichtausdehnung und Blaseneigenschaften im blasenbildenden Regime. Es zeigte sich ebenfalls, dass die Wahl des Reibungspackungslimits, Widerstandsmodells und Reflektionskoeffizienten nur einen geringen Einfluss auf die Blaseneigenschaften hat. Bei höheren Geschwindigkeiten, wenn sich die Wirbelschicht im stoßenden oder turbulenten Regime befindet, stiegen allerdings die Abweichungen an und das Two-Fluid Model konnte die Wirbelschichthydrodynamik für freie Wirbelschichten nicht mehr zuverlässig berechnen.

Für blasenbildende Wirbelschichten zeigten experimentelle Messungen und numerische Simulationen, dass eingetauchte horizontale Rohrbündel keinen oder nur einen marginalen Einfluss auf den Druckverlust und die Wirbelschichtausdehnung haben. Die Blasenhydrodynamik wurde demgegenüber stark von der Anordnung der eingetauchten Rohre beeinflusst und bestimmt. In freien, blasenbildenden Wirbelschichten stieg die Blasengröße und -geschwindigkeit mit zunehmender Höhe und Leerrohrgeschwindigkeit an. In Wirbelschichten mit eingetauchten Rohren wurden solche generellen Trends gestört. Die Rohre beschränken ein schnelles Wachsen der Blasen. Als Folge daraus waren die mittleren Blasengrößen und -geschwindigkeiten in der Nähe der Rohrbündel geringer als in freien blasenbildenden Wirbelschichten. Ergebnisse von unterschiedlichen Partikelgrößen zeigten, dass Blasengröße, -aufstiegsgeschwindigkeit und Wirbelschichtausdehnung in freien Wirbelschichten mit zunehmender mittlerer Partikelgröße ansteigen. In Wirbelschichten mit dicht gepackten horizontalen Rohren waren die mittleren Blaseneigenschaften demgegenüber nahezu unabhängig von den Partikelgrößen.

Table of Contents

Acknowledgements	I
Summary	II
Zusammenfassung	IV
Table of Contents	VI
List of Figures	IX
List of Tables	XVI
Nomenclature	XVII
1 General Introduction	1
1.1 Fluidization and Fluidized Beds	1
1.2 Powder Classification	3
1.3 Steam Fluidized Bed Drying of Lignite	5
1.4 Motivation and Objective	10
1.5 Outline of the Thesis	11
2 State of the Scientific Knowledge	13
2.1 Introduction	13
2.2 Experimental Techniques	14
2.2.1 Intrusive and nonintrusive measurement techniques	14
2.2.2 Digital imaging technique	20
2.3 CFD Models for Gas-Solid Fluidized Beds	23
2.3.1 The Eulerian-Lagrangian model	23
2.3.2 The Eulerian-Eulerian model	25
2.4 Gas-Solid Fluidized Beds Containing Immersed Tubes	31

3 Numerical Modeling using the Two-Fluid Model	35
3.1 Governing Equations.....	35
3.2 Interphase Momentum Transfer Coefficient.....	36
3.3 The Kinetic Theory of Granular Flow	38
3.3.1 Gas phase stress tensor	42
3.3.2 Solid phase stress tensor.....	43
3.3.3 Radial distribution function.....	45
3.3.4 Solid pressure	47
3.3.5 Frictional models.....	47
3.4 Solution Method.....	49
3.4.1 Grid size and time steps	50
3.4.2 Initial and boundary conditions.....	51
4 Experimental Technique	53
4.1 Experimental Setup.....	53
4.2 Mean Particle Size and Size Distribution.....	54
4.3 Automated Digital Image Analysis Technique.....	56
4.3.1 Image acquisition and data processing.....	56
4.3.2 Calibration and validation of the DIAT	62
5 Theoretical Predictions and Experimental Measurements	65
5.1 Pressure Drop and Minimum Fluidization Velocity	65
5.1.1 Theoretical background.....	65
5.1.2 Experimental measurements	68
5.2 Bed Expansion	72
5.2.1 Theoretical background.....	72
5.2.2 Experimental measurement.....	76
5.3 Bubble Properties.....	81
5.3.1 Bubble diameter	82
5.3.2 Bubble rise velocity.....	87

6	Experimental Validation of the Two-Fluid Model.....	91
6.1	Simulation Parameters	91
6.2	Bubble Definition and Averaging Period	92
6.2.1	Bubble definition.....	92
6.2.2	Averaging period.....	94
6.3	Grid Size Dependency	99
6.4	Two-and Three-Dimensional Comparison	101
6.5	Friction Packing Limit	108
6.6	Inter-Phase Momentum Transfer Coefficient	111
6.7	Solid-Wall Boundary Conditions.....	113
7	Influence of Immersed Horizontal Tube Banks and Mean Particle Size	117
7.1	Influence of Horizontal Tube Banks.....	118
7.1.1	Pressure drop	118
7.1.2	Bed expansion	119
7.1.3	Bubble properties	120
7.2	Influence of Mean Particle Sizes	135
7.2.1	Pressure drop.....	135
7.2.2	Bed expansion	136
7.2.3	Bubble properties	139
8	Conclusions and Future Work.....	151
8.1	Conclusions.....	151
8.2	Recommendations for Future Work.....	155
9	Bibliography	157
	Appendices.....	181

List of Figures

Figure 1.1: Various regimes of fluidization (after Lim et al. 1995)	2
Figure 1.2: Geldart's Classification of powders (Geldart, 1973).....	4
Figure 1.3: Schematic diagram of the pressurized steam fluidized bed drying (PSFBD) process at the Brandenburg University of Technology Cottbus (BTU Cottbus).....	9
Figure 3.1: Comparison of different interphase momentum transfer coefficients; $Re_p=50$, $d_p=347 \mu\text{m}$	37
Figure 3.2: Influence of particle-particle restitution coefficients on the dissipation of granular energy; $g_0=5$, $d_p=347 \mu\text{m}$, $\Theta=0.1 \text{ m}^2/\text{s}^2$	41
Figure 3.3: Comparison of different solid shear viscosity expressions (a) Kinetic contribution; (b) Total (Kinetic-Collisional) contribution; $g_0=5$, $e=0.9$	44
Figure 3.4: Dimensionless solid shear viscosity for different restitution coefficient; $g_0=5$	45
Figure 3.5: Comparison of different radial distribution functions; $\varepsilon_{s,\text{max}}=0.65$	46
Figure 4.1: Experimental setup; (a) hydraulic scheme, (b) optical scheme.....	53
Figure 4.2: Tube bank geometries and arrangement: staggered (S) and in-line (I).	55
Figure 4.3: Size distribution of the two of the particles used.	56
Figure 4.4: Time-averaged grayscale histogram.....	57
Figure 4.5: Bubble delineation; original image (left), grayscale image (middle) and binary image (right).	58
Figure 4.6: Bubble dimensions.	59
Figure 4.7: Bubble matching and numbering for the detected bubbles in two consecutive time frames.	63
Figure 4.8: Comparison of simulation results between manual calculation and DIAT; (a) bubble diameter, (b) bubble rise velocity. Geometry and parameters from Hull et al. (1999).....	64
Figure 5.1: Pressure drop versus superficial velocity for uniformly sized spherical particles.	66
Figure 5.2: Pressure drop measurements for different bed geometries and particle sizes.	69
Figure 5.3: Bed pressure drop versus superficial velocity for the NT geometry and two particle sizes.	70

Figure 5.4: Bed pressure drop versus superficial velocity for the particle size of 347 μm and two bed geometries.....	70
Figure 5.5: Measured minimum fluidization velocity for different particle sizes and bed geometries.	71
Figure 5.6: Different definitions of bed expansion ratio and comparison between experiment and simulation; Data from Taghipour et al. (2005).....	73
Figure 5.7: Delineation of bed boundary for bed expansion calculation using DIAT; left actual image, right delineated image.....	77
Figure 5.8: Comparison of bed expansion ratio calculated using the DIAT and pressure drop measurements.	78
Figure 5.9: Variation of bed expansion ratio with excess gas velocity ($U-U_{mf}$) for different particle sizes and bed geometries.	78
Figure 5.10: Comparison of bed expansion ratio with model predictions from Equation 5.24 and model proposed by L�fstrand et al. (1995) for the bed without immersed tubes (NT) and different particle sizes.	79
Figure 5.11: Comparison of bed expansion ratio between model predictions and experimental data from literature; (a) Taghipour et al. (2005), (b) Llop et al. (2000).	80
Figure 5.12: Bed expansion ratio for the bed with dense staggered immersed tubes (S6) and different particle sizes: comparison between model prediction and experimental measurements.	81
Figure 5.13: Comparison of mean bubble diameter between experiment and model predictions, $U_{mf}=0.087$ m/s and velocity ratio (U/U_{mf}) as indicated on the respective lines; solid lines-Equation 5.33, and dashed lines-Equation 5.30.....	84
Figure 5.14: Comparison of mean bubble diameter between experiment and model predictions, $U_{mf}=0.504$ m/s and velocity ratio (U/U_{mf}) as indicated on the respective lines; solid lines-Equation 5.33, and dashed lines-Equation 5.30.....	85
Figure 5.15: Comparison of mean bubble diameter between experiment and model prediction of Equation 5.33; $U_{mf}=0.144$ m/s.....	85
Figure 5.16: Comparison of mean bubble diameter between experiment and model prediction of Equation 5.33; $U_{mf}=0.238$ m/s.....	86

Figure 5.17: Comparison of mean bubble rise velocity between experiment and model predictions, $U_{mf}= 0.087$ m/s and velocity ratio (U/U_{mf}) as indicated on the respective lines; solid lines-Equation 5.37, and dashed lines-model by Lim et al. (1993).....	89
Figure 5.18: Comparison of mean bubble rise velocity between experiment and model predictions, $U_{mf}= 0.504$ m/s and velocity ratio (U/U_{mf}) as indicated on the respective lines; solid lines-Equation 5.37, and dashed lines-model by Lim et al. (1993).....	89
Figure 5.19: Comparison of mean bubble rise velocity with experiment and model prediction of Equation 5.37; $U_{mf}=0.144$ m/s.	90
Figure 5.20: Comparison of mean bubble rise velocity with experiment and model prediction of Equation 5.37; $U_{mf}=0.238$ m/s.	90
Figure 6.1: Instantaneous solids volume fraction contour for S6 tube arrangement; $\Delta t=0.02$ s.....	93
Figure 6.2: Mean bubble aspect ratio for different bubble boundaries (BB); $d_p=246$ μm , $U=2.5U_{mf}$	93
Figure 6.3: Mean bubble diameter for different bubble boundaries (BB); $d_p=246$ μm , $U=2.5U_{mf}$	94
Figure 6.4: Mean bubble rise velocity for different bubble boundaries (BB); $d_p=246$ μm , $U=2.5U_{mf}$	94
Figure 6.5: Time-averaged bubble aspect ratio for different averaging times (AT); $d_p=246$ μm ; $U=2.5U_{mf}$	95
Figure 6.6: Time-averaged bubble diameter for different averaging times (AT); $d_p=246$ μm ; $U=2.5U_{mf}$	96
Figure 6.7: Time-averaged bubble rise velocity for different averaging times (AT); $d_p=246$ μm ; $U=2.5U_{mf}$	96
Figure 6.8: Mean bubble aspect ratio for different averaging periods (AP); $d_p=246$ μm ; $U=2.5U_{mf}$	97
Figure 6.9: Mean bubble diameter for different averaging periods (AP); $d_p=246$ μm ; $U=2.5U_{mf}$	97

Figure 6.10: Mean bubble rise velocity for different averaging periods (AP); $d_p=246 \mu\text{m}$; $U=2.5U_{mf}$	97
Figure 6.11: Mean bubble aspect ratio for different sampling frequencies (SF); $d_p=246 \mu\text{m}$; $U=2.5U_{mf}$	98
Figure 6.12: Mean bubble diameter for different sampling frequencies (SF); $d_p=246 \mu\text{m}$; $U=2.5U_{mf}$	98
Figure 6.13: Mean bubble rise velocity for different sampling frequencies (SF); $d_p=246 \mu\text{m}$; $U=2.5U_{mf}$	99
Figure 6.14: Comparison of mean bubble diameter for different grid sizes, $d_p=347 \mu\text{m}$, $U=2U_{mf}$	99
Figure 6.15: Comparison of mean bubble rise velocity for different grid sizes, $d_p=347 \mu\text{m}$, $U=2U_{mf}$	100
Figure 6.16: Comparison of bubble aspect ratio between 2D and 3D simulations for the bed without tubes (NT), $d_p = 246 \mu\text{m}$	103
Figure 6.17: Comparison of bubble aspect ratio between 2D and 3D simulations for the bed with dense staggered tubes (S6), $d_p = 246 \mu\text{m}$	103
Figure 6.18: Comparison of mean bubble diameter between 2D and 3D simulations for the bed without tubes (NT), $d_p = 246 \mu\text{m}$	105
Figure 6.19: Comparison of mean bubble diameter between 2D and 3D simulations for the bed with dense staggered tubes (S6), $d_p = 246 \mu\text{m}$	105
Figure 6.20: Comparison of mean bubble diameter between 2D and 3D simulations, $d_p =$ $347 \mu\text{m}$, $U=2.0U_{mf}$	105
Figure 6.21: Comparison of mean bubble rise velocity between 2D and 3D simulations for the bed without tubes (NT), $d_p = 246 \mu\text{m}$	106
Figure 6.22: Mean bubble rise velocity as a function of bubble diameter for the bed without tubes (NT), $d_p = 246 \mu\text{m}$	107
Figure 6.23: Comparison of mean bubble rise velocity between 2D and 3D simulations for the bed with dense staggered tubes (S6); $d_p = 246 \mu\text{m}$	107
Figure 6.24: Comparison of mean bubble rise velocity between 2D and 3D simulations; $d_p =$ $347 \mu\text{m}$, $U=2.0U_{mf}$	108

Figure 6.25: Comparison of bubble aspect ratio between experiment and simulation for different friction packing limits (FPL); $d_p=246 \mu\text{m}$, $U=2.5U_{mf}$.	110
Figure 6.26: Comparison of bubble diameter between experiment and simulation for different friction packing limits (FPL); $d_p=246 \mu\text{m}$, $U=2.5U_{mf}$.	110
Figure 6.27: Comparison of bubble rise velocity between experiment and simulation for different friction packing limits (FPL); $d_p=246 \mu\text{m}$, $U=2.5U_{mf}$.	111
Figure 6.28: Comparison of mean bubble aspect ratio between experiment and simulation using different drag models; $d_p=246 \mu\text{m}$, $U=2.5U_{mf}$.	112
Figure 6.29: Comparison of mean bubble diameter between experiment and simulation using different drag models; $d_p=246 \mu\text{m}$, $U=2.5U_{mf}$.	112
Figure 6.30: Comparison of mean bubble rise velocity between experiment and simulation using different drag models; $d_p=246 \mu\text{m}$, $U=2.5U_{mf}$.	112
Figure 6.31: Comparison of bubble aspect ratio between experiment and simulation for different solid-wall boundary conditions and specularly coefficients (SC); $d_p=246 \mu\text{m}$, $U=2.5U_{mf}$.	115
Figure 6.32: Comparison of bubble diameter between experiment and simulation for different solid-wall boundary conditions and specularly coefficients (SC); $d_p=246 \mu\text{m}$, $U=2.5U_{mf}$.	115
Figure 6.33: Comparison of bubble rise velocity between experiment and simulation for different solid-wall boundary conditions and specularly coefficients (SC); $d_p=246 \mu\text{m}$, $U=2.5U_{mf}$.	115
Figure 7.1: Time-averaged bed pressure drop versus excess gas velocity ($U-U_{mf}$).	118
Figure 7.2: Measured and predicted time-averaged bed expansion ratio versus excess gas velocity ($U-U_{mf}$) for different bed geometries.	120
Figure 7.3: Comparison of the mean bubble aspect ratio for different tube bank geometries and arrangements; $d_p=246 \mu\text{m}$, $U=2.0U_{mf}$.	122
Figure 7.4: Comparison of the mean bubble shape factor for different tube bank geometries and arrangements; $d_p=246 \mu\text{m}$, $U=2.0U_{mf}$.	122
Figure 7.5: Influence of gas superficial velocity on the mean bubble aspect ratio for beds with and without immersed tubes; $d_p=246 \mu\text{m}$.	123

Figure 7.6: Influence of gas superficial velocity on the mean bubble shape factor for beds with and without immersed tubes; $d_p=246 \mu\text{m}$	123
Figure 7.7: Influence of tube packing density on the mean bubble aspect ratio for the staggered and in-line tube arrangements; $d_p=246 \mu\text{m}$, $U=3.0U_{mf}$	124
Figure 7.8: Influence of the tube packing density on the mean bubble shape factor for the staggered and in-line tube arrangements; $d_p=246 \mu\text{m}$, $U=3.0U_{mf}$	124
Figure 7.9: Comparison of the mean bubble aspect ratio for the different tube bank arrangements; $d_p=347 \mu\text{m}$, left- $U=2.0U_{mf}$, right- $U=4.0U_{mf}$	125
Figure 7.10: Comparison of the mean bubble shape factor for different tube bank arrangements; $d_p=347 \mu\text{m}$, left- $U=2.0U_{mf}$, right- $U=4.0U_{mf}$	125
Figure 7.11: Comparison of the mean bubble diameter for different tube bank geometries and arrangements; $d_p=246 \mu\text{m}$, $U=2.0U_{mf}$	126
Figure 7.12: Influence of gas superficial velocity on the mean bubble diameter for beds with and without immersed tubes; $d_p=246 \mu\text{m}$	126
Figure 7.13: Comparison of the mean bubble diameter for different tube bank arrangements; $d_p=347 \mu\text{m}$, left- $U=2.0U_{mf}$, right- $U=4.0U_{mf}$	127
Figure 7.14: Bubble frequency as a function of bed height; $d_p=246 \mu\text{m}$, $U=4.0U_{mf}$	129
Figure 7.15: Influence of tube packing density on the mean bubble diameter for the staggered and in-line tube arrangements; $d_p=246 \mu\text{m}$, $U=3.0U_{mf}$	130
Figure 7.16: Time-averaged solid volume fraction of the NT, S6 and I6 tube geometries; $d_p=246 \mu\text{m}$ and $U=2.5U_{mf}$	131
Figure 7.17: Comparison of the mean bubble rise velocity for different tube bank geometries and arrangements; $d_p=246 \mu\text{m}$, $U=2.0U_{mf}$	132
Figure 7.18: Influence of gas superficial velocity on the mean bubble rise velocity for beds with and without immersed tubes; $d_p=246 \mu\text{m}$	132
Figure 7.19: Influence of tube packing density on the mean bubble rise velocity for the staggered and in-line tube arrangements; $d_p=246 \mu\text{m}$, $U=3.0U_{mf}$	134
Figure 7.20: Companion of the mean bubble rise velocity for different tube bank arrangements; $d_p=347 \mu\text{m}$, left- $U=2.0U_{mf}$, right- $U=4.0U_{mf}$	134
Figure 7.21: Static bed pressure drop profile predicted by numerical simulations.	136

Figure 7.22: Bed expansion for different particle sizes and fluidized bed without tubes (NT); experimental measurement (left), numerical prediction (right).....	137
Figure 7.23: Bed expansion for different particle sizes and fluidized bed with dense staggered tubes (S6); experimental measurement (left), numerical prediction (right).	137
Figure 7.24: Time-averaged solids volume fraction contours; $d_p=592 \mu\text{m}$	141
Figure 7.25: Comparison of the mean bubble aspect ratio for different mean particle sizes for NT; $U=2.0U_{mf}$	144
Figure 7.26: Comparison of the mean bubble shape factor for different mean particle sizes for NT; $U=2.0U_{mf}$	144
Figure 7.27: Comparison of the mean bubble aspect ratio for different mean particle sizes for NT; $U=4.0U_{mf}$	144
Figure 7.28: Comparison of the mean bubble aspect ratio for different mean particle sizes for S6; $U=2.0U_{mf}$	145
Figure 7.29: Comparison of the mean bubble shape factor for different mean particle sizes for S6; $U=2.0U_{mf}$	145
Figure 7.30: Comparison of the mean bubble diameter for different mean particle sizes for NT; $U=2.0U_{mf}$	147
Figure 7.31: Comparison of the mean bubble diameter for different mean particle sizes for NT; $U=4.0U_{mf}$	147
Figure 7.32: Comparison of bubble frequency for different mean particle sizes; $U=4.0U_{mf}$	148
Figure 7.33: Comparison of the mean bubble diameter for different mean particle sizes for S6; $U=2.0U_{mf}$	148
Figure 7.34: Comparison of the mean bubble rise velocity for different mean particle sizes for NT; $U=2.0U_{mf}$	149
Figure 7.35: Comparison of the mean bubble rise velocity for different mean particle sizes for NT; $U=4.0U_{mf}$	149
Figure 7.36: Comparison of the mean bubble rise velocity for different mean particle sizes for S6; $U=2.0U_{mf}$	150

List of Tables

Table 4.1: Sieve size distribution and mean particle size.....	56
Table 5.1: Bed pressure drop for various particle sizes and tube geometries at U_{mf}	68
Table 5.2: Measured minimum fluidization velocity of the different particle classes under different tube geometries.	71
Table 6.1: Summary of physical properties and simulation parameters.....	91
Table 6.2: Closure equation used in the simulations.	92
Table 6.3: Comparison of simulation time for different grid sizes and flow domains.	100
Table 6.4: Comparison between 2D and 3D simulations for bed pressure drop; $d_p=246 \mu\text{m}$	102
Table 6.5: Comparison between 2D and 3D simulations for bed expansion ratio; $d_p=246$ μm	103
Table 6.6: Comparison of bed expansion ratio predicted using different friction packing limits; $d_p=246 \mu\text{m}$, $U=2.5U_{mf}$	109
Table 6.7: Comparison of bed expansion ratio predicted using different drag models; $d_p=246 \mu\text{m}$, $U=2.5U_{mf}$	111
Table 6.8: Comparison of bed expansion ratio predicted using different solid-wall boundary conditions; $d_p=246 \mu\text{m}$, $U=2.5U_{mf}$, SC =specularity coefficient.	114
Table 7.1: Simulation parameters.....	117
Table 7.2: Time-averaged bed static pressure drop in kPa.	119
Table 7.3: Time-averaged static bed pressure drop for different mean particle sizes in kPa.	135
Table 7.4: Theoretical minimum slugging velocity for different mean particle sizes.....	140

Nomenclature

Abbreviations:

2D	Two-dimensional
3D	Three-dimensional
AR	Aspect ratio
BB	Bubble boundary
BC	Boundary condition
CFD	Computational fluid dynamics
CVM	Constant viscosity model
DDWT	Druckaufgeladene Dampf-Wirbelschicht-Trocknung
DIAT	Digital image analysis technique
DPM	Discrete particle model
FPL	Friction packing limit
I3	In-line arrangement with three rows of tubes
I4	In-line arrangement with four rows of tubes
I6	In-line arrangement with six rows of tubes
KTGF	Kinetic theory of granular flow
NT	Freely bubbling bed without immersed tubes
RMS	Root mean square
S3	Staggered arrangement with three rows of tubes
S4	Staggered arrangement with four rows of tubes
S6	Staggered arrangement with six rows of tubes
SC	Specularity coefficient
SF	Shape factor
TFM	Two-fluid model
WTA	Wirbelschicht-Trocknung mit interner Abwärmenutzung

Symbols:

A	Constant in Syamlal and O'Brien (1989) drag model
a	Constant in Wen and Yu equation, Equation 5.9
A_B	Project area of a bubble, m^2
A_{c_bed}	Cross-sectional area of the bed, m^2
B	Constant in Syamlal and O'Brien (1989) drag model
b	Constant in Wen and Yu equation, Equation 5.10
c	Compaction modulus, Equation 2.3
C_1	Constant in Wen and Yu equation, Equation 5.12
C_2	Constant in Wen and Yu equation, Equation 5.13
C_d	Drag coefficient

d	Diameter, m
D_{bed}	Diameter of the bed, m
d_t	Tube diameter, m
\overline{D}_s	Strain rate tensor, s^{-1}
d_x	Horizontal extreme of a bubble, m
d_y	Vertical extreme of a bubble, m
e	Coefficient of restitution
E	Exponent in Equation 5.36
F	Exponent in Equation 5.36
f_B	Bubble growth factor in Equation 4.7
Fr	Constant in Johnson et al. (1990) friction model, N/m^2
G	Solids elastic modulus, Pa
g	Gravitational acceleration, m/s^2
g_0	Radial distribution function
h	Distance above the distributor, m
H_0	Fixed bed height, m
H_{mf}	Bed height at minimum fluidization velocity, m
H_f	Fluidized bed height, m
h_{correc}	Corrected bed height above the distributor, m, Equation 5.35
h^*	Maximum bubble height, m, Equation 5.35
I	Unit tensor
I_{2D}	Second invariant of the deviatoric stress tensor, s^{-2}
J_s	Granular energy transfer, $kg/m/s^3$
k	Granular energy diffusion coefficient, $kg/m\cdot s$
K	Factor for the excess gas flow in Equation 5.32
l_t	Length of tubes, m
m_i	Mass percentage of particles
N	Number of bubbles properties, Equation 4.10
n	Constant in Johnson et al. (1990) friction model
N_t	Number of tubes
N_r	Number of tubes rows
n_f	Number of frames
p	Constant in Johnson et al. (1990) friction model
P	Pressure, Pa
P_s	Solids pressure, Pa
P_B	Bubble perimeter, m
P_v	Vertical tube pitch, m
Q	Exponent in Equation 5.32
q	Diffusion of fluctuating energy, kg/s^3
Q_B	Visible bubble flow rate, m^3/s
R	Exponent in Equation 5.32

Re	Reynolds number
S	Exponent in Equation 5.32
t	Time, s
U	Gas superficial velocity, m/s
u_g	Gas phase velocity, m/s
u_s	Solid phase velocity, m/s
U_{mf}	Minimum fluidization velocity, m/s
u_t	Terminal velocity, m/s
u'	Fluctuating velocity, m/s
V_B	Volume occupied by bubbles, m^3
W	Bed width, m
x	Horizontal (radial) coordinate, m
y	Vertical (axial) coordinate, m

Greek Letters:

β	Interphase drag coefficient, $kg/m^3/s$
γ_s	Dissipation of fluctuating energy, $kg/m/s^3$
Δ	Delta
δ	Bed expansion ratio
ϵ_g	Gas phase volume fraction
ϵ_s	Solid phase volume fraction
ϵ_g^*	Compaction gas phase volume fraction
ϵ_t	Relative volume fraction of the tube banks, Equation 5.28
Θ	Granular temperature, m^2/s^2
θ	Bubble property, Equation 4.10
λ	Bubble coalescence parameter, Equation 5.30
μ_g	Gas phase shear viscosity, Pa·s
μ_s	Solid phase shear viscosity, Pa·s
ξ_g	Gas phase bulk viscosity, Pa·s
ξ_s	Solid phase bulk viscosity, Pa·s
ρ_g	Gas phase density, kg/m^3
ρ_s	Solid phase density, kg/m^3
τ_g	Gas phase shear stress tensor, N/m^2
τ_s	Solid phase shear stress tensor, N/m^2
φ	Bubble rise velocity coefficient in Equation 5.36
ϕ	Angle of internal friction, $^\circ$
ϕ_s	Particle sphericity
ϕ'	Specularity coefficient
ψ	Coefficient for the excess gas flow in Equation 5.36

Subscripts:

B	Bubble
col	Collisional
correc	Corrected
dB	Daughter bubble
dense	Dense
dilute	Dilute
f	Frictional
g	Gas phase
int	Initial
kin	Kinetic
max	Maximum
mf	Minimum fluidization
min	Minimum
p	Particle
pB	Parent bubble
s	Solid phase
sl	Slip

1 General Introduction

1.1 Fluidization and Fluidized Beds

Fluidization is a process by which solid particles are suspended and transformed into a fluid-like state by an upward flowing gas or liquid (Kunii and Levenspiel, 1991). When a fluid flows through a bed of fine particles contained in a vessel, at a certain velocity the frictional (drag) force between the flowing fluid and particles becomes large enough to counterbalance the gravity (weight of the particles) and the particles start to ‘float’ in the vessel. At this stage, the pressure drop through any section of the bed equals the weight the particles in that section. This is referred to as an incipiently fluidized bed or a bed at minimum fluidization and the superficial velocity corresponding to this condition is termed as the minimum fluidization velocity (U_{mf}). Beyond this velocity, the resistance to the flow is maximum and bed pressure drop becomes constant with increasing flow. In gas-solid systems, when the velocity is increased beyond the minimum fluidization velocity the particles are lifted higher and the porosity increases with it, and gas bubbles are formed. Such a bed is called bubbling fluidized bed. At even higher velocities, the gas bubbles coalesce and grow as they rise and their size may reach the diameter or width of the vessel in which case the slug flow regime prevails and the gas bubbles are termed as slugs. At sufficiently high gas flow rate, the terminal fall velocity of the solids is exceeded, the upper surface of the bed disappears, entrainment becomes appreciable, and instead of bubbles, one observes a turbulent motion of solid clusters and voids of gas of various sizes and shapes. This is the turbulent fluidized bed. With further increase in gas velocity, solids are carried out of the bed with the gas. In this state we have disperse-, dilute- or lean-phase fluidized bed with pneumatic transport of solids. The different regimes of gas-solid fluidized beds are schematically shown in Figure 1.1.

Gas-solid fluidized beds are widely applied in many chemical and physical processes such as catalytic cracking of oil, gas phase polymerization of olefins and fluidized bed granulation, coal carbonization and gasification to name few (Kunii and Levenspiel, 1991). Their interest in power generations is becoming unabated in recent years, due to the development of circulating fluidized bed combustion chambers. In addition, drying of low-grade brown coals (lignite and sub-bituminous) using fluidized bed to enhance the efficiency of the power plants is becoming a subject of intense research in recent years. The wide use of fluidized bed reactors in industrial processes is due to their several advantageous properties including:

- nearly isothermal conditions due to intense gas-solid mixing
- excellent heat and mass transfer properties
- large gas-solid area due to the small size of the particles
- smooth transport of solids due to liquid-like behavior of the bed

- uniform solid product in batch processes due to intense mixing
- possibility of continuous and large-scale operations

However, these reactors have several drawbacks that provide a strong motivation for further studies and developments. These include:

- difficulty in scaling-up and design
- erosion of vessel and internals that work as heat exchangers
- formation of agglomerates
- lower chemical conversion and non-uniform products due to non-uniform solids residence time during continuous operation
- high particle entrainment which leads to expensive solid separation

These drawbacks are bottlenecks for practitioners to reliably design and scale-up commercial fluidized bed reactors. This makes their design and scale-up to rely more on experience and empirical correlations than fundamentals. The main reason of this is that the complex gas-particle two-phase flows, coupled with heat and mass transfer and chemical reactions that occur in these systems is not yet fully understood.

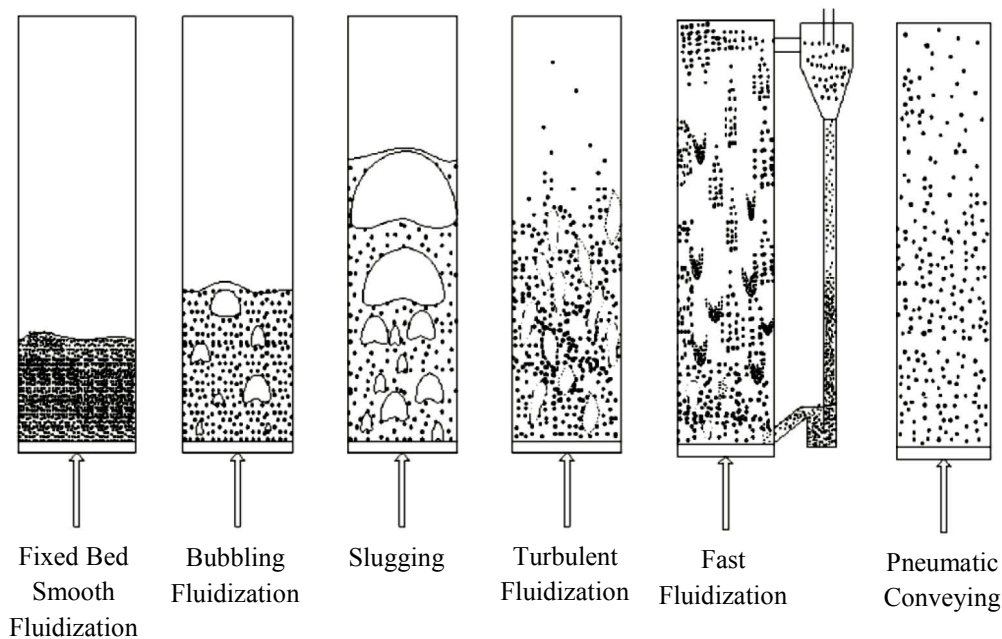


Figure 1.1: Various regimes of fluidization (after Lim et al. 1995)

In bubbling fluidized beds, bubble characteristics such as size, shape, velocity, distribution have a vital influence on the hydrodynamics of the bed and hence on its performance as a chemical reactor and/or a heat exchange unit. The extent of gas-solid mixing and segregation, heat and mass transfer as well as reaction conversion is governed by the number, size and motion of bubbles passing through the bed (Kunii and Levenspiel, 1991). As a result, measurement and prediction of bubble properties in fluidized beds has been a major research subject since the 1940's when the fluid catalytic cracking (FCC) process was first introduced. However, prediction of

bubble characteristics is extremely complex as bubbles can grow, coalesce, split or even disappear as they move from the distributor where they are formed to the top of the bed where they finally erupt. In many industrial applications such as superheated steam fluidized bed lignite dryer, heat exchanger tubes are generally inserted to enhance the rate of heat and mass transfer. However, the bubble behavior is influenced by the geometry and arrangement of the internals that worsen the scenario. Therefore, successful design and scale-up of gas-solid fluidized beds come only after a sound understating of the bubble and bed hydrodynamics is achieved. This will lead to better optimize the design, scale-up and operation of gas-fluidized beds as well as to extend their use to novel applications.

Several experimental techniques have been developed for the past years in an attempt to measure and study the size, velocity and distribution of bubbles in laboratory-scale fluidized beds. Unfortunately, these laboratory-scale data do not necessarily scale-up accurately. To understand best the hydrodynamics in a commercial-scale fluidized bed reactor, it is necessary to study a vessel of that size. However, such experiments are not only prohibitive due to their capital and operational cost but also provide little information on the bubbling properties of the bed. Thus, together with the development of dedicated experimental techniques the development of fundamental hydrodynamic models is of utmost importance to achieve a better understanding of fluidization (Hoomans, 2000). Eventually this will lead to the improvement of existing processes, improved scale-up and the design of more efficient future processes. It is believed that validated Computational Fluid Dynamics (CFD) models can contribute to the successful understanding of bubble characteristics hence the design and optimization of these industrially relevant reactors. However, further model development and validation of the models is still needed.

1.2 Powder Classification

The fluidization behavior of particles depends on their size and density. Small particles with a low density are more easily fluidized than large and heavy particles, as the gravity acting on the latter type is much larger. On the other hand, the inter-particle forces on small particles are relatively more important than the same forces acting on large particles, causing small particles to exhibit a certain (velocity) range of homogeneous expansion. If the particles are fine or sticky, the bed will be cohesive. It will then tend to form channels through which the aeration gas will escape rather than being dispersed through the interstices supporting the particles. In the other extreme: if the particles are too large and heavy the bed will not fluidize well either, but tend to be very turbulent and form a spout. According to their fluidization behavior at atmospheric pressure and air as a fluidizing gas, Geldart (1973) classified powders into four different types as shown in Figure 1.2. Detail description of the different powder classifications can be found in the paper by Geldart (1973) or the book by Geldart (1986).

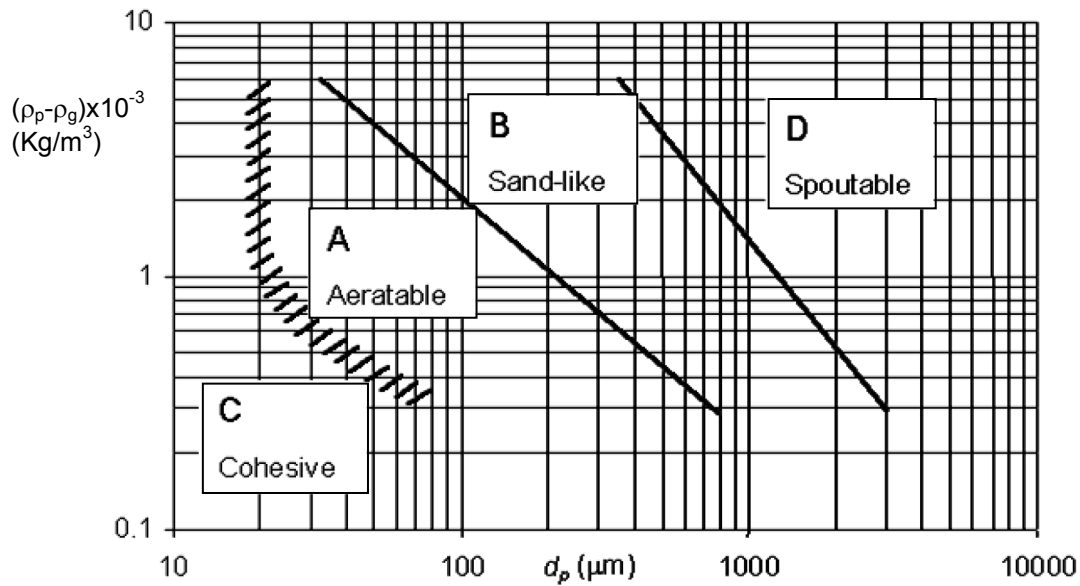


Figure 1.2: Geldart's Classification of powders (Geldart, 1973)

Group A is designated as 'aeratable' particles. These powders have small mean particle size ($d_p < 130 \mu\text{m}$) and/or low particle density ($< \sim 1400 \text{ kg/m}^3$). A typical example of this group is the fluid cracking catalysts. These powders fluidize easily, with smooth fluidization at low gas velocities without the formation of bubbles. With increasing superficial velocity above the U_{mf} , these powders expand considerably until the minimum bubbling velocity, U_{mb} at which bubbles start to form. This is due to the slight cohesiveness of the powders. The minimum bubbling velocity U_{mb} is always greater than minimum fluidization velocity U_{mf} . Bubbles appear to split and coalesce very frequently, resulting in a restricted bubble size.

Group B is called 'sandlike' particles and some call it bubbly particles. Most particles of this group have size 60 to 500 μm and density from 1000 to 4000 kg/m^3 . In contrast to Group A, Group B particles have negligible inter-particle forces and once the minimum fluidization velocity is exceeded, the excess gas appears in the form of bubbles. Bubbles in a bed of Group B particles can grow to a large size. Bed expansion is relatively small compared to Group A and the bed collapses very rapidly when the gas supply is cut off. Typically used Group B materials are glass beads (ballotini) and coarse sand.

Group C is called 'cohesive' or very fine powders. Their sizes are usually less than 20 μm , and they are extremely difficult to fluidize under normal conditions because the inter-particle forces are greater than those the fluid can exert on the particle. The powder lifts as a plug in small diameter tubes or forms channels that can extend from the distributor to the bed surface. Fluidization can usually be made possible or improved by the use of mechanical stirrers or vibrators that break up the stable channels. The bed pressure drop across the bed is lower than the theoretical

value (bed weight per unit cross sectional area). Examples of Group C materials are talc, flour and starch.

Group D is called ‘spoutable’ and the materials are either very large or very dense. They are difficult to fluidize in deep beds. All but all bubbles rise more slowly than the interstitial gas velocity, so that gas flows into the base of the bubble and out of the top, providing a mode of gas exchange and bypassing which is different from that observed with Group A or B powders. Unlike Group B particles, as velocity increases, a jet can be formed in the bed and material may then be blown out with the jet in a spouting motion. Roasting coffee beans, lead shot and some roasting metal ores are examples of Group D materials.

1.3 Steam Fluidized Bed Drying of Lignite

Fluidized bed drying is ideal for a wide range of particulate or granular solids that can be readily fluidized and has found widespread usage in various industries including those in power generation, chemicals, pharmaceutical and biochemical, food and dairy products, and polymers (Reay, 1986; Chandran et al., 1990; Kunii and Levenspiel, 1999). They have the advantage of high drying rate due to their excellent gas-particle contact in the bed that offers high rates of heat and mass transfer. Moreover, the thermal efficiency of these systems is high, and it is possible to achieve a nearly uniform and closely controllable temperature in the bed (Reay, 1986; Chandran et al., 1990). Other advantages include smaller flow area because of its large hold-up of solids, relatively lower capital and maintenance cost as there are no moving parts, ease of control, and easy material transport inside the dryer. However, there are some limitations that include: high pressure drop, high electrical power consumption, poor fluidization quality of some particulate products such as very sticky materials, possibility of non-uniform product quality as a result of non-uniform residence time during continuous operation, erosion of pipes and vessels, entrainment of fine particles, attrition or pulverization of particles, and agglomeration of fine particles. These limitations are generally related to the lack of fundamental understanding of the fluidized bed hydrodynamics specially bubbling behavior as described above.

In recent years, drying low rank coals in fluidized beds is getting more attention from power generation industry as well as academia. Low rank coal (also known as brown coal, mainly lignite) is an integral part of power generation in the world. In Germany, the largest producer of lignite, for example, lignite covers one quarter of the total electricity production of the country. Lignite can be used as replacement for more expensive bituminous coals, either as blending components in existing boilers, or in new boilers designed for use of lignite. However, the high amount of moisture in lignite leads to higher energy requirements during combustion, high amount of stack gas flow, lower plant efficiency and potential safety hazards during transportation and storage. Thus, the use of lignite requires drying as a pre-processing step as an essential component in any fuel upgrading processes (Karthikeyan et al., 2009).

In conventional pulverized lignite fired power plants, lignite drying is realized in the coal mills by hot flue gases that are re-circulated from the steam generator furnace at temperatures between 900 and 1000 °C. The evaporated lignite moisture leaves the power plant as a component of the flue gas stream, which resulted in a substantial loss of exergy and consequently the overall efficiency is relatively low. Moreover, the flue gas volume considerably increased. By drying the lignite outside the main process at lower temperature level, these effects can be significantly reduced. For this purpose there are some dryers developed to choose from and were discussed in detail by Pikon and Mujumdar (2006) along with their advantages and limitations. An important issue to be considered while drying lignite is the energy used to remove the huge amount of moisture from comparatively low value coal type. An energetically efficient, cost-effective and safe drying process is necessary to improve the overall efficiency and lead to higher returns. In power generation, where continuous drying with large amount of lignite is needed, fluidized bed dryers are suitable and appropriate technologies in this regard. In addition to their excellent heat and mass transfer characteristics, fluidized bed dryers offers smooth operation and easy control of the process with continuous drying and handling of large quantities of lignite.

In drying of lignite in fluidized bed dryers, selecting the appropriate drying medium and/or fluidizing gas is crucial for the safe and efficient operation of the drying process. Traditionally, drying medium such as air, flue gases and superheated steam have been used (Mujumdar, 2006). Two important issues have to be taken into account while selecting appropriate drying and/or fluidizing medium for lignite. The first is that it is necessary to regenerate the enthalpy from the evaporated moisture of the lignite. Since drying lignite is an energy intensive process and is accompanied by the release of huge amount of moisture at appreciably higher enthalpy, any upgrading of lignite through external drying should be equipped with some way of reusing or regenerating the steam enthalpy from the vaporized moisture. The second is that it is important not to have high oxygen content in the drying gas to avoid explosion and fire hazard. Lignite is more susceptible to fire and explosion hazards due to spontaneous combustion as a result of self-heating caused by its reactive nature (Karthikeyan et al., 2008). Therefore, selecting the drying medium is very important for safe operation of lignite drying process and minimize the cost and energy consumption thereafter improve the power plant efficiency. Among different gases used, superheated steam is an attractive alternative in this regard. The use of superheated steam for drying lignite has a number of advantages (Pikon and Mujumdar, 2006; Wilson et al., 1997), including:

- improve safety through the reduced risk of explosion or fire (due to lack of oxygen)
- increase drying rates, depending on the steam temperature
- increase thermal efficiency as the energy in the exhaust stream can be recovered easily
- reduce significantly dust emission
- improve coal grindability
- reduce sulphur and sodium contents.

While the energy necessary in order to evaporate the moisture can be provided by the fluidizing gas, in lignite drying applications additional heat is supplied by steam tubes immersed in the fluidized bed. In this way, the temperature level of the process is increased, which over proportionally increases the vapor uptake capacity of the steam, resulting in significant decrease of the necessary dryer cross-sectional area and fluidizing gas demand (Reay, 1986). It was reported that using superheat steam drying of lignite in fluidized beds with horizontal heat exchanger tubes and reusing the coal/steam enthalpy, an efficiency increase of 3 to 5 % of the power plant is possible (Leithner, 2002; Wick and Kallmeyer, 1997).

The concept of superheated steam drying in a fluidized bed with internal heat exchangers was originally developed by Professor O.E. Potter of Monash University in Australia in mid-80's (Karthikeyan et al., 2009). Potter et al. (1983, 1990) have described these early-developed steam fluidized beds for lignite drying along with some experimental measurements. They showed that extremely favorable heat transfer rates as well as drying efficiencies are obtained when drying brown coal in a steam-fluidized bed with internal heat exchanger tubes immersed within it. This concept was later refined and developed by RWE Power AG into the WTA (Wirbelschicht-Trocknung mit interner Abwärmenutzung) superheated steam drying process (Klutz et al., 1996). The WTA technology is based on the principle of stationary fluidized bed with low bed expansion. The energy required for drying is supplied via heat exchangers that are integrated in the fluidized bed dryer and heated with steam. Drying takes place in virtually 100 % pure steam that is slightly superheated. Over the past 20 years, RWE Power AG has developed three variants of the WTA fluidized bed of superheated steam dryer depending on the use of the vapor enthalpy (Klutz et al., 2010). The first WTA variant contains a condenser for condensing the vaporized moisture from the lignite. The condenser is usually a low-pressure feedwater heater that utilizes the heat released from the vapor to preheat the boiler feedwater. The second WTA dryer includes a vapor re-compressor to recover the latent heat and reuse the heat in the dryer's heat exchangers with and without integrated lignite pre-heating. The steam is compressed to 4 bar and 150 °C for heating the fluidized bed in the dryer via submerged tubular heat exchanger bundles in which this steam is condensed. The third is of low-cost variant without use of the vapor, such can be deployed, e.g. to improve the calorific value of moisture-and ash-rich lignite. The WTA was successfully used to dry lignite from 55-60 % moisture content down to 12 % moisture (Klutz et al., 2008). These WTA processes are operating at atmospheric or even low pressure of 50 mbar and slightly superheated steam with temperature of around 110 °C. It was reported that the WTA process consumes 80 % less energy compared to rotary steam tube dryer with 80 % less dust emission and lower capital investment (Klutz et al., 2008).

Considering the investment cost involved for an atmospheric drying plant such as the WTA, the improvement for the cost-benefit ratio in relation to the prime power production costs is not sufficient (Leidich et al., 2005). Thus, an alternative technology was proposed by employing a pressurized fluidized bed drying process. By doing so, it is not only an increased in efficiency of 4 to 5 % is achieved, but also keeps the costs of the pressurized drying process below the poten-

tial investment cost savings as compared to the atmospheric drying process (Leidich et al., 2005). This concept named as DDWT (Druckaufgeladene Dampf-Wirbelschicht-Trocknung) was developed and a pilot test facility was built at the Chair of Power Plant Technology, Brandenburg University of Technology Cottbus (BTU Cottbus) (Martin et al., 2007). The process is similar to WTA with internal heating of fluidized bed except high pressure steam is used for drying purpose. The test facility has a capacity of 0.5 t/h for system pressures of 1.1 to 6.5 bars abs and its schematic diagram is shown in Figure 1.3. Detail constructional and process description and experimental results can be found in Martin et al. (2007), Lechner et al. (2009) and Hoehne et al. (2010). Lechner et al. (2009) and Hoehne et al. (2010) have carried out successive experiments using the test facility for different particle sizes and pressure levels. The experiments were carried out to dry 240-500 kg/h of lignite from 50-60 % moisture to 5-30 %. They reported that a mean heat transfer coefficient of 250-300 W/(m²K) can be achieved depending on the type of coal and the coal particle size. They also have reported the effect of steam pressure, velocity and particle size on heat transfer coefficient. It was found that the overheating of fluidized bed results in removal of more water as the temperature required to remove the water in the capillaries is more than the required temperature for surface water. As a result of higher heat transfer coefficient at higher pressure the heat transfer area is reduce which gives small and compact dryer, it is also possible to get steam at higher temperature to reuse in the power plant cycle. Generally, increasing the operating pressure and temperature in fluidized bed steam dryer increased the drying rate and improved the system efficiency as pressure improves the fluidization quality. Promising results of the test facility at BTU Cottbus have led to scaling-up to a pilot plant with a capacity of 10 tons per hour at Schwarze Pumpe power plant in Germany. Since its start-up in 2009, the plant is running successfully and is capable of reducing the coal moisture to 5-20 % (Hoehne et al., 2010).

Despite some progresses and promising results were obtained for the last 20 years, fluidized bed steam drying of lignite have not been successfully utilized in industrial scale yet. Keeping in mind the fact that lignite is not a high value product it is clear that power plant companies are reluctant to use thermal drying for low rank coal as there is hardly any value addition using existing drying systems. Hence, it is necessary to use very energy-efficient drying systems to make it cost-effective so that the cost of such dryers is minimal. In this regard, the pressurized steam fluidized bed drying is a promising technology, but there are still many works to be done in order to improve its design and scale-up in industrial scale. The performance of these fluidized beds highly depends on the quality of fluidizations that is determined by the size and shape of the particles, superficial velocity, and immersed tube geometries. At least these three control parameters should be properly selected in order to maintain the optimum gas-solid flow patterns within the dryer, to help good product quality and minimizing drying time. The particle physical characteristics are a function of the granule preparation as well as the moisture content. While bed geometry such as immersed tube bank geometry is set during the design and construction of the dryer, superficial gas velocity may be manipulated throughout the drying process.

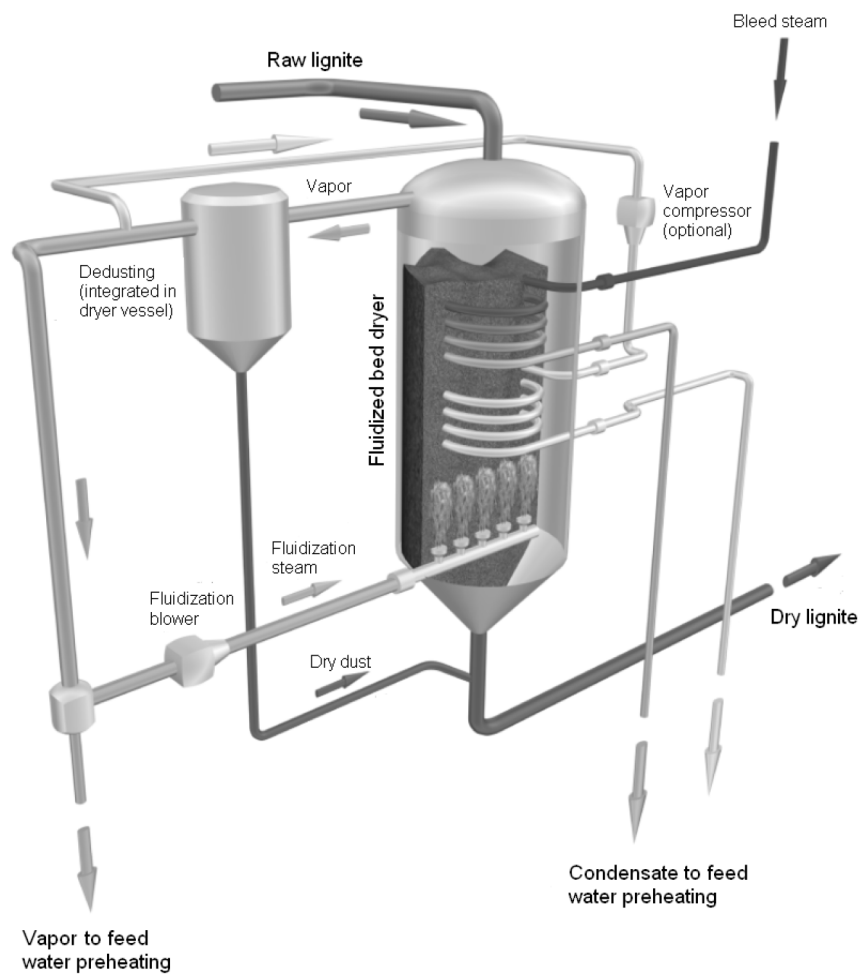


Figure 1.3: Schematic diagram of the pressurized steam fluidized bed drying (PSFBD) process at the Brandenburg University of Technology Cottbus (BTU Cottbus).

The selection of an appropriate superficial gas velocity is critical for the efficient implementation of fluidized bed drying that determines the optimum fluidization regime. In drying process, high heat and mass transfer is desirable which leads to reduced drying times. The intimate contacting of the gas with the solids provided in the turbulent regime is attractive for this purpose since bypassing of the gas present in the bubbling regime is eliminated. However, the vigorous mixing provided in this regime also leads to a potential increase in entrainment of fine particles and attrition of the particles. It is desirable to reduce both of these effects. Therefore, fluidized bed dryers are preferably operated in the regimes of smooth and bubbling fluidization. Bubbling fluidized beds are one of the most convenient means for interaction between solid and gas flow, mainly due to the good mixing and high heat and mass transfer rate induced by the motion of bubbles. Makkawi et al. (2007) reported that the quality of fluidization in bubbling fluidized beds is generally controlled by the bubble hydrodynamics such as bubble shape, size, distribution and rise velocity. They showed that the overall mass transfer during drying depends on the bubble diameter and velocity and correlated the mass transfer coefficient as a function of bubble

diameter and rise velocity. Vigorous bubble action gives better particle circulation and mixing, and thus increases the contacting efficiency between the bed and the heat transfer surface. In superheated steam fluidized bed drying of lignite, since the heat transfer arising from the temperature difference between the lignite and drying steam governs the moisture transfer, bubble characteristics of the bed play significant role in the drying rate and drying characteristics. Therefore, the design of bubbling fluidized bed dryer requires understanding of the complex bubble hydrodynamics and its implication in the heat and mass transfer mechanism.

1.4 Motivation and Objective

Conversion and utilization of energy from fossil fuels is becoming the center of arguments due to the limited resources and their environmental impacts. Concerning the future fuel mix, energy outlooks tend to agree that the contribution of renewable energy sources will increase, but will not dominate the electricity generation sector until at least 2030, while the nuclear power plant capacity will either shrink or remain unchanged. Therefore, fossil fuel power plants will remain the backbone of electricity-generating sector. Continuing reliance on fossil fuels necessitates the deployment of power plant technologies with minimal possible carbon footprint, such as advanced power plants that capture most of the CO₂ generated. However, such power plants will be more expensive to build and operate than similar plants that do not capture CO₂. Hence, these technologies would not be deployed in the absence of financial incentives. Moreover, power plants with carbon capture facilities are less efficient than conventional power plants, so their deployment could lead to an increase in fossil fuel consumption with impacts on the security of the supply. Therefore, the best solution would be to increase the efficiency of the conventional power plants. This has not only an economic advantage, but also reduces the fuel consumption, hence reduces the CO₂ production and provides better security of supply.

Coal is the major fuel for the generation of electricity in the world. In Germany, almost half of the total electricity came for coal-fired power plants. Germany is the largest lignite producer in the world with an annual production of 178 million tons and a share of 19 %. The three German mining areas (the Lusatian, the Central German, and the Rhineland) provide lignite reserves amounting to 6600 million tons and resources amounting to 76 billion tons (BMW_i, 2006). In 2009, 24 % the electricity production is covered by lignite followed by nuclear energy (23 %), hard coal (18 %), renewable energy (16 %), and natural gas (13 %) (BDEW, 2010). Its share is expected to increase in the future due to the shrinking and phase out of nuclear power plants approx. by the year 2021. However, compared to hard coal, lignite contain significant amount of moisture that resulted in lower heating value. Typically, the moisture content of German lignite ranges from 50-60 wt-%. Such high fuel moisture has several adverse effects on the operation of a pulverized coal power plant such as higher fuel flow rate (tonnage), higher stack flue gas flow rate, higher station service power, lower plant efficiency, and higher mill, coal pipe and burner

maintenance requirements. Thus, developing coal dewatering and drying processes could reduce some problems arising from the use of these fuels.

In conventional pulverized lignite fired power plants, lignite drying is realized by re-circulating hot flue gases that resulted in reducing the overall power plant efficiency as well as considerably increasing the flue gas volume. Therefore, by drying the lignite outside the main process at lower temperature level or by mechanical means these effects can be significantly reduced. As discussed in section 1.3, a fluidized bed dryer using superheated steam is the most suitable and appropriate technology for this purpose. With this technology, it is possible to develop a safe, cost-effective and sustainable drying system. Due to their higher rate of heat and mass transfers, these dryers have higher thermal efficiency and lower drying time. Moreover, they can be integrated to existing and new power plants without major modification of the power plant process. This makes the dryer small and compact. However, the design and scale-up of such dryers have been complicated and insufficient mainly due to lack of comprehensive understanding of the complex gas-solid flow dynamics. Since the performance of bubbling fluidized beds highly depends on the bubbling behavior, a good understanding of the bubble hydrodynamics (such as bubble size, velocity, shapes, flow pattern) is necessary to understand bubble-related phenomena such as solids mixing and segregation, reaction conversion, heat and mass transfer, erosion of heat transfer tubes, and particle entrainment (Lim et al., 1995). This will lead to an improved understanding of the design and scale-up procedure of fluidized bed lignite dryers.

Therefore, the main objective of this work is to investigate thoroughly the bubble hydrodynamics of fluidized beds with immersed horizontal tubes in order to improve the understanding of the bed hydrodynamics thereafter the heat and mass transfer and drying rate. Its focus was to investigate the influence of different tube bank geometries, superficial gas velocity and particle size on bubble characteristics such as bubble shape, bubble diameter and bubble rise velocity. In this study, both experimental and numerical techniques were employed. For the experimental measurements a novel nonintrusive digital image analysis technique was developed. The technique was validated and equally applicable for the analysis of numerical results. For the numerical studies, the two-fluid model based on the kinetic theory of granular flow was used. The model was thoroughly validated using the experimental data for bubble properties and bed expansion.

1.5 Outline of the Thesis

The dissertation is organized in eight chapters. Chapter 1 introduces fluidization technology and regimes, their application and classification of powders. It discusses the use of fluidized beds in lignite drying and describes the motivation and research questions of the dissertation. It outlines the objective of the thesis and its scope.

In Chapter 2, a concise review of experimental and numerical techniques used for the study of bubbling behavior of fluidized beds is presented. The focus of the review lays on the most widely used experimental techniques particularly the digital image analysis technique and the two-fluid model of numerical modeling. Moreover, a review on the influence of internal obstacles on the bubble hydrodynamics of fluidized beds is presented.

In Chapter 3, a detail description of the two-fluid model is presented. The governing equations and closure equation based on the principle of the kinetic theory of granular flow are discussed. Different closure equations available in the literature are summarized and compared. Moreover, simulation parameters used such as the initial and boundary conditions, discretization schemes, grid size and time steps are presented.

Chapter 4 describes the detail experimental setup and measurement technique used in this dissertation. Detail description of the in-house software developed for the automation of the digital image analysis technique as well as its validation is presented. In this chapter the particle characteristic such as size distribution and mean particle size are also presented.

In Chapter 5 a theoretical background and theoretical modeling of the bed expansion and bubble properties such as diameter and rise velocity are presented. New theoretical correlations were developed for the bubble diameter, bubble rise velocity and bed expansion ratio. Detail validation of these models with existing correlations and experimental measurements is also presented.

In Chapter 6 a comprehensive validation of the two-fluid model using experimental measurements of bubble characteristics and bed expansion for different bed geometries, particle sizes and superficial velocities is presented. The influence of bubble definition and averaging periods on the simulation results as well as different modeling parameters such as drag coefficients, friction packing limits and solid-wall boundary conditions are presented. Moreover, the influence of 2D and 3D simulations and grid sizes on the bubble properties as well as bed expansion is discussed.

In Chapter 7 detail investigation of the influence of tube bank geometry and arrangement, superficial velocity and particle sizes on the bubbling behavior as well as bed expansion and pressure drop are presented. Moreover, comprehensive comparison of the experimental measurements and simulation results are presented.

The thesis ends with conclusions and recommendations of the research findings and by outlining future works in Chapter 8.

2 State of the Scientific Knowledge

2.1 Introduction

Nowadays gas-fluidized beds have widespread applications in the petroleum, chemical, metallurgical and energy industries. However, their current understanding of the complex fluid-particle two-phase flow patterns coupled with heat and mass transfer and chemical reactions, is still insufficient for practitioners to reliably design and scale-up commercial fluidized bed reactors (Deen et al., 2007). The reason for this shortcoming is that the flow behavior of fluidized beds is complex and much of the design criteria are specific to the system size/geometry and limited operating conditions.

In dense bubbling gas-solid fluidized bed systems, the bed has regions of very low solid concentration, which is referred to as bubbles and regions of higher solids density, which is referred to as the emulsion phase. The fluidization quality hence the performance and efficiency of these fluidized beds highly depends on the distribution of the bubbles and their physical properties in the bed. The dynamics of the bubbles dictate the flow of gas and solids, mixing of solids and therefore the heat and mass transfer of the reactor. These bubbles are also a source of heterogeneity that will reduce the efficiency of contact between the gas and particles, and they usually move faster than the surrounding gas so that the residence time of the gas associated with them is reduced (Kaart et al., 1999). Therefore, fundamental understanding of the bubbling behavior of fluidized beds is necessary to understand bubble-related phenomena such as solids mixing and segregation, reaction conversion, heat and mass transfer, erosion of heat transfer tubes and particle entrainment (Lim et al. 1995). This will lead to improve the scale-up and design procedures thereafter their performance and efficiency. However, the physical mechanisms that contribute to bubble formation and their dynamics are not fully comprehended principally due to the difficulty in measuring their physical and geometrical properties in the entire bed cross-section.

The parameters characterizing bubbles are their shape, size, distribution, frequency of occurrence, and rise velocity. Ideally, for there to be good quality of fluidization bubbles should be large in number but small in size, homogeneously distributed over the bed volume and have low rise velocities. Practically bubbles are irregular in shape and size, inhomogeneously distributed over the bed volume and with much higher rise velocity than the interstitial gas velocity. Moreover, bubbles can break-up, coalesce and disappear in the bed as they rise from the distributor along the bed height that worsens the scenario. Thus, measuring and analyzing of bubble characteristics over the entire bed is a very complex and tedious task. The successful approach toward the understanding of such complex flows requires reliable experimental data, which, in turn, depends on the implementation of sophisticated measuring techniques capable of preferably nonintrusive investigation as well as the ability to provide the required information over the

entire flow field. In addition, it is desirable that such techniques are amenable for automation to reduce extensive human involvement in the data collection process. For the last 70 years or more, several experimental techniques were extensively applied to study the bubble behavior. Using many of the experimental techniques, it is difficult to visually observe the flow structure thus the bubble dynamics of the bed due to the harsh environment and opaque nature of the gas-solid flow structure of fluidized beds. In addition, these experimental techniques produce limited, specific, and expensive results. As a result, little success has been achieved so far and the bubble behavior is still not well understood. In recent years as a result of rapid growth of computer technology, CFD models are becoming a valuable and indispensable research means. However, these computer models require intensive validation using reliable experimental data for a wide range of particle size, fluidized bed geometry and operating conditions. In the following sections, concise reviews of the experimental and numerical techniques used in measuring and analyzing bubble properties in gas-solid fluidized bed were presented. Moreover, the influence of immersed horizontal tubes on the bubbling behavior was reviewed.

2.2 Experimental Techniques

Since the inception of fluidized beds in the early 1940s, a large number of measurement techniques have been developed and utilized for the study of the fluid dynamics of the systems. A number of excellent reviews have been published in the past regarding these measurement techniques including those early reviews by Grace and Baeyens (1986), Cheremisinoff (1986), Yates and Simons (1994) and Simons (1995). In relatively recent publications Chaouki et al. (1997a,b) extensively reviewed nonintrusive measurement techniques for multiphase flows in general. Werther (1999) gave an overview of measurement techniques in fluidized beds, with emphasis on applicability in industrial practice. van Ommen and Mudde (2008) reviewed experimental techniques used in the study of voidage distribution in dense gas-solid fluidized beds.

2.2.1 Intrusive and nonintrusive measurement techniques

The measurement techniques utilized for the study of gas-solid fluidized beds can be broadly classified into two categories depending on the nature and position of the sensors used: (i) intrusive techniques, namely those based on resistance, inductance, impedance, piezoelectric or thermal probes, and (ii) nonintrusive techniques, among others those based on photographic and imaging, tomography, light scattering and laser techniques. Unfortunately, many of the measurement techniques developed are suitable for measurement of the local void fraction and particle distribution; the techniques that are available for measurement of bubble size and velocity are few in number. In the following sections, only the most frequently used measurement techniques for bubble characteristics were presented.

2.2.1.1 Intrusive measurement techniques

Numerous experimental studies have used immersed probes to determine bubble parameters. Their operations are based on a variety of physical effects such as electrical impedance and optical principle. The electrical impedance probes used conductive, resistive or capacitive effect. The conductive and resistive probes are not suitable for non-conductive gas-solid fluidized beds and can only be used with liquids and electrically conductive solids (Matsuura and Fan, 1984; Safoniuk et al. 2002). On the other hand, the capacitance probes can be used in non-polar media such as gas-solid fluidized beds.

The capacitance of a gas-solid mixture is a strong function of the concentration of solids in the mixture and capacitance probe will respond to a change in the local solid concentration, such as when a gas bubble passes the probe. Therefore, capacitance probe make use of the difference in the dielectric constant associated with each phase for phasic discrimination. Geldart and Kelsey (1972) appear to be the first to investigate the bubble motion in thin two-dimensional (2D) and three-dimensional (3D) beds using capacitance probes in an attempt to correlate three- and two-dimensional bubble sizes. Their probe head consisted of two parallel plates and its response was compared to the direct observations made by cine filming of 2D bed. Their results were not good due to the highly intrusive nature of their probe. They concluded that interpretation of capacitance probe results in terms of bubble sizes, bubble voidages or cumulative numbers of bubble passing a given level should be treated with some reserve. Gunn and Al-Doori (1985) used somewhat similar but more detailed investigation of bubble probe interactions. They measured bubble velocities, dimensions and flow rates in a 2D fluidized bed, and compared the results with measurements from cine photography. They found that both sets of measurements agreed only when the conditions of electrical measurement were arranged to exclude spurious signals. They also stressed the importance of proper calibration of the probe.

Werther and Molerus (1973a,b) carried out a meticulous study on the design and use of capacitance probe that has been the benchmark for subsequent work in this area. They developed a miniaturized capacitance probe with central protruding needle. With this probe, they were able to reduce the disturbance of the bed. The probe was able to measure bubble parameters such as local value of bubble gas flow, bubble volume fraction, mean pierced bubble length, and mean bubble rise velocity. Werther and Molerus (1973b) reported detailed experimental results on bubble behavior for fluidized beds with different diameters and with different sizes and densities. They found that close to the distributor a zone of increasing bubble formation exist in an annulus close to the wall. This zone moves towards the centre of the bed with increasing height above the distributor. Almstedt and Co-workers applied this technique extensively to study bubble hydrodynamics of fluidized with and without immersed tubes (Almstedt and Zakkay, 1990; Olowson and Almstedt, 1990; Olowson and Almstedt, 1992; Olowson, 1994; Olsson et al., 1995; Wiman and Almstedt, 1997; Wiman and Almstedt, 1998). They extensively studied the influence of pressure, superficial velocity, and tube bank geometry on the hydrodynamics of

bubbling fluidized beds with and without immersed horizontal tubes. Other recent work was that of van Lare et al. (1997) who applied a two-point capacitance probe to characterize the bubble behavior in a fluidized-bed reactor. Surprisingly this technique has not been utilized in recent years primarily due to some potential problems in applying this method in bubbling fluidized beds. Bubbles that are rising in a direction not aligned with the two probes lead to major errors. Another serious shortcoming of capacitance probes is that they must be calibrated for every fluid-solid system and operating condition (in particular temperature and pressure).

Another important intrusive measurement technique widely used in measuring bubble characteristics in fluidized beds is the fiber optical probe (Mainland and Welty 1995; Crowe et al., 1998). An optical fiber probe system consists of a probe head, a light source, a photo detector and the signal processing unit. These probes exploit the difference in the index of refraction of the two phases. Depending on which phase exists at the probe's tip the light from the tip is reflected or refracted. They are relatively simple, have high accuracy and relatively low cost. In addition, optical probes are suitable for both low and high-temperature conditions and are not sensitive to the physical properties of the gas-solid constituents thus there is no need to calibrate for particular system or operating conditions (Mainland and Welty, 1995). One of the main disadvantages of the optical fiber is that the interpretation of the electrical signal generated by the probes is a potential source of error (Yates and Simons, 1994; Mainland and Welty, 1995).

Optical fiber probes have been widely applied for the measurement of particle velocity and particle concentration than bubble properties measurements. Though the use of optical fibers is started in the early 80's (e.g. Ishida and Shirai, 1980; Hatano and Ishida, 1981; Glicksman et al., 1987), more works on measurement of bubble properties have been published in the last couple of decades. Mainland and Welty (1995) used an optical probe to calculate bubble properties such as bubble frequency, local bubble residence time, bubble velocity, pierced length, bubble size, and visible bubble flow in a 2D bed. The bubble information obtained from the probe signal was confirmed by comparison with visual information (videotape) of 2D bed. Schweitzer et al. (2001) used an optical fiber probe to measure the gas hold up and bubble rise velocity in gas solid fluidized bed and slurry bubble column. Kim et al. (2003) used a transmission type of optical probe to measure bubble frequency around the circumference of an immersed heat transfer tubes. Sobrino et al. (2009) investigated the effect of rotating distributor on the size, spatial distribution and frequency of the bubbles in fluidized beds. Pugsley et al. (2003) used fiber optical probe for verification of electrical capacitance tomography (ECT) measurements in bubbling fluidized bed. More recently, Liu et al. (2010) used this technique to validate bubble size obtained from pressure fluctuations measurement.

2.2.1.2 Nonintrusive measurement techniques

The intrusive measurement techniques are generally cheaper and more convenient and their use has helped to advance the understanding of gas-solid fluidized bed hydrodynamics considerably.

However, the results from these techniques are usually not sufficient to explain the intricate behavior of bubbles. These intrusive probes have some drawbacks. Firstly, these probes are intrusive and may disturb the flow that they are intended to measure. Rowe and Masson (1981) reported that there are always uncertainties in the extent to which such probes interfere with the flow of gas and bubbles, thus their measurements are always subjected to doubts. Secondly, measurement ports must be created at several angular positions around the circumference and/or bed height or it is required to move the measurement probes through the whole volume of the bed in order to map the entire flow field of the fluidized bed. In addition, these probes usually measure the pierced bubble length instead of mean characteristic bubble diameter. The interpretation and conversion of the pierced length to mean bubble diameter is not straightforward as it needs complex algorithm and computational effort (Lim and Agarwal, 1990; Liu and Clark, 1995). Therefore, despite some limitations, the nonintrusive techniques are to be preferred for an accurate measurement of fluidized bed hydrodynamics specially bubble properties.

In the last 20 years, advances in instrumentation technology as well as in computer control have led to spectacular progress in the development of nonintrusive measurement and flow visualization techniques for multiphase flows (Chaouki et al., 1997a). Excellent review of these various nonintrusive measurement techniques can be found elsewhere in the literature (Chaouki et al., 1997a,b). Unlike to the intrusive techniques, nonintrusive techniques provide good visual observation without interfering with the fluidization process. Generally, these nonintrusive measurement techniques used for measuring bubble characteristics can be broadly categorized as photography and cinematography, tomography, and pressure fluctuation techniques. Photography and/or cinematography are the oldest and simplest nonintrusive measurement techniques. Pictures of the dispersion are taken through plane parallel windows installed in the fluidized bed column. The pictures or cine films of the bed can be visualized by either video camera or X-ray transmission. In recent development of the technique computerized image processing are incorporated to automate the calculation of bubble properties that leads to digital image analysis technique. This technique is becoming a promising method and has been used in this work. Detail discussion of this technique is presented in section 2.2.2 below.

Process tomography is another important nonintrusive measurement technique that is based on mapping the entire cross-section of a process vessel. Depending on the imaging technique, there are several tomographic techniques such as γ -ray and X-ray tomography, positron emission tomography, X-ray and neutron transmission radiography, nuclear magnetic resonance imaging, electrical capacitance tomography, optical tomography, ultrasonic tomography and microwave tomography. Detail discussion of these different tomographic techniques is available in the literature (Chaouki et al., 1997a). Among these the Electrical Capacitance Tomography (ECT) and X-ray techniques are regarded as the two types of the most attractive techniques in fluidized bed hydrodynamic investigations (Halow, 1997; Werther, 1999).

The basic principle of the ECT technique is to measure the permittivity distribution of two-conducting materials, in a containing vessel, by measuring the capacitance between electrode pairs placed around the column circumference. In gas-solid fluidized beds, it exploits the difference in relative permittivity of the two phases in order to produce images of the distribution of these phases over the bed cross-section. This allows for the calculation of key bubble or void properties such as diameter and velocity (Halow, 1997; McKeen and Pugsley, 2003). One of the major disadvantages of this technique is that it requires image reconstruction that requires complex algorithms and consumes significant time. Sometimes such reconstruction may also lead to some artifacts (Mudde, 2010). Another disadvantage is that ECT has low spatial resolution, though it has high temporal resolution compared to other tomographic techniques such as those based on X-ray transmission. Moreover, this technique measures bubble characteristics at the specified location where the sensors are located. Hence, it is difficult to analyze bubble properties along the entire bed cross-section.

There are several works published regarding the use of ECT for fluidized bed studies (Halow, 1997; Chaouki et al., 1997a; Dyakowski et al., 1997; Chaplin and Pugsley, 2005; White, 2005; Makkawi and Ocone, 2007). However, the majority of these works focused on the voidage and solid distribution of the bed cross-section. Halow and Nicoletti (1992) and Halow et al. (1993) used a high-speed three-dimensional capacitance imaging technique to measure voidage distributions and bubble properties such as size and rise velocity. They observed different forms of coalescence and develop a correlation for bubble rise velocity by including the bubble length as the primary dimension defining the bubble. Wang et al. (1995) used ECT to investigate the flow pattern near the distributor plate for bubbling, slugging and turbulent regimes. They also measured bubble length for the bubbling and slugging regimes. Makkawi and Wright (2004) studied the hydrodynamic change resulting from the addition of small quantity of liquid into a dry fluidized bed. They quantified the change in regime transition velocities, pressure drop, bubble rise velocity, bubble frequency and bubble flow rate. Cao et al. (2008) investigated the influence of pressure on the bubble size and average bed voidage in a circular 3D bed using ECT technique. They used the results obtained from this technique to validate CFD simulations. Recently, Deen et al. (2010) used ECT and measured bubble size and rise velocity by cross correlation of two planes in a pressurized fluidized bed. They studied the influence of pressure on bubble size and rise velocity. They reported that at higher pressure bubbles possessed a more uniform size and were in general smaller with lower rise velocity.

Another important tomographic technique widely used in fluidized bed studies is the X-ray tomography. The transmission of X-rays through a heterogeneous medium is accompanied by attenuation of the incident radiation, and the measurement of this attenuation provides a measure of the line integral of the local mass density distribution along the path traversed by the beam (Chaouki et al., 1997a). The measurement of several such beams at different spatial and angular orientations with respect to the test section or volume, followed by an image reconstruction procedure, provides a density distribution of phases. Since the data collection is automated and the

reconstruction process is performed using a computer, the process is referred to as either computer-assisted tomography (CAT) or computed tomography (CT). Compared with the ECT technique, XCT provides higher spatial resolution (Wu et al., 2007); however, X-ray tomography is slower and more expensive. Though, XCT have been most frequently used for particle distribution and local time-averaged gas holdup (Kumar and Dudukovic, 1997; Chaouki et al., 1997a; Wu et al., 2007; Franka and Heindel, 2009), others such as Kia et al. (2000, 2005), Mudde (2010) applied the technique to analyze bubbles motion in a fluidized bed.

Apart from the X-ray tomography, X-ray imaging has played significant role in the study of fluidized beds hydrodynamics, especially bubble hydrodynamics. X-ray imaging is a technique based on the same principle as X-ray tomography, but the attenuation of the beam emitted by the X-ray source is registered by sheets of film or an image intensifier camera (Yates and Simons, 1994). The registered images are then recorded on a cine camera or video-recorder and transferred to a computer for processing and analysis. The most substantial early work on fluidization research using X-ray radiography has been performed by Rowe, Yates and co-workers at University College London since the 1960's (e.g. Rowe and Partridge, 1965; Rowe et al., 1978; Hoffmann and Yates, 1986; Yates et al., 1994; Buyevich et al., 1995). They extensively studied the effects of gas distributor, elevated temperatures and pressures, and co-axial nozzles on the dynamic properties of bubbles (growth, splitting, coalescence, velocity, wake and emulsion phase). Other major contributions in recent years came from the work of Kantzas and co-workers (e.g. Zarabi and Kantzas, 1998; Kantzas et al., 2001; Kantzas, 1994; Hulme and Kantzas., 2004; van der Lee et al., 2005; Wu et al., 2007a,b). They also reported the behavior of bubbles in fluidized bed. van der Lee et al. (2005) used both X-ray imaging and pressure fluctuation measurements to calculate bubble diameter and compared the two techniques. They also used the results to validate 2D CFD simulations. He et al. (2007) measured bubble properties such as diameter, rise velocity using X-ray imaging, and compared with CFD simulations of 2D fluidized bed. On the other hand, Wu et al. (2007b) used similar technique to measure bubble diameter in 3D beds and compared the results with literature correlations. Though X-ray imaging techniques can be used for 3D beds, these methods are not very practical for large diameter beds in presence of swarms or multiple bubbles, since it just shows a 2D projection of the 3D objects. Thus, they are still limited and best suited to pseudo-2D fluidized beds. Another disadvantage of the X-ray photography is that it is more expensive than other imaging techniques such as digital imaging.

Another important nonintrusive measurements technique used to study fluidized bed hydrodynamics is the pressure measurements. In fact, they are the most common measurement techniques used in fluidized bed reactors (Yates and Simons, 1994). Together with temperature measurements, it is the only measurement technique that is applied in industry on a routine basis (Werther, 1999). Either the time-averaged pressure measurements or the pressure fluctuation signal can be used to measure fluidized bed hydrodynamics with the time-resolved or pressure fluctuation measurements are widely applied to estimate bubble characteristics. Pressure differ-

ential transducers are the simplest and least expensive detection devices, but the interpretation of the pressure records is difficult and needs extensive experimental validation that makes the technique less attractive for bubble property measurement. The reason is that the local pressure fluctuations are composed of multiple sources, including local bubble passage, global bed oscillations and propagating pressure waves originating in other locations.

Davidson (1961) first proposed that bubble diameter could be estimated by the amplitude of bubble-passage-induced pressure fluctuations. Since then many researchers have adopted the technique to estimate bubble size as well as bubble rise velocity including those early works by Fan et al. (1983), Viswanathan and Rao (1984) and Sitnai (1982). Clark et al. (1991) used data from slugging bed and showed that, in principle, one differential pressure transducer connected to two vertically spaced probes is sufficient to obtain these bubble characteristics. Ramayya et al. (1996, 1998) used both point pressure fluctuation pressure differential measurements and employed simulated data to show that it is also possible to obtain similar information from vertically as well as horizontally spaced probes. Clark et al. (1996) proposed a method to obtain a local bubble-size distribution from chord-length data derived from differential pressure measurements obtained in a freely bubbling bed. Santana and Macias-Machin (2000) proposed an improved method that could cope with bubbles rising at an angle. An alternative approach to obtain the bubble size distribution by statistical analysis of absolute pressure fluctuations measurement at one position is proposed by Bai et al. (2005). van der Schaaf (2002) proposed a power spectral decomposition method to obtain the time-averaged bubble diameter at a given height using two absolute pressure fluctuation measurements. van der Lee et al. (2005) used pressure fluctuation measurements via the method outlined by van der Schaaf et al. (2002) to calculate bubble diameter. They compared their results with results obtained from X-ray imaging technique and CFD simulations.

2.2.2 Digital imaging technique

Photographic technique is the simplest, and many researchers have adopted this method to establish bubble properties in fluidized beds. The technique uses a CCD camera or digital video camera to capture images of the inside bed dynamics through a transparent wall. The images are then processed to discriminate the bubbles from the emulsion phase and measure their properties. In the early use of imaging techniques, the analysis of the images to compute bubble properties such as diameter, rise velocity was quite a laborious and time-consuming task, and required subjective interpretation in the delineation of bubble-solid boundaries. In recent years, significant improvement in automation and development of digital imaging systems has significantly improved the procedure and paved the way for the use of this technique for the study of bubble characteristics in fluidized beds. The high level of automation for the analysis of image acquisition and data processing procedures has dramatically alleviated the laborious manual effort needed for the analysis of large number of bubbles. Automation of the analysis procedure means that a large number of images can be captured for any data set improving the statistical

accuracy of any ensemble estimates produced. Moreover, this technique provides rigorous and detailed information about the flow structure of the entire bed without interfering with the flow dynamics. As a result, many researchers see the digital imaging analysis technique as a powerful method for the analysis of bubble properties. The major drawback of this method is that it can only be effectively used in pseudo-2D beds. In fact, the use of pseudo-2D beds can be valuable, e.g. to obtain an understanding of the underlying flow mechanism in fluidized beds, calibration of other types of measurement equipment and for validation of numerical models in which this technique can play a fundamental role.

Agarwal and co-workers (Lim et al., 1990, 1993; Lim and Agarwal, 1990, 1992) pioneered the use of Digital Image Analysis Technique (DIAT) in fluidized bed studies and their works were summarized by Agarwal et al. (1997). They performed experimental studies on bubble characteristics and solid tracer concentration profiles on a 2D bed with and without immersed obstacles. Hull et al. (1999, 2000) reported additional results of bubble characteristics and tracer concentrations of beds with and without internal obstacles. Mudde et al. (1994) used DIAT to measure the local hold-up, and bubble size, shape and velocity in a bubbling fluidized bed. Special focus was given to the determination of shape properties of spherical-cap bubbles. They were able to decompose the contour of the bubbles in order to determine the wake angle and wake area.

In later studies, Goldschmidt et al. (2003) developed DIAT to measure bed expansion and segregation dynamics in dense gas-fluidized beds of mono-disperse and binary mixtures of fluidized beds. They employed different colored particles and RGB images decomposition, for the study of the extent of mixing and segregation. Caicedo et al. (2003) used the technique to measure bubble aspect ratio and shape factor in a 2D gas-solid fluidized bed. They measured the distribution of these quantities as a function of gas velocity. They found that the bubble aspect ratio and shape factor follow a normal distribution. They also studied the influence of relative humidity, particle size, and bed width and height on these bubble characteristics. Shen et al. (2004) developed DIAT and measured bubble properties such as size and rise velocity in a two dimensional bed as a function of bed height as well as the axial and radial distribution of bubbles and the gas through flow. They developed correlations for bubble diameter and rise velocity based on their experimental results. They found that for Group B particle and a given superficial velocity if the bed height is sufficient bubble diameter could be able to reach a maximum value at a certain height. Prieto et al. (2003) used digital imaging technique to investigate the size distribution of bubbles in 2D fluidized bed. They studied the vertical and lateral bubble size distribution and they found that the size distribution for the bubbles in a slice of the bed was skewed, varying with the location of the slice. Utikar and Ranade (2007) investigated the hydrodynamics of single jet 2D fluidized bed. They used experimental results obtained from digital image analysis to validate CFD results of bubble diameter and rise velocity distribution. Lim et al. (2006, 2007) used DIAT to investigate bubble distribution and behavior in a planar gas-solid fluidized bed. In their work, frequency domain and statistical analyses of the bed bubble void fraction were used

to describe the bed dynamics. Laverman et al. (2008) developed a method by coupling the particle image velocimetry (PIV) with digital image analysis technique. With this method, they were able to simultaneously measure the emulsion phase circulation pattern and bubble characteristics. The average bubble diameter as function of the axial position and the average bubble rise velocity as a function of the average bubble diameter for different fluidization velocities, bed aspect ratios and bed widths were measured and compared with literature correlations. They observed a significant influence of particle raining through the roof of the bubbles on the time-averaged velocity profile.

Busciglio et al. (2008, 2009) developed an automated DIAT using in-house code that allowed for the simultaneous measurement of various bubble properties, such as bubble size and bubble velocity distributions, bed height and bubble-phase hold-up. They extensively studied the distribution of bubble size, velocity and aspect ratio. Their method was flexible to handle both experimental and numerical results. They compared and validated numerical results obtained by the Eulerian-Eulerian two-fluid model with experimental data of bed expansion, bubble hold-up, bubble size distribution, and aspect ratio. More recently, Busciglio et al. (2010) extended their previous works and performed statistical analysis of bubble size distribution for different particle systems and fluidization gas velocities. They observed bimodal shape of local bubble size distribution, which they primarily attributed to the simultaneous presence of coalescence and splitting phenomena.

Almost all of the research works described above are based on pseudo-2D bed without internal obstacles. In the open literature, only Hull et al. (1999, 2000) were able to use the DIAT for fluidized beds with immersed obstacles. In fact the DIAT used by them was similar to the one used by Lim et al. (1990, 1993) for fluidized beds without immersed tubes. It is not clear in their papers how they account the presence of immersed tubes for the analysis bubble properties. Probably since they used only few immersed tubes (8 and 9), the technique developed for beds without tubes can be applied with little error for their case. However, it is believed that for dense tube bank geometry, the presence of tubes significantly alter the dynamics of the bubbles. Thus, appropriate algorithm is necessary to account the frequent splitting and coalescence of bubbles in the tube bank region in developing the DIAT. Therefore, in this work, a fully automated and robust digital image analysis technique was developed to analyze bubble properties in 2D fluidized beds with and without immersed tubes. By the use of purposely-developed in-house software, it was possible to automate fully the image acquisition and data processing procedure. Thus, it was possible to compute simultaneously a large number of bubble properties, allowing at the same time a meaningful statistical analysis that is fundamentally necessary given the nature of fluidized beds.

2.3 CFD Models for Gas-Solid Fluidized Beds

Experimental techniques are usually expensive and provide specific results. Moreover, due to the harsh environment and opaque nature of gas-solid flow structure of fluidized beds, it is difficult to observe the flow structure of the bed using many of the experimental techniques discussed above. In case of parametric study, it is practically difficult or even impossible to vary the geometry and operating conditions during experimentation. Therefore, in recent years, together with the rapid increase in computational power and development of numerical methods, fast growth of interest in understanding the physical mechanisms responsible for the complex behavior of gas-solid systems has helped to spark the development of fundamental approaches based on Computational Fluid Dynamics (CFD). Though empirical correlations are still largely used for designing gas-solid fluidized beds, CFD models have been seen as fundamental tools in the study of the hydrodynamics and to aid in the design process of these systems.

Most literatures give tribute to the paper by Davidson (1961) as the first to apply the concept of hydrodynamic model in fluidized beds in his analysis of a single isolated bubble rising in an unbounded fluidized bed. However, Jackson and his co-workers were the first who made a breakthrough in CFD modeling of fluidized bed in the mid 60's (Jackson, 1963; Anderson and Jackson, 1967). Many other researchers such as Murray (1965), Soo (1967), Ishii (1975) were also intensively engaged in developing mathematical models for these systems and reached in similar results as Jackson and his co-workers. Since then many have made significant efforts to develop detailed microbalance models to study the complex hydrodynamics of gas-fluidized beds (Gidaspow, 1994; Enwald et al., 1996; Jackson, 1997; Kuipers and Van Swaaij, 1998). Broadly speaking, there are two types of computer models widely applied today, the Eulerian-Eulerian (continuum) model (Anderson and Jackson, 1967; Ishii, 1975) and the Eulerian-Lagrangian (continuum-discrete) method (Tsuji, 1993; Hoomans et al., 1996). Both consider the gas phase as a continuum and the flow fields at sub-particle level are not resolved and empirical equations are applied for the gas-particle interaction.

2.3.1 The Eulerian-Lagrangian model

In Eulerian-Lagrangian model, which is usually referred as the Discrete Particle Model (DPM), the gas phase is considered as continuous while the solid phase is treated as discrete ones. Hence, the Newtonian equations of motion for each individual particle are solved taking into account the effects of particle-particle and particle-wall collisions that eliminate the need of additional closure laws to describe the interactions. Depending on the description of particle collisions, two different approaches of the DPM are available; namely, the soft-sphere approach and hard-sphere approach.

2.3.1.1 Soft-sphere approach

In the soft-sphere approach the particles are allowed to overlap slightly hence assumed to undergo deformation during their contact, and the contact forces are subsequently calculated from the deformation history of the contact using a contact force scheme of a simple mechanical analogy involving a spring, a dash pot and a slider analogue. The 2D soft-sphere approach to gas-fluidized beds was first applied by Tsuji et al. (1993), where a linear-spring/dashpot model was employed. The detailed derivation of the particle-particle collision forces are described in their previous paper Tsuji et al. (1992) when they use DPM to simulate a plug flow in a horizontal pipe pneumatic conveying system. Later Kawaguchi et al. (1998) extended the work to three dimensional fluidized beds by taking into account the friction and wall effect of the front and rare walls which were neglected by Tsuji et al. (1993) and also extending the motion of the solid particles to three dimensional which was not before. Xu and Yu (1997) independently developed a 2D model of a gas-fluidized bed. However, in their simulations a collision detection algorithm that is normally found in hard-sphere simulations was used to determine the first instant of contact precisely. The advantage of the soft-sphere approach is that it allows modeling of multiple collision of particle with more than one particle although the net contact force is obtained from the addition of all pair-wise interactions. The soft-sphere models are essentially time-driven where the time step should however be carefully chosen in calculating the contact force.

2.3.1.2 Hard-sphere approach

Hoomans et al. (1996) first reported the application of the hard-sphere discrete particle model when they developed and applied for their simulation of bubble and slug formation in a 2D fluidized bed. They assumed rigid particles to interact through binary, quasi-instantaneous collisions. Particle collision dynamics were described by collision laws, which account for energy dissipation due to non-ideal particle interaction by means of the empirical coefficients of normal and tangential restitution and the coefficient of friction. Thus, interaction forces are assumed impulsive and hence particles only exchange momentum by means of collisions. In the simulation, the collisions were processed one by one according to the order in which the events occur. Hoomans (2000) extended this approach to include the particle size distribution in their study of bubble formation and segregation phenomenon in dense fluidized beds. Hoomans (2000) and Ouyang and Li (1999) used this approach to study cluster formation in risers. Goldschmidt et al. (2001) have further used this model in connection with the kinetic theory of granular dynamics. For not too dense systems, the hard-sphere models are considerably faster than the soft-sphere models. Since the occurrence of multiple collisions at the same instant cannot be taken into account, the hard-sphere approach is not suitable for dense particle systems, which are characterized by multiple collisions. Recently, Deen et al. (2007) and Zhu et al. (2008) have reviewed the state of the art of the Eulerian-Lagrangian Model with detail description and governing equations of the soft-sphere and hard-sphere approaches and their major application in the study of fluidized beds.

2.3.2 The Eulerian-Eulerian model

Practically the motion of gas-particle flow systems present in fluidized beds should be expressed at least by the Eulerian-Lagrangian approach with the Newtonian equations of motion for the suspended particles and locally averaged Navier-Stokes equation for the fluid phase. However, when the system of interest comprises a large number of closely spaced particles, as in the case of fluidized bed, the problem is far too difficult to allow direct solution by tracking individual particles. Despite the rapid growth in computer capacity, it is only possible to track less than 10^6 particles (much less than the practical number of particles found in industrial scale fluidized beds) using the DPM. Since both CPU time and the required memory scales linear with the number of particles, it is obvious that DPM simulations of industrial size fluidized beds are beyond the capability of commercially available computer facilities. Therefore, these models are not natural choices for hydrodynamic modeling of engineering scale systems in the near future. For practical purposes, it is necessary to seek some method of simplifying it so that it can be described by a relatively small number of partial differential equations. One way of simplifying this problem is to replace the point mechanical and fluid mechanical variables by an appropriate locally average value of the corresponding variables to formulate the integral balances for mass, momentum and energy for a fixed control volume containing both phases. Hence describing the motion of the fluid and particles as though they are interpenetrating continua (Anderson and Jackson, 1967; Ishii, 1975). Though the local instantaneous value of variables vary rapidly on a scale comparable with the particle spacing the averaged variables are smoothed by averaging over regions large compared with the particle spacing but small compared with the size of complete system. The equations employed are a generalization of the Navier-Stokes equations for interacting continua. This means that instead of knowing the positions and velocities of each particle, only the volume fraction of each phase and the average volume flow pattern are known. With this model, larger scale simulations can be performed, using less computation time. In addition, such averaging techniques allow us to use relatively coarser grids and longer time steps so that the computational effort is significantly reduced. On the other hand, the averaging technique employed in such models introduces more unknowns than the number of equations available thus, forces us to include additional expressions to close the set of equations. These closure laws, which represent the interaction between particle-gas, particle-particle and particle-wall, are (semi)empirical and inconsistent thus highly influence the accuracy of the model. Moreover, the continuum model suffers from some critical limitations in modeling of the gas-solid flow. It does not provide information about the hydrodynamics of individual particles and thus has limitations in predicting certain discrete flow characteristics such as particle size and density effect. Even though this model has such limitations, it remains the only feasible approach for performing parametric investigation and scale-up and design studies of industrial scale systems and dense gas-solid beds (van Wachem, 2001; van der Hoef, 2008). Detail comparison of the Eulerian-Lagrangian approach and the Eulerian-Eulerian approach can be found elsewhere in the literature (e.g., Gera et al., 1998; Goldschmidt et al., 2002, 2004; Chiesa et al., 2005; van der Hoef et al., 2008).

In the Eulerian framework, it is possible to consider more than one particle classes that allow the analysis of different particle size and density. Such models are termed as Multi-Fluid Models (MFM). However, such models are found to be very complex and difficult to simulate as the computational volumes may contain different classes of particles and hence difficult to account the interaction between the particles in a computational cell. Thus, the Eulerian-Eulerian approach is suitable and more appropriate if one considers only one particle phase. Thus, the model comprises only two interacting phases (the gas phase and one particle phase). In this case, the model is usually termed as the Two-Fluid Model (TFM).

The first governing equations of the TFM for gas-solid two-phase systems were reported by Anderson and Jackson (1967). They derived from first principles separate conservation equations for both phases with the idea of local mean variables. They use the mathematical definition of local mean variables to translate the point Navier-Stokes equations for the fluid and the Newtonian equations of motion for the particles directly into continuum equations representing momentum balances for the fluid and solid phases hence adopting the special averaging technique. The technique is replacing the point mechanical variables by local mean variables obtained by averaging the point variables over regions that contain many particles. Ishii (1975) has separately derived similar governing equations for TFM. These two models were discussed and compared by van Wachem et al. (2001) and concluded that the model developed by Anderson and Jackson (1967) is more appropriate for gas-solid systems while that of Ishii (1975) is suitable for gas-liquid flows.

Owing to the continuum description of the particulate suspension, the TFM requires additional closure laws for the solid rheology. Two important transport variables that appear in the momentum equation of the solid phase are the solid stress tensor and solid pressure. These variables depend strongly on the collisional behavior of the individual particles, hence difficult to express. So far, there are two types of approaches to treat these variables. The first one is commonly known as the Constant Viscosity Model (CVM) and was applied by many of the early TFM computer simulations (e.g. Gidaspow and Ettehadieh, 1983; Tsuo and Gidaspow, 1990; Kuipers et al., 1992, 1993; Enwald et al., 1996). This approach assumes a constant value for the solid viscosity obtained from some experimental and empirical correlations. The solids phase pressure, which prevents particles from reaching impossibly low values of void fraction, was assumed to depend on the solid volume fraction and it is determined from experiments and was modeled as:

$$\nabla P_s = G(\varepsilon_g) \nabla \varepsilon_g \quad (2.1)$$

Thereby the solids phase elasticity modulus, $G(\varepsilon_g)$, was taken from simple theory of powder and is defined by:

$$G(\varepsilon) = \frac{dP_s(\varepsilon_g)}{d\varepsilon} \quad (2.2)$$

Bouillard et al. (1989) proposed a generalized solid phase elastic modulus, $G(\varepsilon_g)$, based on Orr's (1966) simple theory of powder compaction, of the form:

$$G(\varepsilon) = G_0 \{ \exp [c (\varepsilon_g^* - \varepsilon_g)] \} \quad (2.3)$$

Where, G_0 represents the normalizing units factor, c the compaction modulus and ε_g^* the compaction gas phase volume fraction. Kuipers et al. (1992) used this approach with the values of $G_0 = 1$ Pa, $c = 100$ and $\varepsilon_g^* = 0.45$.

The advantage of this model is its simplicity and thus easy to implement in a computer codes. However, it is difficult to take into account the underlying characteristics of the solid phase rheology due to mutual particle collisions.

The second approach makes use of the Kinetic Theory of Granular Flow (KTGF) and develops some relations as a function of the particle velocity and position (Ding and Gidaspow, 1990). One of the advantages of the KTGF is that it can give a more fundamental insight of the particle-particle interactions, thus the particle pressure, particle viscosity, and other transport coefficients that are used in the TFM can be derived. This model is an extension of the classical Kinetic Theory of Dense Gases (Chapman and Cowling, 1970). It was first developed for granular flows by Jenkin and Savage (1983) and Lun et al. (1984) for smooth, spherical and nearly elastic particles. Later Sinclair and Jackson (1989) applied this theory to model gas-solid flow in a pipe. The model was further developed and applied to dense gas-solid fluidized beds by Ding and Gidaspow (1990) and Gidaspow (1994). The extensions were made to include the dissipation of kinetic fluctuation energy in the granular medium during mutual non-ideal particle-particle collisions due to inelastic deformation and friction of particles with the surrounding fluid.

In gas-solid two-phase flow, the interaction of the particles and the gas is restricted to a mutual drag force, whose value depends on the concentration of the particles and the difference between the local average values of the velocities of the gas and particle phases. Since the gas does not slip freely at the wall of the vessel, there is a gas velocity profile in fully developed flow, with the maximum velocity on the axis of the pipe, and a corresponding profile of particle velocity is induced by the drag forces exerted by the gas on the particles. As a result of this shearing motion the particles collide with each other, resulting in a random granular motion of particle. Thus, the instantaneous velocity of the particles can be decomposed into a local mean velocity and random fluctuation velocity. The particle velocity fluctuations generate an effective pressure in the particle phase, together with an effective viscosity that resists shearing of the particle assembly. Similar to the usual thermodynamic temperature in gases, a pseudo-temperature, known as the granular temperature Θ is defined as one third of the mean square of the random component of

the velocity (Jenkins and Savage, 1983). This granular temperature is a measure of the particle velocity fluctuation and varies with time and position in the fluidized bed. Therefore, both the effective pressure and the effective viscosity are functions of this granular temperature. Thus, an additional conservation equation representing a balance for this kinetic energy of the random motion of the particles is required to determine the pseudo (granular) temperature distribution. This pseudo-thermal energy is generated by the working of the effective shear stresses in the particle phase, dissipated by the inelasticity of collisions between particles and conducted from place to place as a result of gradients in the particle temperature. For detail discussions and derivation of the kinetic theory, interested readers are referred to the book by Gidapow (1994) and papers by Jenkins and Savage (1983), Lun et al. (1984), Ding and Gidaspow (1990) and Nieuwland et al. (1996b). The governing and closure equations of the TFM based on the kinetic theory are also presented in Chapter 3 of this book.

Generally, the kinetic theory model is more complex and time-consuming to solve, but many researchers believed that it is a more fundamental approach than the CVM and can be applied for a wider range of problems. The major drawback of the kinetic theory is that it is limited to slightly inelastic collisions hence does not allow for particle rotation and energy losses resulting from non-ideal collisions due to friction and tangential restitutions are not accounted for. It also does not allow for non-instantaneous interaction between particles, such as contact friction. Patil et al. (2005a) carried out simulations and compared the performance of the CVM and KTGF models for a 2D fluidized bed equipped with a jet in the center. They observed that the initial growth rate of a bubble formed at a nozzle in a fluidized bed with a jet is strongly determined by the exchange velocity of gas between the bubble and the emulsion phase, which is mainly determined by the drag experienced by the gas percolating through the bubble boundary. Since the compaction around the bubble interface is not much influenced by particle-particle interactions, the bubble growth rate predicted by the KTGF model not accounting for frictional stresses and the CVM are very similar and are hardly affected by the coefficient of restitution. They observed that the prediction of the KTGF improved significantly when the most dominant frictional stresses were taken into account. In their second publication, results of freely bubbling bed were reported (Patil et al., 2005b). They found that the average bubble size distribution predicted by the KTGF showed better agreement with correlations as well as experimental data while the rise velocity predicted by both approaches were approximately the same and in good agreement with correlations available in the literature. Johansson et al. (2006) have also compared the performance of the CVM and KTGF and found that the KTGF showed better agreement of the bubble properties compared with experimental measurements.

Over the past 20 years, a large number of researchers have devoted significant effort to apply and validate the TFM based on the KTGF for different flow regimes and particle classes. Sinclair and Jackson (1989), Pita and Sundaresan (1991), Hrenya and Sinclair (1997) have applied the kinetic theory for gas-solid flows in vertical pipes. Many investigators have successfully used this theory for studying particle and gas flow behavior in the riser section of circulat-

ing fluidized beds, (e.g. Nieuwland et al., 1996b; Samuelsberg and Hjertager, 1996; Neri and Gidaspow, 2000; Benyahia et al., 2000; Almuttahir and Taghipour, 2008). Other have applied it for spouted beds (e.g. Huilin et al., 2004; Du et al., 2006; Shuyan et al., 2009).

The TFM has been applied more for bubbling regime than any other fluidization regime and the early studies of bubbling bed simulations were extensively reviewed by Gidaspow (1994), Enwald et al. (1996), and Kuipers and van Swaij (1998). Simulations of bubbling fluidized beds were performed with either central jet or freely bubbling beds. Ding and Gidaspow (1990) simulated a 2D bubbling fluidized bed of a Geldart group B material with a gas jet at the inlet. In fact, they were the first to apply the TFM based on the kinetic theory for dense gas-solid fluidized bed systems. They validated the 2D simulation results by comparing the time-averaged voidages resulting from the simulations with the ones measured experimentally on a two-dimensional fluidized bed, although no further estimate of bubble size was conducted. Kuipers et al. (1993) simulated the behavior of a single bubble in a 2D gas fluidized bed with a central orifice. Simulated bubble sizes were compared with experimentally measured data and with predictions obtained by the two-phase theory. Their preliminary calculations showed that the sensitivity of computed bubble size with respect to the bed rheology (i.e. the solid phase viscosity) is quite small, although the bubble shape appeared to be much more sensitive to the bed rheology. Gera et al. (1998) compared simulation results of bubble formation, motion and eruption for a single isolated bubble predicted by the TFM with simulation results from the DPM and experimental observations. Boemer et al. (1997) summarized different forms proposed for the TFM and investigated the prediction of these models by performing simulations of a 2D fluidized bed with central jet. The results of bubble formation process were compared with experimental observations from the literature and showed good agreement. Patil et al. (2005a) compared the performance of the CVM and KTGF models for a 2D fluidized bed equipped with a jet in the center. They observed that bubble growth at a nozzle with a jet is mainly determined by the drag experienced by the gas percolating through the compaction region around the bubble interface, which is not much influenced by particle-particle interactions, so that the KTGF and CVM give very similar predictions. Cao et al. (2008) applied the TFM for simulating a pressurized jetting 3D fluidized bed and compared results of bubble size and average bed voidage with experimental data obtained using electrical capacitance tomography. They observed that at higher pressure the bubble size decreased.

Boemer et al. (1998) extended their previous work (Boemer et al., 1997) to freely bubbling fluidized bed. They performed numerical simulation using the Eulerian TFM and verified the predicted bubble characteristics with empirical models from literatures and their own experiment obtained from a 2D lab-scale fluidized bed by the use of video system. Similarly Patil et al. (2005b) extended their previous work (Patil et al., 2005a) to freely bubbling bed. They observed that the average bubble size distribution and rise velocity predicted by the KTGF showed better agreement with correlations as well as experimental data. Goldschmidt et al. (2001) studied the influence of particle-particle coefficient of restitution on bed dynamics and reported that the

hydrodynamic of dense gas solid fluidized beds (i.e. bubble behavior) strongly depends on the coefficient of restitution. When more energy is dissipated, simulations showed stronger pressure fluctuations (i.e. more vigorous bubbling). In contrary, Patil et al. (2005a) and Lindborg et al. (2007) reported that the bubble size and rise velocity are not sensitive to restitution coefficient. Hulme et al. (2005) performed simulations of freely bubbling bed and studied the influence of time step, differencing scheme, frictional stress, and closing equations on bubble diameter and rise velocity. They validated their result by comparing with experimental data obtained using X-ray fluoroscopy. Owoyemi and Lettieri (2005) performed simulations using 2D CFD of gas solid fluidized beds of two Geldart Group B industrial powders of natural and synthetic rutile and compared the results of bed height, bubble diameter, and bed voidage with experimental data. Pain et al. (2001a,b, 2002) developed a two-fluid CFD model based on a finite element formulation and studied the dynamics of beds for both the bubbling and slugging regimes. They also investigated the formation, elongation, coalescence and eruption of bubble. Gelderblom et al. (2003) applied the TFM model to simulate the bubbling/collapsing behavior of Geldart groups C, A and B powders. The computed bubble sizes were found in agreement with the classical expression for the maximum bubble size (Davidson and Harrison, 1963).

On the other hand, many researchers used the TFM and studied the macroscopic bed characteristics such as bed expansion, pressure drop, and voidage and solid distributions. Taghipour et al. (2005) studied the time averaged solid volume fraction, bed expansion ratio, pressure drop and qualitative gas-solid flow pattern and compared with the experimentally obtained pressure drop data and local voidage calculations using reflective optical fiber probe. The model was able to predict qualitatively the experimental results. However, large errors as much as 30–50 % in the prediction of bed voidage and pressure drops were observed. Similar studies were performed by Vejahati et al. (2009) who simulated 2D fluidized beds using different models from the literature. They measured the time averaged bed expansion and pressure drop and compared with their own experimental results. They found that all the models showed an acceptable qualitative agreement with experimental data. Hamzehei and Rahimhadeh (2009), and Hamzehei et al. (2010) also performed simultaneous simulations of bed hydrodynamics and heat transfer using the TFM. Their simulation results of bed pressure drop, bed expansion and temperature distribution were in good agreement with their own experimental data.

The most significant contribution for validating the TFM came from van Wachem and co-workers. They performed extensive studies and validations of the TFM via time-averaged bubble properties (van Wachem et al., 1998) and instantaneous bed characteristics (van Wachem et al., 1999). In their paper, van Wachem et al. (1998) validated the simulation results of bubbling fluidized beds using correlations for bubble size and bubble rise velocity available in the literature. Based on 2D simulation results, they compared the bubble sizes obtained from simulations of a freely bubbling gas fluidized bed of a Geldart group B powder with predictions given by Darton et al. (1977) correlation. Their results showed that simulated bubble diameters were slightly smaller in the higher part of the fluidized bed, which was attributed to the deficiency of

the technique used by Darton to capture small bubbles' diameters. In their later publication, van Wachem et al. (1999), they studied the dynamic characteristics of the gas-solids behavior at different superficial gas velocities, column diameters and pressures. They evaluated the velocity of pressure and voidage waves through the bed, the power of the low and high frequencies of the pressure and voidage fluctuations, the reorientation of the gas-solids flow just above minimum fluidization. By comparing the results with trends predicted by appropriate empirical correlations and experimental data, they demonstrated that the TFM simulations are able to correctly reproduce the dynamic characteristics of laboratory-scale fluidized beds. Later van Wachem et al. (2001) presented a comprehensive review of the TFM in terms of both the form of the governing equations and the closure relations. They performed simulations using these various forms from the literature and the resulting hydrodynamics through CFD simulations of fluidized beds with central jet and freely bubbling beds were compared with experimental data from the literature. They showed that flow predictions are not sensitive to the use of different solid stress models or radial distribution functions, as different approaches are very similar in dense flow regimes. The application of a different drag model, however, significantly influences the flow of the solids phase. van Wachem and Almstedt (2003) presented detail derivation of the governing equations and closure relations from the kinetic theory. They also discussed the limitations and capabilities of the models. Johansson et al. (2006) used experimental results of the means of power spectral density distributions of fluctuating pressure signals and bubble statistics obtained from capacitance probe measurements to validate simulations results from TFM based on the kinetic theory and constant particle viscosity approaches. They found that the KTGF model gave a more evenly distributed bubble flow profile over the bed cross-section and were in better agreement with the experimental results.

The majority of numerical studies for bubbling fluidized beds discussed above are for simple 2D plane bed geometry without internal obstacles. Numerical studies using complex bed geometries such as with immersed tubes are few in the open literature. Even those available are mainly concerned with either to investigate the heat transfer between the emulsion phase and the immersed tubes (Schmidt and Renz, 2000, 2005; Gao et al., 2007) or to predict the solid and void distribution around the immersed tubes in an attempt to study the erosion characteristics of the tubes (Bouillard et al., 1989; Lyczkowski et al., 1989; Gamwo et al., 1999; Pain et al., 2001b; He et al., 2009). Numerical studies of bubble characteristics in fluidized beds in the presence of immersed obstacles are quiet few in the literature and are presented below.

2.4 Gas-Solid Fluidized Beds Containing Immersed Tubes

In many industrial fluidized beds, immersed tubes are used to enhance the rate of heat and mass transfer, and rate of chemical conversion. In addition, these immersed tubes promote smooth fluidization by suppressing the growth and rise velocity of bubbles. They promote good mixing and reduce gulf circulation of particles in order to promote homogenous distribution. However,

their presence was seen to significantly alter the fluidized bed hydrodynamics. The presence of tubes in fluidized beds can strongly influence both the gas flow pattern through the bed and the size distribution of gas bubbles within the bed. This in turn influences the overall solids mixing thereafter the heat and mass transfer rates and chemical conversion. However, as criticized by Sitnai and Whitehead (1985) and can be seen afterwards, the vast majority of investigations reported on beds containing tubes have been devoted in an attempt to improve the heat transfer coefficients between the bed and the immersed tubes despite the fact that the heat transfer coefficient is not a strong function of the fluidizing velocity or even the tube geometry. The important effects that tubes have on bubbling behavior hence the overall solids mixing and gas flow distribution have not been investigated in the same detail. Tubes appear to limit the size of bubbles by preventing the formation of rapidly growing bubbles (Yates et al., 1990; Hull et al., 1999; Asegehegn et al., 2011). Since the overall solids mixing and gas distribution are governed by the size, distribution, and velocity of bubbles within the bed, fundamental understanding of the bubbling behavior of fluidized beds in the presence of internals has practical importance in the design and scale-up of these reactors.

Sitnai and Whitehead (1985) had comprehensively summarized early experimental studies regarding the influence of immersed obstacles on the hydrodynamics of gas-solid fluidized beds. Therefore, this review concentrate on studies reported since 1985 and mainly focuses on the influence of tubes on the bed hydrodynamics. Using X-ray imaging, Yates and Ruiz-Martinez (1987) had studied the interaction between immersed tube bundles and individual bubble injected singly into a fluidized bed. They found that tubes were the major sources of bubble breakup and the amount of breakup were functions of the separation between the tubes, the tube diameter and the size of bubbles at the moment of impact against a row of tubes. It was also found that below a minimum value of the vertical separation between rows bubble splitting is drastically reduced due to bridging across the tubes. Later Yates et al. (1990) extended to a freely bubbling fluidized bed and studied the bubble characteristics by varying the tube geometries and fluidization velocity. They concluded that there are clear differences between the hydrodynamics of tube free fluidized beds and those of beds containing a bank of tubes. The presence of tubes was found to significantly reduce the overall growth of bubbles and the authors developed a model for bubble growth. However, their model was solely based on measurements of regions above and below the tube bank and no measurement was done inside the tube bank region. Thus, their model lacked to show the actual bubble growth in the tube bank region. Rafailidis et al. (1992) and Clift and Rafailidis (1993) measured the gas pressure and bubble motion near an immersed tube in two and three-dimensional bed. They found that the pressure change around the tube is much less than in the bed remote from the tubes. They also observed that bubbles injected below the tube were drawn towards the tube, which is determined by the gas pressure around the tube. This particle free layer acted as a low-resistance gas path; so that the edge of the layer can be treated to a first approximation as a constant pressure gas surface and gas is drawn towards the tube to form the streams of bubbles that emerge at the sides.

Almstedt and coworkers (Olowson, 1994; Olsson et al., 1995; Olsson and Almstedt, 1995; Wieman and Almstedt, 1997; Löfstrand et al., 1995; Johansson et al., 2004) contributed significant work to the study of the influence of immersed horizontal tube banks on fluidized bed hydrodynamics. They measured bubble characteristics such as mean bubble rise velocity, bubble frequency, mean pierced length, bubble volume fraction, and visible bubble flow rate using capacitance probe while the absolute gas velocity through the bubbles were measured using Pitot-static pressure probe. They studied thoroughly the influence of pressure, superficial velocity and different tube bank geometries on bubble behavior and gas flow distribution. They reported that at lower pressures, the bubble pierced length is larger with tubes in the bed than without (Olsson et al., 1995). This does not agree with the well know concept that tubes limit the growth of bubbles. The reason for this discrepancy is that these authors measured the pierced length rather than the mean bubble diameter. As explained by Asegehegn et al. (2011) bubble elongate vertical as they pass between tubes in a row and they have higher aspect ratio (ratio of vertical extreme to horizontal extreme) than in the tube free region of the bed. Since the pierced length of a bubble measured by the capacitance probe is equivalent to the vertical length of the bubble, the mean pierced length measured for bubble with horizontal tubes are larger than without tubes. Thus, their conclusion could be the other way round if the mean bubble diameter were measured (Yates et al., 1990; Hull et al., 1999; Asegehegn et al., 2011). Moreover, since their measurement is restricted to a particular point of the bed height, it was not clearly shown the influence of tubes on the behavior of bubbles across the bed cross-section.

Hull et al. (1999) on the other hand studied the effect of the tube bank on bubble hydrodynamics in a 2D bed using digital image analysis technique. They presented the experimental observations on the variation of bubble characteristics within and outside the tube bank. They successfully estimated the bubble growth and rise velocity over the bed height and developed semi-empirical correlations for bubble size and rise velocity based on these data. In their model development, they reported that the vertical spacing between tubes played significant role in the growth of bubbles. This is in contrary to Yates et al. (1990) who neglect this parameter in their model. Though they successfully showed the growth of bubbles in fluidized bed with horizontal tubes across the entire bed height, their studies were limited to only one particle size and two tube arrangements (staggered and inline) with very few tubes.

With respect to numerical studies of bubble and particle motions in fluidized beds containing tube banks, little have been reported. The use of numerical simulation for fluidized beds with immersed tubes was initiated first by Lyczkowski and co-workers (Lyczkowski et al., 1987, 1989; Bouillard et al., 1989; Ding and Lyczkowski, 1992; Gamwo et al., 1999). They presented a computer software package to predict the dynamics and erosion rates in fluidized bed tube banks by using the TFM. In their model, the tubes had to be treated by rectangular objects due to the limitation of computer capacity. Later Ding and Lyczkowski (1992) extended the above model to simulate a 3D bed. Bouillard et al. (1989) presented results of the porosity distribution in a 2D fluidized bed with a rectangular jet and a single rectangular pipe immersed. The simula-

tion results of the time averaged porosity distribution were in good agreement with experimental data measured using γ -ray densitometer. They observed that the porosity was higher at the bottom of the tube and lower at the top. Gamwo et al. (1999) studied the solids flow pattern of a 3D bed with staggered horizontal tubes and compared the results with experimental data obtained for the ensemble-and time-averaged solids velocity field. They found good agreement between the computed and experimental solids flow patterns and axial velocities. Recently Lyczkowski et al. (2010) extended this work and measured bubble diameter and rise velocity at three probe points. However, they did not measure and explain the influence of tubes on the growth and rise velocity of the bubbles.

Other than the above group, few researchers have applied the TFM for fluidized beds with internals. Pain et al. (2001b) used the finite element method formulation and performed numerical simulation of solid flow pattern of fluidized bed with a single cylindrical obstruction. Yurong et al. (2004) studied the behavior of particles and bubbles using the TFM and used a body fitted coordinate system in order to match the boundaries of the immersed tubes. They investigated a bed with single and three tubes and they mainly focus on the validation of their model. Schmidt and Renz (2005) and Gao et al. (2007) also measured the solid volume fraction distributions around immersed tubes and gas flow behavior near immersed tubes respectively. However, their focuses were on the calculation of the heat transfer coefficients between the emulsion phase and the immersed tubes. Gustavson and Almstedt (2000) simulated a 2D bubbling fluidized bed containing two horizontal heat exchanger tubes and compared bubble properties at different pressure levels with the experimental data of a 3D bed obtained by Olowson (1994) using capacitance probe measurements. They found that the computed bubble properties agreed well with experimental data at higher pressures and deviated at lower pressures. Das Sharma and Mohan (2003) used the experimental results of Hull et al. (1999) to validate their numerical simulation of bubble properties. More recently, Asegehegn et al. (2011) performed numerical simulations using the TFM for fluidized beds with immersed tubes and the results were in good agreement with experimental data published elsewhere in the literature (Hull et al., 1999).

The above mentioned numerical studies are limited to beds with single or few numbers of immersed tubes. Moreover, many of them are not sufficiently validated with appropriate experimental data. Their validations are mainly qualitative comparison such as voidage distribution, solids circulation and solids velocity near the tube surface in an attempt to investigate the erosion characteristics of the tubes and rate of heat transfer between the tubes and the bed. So far, numerical studies of bubbling characteristics of fluidized beds with dense immersed tube banks are not reported. Taking this as a motivation, this dissertation attempts to fill this gap in the study and understanding of the complex flow dynamics of fluidized beds with internal obstacles. Thus, comprehensive studies of the bubbling behavior of fluidized beds with dense and sparse tube bank geometries were performed using a novel digital image analysis technique and the two-fluid kinetic theory model. The influence of immersed tube banks, particle size and superficial velocities were thoroughly investigated.

3 Numerical Modeling using the Two-Fluid Model

The Eulerian-Eulerian Two-Fluid Model (TFM) treats both the gas and the solid phases as continuous and interacting. Therefore, separate conservation equations for mass and momentum are solved for each phase with an appropriate interaction term between them. These conservation equations describe the mean motion of the gas-solid two-phase system and can in fact be seen as a generalized form of the Navier-Stokes equations. This means instead of knowing the positions and velocities of each particle, only the volume fraction of each phase in a computational cell and the average volume flow pattern are known. Such averaging techniques allow using relatively coarser grids and longer time step so that the computational effort is significantly reduced compared to the Eulerian-Lagrangian approach.

3.1 Governing Equations

Hydrodynamic models of gas-solid fluidization use the principles of conservation of mass and momentum. These governing equations can be derived either using ensemble or volume averaging techniques as done by Anderson and Jackson (1967) or from the kinetic theory of granular flow as described by Ding and Gidaspow (1990) and Gidaspow (1994). Interested readers are referred to these references for detail derivation of the governing equations. Both approaches resulted in similar conservation equations for mass and momentum. In this work, separate phase continuity and momentum equations for transient and isothermal non-reactive two-phase flow are used and given below.

The conservation of mass for both the gas and the solid phase can be written as:

$$\frac{\partial(\varepsilon_g \rho_g)}{\partial t} + \nabla \cdot (\varepsilon_g \rho_g \mathbf{u}_g) = 0 \quad (3.1)$$

$$\frac{\partial(\varepsilon_s \rho_s)}{\partial t} + \nabla \cdot (\varepsilon_s \rho_s \mathbf{u}_s) = 0 \quad (3.2)$$

The volume fractions are related as:

$$\varepsilon_s + \varepsilon_g = 1 \quad (3.3)$$

Where ε is the volume fraction, ρ is the density and \mathbf{u} is the velocity vector with the subscripts g for the gas phase and s for the solid.

The conservation of momentum for the gas and the solid phase are described by:

$$\frac{\partial(\varepsilon_g \rho_g \mathbf{u}_g)}{\partial t} + \nabla \cdot (\varepsilon_g \rho_g \mathbf{u}_g \mathbf{u}_g) = \nabla \cdot \bar{\bar{\boldsymbol{\tau}}}_g - \varepsilon_g \nabla P - \beta(\mathbf{u}_g - \mathbf{u}_s) + \varepsilon_g \rho_g \mathbf{g} \quad (3.4)$$

$$\frac{\partial(\varepsilon_s \rho_s \mathbf{u}_s)}{\partial t} + \nabla \cdot (\varepsilon_s \rho_s \mathbf{u}_s \mathbf{u}_s) = \nabla \cdot \bar{\bar{\boldsymbol{\tau}}}_s - \varepsilon_s \nabla P - \nabla P_s + \beta(\mathbf{u}_g - \mathbf{u}_s) + \varepsilon_s \rho_s \mathbf{g} \quad (3.5)$$

In Equations (3.4) and (3.5), the left hand side is the net change of momentum for the two phases. The right hand side includes the forces:

- Viscous force $\nabla \cdot \bar{\bar{\boldsymbol{\tau}}}_i$
- Static pressure force $\varepsilon_s \nabla P$
- Interphase force (drag) $\beta(\mathbf{u}_g - \mathbf{u}_s)$
- Gravitational force $\varepsilon_i \rho_i \mathbf{g}$
- Solid pressure force ∇P_s

In gas-solid bubbling fluidized beds, other forces such as added mass effect, lift force, and Basset force are assumed negligible (Boemer et al., 1997). The momentum balance in Equation 3.4 can be reduced to the well-known Navier-Stokes equation with $\varepsilon_g = 1$ and $\beta = 0$.

3.2 Interphase Momentum Transfer Coefficient

In gas-solid multiphase flow the interaction of the particles and the gas is restricted to a mutual momentum transfer (drag force), whose value depends on the concentration of the particles and the difference between the local average values of the velocities of the gas and particle phases. This drag force is added to the total force on the momentum equations of each phase. The drag force between gas and solid phases is an important and dominant force in modeling gas-solid systems and is generally represented by the product of a momentum transfer coefficient, and the slip velocity ($\mathbf{u}_g - \mathbf{u}_s$) between the two phases. Usually, the momentum transfer coefficient, β , for gas-solid systems is expressed in terms of empirical equations and several such correlations have been reported in the literature, including those of Wen and Yu (1966), Gidaspow (1994), and Syamlal and O'Brien (1989) which are frequently used in CFD models. These three models are given below and their comparison as a function of solid volume fraction is plotted in Figure 3.1.

Wen and Yu (1966)

$$\beta = \frac{3}{4} C_d \frac{\varepsilon_g (1 - \varepsilon_g)}{d_p} \rho_g |\mathbf{u}_g - \mathbf{u}_s| \varepsilon_g^{-2.65} \quad (3.6)$$

Where,

$$C_d = \begin{cases} \frac{24}{\varepsilon_g Re_p} \left[1 + 0.15(\varepsilon_g Re_p)^{0.687} \right] & \text{for } Re_p \leq 1000 \\ 0.44 & \text{for } Re_p > 1000 \end{cases} \quad (3.7)$$

The particle Reynolds number is given by:

$$Re_p = \frac{\rho_g |\mathbf{u}_g - \mathbf{u}_s| d_p}{\mu_g} \quad (3.8)$$

Gidaspow (1994)

$$\beta = 150 \frac{(1-\varepsilon_g)^2}{\varepsilon_g} \frac{\mu_g}{(d_p)^2} + 1.75(1-\varepsilon_g) \frac{\rho_g}{d_p} |\mathbf{u}_g - \mathbf{u}_s| \quad \text{for } \varepsilon_g \leq 0.8 \quad (3.9)$$

$$\beta = \frac{3}{4} C_d \frac{\varepsilon_g(1-\varepsilon_g)}{d_p} \rho_g |\mathbf{u}_g - \mathbf{u}_s| \varepsilon_g^{-2.65} \quad \text{for } \varepsilon_g > 0.8 \quad (3.10)$$

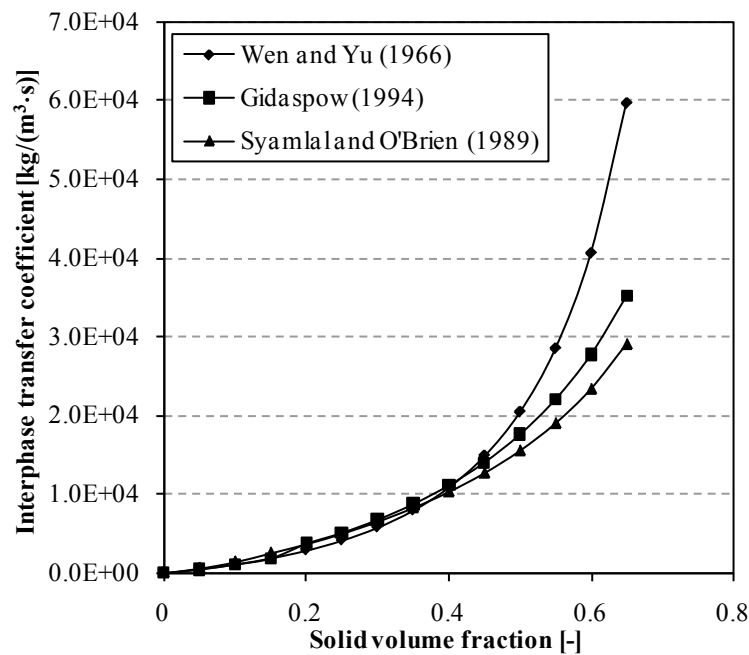


Figure 3.1: Comparison of different interphase momentum transfer coefficients; $Re_p=50$, $d_p=347$ μm .

Syamlal and O'Brien (1989)

$$\beta = \frac{3}{4} C_d \frac{\varepsilon_g(1-\varepsilon_g)}{u_t^2 d_p} \rho_g |\mathbf{u}_g - \mathbf{u}_s| \quad (3.11)$$

Where,

$$C_d = \left(0.63 + \frac{4.8}{\sqrt{Re_p/u_t}} \right)^2 \quad (3.12)$$

$$u_t = 0.5 \left(A - 0.06Re_p + \sqrt{(0.06Re_p)^2 + 0.12Re_p(2B - A) + A^2} \right) \quad (3.13)$$

$$A = \varepsilon_g^{4.14}, B = 0.8\varepsilon_g^{1.28} \quad \text{for } \varepsilon_g \leq 0.85 \quad (3.14)$$

$$A = \varepsilon_g^{4.14}, B = \varepsilon_g^{2.65} \quad \text{for } \varepsilon_g > 0.85 \quad (3.15)$$

3.3 The Kinetic Theory of Granular Flow

The averaging technique employed in the TFM introduces more unknowns than the number of equations available thus, forces to include additional expressions to close the set of equations. These closure laws, which represent the interaction between particle-gas, particle-particle and particle-wall, are (semi)empirical and inconsistent thus highly influence the accuracy of the model. Thus, the key to accurate modeling lies to a large extent in the closure laws used. One of the most important closure relations is the drag force between the two phases as described in section 3.2. Other important closure relations in the TFM are closure laws used to describe the rheology of the fluidized particles that arise owing to the continuum description of the particulate suspension. As explained in section 2.3.2 these closure equations can be derived either from the constant viscosity model (CVM) or from the principle of Kinetic Theory of Granular Flow (KTGF). Though the CVM is relatively simple and easy to implement in a computer code, it is difficult to take into account the underlying characteristics of the solid phase rheology arising from mutual particle collisions. Thus, in most recent continuum models constitutive equations according to the KTGF are usually incorporated. The KTGF provides explicit closures that take energy dissipation due to non-ideal particle-particle collisions into account by means of the coefficient of restitution. Therefore, it is a more fundamental choice than the CVM.

The KTGF is basically an extension of the classical kinetic theory of dense gases. The extensions were made to include the dissipation of kinetic fluctuation energy in the granular medium during mutual non-ideal particle-particle collisions due to inelastic deformation and friction of particles with the surrounding fluid. Thus, it can give a more fundamental insight of the particle-particle interactions, thus the particle pressure, particle viscosity, and other transport coefficients that are used in the TFM. For complete description and mathematical formation of the KTGF and subsequent derivation of the conservation equation of the granular temperature and constitutive equations, interested readers are referred to the books by Chapman and Cowling (1970) and

Gidaspow (1994) and the papers by Jenkins and Savage (1983), Lun et al. (1984), Ding and Gidaspow (1990). In this chapter, only the basic equations and their description are presented.

As a result of shearing motion, particles collide with each other, resulting in a random granular motion of particle. Thus, the actual instantaneous velocity of the particles can be decomposed into a local mean velocity and random fluctuation velocity. As a measure of the specific kinetic energy of the random fluctuating component of the particle velocity, a pseudo-temperature, known as the granular temperature Θ is defined as one-third of the square of the particle fluctuation velocity, Equation 3.16. The granular temperature is similar to the usual thermodynamic temperature in gases. It is the measure of the particle velocity fluctuation mainly due to the particle-particle collision and varies with time and position in the fluidized bed. Thus, both the effective pressure and the effective viscosity strongly depend on the granular temperature. As a result, an additional conservation equation representing a balance for this kinetic energy of the random motion of the particles is required to determine the pseudo temperature distribution. The granular temperature Θ is defined based on the solid fluctuating velocity u' as:

$$\Theta = \frac{1}{3} u'^2 \quad (3.16)$$

The variation of the particle velocity fluctuations is described by a separate conservation equation, the so-called granular temperature equation:

$$\frac{3}{2} \left(\frac{\partial(\varepsilon_s \rho_s \Theta)}{\partial t} + \nabla \cdot (\varepsilon_s \rho_s \mathbf{u}_s \Theta) \right) = (-P_s \bar{\mathbf{I}} + \bar{\boldsymbol{\tau}}_s) : \nabla \mathbf{u}_s - \nabla \cdot \mathbf{q} - \gamma_s + J_s \quad (3.17)$$

The left hand side of this equation is the net change of fluctuating energy. The first term on the right hand side is the generation of fluctuating energy due to local acceleration of the particles, which includes the solid pressure and shear tensor. The second term is the diffusion of fluctuating energy defined by a gradient of the granular temperature with a diffusion coefficient k :

$$\mathbf{q} = k \nabla \Theta \quad (3.18)$$

The diffusion coefficient k is usually written as the sum of kinetic and collisional contributions that are attributed to the dilute and dense region respectively.

$$k = k_{dilute} + k_{dense} \quad (3.19)$$

In the literature, there are different equations proposed for the diffusion coefficient among them are those by Lun et al. (1984), Syamlal et al. (1993) and Gidaspow (1994). Though all of them are derived from the kinetic theory, they have slight differences.

Lun et al. (1984)

$$k_{dilute} = \frac{25}{4} \frac{d_p \rho_s \sqrt{\pi \Theta}}{g_0 (1+e)(49-33e)} \left[1 + \frac{3}{5} (1+e)^2 (2e-1) \varepsilon_s g_0 \right] \quad (3.20)$$

$$k_{dense} = 15 \frac{d_p \rho_s \sqrt{\pi \Theta}}{(49-33e)} \left[1 + \frac{3}{5} (1+e)^2 (2e-1) \varepsilon_s g_0 + \frac{64}{15\pi} (49-33e)(1+e) \varepsilon_s g_0 \right] \quad (3.21)$$

Syamlal et al. (1993) used similar approach as Lun et al. (1984) but neglected the kinetic contribution (k_{dilute}).

Gidaspow (1994)

$$k_{dilute} = \frac{75}{192} \frac{d_p \rho_s \sqrt{\pi \Theta}}{g_0 (1+e)} \left[1 + \frac{6}{5} (1+e) \varepsilon_s g_0 \right]^2 \quad (3.22)$$

$$k_{dense} = 2 \varepsilon_s^2 \rho_s d_p g_0 (1+e) \sqrt{\Theta/\pi} \quad (3.23)$$

Boemer et al. (1997) and van Wachem et al. (2001) compared these three different models for the diffusion coefficient and found that all three yield the same thermal conductivity at high solid volume fraction. The model of Syamlal et al. (1993) deviate from the others for solids volume fractions less than 0.3 due to the negligence of the kinetic contribution in the model.

The third term on the right hand side of Equation (3.17) is the dissipation of fluctuating energy due to inelastic particle-particle collision. Jenkins and Savage (1986) were the first to describe this parameter as:

$$\gamma_s = 3(1-e^2) \varepsilon_s^2 \rho_p g_0 \Theta \left[(4/d_p) \sqrt{\Theta/\pi} - \nabla \cdot \mathbf{u}_s \right] \quad (3.24)$$

The term $\nabla \cdot \mathbf{u}_s$ was usually neglected as was done by Lun et al. (1984) and later by Syamlal et al. (1993). It may lead to negative dissipation (Boemer et al. 1997).

$$\gamma_s = 12(1-e^2) \frac{\varepsilon_s^2 \rho_s g_0}{d_p \sqrt{\pi}} \Theta^{3/2} \quad (3.25)$$

This dissipation term is usually taken into account by the magnitude of the particle-particle coefficient of restitution. The coefficient of restitution represents the fraction of energy dissipated due the inelastic collision of particles. It varies between 1, for fully elastic collisions without loss of kinetic energy, hence the dissipation becomes zero and 0 for fully inelastic collisions, hence the dissipation tends to infinity. For glass beads many investigators used different values ranging from 0.9 to 0.99 (Taghipour et al., 2005) with 0.9 preferred by many claiming that it provides

better agreement with experimental results (e.g. Taghipour et al., 2005; Patil et al., 2005b; Hulme et al., 2005). However, experimental tests suggested that the mean restitution coefficient for glass beads ranges 0.97 ± 0.02 (Goldsmith, 1960; Foerster et al., 1994). Moreover, it should be noted that the KTGF has been derived for slightly inelastic spheres and its application for particle restitution coefficient less than 0.9 is doubtful. Thus, in this work a coefficient of restitution of 0.95 was used. Figure 3.2 shows the variation of the dissipated granular energy with different coefficients of restitution.

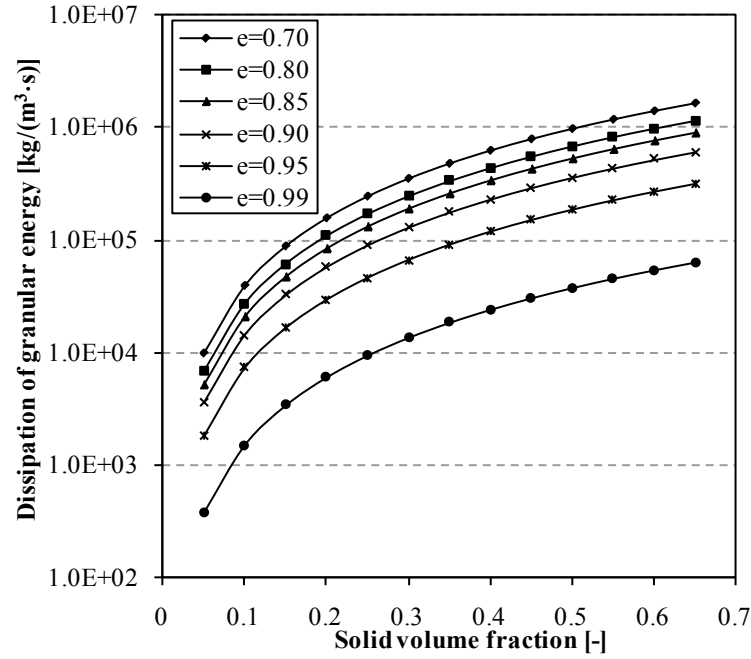


Figure 3.2: Influence of particle-particle restitution coefficients on the dissipation of granular energy; $g_0=5$, $d_p=347 \mu\text{m}$, $\Theta=0.1 \text{ m}^2/\text{s}^2$.

The last term in Equation (3.17) is the exchange of fluctuation energy between gas and solid phases, which accounts for the loss of granular energy due to friction with the gas and it is usually calculated according to Gidaspow (1994) as:

$$J_s = -3\beta\theta \quad (3.26)$$

Instead of solving the complete granular temperature equation (Equation 3.17), Syamlal et al. (1993) proposed an algebraic form of the equation. They assume a local equilibrium between generation and dissipation of the granular energy as these terms are the most dominant terms in dense regions. Thus, the convection and diffusion terms can be neglected. By neglecting these terms and retaining only the generation and the dissipation terms, Equation (3.17) reduces to:

$$0 = (-P_s \bar{\mathbf{I}} + \bar{\boldsymbol{\tau}}_s) : \nabla \mathbf{u}_s - \gamma_s \quad (3.27)$$

After Syamlal et al. (1993), Equation 3.27 can be rewritten in algebraic form as:

$$\Theta = \left(\frac{-K_1 \varepsilon_s \text{tr}(\overline{D}_s) + \sqrt{(K_1 \varepsilon_s)^2 \text{tr}^2(\overline{D}_s) + 4K_4 \varepsilon_s [2K_3 \text{tr}(\overline{D}_s^2) + K_2 \text{tr}^2(\overline{D}_s)]}}{2\varepsilon_s K_4} \right)^2 \quad (3.28)$$

Where, \overline{D}_s is the solids strain rate tensor, and the abbreviations are given by:

$$K_1 = 2(1 + e)\rho_s g_0 \quad (3.29)$$

$$K_2 = \frac{4}{3\sqrt{\pi}} d_p \rho_s (1 + e) \varepsilon_s g_0 - \frac{2}{3} K_3 \quad (3.30)$$

$$K_3 = \frac{d_p \rho_s}{2} \left\{ \frac{\sqrt{\pi}}{3(3-e)} \left[1 + \frac{2}{5} (1 + e)(3e - 1) \varepsilon_s g_0 \right] + \frac{8\varepsilon_s}{5\sqrt{\pi}} g_0 (1 + e) \right\} \quad (3.31)$$

$$K_4 = \frac{12(1-e^2)\rho_s g_0}{d_p \sqrt{\pi}} \quad (3.32)$$

Boemer et al. (1997) and van Wachem et al. (2001) showed that using the algebraic form instead of the full partial differential equation hardly affects the granular temperature in the bubbling regime while significant computational time can be saved. More recently Chen et al. (2011) also reported that the predicted bed expansion height, bubble size and bubble rise velocity were not influenced by the simplification while as much as 22 % of the computational time was saved. Moreover, using this algebraic equation much faster convergence and stable solution is obtained during simulation.

3.3.1 Gas phase stress tensor

Gases are usually assumed to be Newtonian fluids; thus, the viscous stress tensor is modeled using the Newtonian stress-strain relation as:

$$\overline{\boldsymbol{\tau}}_g = -\varepsilon_g \left[\left(\xi_g - \frac{2}{3} \mu_g \right) (\nabla \cdot \mathbf{u}_g) \overline{\mathbf{I}} + \mu_g (\nabla \mathbf{u}_g + (\nabla \mathbf{u}_g)^T) \right] \quad (3.33)$$

For the gas phase, the bulk viscosity ξ_g is usually set to zero, while the shear viscosity μ_g is assumed to be constant.

3.3.2 Solid phase stress tensor

The solid phase is also assumed to be Newtonian and the stress tensor is given by:

$$\bar{\bar{\tau}}_s = -\varepsilon_s \left[\left(\xi_s - \frac{2}{3} \mu_s \right) (\nabla \cdot \mathbf{u}_s) \bar{\bar{\mathbf{I}}} + \mu_s (\nabla \mathbf{u}_s + (\nabla \mathbf{u}_s)^T) \right] \quad (3.34)$$

In fluidized beds the bulk and shear viscosities of the particulate phase are of the same order and thus the bulk viscosity is not neglected.

3.3.2.1 Solid bulk viscosity

The solid bulk viscosity describes the resistance of the particle suspension against compression and expansion. In the literature, there is general agreement on the form of the solids bulk viscosity, which is given by Lun et al. (1984):

$$\xi_s = \frac{4}{3} \varepsilon_s \rho_s d_p g_o (1 + e) \sqrt{\Theta/\pi} \quad (3.35)$$

3.3.2.2 Solid shear viscosity

The shear viscosity represents the tangential forces due to translational and collisional interaction of particles. In general, it is written as the sum of a collisional and a kinetic part:

$$\mu_{s,KTGF} = \mu_{s,col} + \mu_{s,kin} \quad (3.36)$$

There are several models for the shear viscosity expression available in the literature. All use similar expression for the collision contribution and differ on their expression for the kinetic contribution of the solid shear viscosity. The three most frequently used solids shear viscosity models are those of Lun et al. (1984), Syamlal et al. (1993) and Gidaspow (1994). The collisional contribution of the shear viscosity is generally written as:

$$\mu_{s,col} = \frac{4}{5} \varepsilon_s \rho_s d_p g_o (1 + e) \sqrt{\Theta/\pi} \quad (3.37)$$

The kinetic contribution of the shear viscosity can be written as:

Lun et al. (1984)

$$\mu_{s,kin} = \frac{1}{15} \sqrt{\Theta\pi} \frac{\rho_s d_p g_o \varepsilon_s^2 (1+e)(3/2e-1/2)}{(3/2-1/2e)} + \frac{1}{6} \sqrt{\Theta\pi} \frac{\rho_s d_p \varepsilon_s (3/4e-1/4)}{(3/2-1/2e)} + \frac{10}{96} \sqrt{\Theta\pi} \frac{\rho_s d_p (3/2e-1/2)}{g_o (1+e)(3/2-1/2e)}. \quad (3.38)$$

Syamlal et al. (1993)

$$\mu_{s,kin} = \frac{1}{15} \sqrt{\theta \pi} \frac{\rho_s d_p g_0 \varepsilon_s^2 (1+e)(3/2e-1/2)}{(3/2-1/2e)} + \frac{1}{12} \sqrt{\theta \pi} \frac{\rho_s d_p \varepsilon_s}{(3/2-1/2e)} \quad (3.39)$$

Gidaspow (1994)

$$\mu_{s,kin} = \frac{1}{15} \sqrt{\theta \pi} \rho_s d_p g_0 \varepsilon_s^2 (1+e) + \frac{1}{16} \sqrt{\theta \pi} \rho_s d_p \varepsilon_s + \frac{10}{96} \sqrt{\theta \pi} \frac{\rho_s d_p}{g_0(1+e)} \quad (3.40)$$

Figure 3.3 illustrates the comparison of the three shear viscosity models as a function of solid volume fraction for the kinetic contribution and the sum of kinetic (translational) and collisional. The model of Gidaspow predicts slightly higher shear viscosity (kinetic contribution) than the other two. This is because Gidaspow (1994) does not account for the inelastic nature of the particles in the kinetic contribution of the total stress as Lun et al. (1984) do, claiming this contribution is negligible. Both the Lun et al. (1984) and Gidaspow (1994) showed similar trends and they did not tend to the correct limit of zero as the solid volume fraction approaches zero. The solid shear viscosity of Syamlal et al. (1993) neglects the kinetic streaming contribution, which dominates in dilute-phase flow, but their model tends to zero as the solid volume fraction tends to zero. It is difficult to discriminate between these three different models since few detailed measurements exist. However, the models differ mainly in the dilute region ($\varepsilon_s < 0.3$) which is of minor importance in bubbling fluidized beds. In dense solid systems, there is no difference in the predicted solid viscosity of the models. Since the collisional contribution of the solid shear viscosity dominates at higher solid volume fractions, all models yield the same total solids shear viscosity at high solid volume fraction as shown in Figure 3.3b.

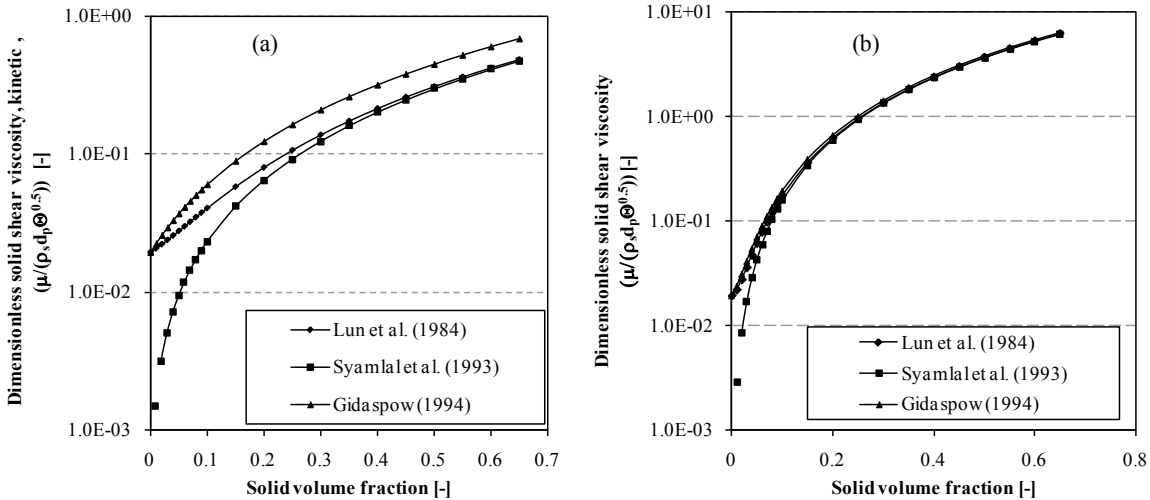


Figure 3.3: Comparison of different solid shear viscosity expressions (a) Kinetic contribution; (b) Total (Kinetic-Collisional) contribution; $g_0=5$, $e=0.9$.

In Figure 3.4, the solid shear viscosity of Gidaspow model was shown as a function of the coefficient of restitution. It is shown that the coefficient of restitution has negligible influence on the magnitude of the shear viscosity for all solid volume fraction values. Since no major difference between the models of Lun et al. (1984) and Gidaspow (1994) was observed, the model of the latter one was arbitrarily selected in this work.

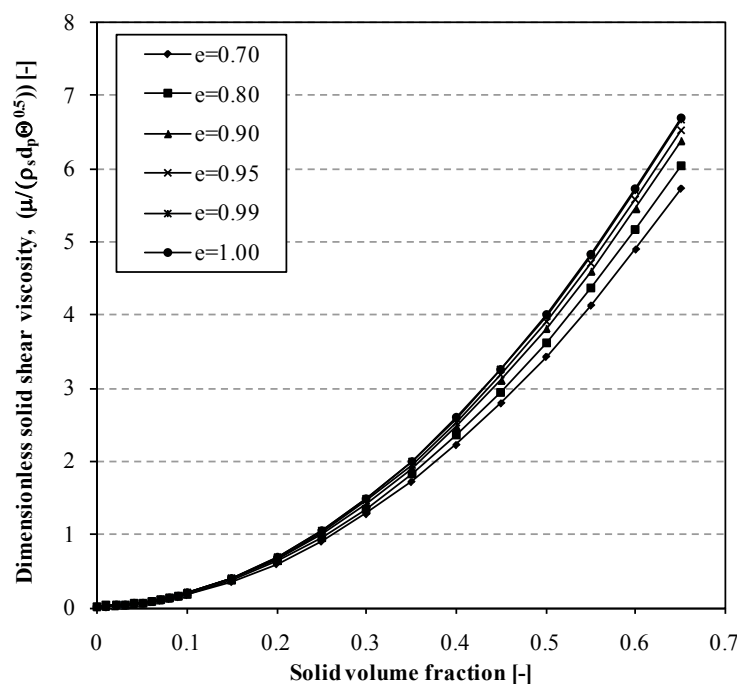


Figure 3.4: Dimensionless solid shear viscosity for different restitution coefficient; $g_0=5$.

3.3.3 Radial distribution function

The radial distribution function can be interpreted as the probability of a single particle touching another particle (probability of particle collision) in the solid phase. Thus, its value increases with increasing solid volume fraction. The value of the radial distribution function varies from one at zero solid volume fractions and tends to infinity when the solid volume fraction reaches the maximum packing limit due to constant contact of the particles. The function allows a tight control of the solids volume fraction, so that the maximum packing is not exceeded and more accurate flow characteristics can be achieved. Lun et al. (1984) employed the Carnahan and Starling (1969) expression for the radial distribution function. This expression, however, does not tend toward infinity as the solid volume fraction reaches its maximum packing limit. Other alternative expressions are proposed by Gidaspow (1994), Lun and Savage (1986), Savage (1988) and Ma and Ahmadi (1986). All these expressions tend to the correct limit at maximum packing limit. The expression of Gidaspow (1994), however, does not approach the correct limit of one as the solid volume fraction approaches zero. The different models are given below and

their comparison as a function of solid volume fraction is plotted in Figure 3.5. In this work, the model of Ma and Ahmadi (1986) was used as it provides better prediction over the whole range of solid volume fraction values compared to the others.

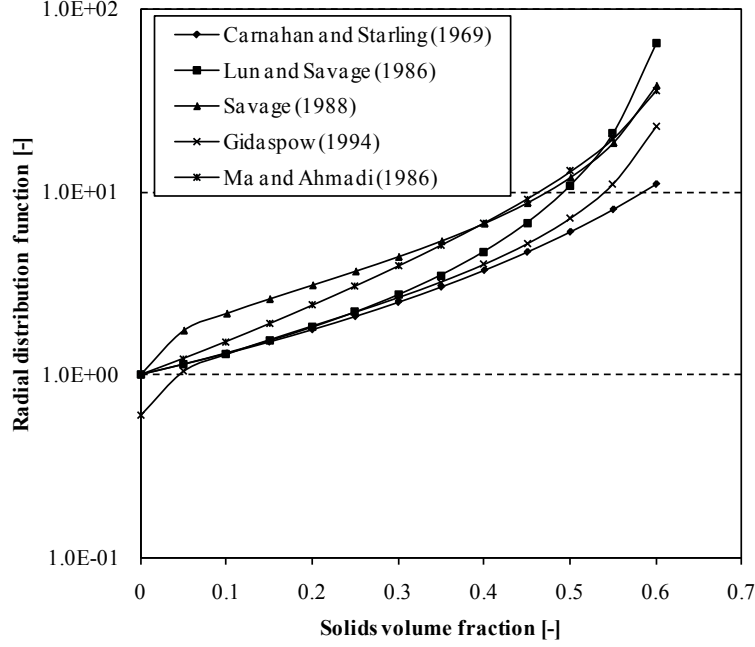


Figure 3.5: Comparison of different radial distribution functions; $\varepsilon_{s,max} = 0.65$.

Carnahan and Starling (1969)

$$g_0 = \frac{1}{1-\varepsilon_s} + \frac{3\varepsilon_s}{2(1-\varepsilon_s)^2} + \frac{\varepsilon_s^2}{2(1-\varepsilon_s)^3} \quad (3.41)$$

Lun and Savage (1986)

$$g_0 = \left(1 - \frac{\varepsilon_s}{\varepsilon_{s,max}}\right)^{-2.5\varepsilon_{s,max}} \quad (3.42)$$

Savage (1988)

$$g_0 = \left[1 - \left(\frac{\varepsilon_s}{\varepsilon_{s,max}}\right)^{1/3}\right]^{-1} \quad (3.43)$$

Gidaspow (1994)

$$g_0 = \frac{3}{5} \left[1 - \left(\frac{\varepsilon_s}{\varepsilon_{s,max}}\right)^{1/3}\right]^{-1} \quad (3.44)$$

Ma and Ahmadi (1986)

$$g_0 = 1 + 4\varepsilon_s \left\{ \frac{1 + 2.5\varepsilon_s + 4.5904\varepsilon_s^2 + 4.515439\varepsilon_s^3}{\left[1 - (\varepsilon_s/\varepsilon_{s,max})^3\right]^{0.67802}} \right\} \quad (3.45)$$

3.3.4 Solid pressure

The solid pressure represents the normal solid-phase forces due to particle-particle interactions and it prevents the solid phase from reaching unrealistic high solid volume fractions and also helps to make the system numerically stable by converting imaginary characteristics into real ones (Kuipers et al., 1992). It is written as the sum of kinetic and collisional term as given by Lun et al. (1984):

$$P_{s,KTGF} = \varepsilon_s \rho_s \theta + 2g_0 \varepsilon_s^2 \rho_s \theta (1 + e) \quad (3.46)$$

3.3.5 Frictional models

The mechanical behavior of flowing granular material results from forces exerted at many points of contacts between different particles. Unless the particle surfaces are perfectly smooth the contact forces have both tangential and normal components, and the surface in contact may or may not be slipping relative to each other. When the particle concentration is low, the assembly of particles is widely spaced, and in vigorous motion, individual contacts are of short duration and may be treated as collisions, analogous in many ways to the encounters between molecules in liquids or gas. For slow deformations at high solids volume fraction as in the case of dense fluidized beds, on the other hand, the particle interaction time may be much larger than the particle mean free flight time that resulted in sustained particle-particle contacts with much higher particle stresses. Therefore, the normal reaction forces and associated tangential frictional forces at these sliding contacts are dominant. Of course, most situations of practical interest of gas-solid flows are intermediate between these two extreme conditions. Therefore, the stresses associated with such semi-permanent contacts (frictional stresses) are significant, if not dominant (Johnson and Jackson, 1987). However, one of the main disadvantages of the TFM is its difficulty to include these effects of particle-particle friction into the governing equations. Even the latest KTGF approach did not account frictional stresses, due to the inherent assumption of binary and quasi-instantaneous collision of smooth spherical particles in its derivation.

The frictional stresses that arise from the sustained particle-particle interaction are composed of the frictional shear viscosity and frictional solid pressure, which includes the tangential and normal frictional forces respectively. Generally, the frictional stress is written in a Newtonian form as:

$$\bar{\tau}_{s,f} = P_{s,f} \bar{\mathbf{I}} + \mu_{s,f} [\nabla \mathbf{u}_s + (\nabla \mathbf{u}_s)^T] \quad (3.47)$$

The total stress transmitted by the particle assembly will be therefore the sum of contributions from these sources, which will be referred to as frictional and the collisional-translational (kinetic) contributions that can be derived from the KTGF. However, given the different nature of theories of both contributions, it is still unclear as to how they should be combined. Johnson and Jackson (1987) assumed that the total stress could be approximated as the sum of frictional and collisional-translation contribution, each calculated as if it acted alone. They suggested that the frictional stresses can be added to the solid stresses from KTGF when, $\varepsilon_s > \varepsilon_{s,\min}$, as:

$$\mu_s = \mu_{s,KTGF} + \mu_{s,f} \quad (3.48)$$

$$P_s = P_{s,KTGF} + P_{s,f} \quad (3.49)$$

Different expressions for the solid frictional shear viscosity ($\mu_{s,f}$) and solid frictional pressure ($P_{s,f}$) are available in the literature and are compared by Benyahia (2008) and Passalacqua et al. (2009). In this study, the Schaeffer (1987) model for the frictional shear viscosity and the Johnson et al. (1990) model for the frictional pressure were used.

$$\mu_{s,f} = \frac{P_s \sin \phi}{2 \sqrt{\bar{I}_{2D}}} \quad (3.50)$$

Where the second invariant of the deviatoric stress tensor in a generalized three-dimensional form is given by,

$$\bar{I}_{2D} = \frac{1}{6} \left[\left(\frac{\partial u_{s,x}}{\partial x} - \frac{\partial u_{s,y}}{\partial y} \right)^2 + \left(\frac{\partial u_{s,y}}{\partial y} - \frac{\partial u_{s,z}}{\partial z} \right)^2 + \left(\frac{\partial u_{s,z}}{\partial z} - \frac{\partial u_{s,x}}{\partial x} \right)^2 \right] + \frac{1}{4} \left[\left(\frac{\partial u_{s,x}}{\partial y} + \frac{\partial u_{s,y}}{\partial x} \right)^2 + \left(\frac{\partial u_{s,y}}{\partial z} + \frac{\partial u_{s,z}}{\partial y} \right)^2 + \left(\frac{\partial u_{s,z}}{\partial x} + \frac{\partial u_{s,x}}{\partial z} \right)^2 \right] \quad (3.51)$$

$$P_{s,f} = Fr \frac{(\varepsilon_s - \varepsilon_{s,\min})^n}{(\varepsilon_{s,\max} - \varepsilon_s)^p} \quad (3.52)$$

Where, the values for $Fr=0.05$, $n=2$ and $p=5$ are used (Johnson et al., 1990). The maximum packing limit ($\varepsilon_{s,\max}$) was taken as 0.65 while the critical value for the solid volume fraction ($\varepsilon_{s,\min}$) at which these frictional stresses are added is taken to be 0.6. A sensitivity analysis for this parameter was performed and is reported in Chapter 6.

3.4 Solution Method

For the solution purpose the commercial CFD code ANSYS FLUENT 12.1 (ANSYS, 2009) was used. It is a state-of-the-art computer program for modeling fluid flow, heat transfer and chemical reactions in complex geometries. The Eulerian multiphase model in ANSYS FLUENT allows for the modeling of multiple, separate, yet interacting phases. It uses a segregated pressure based solver in which the phase momentum equations, the shared pressure, and phasic volume fraction equations are solved in a coupled and segregated fashion (ANSYS, 2009). Using this approach, the pressure field is extracted by solving a pressure correction equation, which is obtained by manipulating continuity and momentum equations. In the segregated algorithm, because the governing equations are non-linear and coupled, the solution loop must be carried out iteratively in order to obtain a converged numerical solution.

For transient simulations such as in gas-solid fluidized beds, the governing equations must be discretized separately in both space and time. For this purpose, ANSYS FLUENT uses a control-volume-based technique to convert the general scalar transport equation to an algebraic equation that can be solved numerically. This is done first by dividing the solution domain into a finite number of small and non-overlapping control volumes (CVs) using a grid. The control volume technique uses the integral form of the conservation equations as a starting point and integrates the transport equation about each control volume, yielding a discrete equation that expresses the conservation law on the control-volume basis. The CV is defined by suitable grid and assigns the computational node to the CV center that stores discrete values of the scalars such as pressure, volume fraction. This yields that the node value represents the mean over the CV volume. The main advantage of the finite volume method is that the spatial discretization is carried out directly in the physical space. Thus, there are no problems with any transformation between coordinate systems. Moreover, it is more flexible as it can be easily implemented on structured as well as unstructured grids. This renders it particularly useful for the treatment of flows in complex geometries like in gas-solid fluidized beds with immersed tubes.

For the spatial discretizations of the continuity equations ANSYS FLUENT offers either the first order upwind or the QUICK (Quadratic Upwind Interpolation for Convective Kinematics). Though, the first order upwind scheme can unconditionally satisfy the boundedness criterion i.e. it will never yield oscillatory solutions, it is numerically diffusive that increases the numerical discretization error such as unphysical bubble shape (Guenther and Syamlal, 2001). This was worst when the flow is not aligned with the mesh (i.e., when it crosses the mesh lines obliquely) that is usually the case in gas-solid multiphase flows in fluidized beds. Therefore, high order interpolation schemes such as QUICK are acceptable for accurate results of complex flows. QUICK scheme is applicable to quadrilateral or hexahedral meshes and has been also used in this work. For the spatial discretization of momentum equation, the second order upwind scheme was employed. In general, the second-order scheme is sufficient and the QUICK scheme will not provide significant improvements in accuracy. For the temporal discretization the second

order implicit was used. The set of algebraic equations resulting from such discretization are solved using a point implicit (Gauss-Seidel) linear equation solver in conjunction with an algebraic multigrid (AMG) method (ANSYS, 2009).

Since the governing equations are solved in a segregated manner, a pressure-velocity coupling is necessary. Thus, the phase-coupled SIMPLE (PC-SIMPLE) algorithm (Vasquez and Ivanov, 2000) was selected for the pressure-velocity coupling. PC-SIMPLE is an extension of the SIMPLE algorithm (Patankar, 1980) to multiphase flows. The velocities are solved coupled by phases, but in a segregated fashion. The block algebraic multigrid scheme used by the density-based solver described in Weiss et al. (1999) is used to solve a vector equation formed by the velocity components of all phases simultaneously. Then, a pressure correction equation is built based on total volume continuity rather than mass continuity. Pressure and velocities are then corrected so as to satisfy the continuity constraint. Detail discussion of the solver and solution methods can be found in the ANSYS FLUENT Theory and User Guides.

3.4.1 Grid size and time steps

A uniform quadratic mesh with size of 5 mm was applied for all geometries studied in this dissertation. To capture the higher velocity gradient near the tubes, grid refinement was performed with 2 mm of grid size at the tube surfaces that grew uniformly at a rate of 10 % up to the universal grid size of 5 mm. In order to study the influence of grid size on the simulation results, grid sensitivity analyses were performed for grid size ranging from 2 mm to 10 mm. With the exceptions of a grid size of 10 mm other sizes (5 mm, 4 mm, 2 mm) provide similar results hence the grid size of 5 mm was preferred taking into account the accuracy and computational time required. Detail results of grid sensitivity analysis are presented in Chapter 5.

The time step for the numerical simulations was chosen based on simulation time, numerical accuracy and simulation stability. Though a time step of 1×10^{-5} s showed excellent convergence and simulation stability, the computation time needed was unacceptable to perform parametric studies with large number of simulation cases. On the other hand, a time step of 1×10^{-4} s resulted in very short computational time, but it suffers from numerical stability especially for higher superficial velocities. Thus, taking into account these two extremes time steps of 5×10^{-5} and 2.5×10^{-5} s were used for the smaller and larger particle sizes respectively. These time steps provide better accuracy of results with acceptable computational time and stable simulation. In a preliminary study of time step sizes, it was found that simulation results were generally independent of the time step size at least for time step sizes ranging between 1×10^{-4} to 1×10^{-5} s. Therefore, the choice of the time step size lays mainly on the computational time needed and simulation stability. No major improvement of simulation accuracy can be achieved by using smaller time steps.

3.4.2 Initial and boundary conditions

3.4.2.1 Initial conditions

The initial conditions of all simulation cases were set to the minimum fluidization condition. The vertical gas velocity was set at the minimum fluidization velocity for the respective particle group. The initial solid volume fraction is also set to the volume fraction at minimum fluidization velocity measured for each particle. The initial bed height was set at bed height at minimum fluidization of 0.5 m.

3.4.2.2 Inlet and outlet boundary conditions

At the inlet, i.e. bottom of the fluidized bed, the so-called velocity inlet boundary condition with uniform superficial velocity of the gas phase was set. This is called the Dirichlet boundary condition. For the solid phase, it is made impenetrable by setting the solid phase axial velocity to zero. At the outlet, i.e. at the top of the fluidized bed, the so called pressure boundary condition was set for the mixture phase. The pressure in the mesh cell at the top of the fluidized bed is fixed at a specified value, which is equal to the atmospheric pressure. Neumann boundary condition is applied to the gas flow velocity, i.e. the derivative of the upward velocity in the horizontal direction are assumed zero. This is achieved by making the height of the freeboard long enough such that a fully developed flow can be physically expected.

3.4.2.3 Wall boundary conditions

For the gas phase on the wall surface, the no-slip boundary condition was set with the flow velocity is set to zero in all directions. The term wall includes both bed walls and the immersed tube walls. However, this is not completely true for the solid particles. When a rigid particle strikes the wall, it rebounds either fully or partially. Hence, it can be assumed the particle to have a zero normal velocity and for the tangential direction along the wall surface the particle velocity may be between the free-slip condition and the no-slip condition. The partial-slip boundary condition proposed by Johnson and Jackson (1987) is most widely used and it is given by Equation 3.53. This expression requires a value for the specularity coefficient, ϕ' . The specularity coefficient is a measurement of the fraction of collisions that transfer momentum to the wall and varies from zero (free-slip condition) to one (no-slip condition). Since direct measurement of specularity coefficient is not possible, different values have been used in numerical simulations by different authors. The influence of the specularity coefficient on numerical results has been performed in Chapter 6. Moreover, the different boundary conditions; namely, the no-slip, free-slip and partial-slip boundary condition were evaluated.

$$\mathbf{F}_w = \frac{\pi}{6} \sqrt{3} \phi' \frac{\varepsilon_s}{\varepsilon_{s,max}} \rho_s g_0 \sqrt{\theta} u_{slip} \quad (3.53)$$

4 Experimental Technique

The design and scale-up of gas-solid fluidized beds requires detail knowledge of the gas-solid fluid dynamic particularly the bubble hydrodynamics that occur in these systems. Unfortunately, the behavior of bubbles such as their size, distribution and rise velocity is still not sufficiently understood due to the lack of reliable measurement techniques to accurately measure bubble characteristics over the entire fluidized bed cross-section. Such reliable experimental techniques will also be vital for proper validation of numerical models that are emerging nowadays as fundamental tool for the analysis of fluidized beds. In this chapter, a detail description of the experimental technique employed in this work is presented.

4.1 Experimental Setup

The experimental studies were performed on a purposely designed and installed fluidized bed. The column is 0.32 m wide, 1.2 m high and 0.02 m thick, almost 2D thus allowing visual observations of bubble dynamics within the bed. The schematic diagram is shown in Figure 4.1.

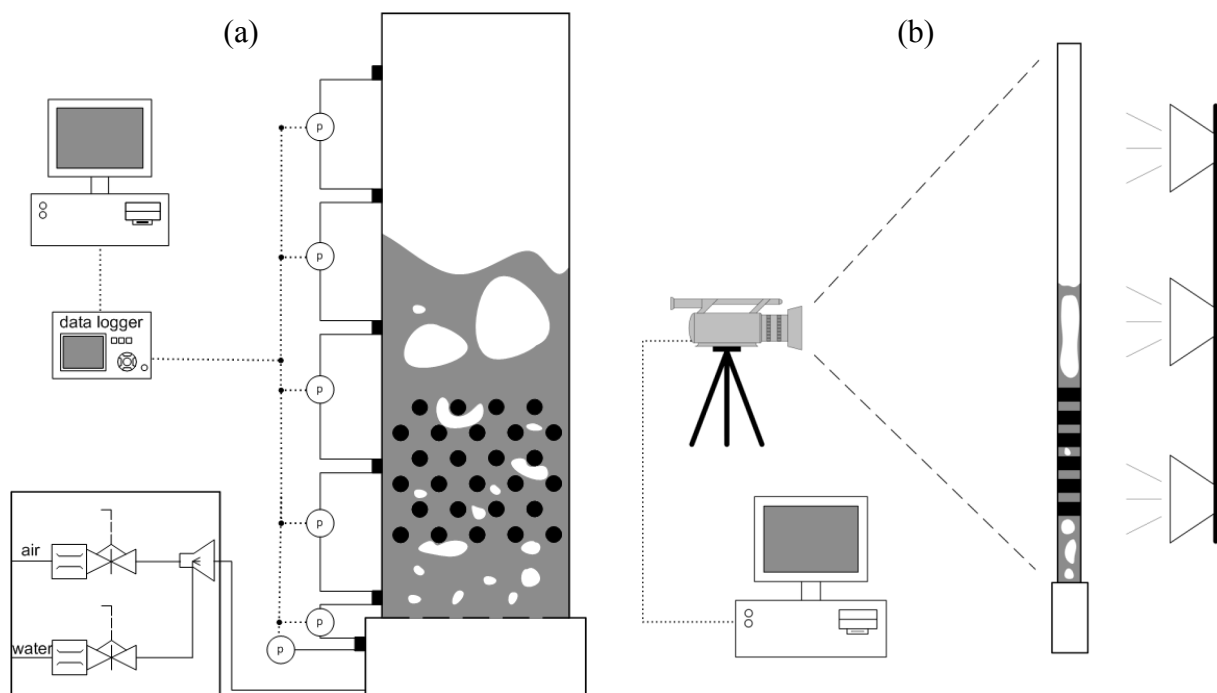


Figure 4.1: Experimental setup; (a) hydraulic scheme, (b) optical scheme.

The front-and back-sides are made of polycarbonate plastic in order to allow easy drilling of holes for assembling of the simulated immersed tubes. Moreover, polycarbonate plastic allows

better transparency of light, which is the main requirement for the use of digital image analysis technique. The simulated immersed tubes are made of polyoxymethylene (POM) plastic and are fixed to the back plate of the bed. The back plate was designed in such a way that it can be easily removed and replaced. Thus, different tube arrangements can be utilized by disassembling the back plate and replacing with another plate of the needed tube geometry. The different tube geometries with the exception of the bed without tubes (NT) are shown in Figure 4.2. A sintered porous plate distributor, whose thickness equal to 6 mm, is placed at the bottom of the particle bed. The distributor together with a windbox below allows equalizing the gas flow and providing the required pressure drop. Air was used as fluidizing gas whose flow rate is measured using thermal mass flowmeter. A water humidifier was mounted on-line with the gas feed. Thus, the relative humidity of the fluidizing air can be kept between 50-70 % to reduce the electrostatic effect that could be generated during fluidization (Park et al., 2002). Using five differential pressures and one gauge pressure measurement devices the pressure drop across the bed height (including the pressure drop across the distributor) can be measured and recorded at a frequency of 1 Hz on a computer along with the air volume flow rate, temperature and relative humidity.

4.2 Mean Particle Size and Size Distribution

Particle size is an important parameter in fluidized beds, which strongly influences the fluidization quality of the bed. As discussed in Chapter 1, different sizes of particles have different fluidization behavior. Though, in practice, any powder has a wide size distribution, in the design and analysis of fluidized beds, the powder is assumed to have a uniform size distribution given by its mean diameter. Moreover, actual powder particles are not always spherical as usually treated. There are different ways of defining the size of particles with the most common ones summarized by Geldart (1986). In this work, the sieve size was used. The particles were first sieved to get a very narrow distribution then analyzed using a particle size analyzer named Partica from HORIBA to get the mean diameter. A typical size distribution for two of the particle classes with mean particle sizes of 246 μm and 347 μm is shown in Figure 4.3. The size distribution for the other particles are given in Appendix A. Using Partica, a given sample of powder is split into different size ranges with mean particle size of $d_{p,i}$ and mass percentage of m_i , then the mean particle size can be calculated as:

$$d_p = 100 / \sum (m_i / d_{p,i}) \quad (4.1)$$

All the particles used in this work are glass beads with particle density of 2500 kg/m^3 and their mean particle sizes as calculated using equation 4.1 are summarized in Table 4.1.

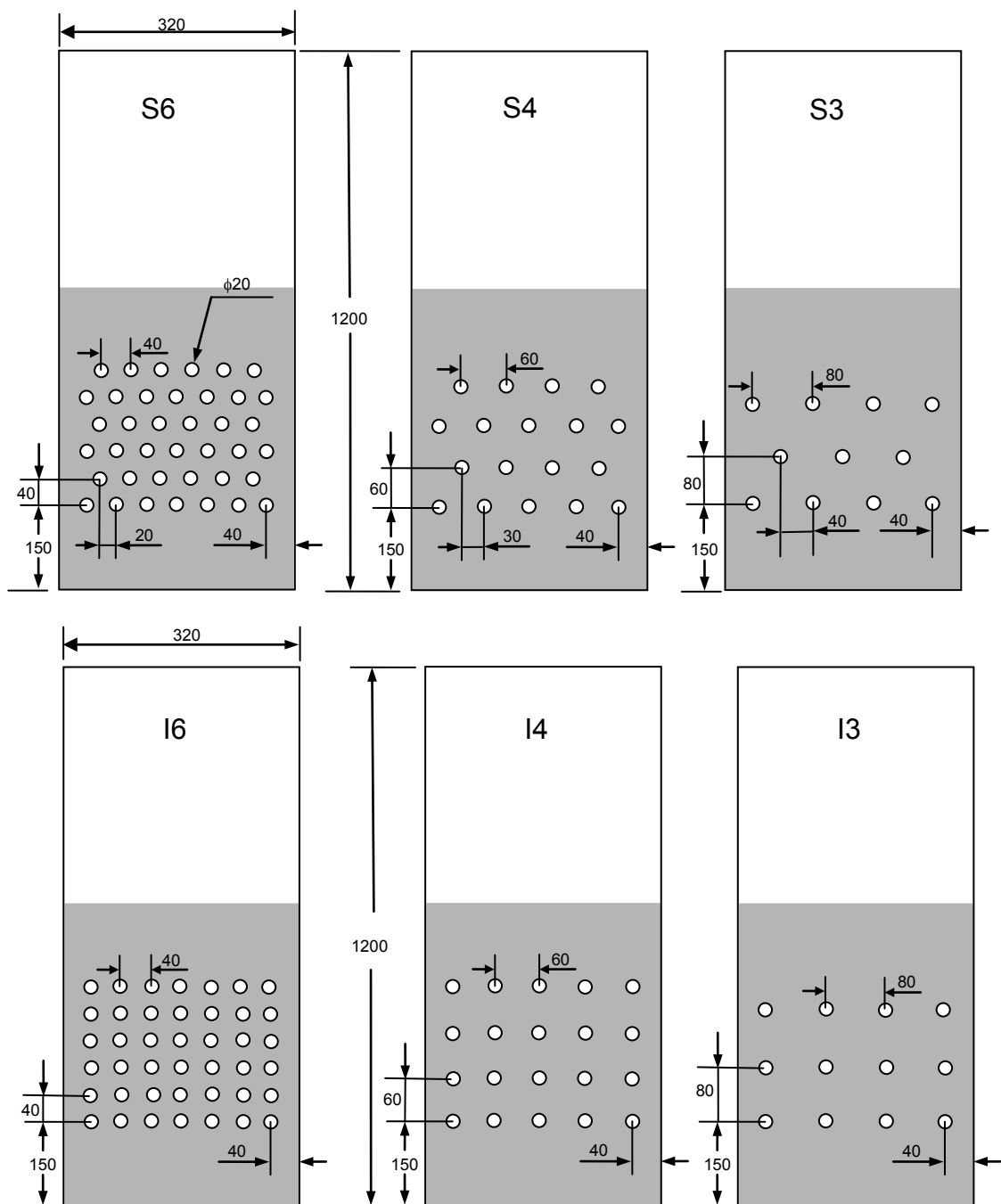


Figure 4.2: Tube bank geometries and arrangement: staggered (S) and in-line (I).

Note: All dimensions are in mm and the drawings are not to scale. The bed without immersed tubes (NT) is not shown to reduce redundancy. The number followed the letters S and I that stand for the staggered and in-line tube arrangement respectively indicates the number of rows in the tube bank. E.g., S6 stands for the staggered tube arrangement with six tube rows, I6 stands for the in-line arrangement with six tube rows and so on.

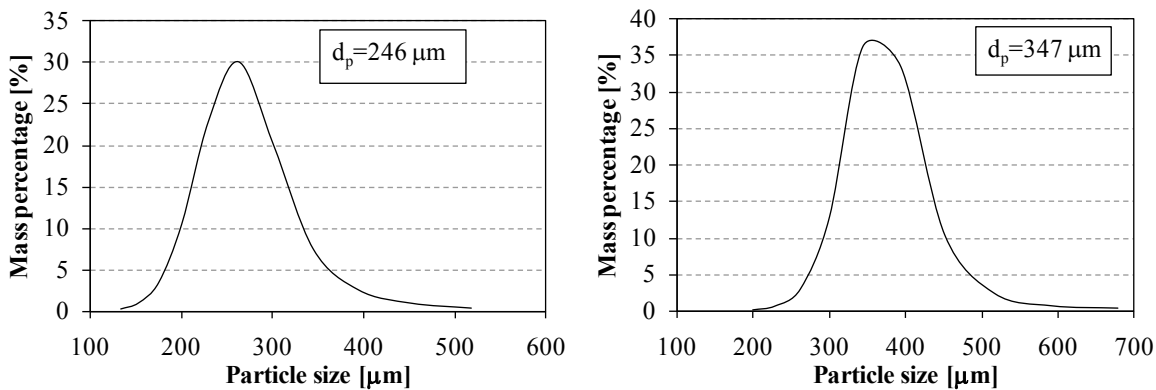


Figure 4.3: Size distribution of the two of the particles used.

Table 4.1: Sieve size distribution and mean particle size.

Sieve size, μm	Mean particle diameter, μm	Geldart's Group
90-180	141	A/B
180-300	246	B
300-400	347	B
400-600	439	B
500-710	592	B/D
710-1000	776	D

4.3 Automated Digital Image Analysis Technique

4.3.1 Image acquisition and data processing

The Digital Image Analysis Technique (DIAT) developed comprises acquiring images using a video camera and then processing and analyzing the images using an in-house software. The in-house software was developed with the help of the MATLAB Image Processing Toolbox to fully automate the procedure of image processing.

4.3.1.1 Image acquisition

Images were captured for the whole bed without selecting any particular region of interest, in order to allow complete bed analysis of the bubbling fluidization dynamics. The flow structure was visualized with the help of a back lighting device and recorded by a commercial digital video camera (Sony, model DCRTRV530E PAL), which was placed in front of the bed, as shown in Figure 4.1b. The digital camcorder allowed images to be captured with a resolution of 1280 x 720 pixels at a rate of 50 frames per second. A uniformly illuminated back light consisted of three cool white high intensity LED floodlights, each equaling 20 W with 240 LED

lights per bulb. To eliminate interference from any external light the room was completely darkened. Bubbles were detected because they transmit light emitted at the back of the bed, which reaches the camera. Hence, white areas represent bubbles while the remaining black area indicates the emulsion phase. With this arrangement, images were recorded for 5 min for each measurement that gave a total of 15,000 frames and more than 150,000 bubbles per measurement for the statistical analysis. This was found to be sufficient for the statistical analysis of bubble properties.

4.3.1.2 Image cropping

Once the images were captured post-processing was performed offline with the in-house software. The first step in the image processing procedure is image cropping. The actual images were cropped to exclude all surroundings including the walls of the fluidized bed from the region of interest. Since the size of images for each experimental case can be different due to the location of the camera, the size of the region of interest (image cropping parameters) was manually selected for each experiment performed.

4.3.1.3 Image conversion and thresholding

In this step the actual RGB images were converted to grayscale then to binary images (black and white). This is an important step in discriminating a bubble from the rest of the bed. Bubble discrimination is usually done with the help of a threshold value for the pixel intensity of the grayscale images. Identifying the proper threshold value for the volume fraction cut-off point (in this case a 0.8 volume fraction for the gas phase) is the critical task of this step.

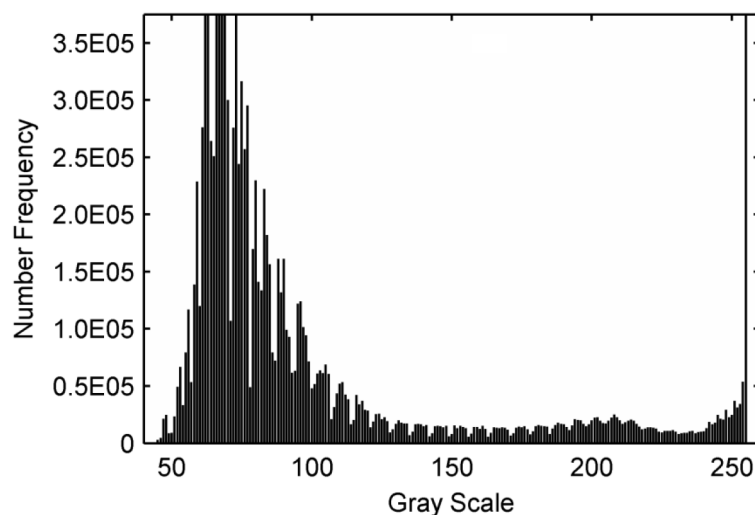


Figure 4.4: Time-averaged grayscale histogram.

The simplest way is to analyze manually the grayscale histogram of pixel intensity, such as the one shown in Figure 4.4. Either individual frame histograms or a time-averaged histogram can be used for this purpose. In this work, a time-averaged grayscale histogram was used to estimate a global threshold value. Such global threshold values can be chosen provided that the lighting system is fairly uniform throughout the bed (Lim et al., 1990). In addition, preliminary analysis was performed with different threshold values that were both lower and higher than the global threshold chosen from the histogram, i.e. within the range of gray intensity from 140 to 230. It was found that bubble diameter varied with the threshold values investigated, while other bubble properties such as shape and rise velocity were found to be independent of these threshold values. As the grayscale threshold value increased bubble diameter decreased and at some point it remained constant. The grayscale value at which bubble diameter was no longer affected was selected as the global threshold value. Based on this global threshold value the boundary of the bubble can be delineated. Figure 4.5 shows the three steps of bubble delineation.

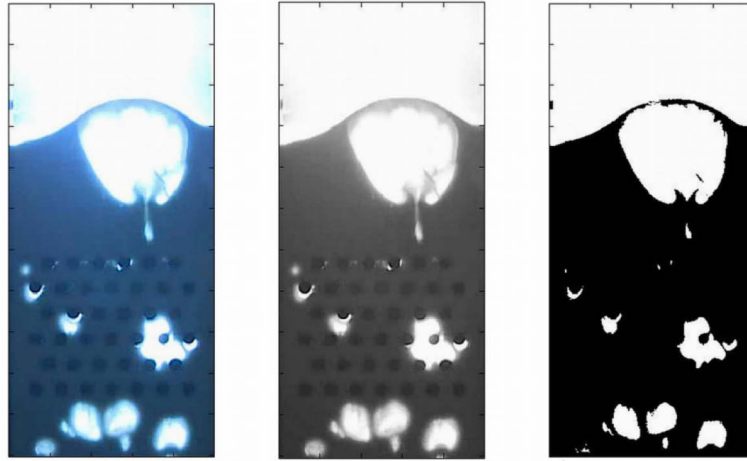


Figure 4.5: Bubble delineation; original image (left), grayscale image (middle) and binary image (right).

4.3.1.4 Bubble property calculation

Once the bubble is delineated and identified, its projected area A_B , horizontal and vertical coordinates of its center of gravity (centroid) and horizontal and vertical extremes are measured. Then the bubble properties – bubble aspect ratio, bubble shape factor, bubble diameter, bubble rise velocity and location of the rise velocity – are calculated using equations 4.2 to 4.6 respectively. The bubble aspect ratio, AR , and shape factor, SF , are defined as:

$$AR = d_y/d_x \quad (4.2)$$

$$SF = \pi d_B/P_B \quad (4.3)$$

Where d_y and d_x are the vertical and horizontal extremes (Figure 4.6), d_B is the equivalent bubble diameter which is defined as a circle of the same projected area and is given by Equation 4.4 and P_B is the bubble perimeter.

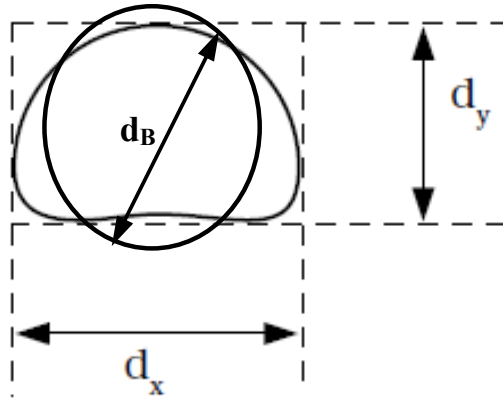


Figure 4.6: Bubble dimensions.

The bubble diameter was calculated from the area equivalent A_B as:

$$d_B = \sqrt{4A_B/\pi} \quad (4.4)$$

To measure bubble properties with bed height the height of the bed was divided into equal sections of 0.01 m high from 0.05 m to 0.5 m above the distributor, which gave 45 horizontal sections. The bubble properties – aspect ratio, shape factor and bubble diameter – were then assigned to one of the sections depending on the location of the vertical coordinate of the centroid and they were assumed to be located at the mid-point of the respective section above the distributor.

The rise velocity was calculated as the difference in the vertical coordinate of the centroid between the consecutive time frames divided by the time interval between the frames.

$$u_B = (y_c(t + \Delta t) - y_c(t))/\Delta t \quad (4.5)$$

Where y_c is the vertical location of the centroid of the bubble, t is the time and Δt is the time interval between consecutive frames, in this case 1/50 s.

The velocity was attributed to the mean vertical height according to:

$$h = (y_c(t + \Delta t) + y_c(t))/2 \quad (4.6)$$

4.3.1.5 Bubble tracking

Calculation of the rise velocity required a correct match between bubbles in consecutive frames. Tracking bubbles from frame to frame and locating their centroid is the most difficult task in the digital image analysis technique because bubbles can coalesce, break-up and even disappear during the interval. The presence of immersed tubes makes the bubbles' dynamics more complicated, which in turn worsen the scenario. The main difference in the bubble tracking algorithm in this work to that of others (e.g. Utikar and Ranade, 2007; Busciglio et al., 2008, 2009) is the inclusion of the immersed horizontal tubes and their influence. These early tracking criteria are mainly based on the position of the centroids and equivalent bubble diameters during two consecutive frames and are simple and sufficient for beds without immersed tubes. However, in the case of beds with immersed tubes, these criteria did not provide realistic results in the tube bank region due to very high bubble splitting, coalescence and rapid changes in bubble shapes. Thus, some modification and additional algorithms were necessary to reasonably account for the behaviors of bubbles in the presence of tubes.

Bubble tracking was done in two stages. In the first step, links between bubbles in the first and second time frames were generated based on the relative distance moved and maximum rise velocity allowed. This also enabled multiple matching. Four criteria were used to construct the link between the bubbles.

- i. $|x_2 - x_1| \leq d_{B,2} + d_t$, where x_1 and x_2 are the x-coordinates of the centroid in the first and second time frames, $d_{B,2}$ is the bubble diameter in the second time frame and d_t is the tube diameter. This condition fixes a window in both a positive and negative direction on the x-axis.
- ii. $0 < y_2 - y_1 \leq d_{B,2} + d_t$, where y_1 and y_2 are the y-coordinates of the centroid in the first and second time frame. This condition fixes a window in the vertical direction. This criterion only allows positive rise velocity.
- iii. $|y_1 - y_2| \leq \Delta y_{max}$, where Δy_{max} is the allowed maximum negative y displacement of the centroid. This condition permits slight negative rise velocity (drop velocity). Previous researchers never included negative rise velocity as bubbles are normally assumed to have only positive rise velocity. However, it was observed that at the bottom of the tubes bubbles can grow without moving upwards which resulted in a lower centroid than in the previous time frame. This gave a negative or zero rise velocity and was briefly explained in Asegehegn et al. (2011). The value of the maximum negative displacement of the centroid (Δy_{max}) can be manually set by observing the individual images. In this work it was limited to 25 % of the diameter of the bubble in the second

time frame. This was also seen to minimize some wrong matches between different bubbles.

- iv. $|u_B| \leq u_{B,max}$, where $u_{B,max}$ is the maximum bubble rise velocity allowed. This criterion fixes the bubble velocity to be below the maximum expected rise velocity. The maximum possible rise velocity is selected manually for each case by inspecting the superficial velocity.

These four criteria create a link between all bubbles in all frames. In the second step wrong links were deleted with the help of criteria associated with splitting, coalescence and the size of bubbles. In general, five different cases for bubble matching can be identified and these were used in deleting the wrong links.

Case 1: A bubble may have only one match: In this case no splitting or coalescence occurred. Thus the equivalent area of the bubble in the second time frame should be slightly bigger or equal to the equivalent area of the bubble in the first time frame. No shrinking of the bubbles was assumed and Equation.4.7 was used.

$$A_{B,d} \leq f_B A_{B,p} \quad (4.7)$$

The bubble growth factor f_B depends on the time interval between frames and superficial velocity and it can be manually selected. From preliminary observation, this was taken to be 1.2.

Case 2: A single bubble has two or more matches: In this case bubble splitting might occur. Thus the sum of the resulting projected areas of the daughter bubbles is less than or equal to the parent bubble area (Clift and Grace, 1985):

$$\sum_{i=1}^n (A_{i,dB}) \leq A_{pB} \quad (4.8)$$

Where $A_{i,dB}$ is the area of the i^{th} daughter bubble and A_{pB} is area of the parent bubble.

In this case the rise velocity was calculated from the centroid of the parent bubble and the mean centroids of the daughter bubbles. If this was not possible, the bubbles that were nearly equal in size and nearest to each other will be matched to calculate the rise velocity. For the second bubble further scanning is performed to find its match or it is considered as a new bubble.

Case 3: Two or more bubbles have a single match: In this case bubble coalescence might occur. If two bubbles coalesce the resulting projected area of the daughter bubble is 10-20 % higher than the sum of the two parent bubbles (Clift and Grace, 1985). Thus,

$$\sum_{i=1}^n (A_{i,pB}) \leq A_{dB} \leq 1.2 \sum_{i=1}^n (A_{i,pB}) \quad (4.9)$$

Where $A_{i,pB}$ is i^{th} parent bubble in the first time frame and A_{dB} is the area of daughter bubble in the second time frame.

Similar to case 2 the rise velocity was calculated from the centroid of the daughter bubble and mean of the centroids of the parent bubbles. Parent bubbles that did not satisfy Equation 4.9 were considered to have disappeared.

Case 4: A bubble disappears: In this case no link was found for a bubble, thus it was assumed to have disappeared in the second time frame.

Case 5: A bubble appears: If a bubble was detected and no match was found in the previous time frame it was assumed to be a new bubble and its rise velocity was not calculated until the next time frame.

4.3.1.6 Time-averaging of bubble properties

Once the instantaneous bubble properties at each section of the bed were calculated number averaging was used to calculate the time-averaged bubble properties with bed height.

$$\theta = \sum_{i=1}^N (\theta_i) / N \quad (4.10)$$

Where θ is any property of the bubble such as diameter, rise velocity, shape factor and aspect ratio, and N is total number of bubble property measurements recorded in a section during the total averaging time considered.

4.3.2 Calibration and validation of the DIAT

After developing the automated DIAT, the in-house software was calibrated and validated with known data. Calibration of the technique was performed using known shapes such as circles, rectangles and ellipses and predefined centroids and displacements. The images were plotted in two frames with specified centroid and area and displacement. The diameter, aspect ratio, shape factor and rise velocity can be calculated manually and compared with results from the DIAT. The equivalent diameter, rise velocity, aspect ratio and shape factor calculated by the software for the different shapes were similar to the actual predefined values. Moreover, in order to validate the reproducibility of the results obtained, different images recorded at different dates for the same bed geometry and operating conditions were analyzed. The code was able to reproduce excellently the results for beds with and without internal obstacles.

For validating the routine especially the bubble tracking algorithm using manual examination, the software is able to generate images showing the links between the tracked bubbles between consecutive time frames with designated bubble number. Figure 4.7 shows a sample of such outputs. With the help of such figures wrong matches and untracked bubbles can be analyzed manually for all frames. Since such procedure is time consuming and usually produce similar results, only a sample of data were analyzed for the bed without tubes (NT) and for beds with dense tube arrangements (S6 and I6). From the data analyzed only less than 5 % of the bubbles were found to be either wrongly matched or totally untracked and was assumed to be the same for all experimental and numerical data analyzed in this work. Since, the total number of bubbles tracked in each experimental test was more than 150,000; the influence of this error margin on the statistical bubble property analysis was insignificant. From Figure 4.7 it can be seen that the software correctly accounts the internal tube slots. During the thresholding and bubble delineation procedure, the tubes were detected as the emulsion phase and were identified as black areas. In calculating the bubble projected area the routine counts the number pixels which are white. Thus, as it is shown, when a tube/s is inside a bubble it is excluded from the calculation of the area of the bubble.

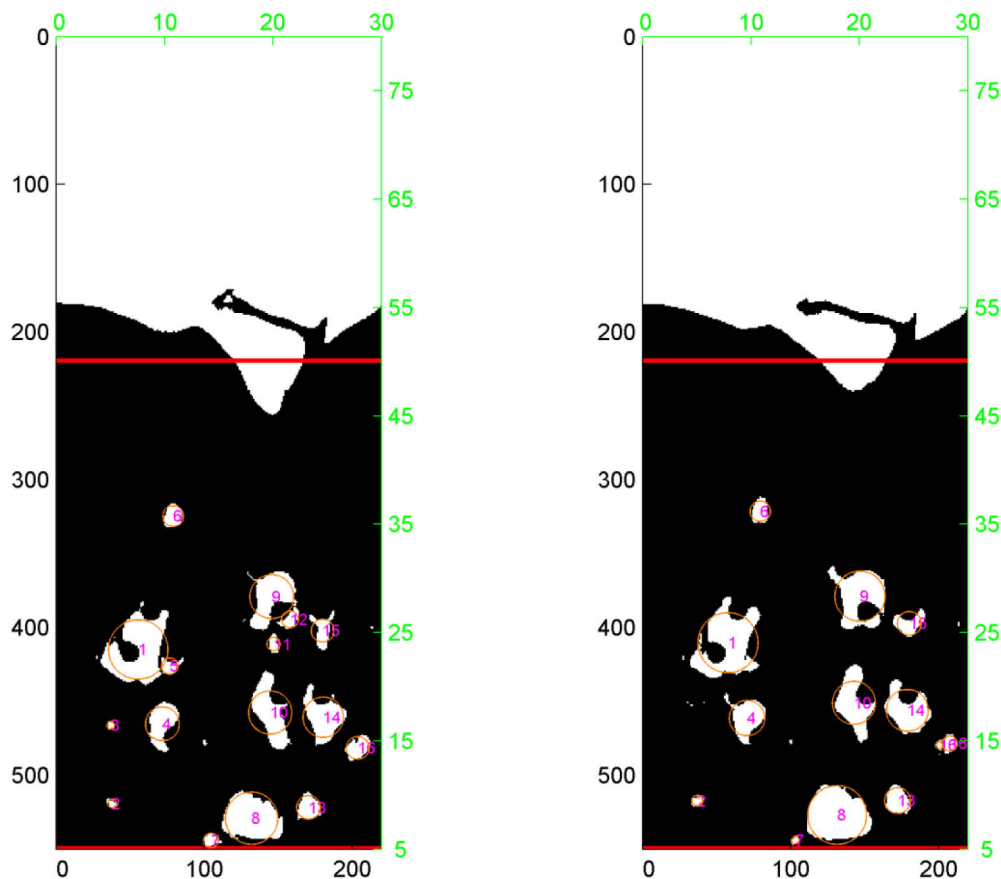


Figure 4.7: Bubble matching and numbering for the detected bubbles in two consecutive time frames.

In addition, the DIAT was validated using manual calculation of bubble properties. As part of a preliminary study of this work, numerical simulations of fluidized beds with and without immersed tubes were performed. The bed geometry and experimental data are obtained from the literature Hull et al. (1999). The simulations were performed using the Eulerian TFM described in Chapter 3 and the results were averaged over 8 s of real flow time. From this a total of 400 frames and over 5000 bubbles were manually analyzed by tracking each bubble. The same simulation results were later analyzed using the DIAT and the results were compared with the manual analysis. Figure 4.8 shows the comparison between manual calculation and from the DIAT for a bed without internals. The results were alike. Similar results were obtained for beds with immersed horizontal tubes.

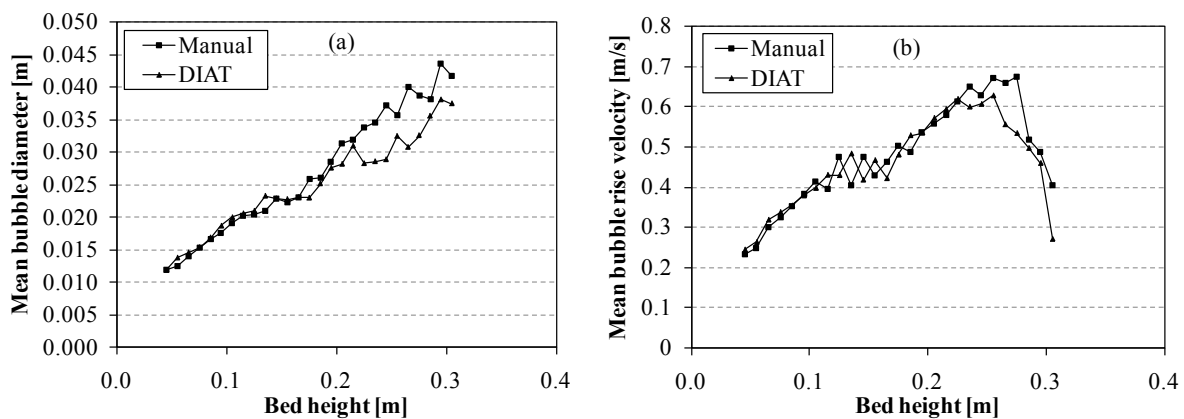


Figure 4.8: Comparison of simulation results between manual calculation and DIAT; (a) bubble diameter, (b) bubble rise velocity. Geometry and parameters from Hull et al. (1999).

5 Theoretical Predictions and Experimental Measurements

5.1 Pressure Drop and Minimum Fluidization Velocity

5.1.1 Theoretical background

Pressure drop across a bed of packed gas-solid system is an important parameter in the study of fluidized beds especially when visual observation is difficult. Figure 5.1 shows a typical pressure drop versus superficial velocity graph for a bed of mono-dispersed and smooth spherical particles. For a given superficial velocity, the pressure drop is measured from the pressure difference between the distributor outlet and the free board. When the superficial gas velocity is zero, the pressure drop is zero and the bed has a certain height. As the superficial velocity starts to increase gradually, the pressure drop increases accordingly while the bed height remains fixed. The straight line region AB is the fixed bed region where the solid particles do not move relative to one another and the pressure drop is approximately proportional to the gas velocity, which usually reaches a maximum at point B. In this region, the frictional pressure drop as a function of gas velocity has been correlated by Ergun (1952) (Equation 5.1).

$$\frac{\Delta P}{H} = 150 \frac{(1-\varepsilon_g)^2}{\varepsilon_g^3} \frac{\mu_g U}{(\phi_s d_p)^2} + 1.75 \frac{(1-\varepsilon_g) \rho_g U^2}{\varepsilon_g^3 \phi_s d_p} \quad (5.1)$$

Where, ε_g is the gas volume fraction (bed voidage), ϕ_s is the sphericity of the particles, d_p is the particle diameter.

At point B the pressure drop is maximum and is slightly higher than the static pressure of the bed. This rise is more noticeable in small vessels and in powders that have been compacted to some extent before the test and is associated with the extra force required to overcome wall friction and adhesive forces between the particles. With further increase in superficial velocity the bed "unlocks", its voidage slightly increased resulting in a decrease in pressure drop to the static pressure of the bed and no longer increases as the superficial velocity is increased while the bed starts expanding in height. This is when the drag force exerted by the upward moving gas on the particles is sufficient to balance the net weight of the bed and the particles float in the gas. In this case, the bed is fluidized and it is represented by the region BC. In this region, the pressure drop across the bed equals the weight of the particles and can be expressed as:

$$\frac{\Delta P}{H} = (1 - \varepsilon_g)(\rho_s - \rho_g)g \quad (5.2)$$

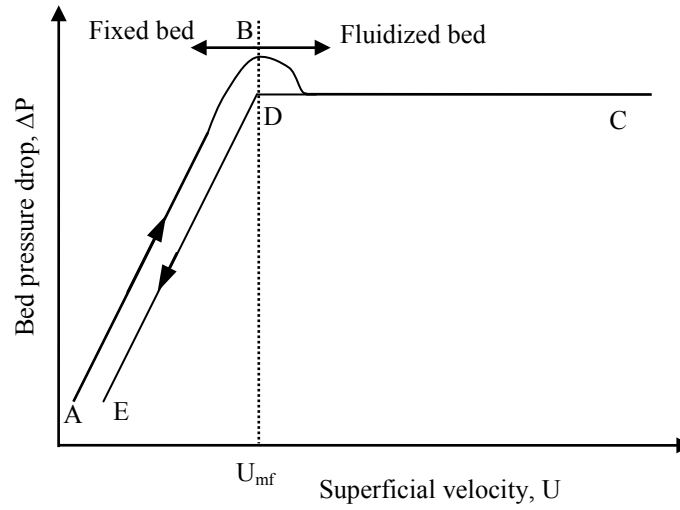


Figure 5.1: Pressure drop versus superficial velocity for uniformly sized spherical particles.

When the superficial velocity is gradually reduced after the bed is fluidized using very high superficial velocity, the fluidized bed settled down along the line CD. The superficial velocity corresponding to point D is called the minimum fluidization velocity. The minimum fluidization velocity is an important parameter to characterize powders as well as an essential parameter in the design and analysis of fluidized beds. Theoretically, the minimum fluidization velocity can be calculated from the Ergun equation (Equation 5.1) for monodispersed and spherical particles provided that the bed voidage at minimum fluidization condition and sphericity are known. Another expression, which is widely used, is that of Wen and Yu (1966). Combining Equations 5.1 and 5.2 at the minimum fluidization condition (i.e., with $\varepsilon_g = \varepsilon_{mf}$)

$$\frac{\Delta P}{H} = 150 \frac{(1-\varepsilon_{mf})^2}{\varepsilon_{mf}^3} \frac{\mu_g U_{mf}}{(\phi_s d_p)^2} + 1.75 \frac{(1-\varepsilon_{mf})}{\varepsilon_{mf}^3} \frac{\rho_g U_{mf}^2}{\phi_s d_p} = (1 - \varepsilon_{mf})(\rho_s - \rho_g)g \quad (5.3)$$

Simplifying,

$$(\rho_s - \rho_g)g = 150 \frac{(1-\varepsilon_{mf})}{\varepsilon_{mf}^3} \frac{\mu_g U_{mf}}{(\phi_s d_p)^2} + 1.75 \frac{\rho_g U_{mf}^2}{\varepsilon_{mf}^3 \phi_s d_p} \quad (5.4)$$

Multiplying both sides by $\frac{\rho_g d_p^3}{\mu_g^2}$,

$$\frac{d_p^3 \rho_g (\rho_s - \rho_g)g}{\mu_g^2} = 150 \frac{(1-\varepsilon_{mf})}{\varepsilon_{mf}^3} \frac{\mu_g U_{mf}}{(\phi_s d_p)^2} \frac{\rho_g d_p^3}{\mu_g^2} + 1.75 \frac{\rho_g U_{mf}^2}{\varepsilon_{mf}^3 \phi_s d_p} \frac{\rho_g d_p^3}{\mu_g^2} \quad (5.5)$$

Thus, the above equation can be rearranged and rewritten as a quadratic equation in Re_{mf} as:

$$Ar = 1.75a(Re_{mf})^2 + 150b(Re_{mf}) \quad (5.6)$$

Where,

$$Ar = \frac{d_p^3 \rho_g (\rho_s - \rho_g) g}{\mu_g^2} \quad (5.7)$$

$$Re_{mf} = \frac{d_p \rho_g U_{mf}}{\mu_g} \quad (5.8)$$

$$a = \frac{1}{\phi_s \varepsilon_{mf}^3} \quad (5.9)$$

and,

$$b = \frac{(1 - \varepsilon_{mf})}{\phi_s^2 \varepsilon_{mf}^3} \quad (5.10)$$

Wen and Yu (1966) showed that there exist a general trend between ε_{mf} and ϕ_s for spherical as well as non-spherical particles. They analyzed a wide range of data for different particle sizes and ε_{mf} values and found that the values of a and b to remain constant with, $a \cong 14$ and $b \cong 11$.

Solving for Re_{mf} from Equation 5.6, gives the correlation proposed by Wen and Yu (1966) as,

$$Re_{mf} = \sqrt{C_1^2 + C_2 Ar} - C_1 \quad (5.11)$$

Where,

$$C_1 = \frac{150b}{2(1.75a)} = \frac{150(1 - \varepsilon_{mf})}{3.5\phi_s} \quad (5.12)$$

and

$$C_2 = \frac{1}{1.75a} = \frac{\phi_s \varepsilon_{mf}^3}{1.75} \quad (5.13)$$

Wen and Yu (1966) suggested values of 33.7 and 0.0408 for the two constants, C_1 and C_2 , respectively. Later different authors based on different databases as summarized by Yang et al. (1985) have suggested several sets of values

It should be noted that the above equations are valid for monodispersed and spherical particles and if the cross-sectional area of the bed is uniform as well as the wall friction is neglected. They are highly sensitive to the bed voidage at minimum fluidization velocity. For polydis-

persed particles, since the smaller particles apt to slip into the void spaces between the larger particles that resulted in an increased bed voidage, the above models could lead to significant error. In these circumstances, only experimental values should be used.

5.1.2 Experimental measurements

The pressure drop across the bed was measured with the help of six pressure taps with one measuring the total gauge pressure at the windbox and the other five measuring the pressure drop at the location of 1.5, 20, 40, 60 and 100 cm above the distributor. The lowest pressure tap measures the pressure drop across the distributor while the rest measure the pressure drop across the consecutive heights of the bed. The total static bed pressure drop is calculated by summing up the pressured drops across the bed height or by subtracting the pressure drop across the distributor from the gauge pressure in the windbox. It should be noted that this pressure tap was connected 1.5 cm above the distributor due to the space needed for the connecting flange. Thus, the measured pressure drop across the distributor includes the pressure drop as a result of 1.5 cm particle bed. The total bed pressure drop is therefore measured from the 1.5 cm above the distributor to the freeboard. This incurred only 3 % deviation over the total static bed pressure drop that can be effectively neglected its effect on the measured pressure drops.

Table 5.1: Bed pressure drop for various particle sizes and tube geometries at U_{mf} .

Mean particle diameter, μm	Bed pressure drop [kPa]							Average % error relative to NT
	NT	S6	S4	S3	I6	I4	I3	
141	6.25	6.20	-	-	6.27	-	-	1.5
246	6.44	6.57	6.51	6.23	6.49	6.48	6.24	1.9
347	6.73	6.77	7.02	6.69	7.05	6.55	6.59	2.6
439	6.84	7.08	6.99	7.05	6.96	6.89	6.97	2.3
592	7.26	7.22	-	-	7.25	-	-	0.3
776	7.81	7.41	-	-	7.74	-	-	4.2
Average % error relative to NT		2.44	1.6	1.4	2.0	0.8	1.5	

The measured pressure drops at the minimum fluidization condition for the different particle sizes and bed geometries are summarized in Table 5.1. It was found that the pressure drop slightly increases with particle size but is nearly independent of the bed geometry. The increase in pressure drop with particle size is due to a decrease in bed voidage for the bigger particles. Since the particle distribution is slightly polydispersed, smaller particle can slip into the space between the bigger ones thus increased the weight of the particles for the same bed height,

which resulted in higher pressure drop. For example for the bed without tubes (NT) and the same bed height of 0.5 at minimum fluidization velocity, the weight of the smaller particle ($d_p=141 \mu\text{m}$) was 4.765 kg while that of the bigger particle ($d_p=776 \mu\text{m}$) was 5.245 kg.

Figure 5.2 shows the pressure drop measurements using different bed geometries and comparison with the theoretical prediction using Equation 5.2. It can be seen that the pressure drop is independent of the presence of tubes. Compared to the theoretical value the experiment gave lower pressure drop. The deviation is higher for the smaller particles.

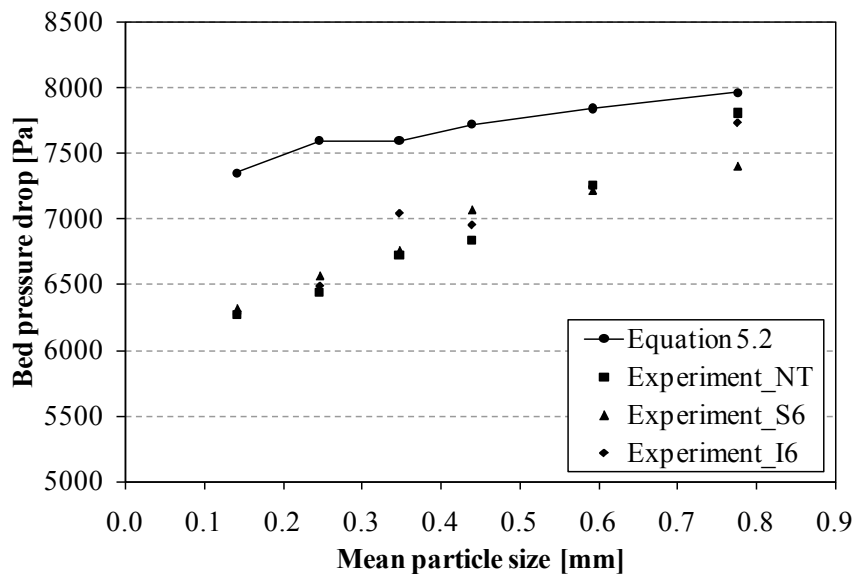


Figure 5.2: Pressure drop measurements for different bed geometries and particle sizes.

The minimum fluidization is generally estimated from the pressure drop versus superficial velocity diagram as shown in Figure 5.1. In the diagram the minimum fluidization velocity, U_{mf} , is located at point B when the superficial velocity is increased and point D when the superficial velocity is decreased. The difference arises due to the initial compaction of the particles. When the superficial velocity is gradually increased from an initial fixed bed the pressure drop is slightly higher due to the higher compaction of the particles. Once it is fluidized the interparticle forces reduced and compaction is also decreased which gives lower pressure drop and the pressure drop profile follows line DE in Figure 5.1 as the superficial velocity is gradually decreased. The minimum fluidization velocity, U_{mf} , is that corresponding to point D. If the bed is sufficiently fluidized to higher superficial velocity and then defluidized before any measurement was taken, the extra force required to overcome the interparticle attractive forces which results in slightly higher pressure loss (point B in Figure 5.1) can be minimized. In this case, the two lines (AB and DE) may be overlapped as was observed in this work. Typical pressure drop versus superficial velocity plots are shown in Figure 5.3 and Figure 5.4 for different particle sizes as well as bed geometries. It can be clearly seen that both the lines for increasing and decreasing the superficial velocity overlaps and the minimum fluidization velocity is the nearly same in

both cases. With this method all the minimum fluidization velocity of the particles and different bed geometries were determined and are tabulated in Table 5.2 below. From these results, it can be seen that the minimum fluidization velocity does not depend on the bed geometry, while increased with increasing particle size. In Figure 5.5 the measured minimum fluidization velocities are compared with well know correlation of Wen and Yu (1966) (Equation 5.11). It was found that the measured values are higher than the theoretical minimum fluidization velocity predicted by the correlation. This is to be expected as the actual particle distribution is polydisperse and the particles are not perfectly smooth which increase the drag force needed thus increased the minimum fluidization velocity.

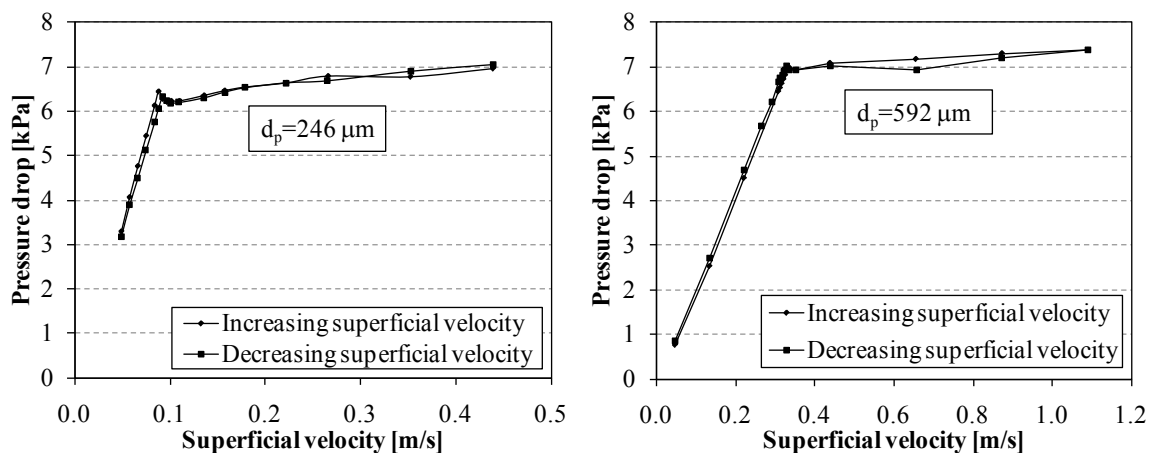


Figure 5.3: Bed pressure drop versus superficial velocity for the NT geometry and two particle sizes.

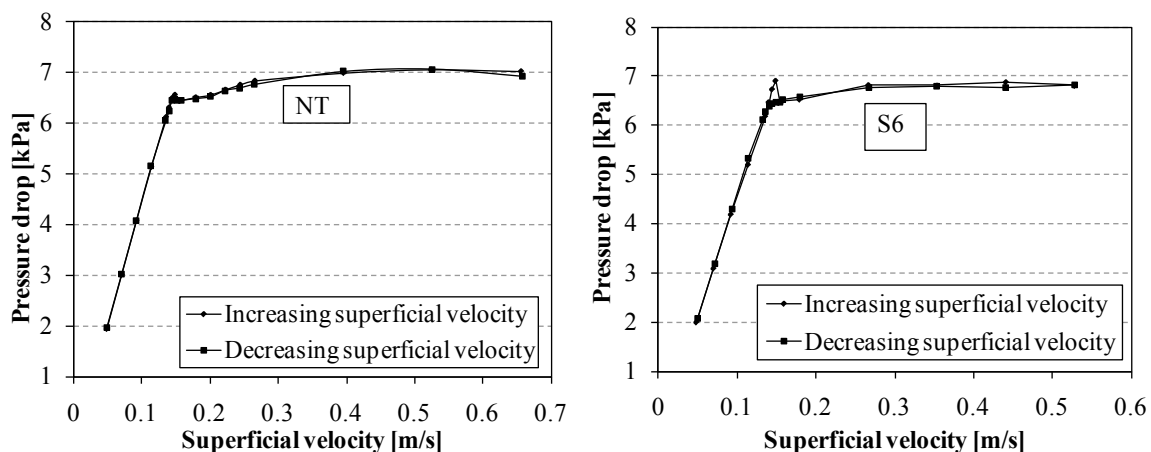


Figure 5.4: Bed pressure drop versus superficial velocity for the particle size of 347 μm and two bed geometries.

The minimum fluidization velocity can be also estimated from visual observation of the bed. It can be deduced that the minimum fluidization occurred when the first bubble appears and moves

along the bed height. This method was seen to provide a good approximation for the bed without immersed tubes as compared to the minimum fluidization velocity calculated from pressure drop measurements. In the case of beds with horizontal tubes, it was found to be difficult to estimate the minimum fluidization velocity from visual observation. In these cases local fluidization occurred at the lower part of the bed before a bubble appeared at the bottom of the bed. Moreover, when a bubble appeared and moved upwards it formed a bridge between the tubes and became stagnant until the gas velocity is sufficiently high to break the bridge. In this case the gas velocity is much higher than the expected minimum fluidization velocity.

Table 5.2: Measured minimum fluidization velocity of the different particle classes under different tube geometries.

Mean particle diameter, μm	Minimum fluidization velocity [m/s]							Average % error relative to NT
	NT	S6	S4	S3	I6	I4	I3	
141	0.054	0.052	-	-	0.049	-	-	9.4
246	0.087	0.090	0.092	0.091	0.087	0.096	0.091	5.3
347	0.144	0.142	0.136	0.134	0.135	0.128	0.135	6.1
439	0.238	0.227	0.219	0.238	0.232	0.226	0.240	3.5
592	0.333	0.314	-	-	0.313	-	-	5.7
776	0.504	0.490	-	-	0.481	-	-	3.7
Average % error relative to NT		3.7	4.0	2.4	4.8	5.4	2.3	

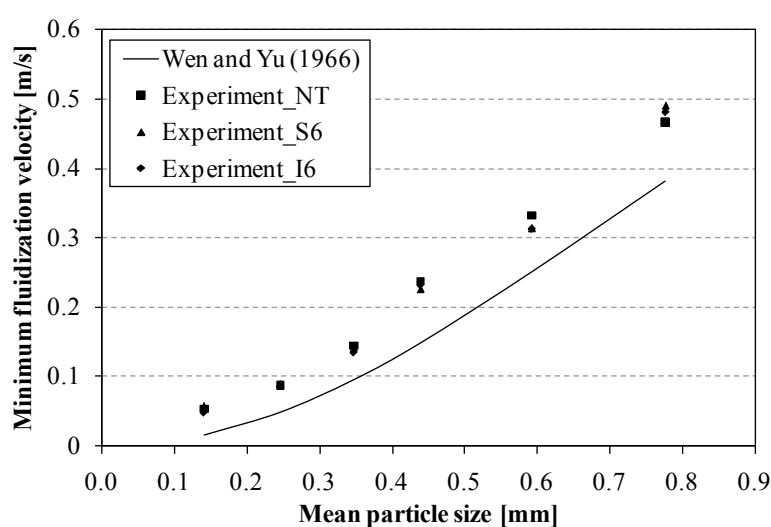


Figure 5.5: Measured minimum fluidization velocity for different particle sizes and bed geometries.

5.2 Bed Expansion

5.2.1 Theoretical background

Bed expansion is one of the most important as well as most reported macroscopic characteristic of fluidized beds (Al-Zahrani and Daous, 1996). The knowledge of the degree of expansion of fluidized beds is essential for the design and operation for several reasons such as for setting the feed height and to ensure adequate freeboard above the bed, to calculate the conversion rate and the relative areas of heat transfer surfaces immersed in the bed and freeboard (Johnsson et al., 1991; Geldart, 2004). In case of fluidized beds with immersed heat transfer tubes, the knowledge of the bed expansion can be helpful to determine to height of the tube bundles. Furthermore, several investigators have studied the bed expansion in order to describe bubble properties, such as size and velocity as well as the gas distribution between the bubble and the particulate phase (Johnsson et al., 1991). The degree of bed expansion is usually expressed in terms of bed expansion ratio. However, there is no consistent definition of the expansion ratio among the researchers with four different expressions available in the literature as given in Equations 5.14 to 5.17.

$$\delta_1 = H_f/H_0 \quad (5.14)$$

$$\delta_2 = H_f/H_{mf} \quad (5.15)$$

$$\delta_3 = \frac{H_f - H_{mf}}{H_{mf}} \quad (5.16)$$

$$\delta_4 = \frac{H_f - H_{mf}}{H_f} \quad (5.17)$$

Where, H_0 is the fixed bed height, H_{mf} is the bed height at minimum fluidization velocity, and H_f is the fluidized bed height at superficial velocity of U above U_{mf}

In Figure 5.6 experimental data for bed expansion ratio reported elsewhere in the literature (Taghipour et al., 2005) is shown. The results were redrawn for the four different ways of definition used in the literature; e.g. δ_1 is used by Taghipour et al. (2005), δ_2 is used by Geldart (2004), δ_3 is used Llop et al. (2000) and δ_4 is used by L fstrand et al. (1995). From the four definitions, δ_2 and δ_3 have been most frequently used in the literature. Though, all authors refer the terms to be bed expansion ratio, the actual values are different in magnitude as well as meaning. The first two definitions shown in Figure 5.6a are basically the ratio between the total fluidized bed height during fluidization to some reference height. This reference height is the fixed bed height in case of δ_1 and the bed height at minimum fluidization velocity in case of δ_2 . These ratios can be best explained as ‘‘bed height ratio’’ instead of bed expansion ratio. These values provide the percentage of the fluidized bed height to that of a reference bed height. For these cases, the

magnitude of bed height ratio (“expansion ratio”) is always greater than one. For the last two equations, δ_3 and δ_4 , the expansion ratio is given as the ratio of the expanded height to some reference height. This reference height is the minimum fluidization bed height in case of δ_3 and the expanded bed height in case of δ_4 . These definitions can be actually called as the bed expansion ratio. They provide the percentage of the expanded height with respect to a reference height used. As shown in the Figure 5.6, all four definitions showed uniform increase of the expansion ratio with gas velocity. A slight difference was from that of δ_4 . The shape of the graph in this case is slightly parabolic and shows a relatively lower increase in the expansion ratio with superficial velocity especially at higher superficial velocities. This is due to the simultaneous increase in the values of the numerator and denominator of the equation with gas velocity. The variation of the expansion ratio with superficial velocity could be best explained if the percentage of the expansion is expressed in relation to some fixed height, which is independent of the superficial velocity such as the minimum fluidization velocity.

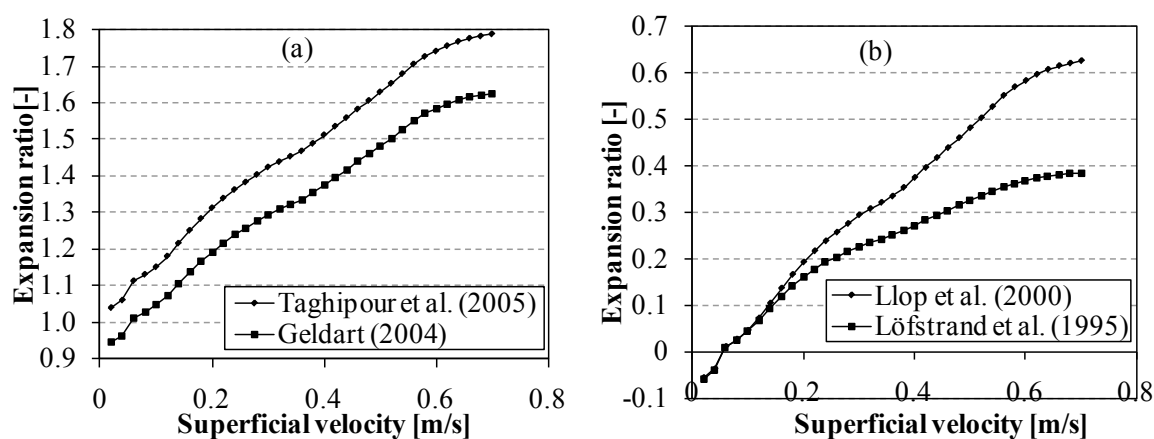


Figure 5.6: Different definitions of bed expansion ratio and comparison between experiment and simulation; Data from Taghipour et al. (2005).

The bed expansion ratio given by δ_1 would have twofold limitations. The first is the consistent measurement of the fixed bed height, H_0 . This depends on particle size distribution, bed geometry and manner of particle packing. Thus, the height is not a reproducible quantity to measure. The second limitation is that it provides fluidized bed height even below the minimum fluidization condition. Fluidization occurs when the superficial velocity is greater than the minimum fluidization velocity. Bed heights below the minimum fluidization height are not therefore considered as fluidized bed height. Even though, the bed expansion ratio given by δ_2 is used by several researchers and can be used for analyzing bed expansion characteristics, it should be best called as the bed height ratio instead of bed expansion ratio. As a result, the definition given by δ_3 is the most the appropriate definition of bed expansion ratio and has been used in this work.

The overall bed expansion is mainly due to the bubble holdup (bubble volume within the bed) and to a lesser extent due to the increase of voidage of the dense phase. For particles belonging

to Geldart's group B and D, the voidage of the dense phase remains at the value of its minimum fluidization condition (i.e. ε_{mf} remains constant). Thus, it is practical to assume that the bed expansion is solely due to the volume of bubbles. With this assumption the change in bed height (the expanded height) as a result of volume of bubble is given as:

$$H_f - H_{mf} = V_B / A_{c_bed} \quad (5.18)$$

Where, H_f is the fluidized bed height, H_{mf} is the bed height at minimum fluidization, V_B is the volume of the bubbles and A_{c_bed} is the cross-sectional area of the fluidized bed.

Now, consider a small element of a bed of height dh at a height of h above the distributor in which the bubble velocity is constant. The residence time of a bubble in this section is $\Delta h / u_B$, where u_B is the rise velocity of the bubble at this particular height. If the visible bubble flow rate is Q_B , then the volume of bubbles V_B in the element is, $Q_B \Delta h / u_B$. In the limit,

$$dV_B = Q_B \frac{dh}{u_B} \quad (5.19)$$

Over the whole bed height,

$$V_B = \int_0^{H_f} Q_B \frac{dh}{u_B} \quad (5.20)$$

The solution of the above equation (Equation 5.20) requires the values Q_B and u_B . The visible bubble flow rate can be expressed in terms of the two-phase theory of Toomey and Johnstone (1952). This theory states that the entire gas flow in excess of the minimum fluidization velocity flows in the form of bubbles. Therefore,

$$Q_B / A_{c_bed} = U - U_{mf} \quad (5.21)$$

However in practice,

$$Q_B / A_{c_bed} < U - U_{mf} \quad (5.22)$$

Because gas short-circuits from bubble to bubble. Hillgardt and Werther (1986) showed that the visible bubble flow rate can be generally expressed as:

$$Q_B / A_{c_bed} = \psi(U - U_{mf}) \quad (5.23)$$

Where the parameter ψ accounts the deviation from the two-phase theory and is a function of bed height, particle type, and bed diameter. Its value usually lies below unity.

The bubble rise velocity, u_B , is a function of bubble diameter, which in turn is a function of bed height above the distributor. Several correlations are available for the bubble rise velocity including those by Davidson and Harrison (1963), Hilligardt and Werther (1986) and Kunii and Levenspiel (1991). A new model for bubbles in 2D fluidized bed is also proposed in this work as explained in section 5.3.2. Substitution of such correlations for u_B and Equation 5.23 for the visible bubble flow rate in Equation 5.20 leads to very complex equation. Llop et al. (2000) have done this by following the work of Hilligardt and Werther (1986). Their expression for the bed expansion ratio (δ_3) is however, too long and too complex to understand. Geldart (2004) on the other hand argued that a calculation of bubble sizes at several levels and use of an average value for the entire bed is sufficient for engineering purpose. Hence, he assumed an averaged bubble rise velocity over the bed height to eliminate the need of integrating Equation 5.20. However, the calculation of an average rise velocity by itself posed another problem and his model need an iterative procedure to arrive at the solution. Löfstrand et al. (1995) followed a different approach. They defined a dimensionless drag force acting on the particles via the Ergun equation (i.e. Equation 5.1) putting the bed voidage at the minimum fluidization condition, ϵ_{mf} , and using the required superficial velocity. Based on this dimensionless drag force they performed a functional relationship with bed expansion data from experiments and using a least-square approximation, they proposed an empirical model that best fits the data. The expansion ratio predicted by this model showed a good agreement with the experimental data. However, as it is shown below, their model highly overpredicted the expansion ratio for smaller particles as well as lower superficial velocities.

In this work, a rather simpler empirical model was proposed based on the experimental measurements of the pseudo-2D test facility described in Chapter 4. The expanded bed heights were estimated using the DIAT described in section 4.3. From a careful analysis of the different correlations for bed expansion, it can be clearly seen that the bed expansion is a function of the excess gas velocity ($U-U_{mf}$), particle properties (mean diameter and density), bed voidage at minimum fluidization velocity and gravitational force. With these parameters, a non-linear regression analysis and data fitting was performed in order to best fit the experimental data. The final empirical model which best fit the experimental data of the NT case is given by:

$$\delta = \frac{H_f - H_{mf}}{H_{mf}} = 4.0 \left[(U - U_{mf})^{0.8} \left(\frac{\epsilon_{mf}}{\rho_s d_p} \right)^{1/2} g^{-2/3} \right] \quad (5.24)$$

The experimental results showed that, the insertion of horizontal tube banks slightly decreased the bed expansion ratio. Based on these experimental observations, the following correlation is proposed for fluidized beds with dense immersed horizontal tube bundles.

$$\delta = \frac{H_f - H_{mf}}{H_{mf}} = 4.0 \left[(U - U_{mf})^{0.8} \left(\frac{\epsilon_{mf}}{\rho_s d_p} \right)^{1/2} g^{-2/3} \right] (1 - \epsilon_t)^{3/2} \quad (5.25)$$

Where, ϵ_t is the relative volume fraction of the tubes, which is a measure of the packing density of the tube bundle and is defined by:

$$\epsilon_t = \frac{\text{Volume of the tubes}}{\text{Volume of the bed containing the tube bundle}} \quad (5.26)$$

$$\epsilon_t = \frac{N_t(\pi/4)d_t^2 l_t}{A_{c_bed}[(N_r-1)p_v+d_t]} \quad (5.27)$$

Where, N_t is the number of tubes, d_t is the diameter of the tubes, l_t is the length of the tubes, N_r is the number of row of tubes, p_v is the vertical pitch and A_{c_bed} is the cross-sectional area of the bed.

In the case of a rectangular bed, if the bed width is w and its thickness (depth) is t , the cross-sectional area is: $A_{c_bed} = w \times t$. Again in a rectangular bed, the length of the tubes is usually equal to the thickness of the bed, thus, Equation 5.27 can be simplified to:

$$\epsilon_t = \frac{N_t(\pi/4)d_t^2}{w[(N_r-1)p_v+d_t]} \quad (5.28)$$

It can be seen that as the total number of tubes approaches zero (towards a bed without internals) Equation 5.25 reduced to Equation 5.24.

5.2.2 Experimental measurement

The easiest way of measuring the bed expansion is to measure the bed height before and after fluidization from visual observations. Though very simple, this method usually leads to large errors as measurement of the expanded bed height is not easy due to the dynamic bed fluctuations as a result of frequent bubble eruption and subsequent collapse of the bed. The most common way of measuring the bed expansion is from the pressure drop measurements. The expanded bed height can be estimated by linearly extrapolating the static pressure drop profile to zero at the freeboard. The pressure drops at different bed heights were measured with the help of six pressure taps described above.

In this work, the expanded bed height was estimated using the DIAT. The technique first discriminates the boundary between the fluidized bed and freeboard region. To discriminate the bed boundary, similar threshold value as in the case of bubble detection was used. Hence, the bed height was measured at which the solid concentration drops below 0.2. Figure 5.7 showed the delineated bed boundary. Once the bed boundary is delineated, for a given frame, each pixel at this boundary was detected and its height above the distributor was measured. The bed height of this particular frame was then calculated as the mean height of the individual pixels. The ex-

panded bed height, H_f , for a given superficial velocity is then estimated by averaging over the total frames recorded as given by Equation 5.29.

$$H_f = \sum_{j=1}^{n_f} \frac{\left(\sum_{i=1}^{n_p} \frac{H_{i,p}}{n_p} \right)}{n_f} \quad (5.29)$$

Where, $H_{i,p}$ is the height of each pixel in a given frame, n_p is the number of pixels in a given frame, n_f is the total number of frames recorded.

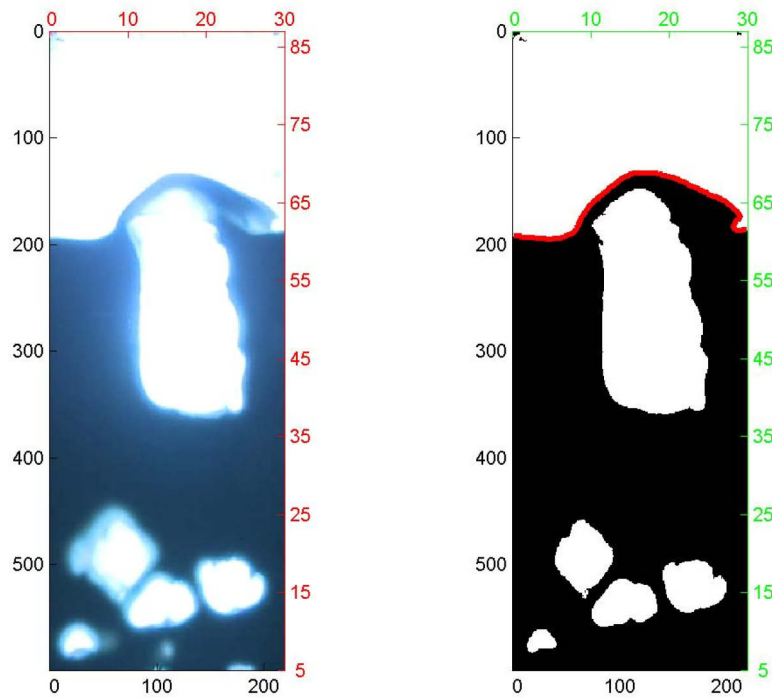


Figure 5.7: Delineation of bed boundary for bed expansion calculation using DIAT; left actual image, right delineated image.

Figure 5.8 shows the results of the bed expansion ratio calculated using the pressure drop measurement and using the DIAT for the no-tube (NT) and the dense staggered (S6) tube arrangements and particle sizes of $347 \mu\text{m}$ and $592 \mu\text{m}$. The results showed that the DIAT gave larger expansion ratio in the case of the bed without internal tubes while both gave similar results in case of beds with internal horizontal tubes. The reason might be due to large bubbles erupted at the top of the bed in case of the NT, which might not adequately accounted for by the pressure drop measurements. Because of the horizontal tubes, such big bubbles were not frequently seen as the tubes promote bubble splitting hence the bubble size is usually smaller. This was discussed in detail in the next section. It is not completely clear as to which method provide the correct result. However, comparison with correlations and observing the variation of the expansion ratio with superficial velocity, the DIAT was believed to give better results. In previous

studies (Asegehegn et al., 2011) it was found that the pressure drop method highly underestimates the bed expansion in case of numerical simulation results. As a result all bed expansion ratios reported in this work are obtained using the DIAT.

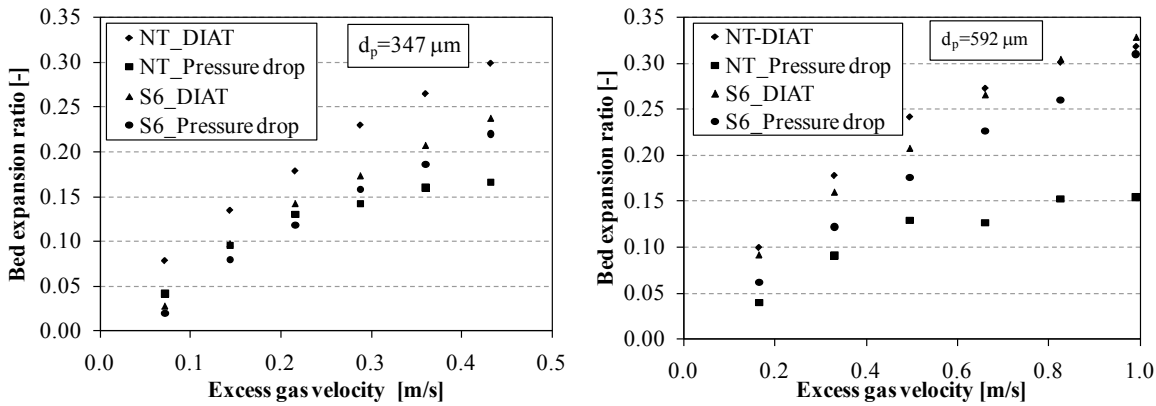


Figure 5.8: Comparison of bed expansion ratio calculated using the DIAT and pressure drop measurements.

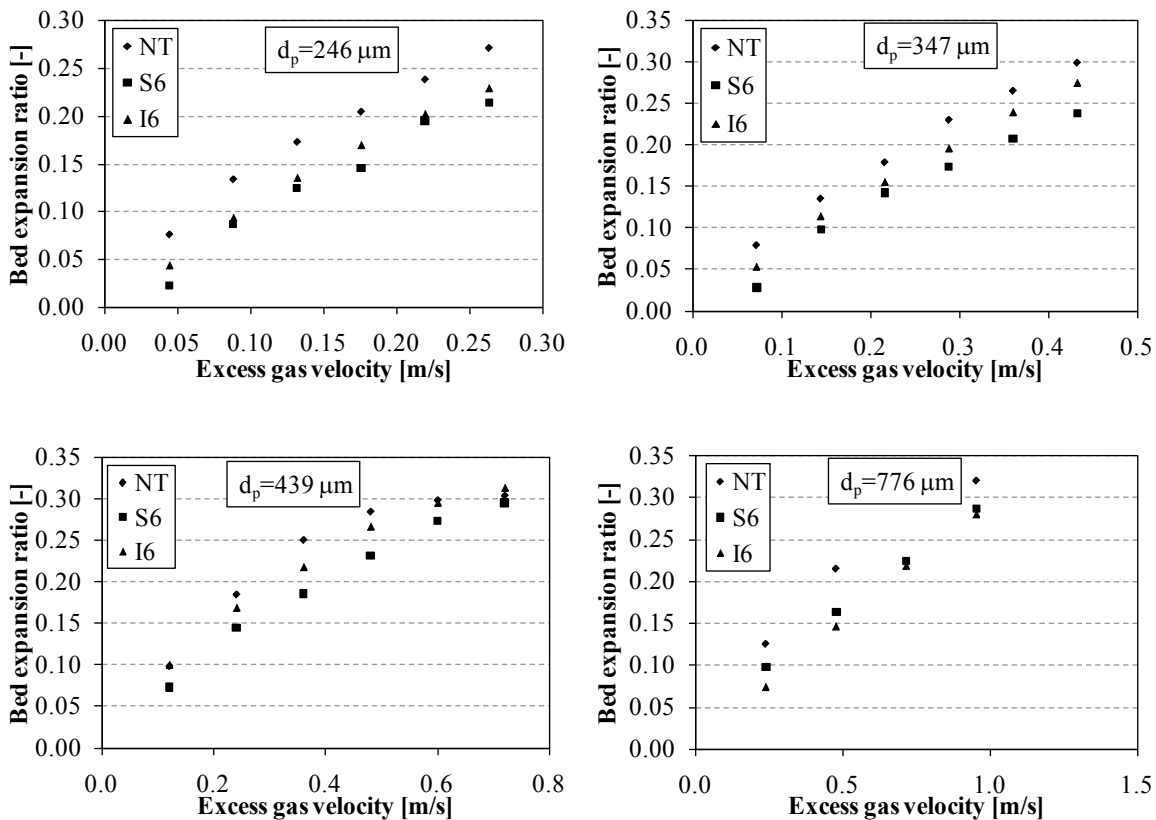


Figure 5.9: Variation of bed expansion ratio with excess gas velocity ($U-U_{mf}$) for different particle sizes and bed geometries.

Figure 5.9 illustrates the measured bed expansion ratios for different particle sizes and bed geometries. It can be seen that the bed expansion increases with excess gas velocity and was found to be slightly lower with dense horizontal tubes banks for powders of Geldart's group B and D.

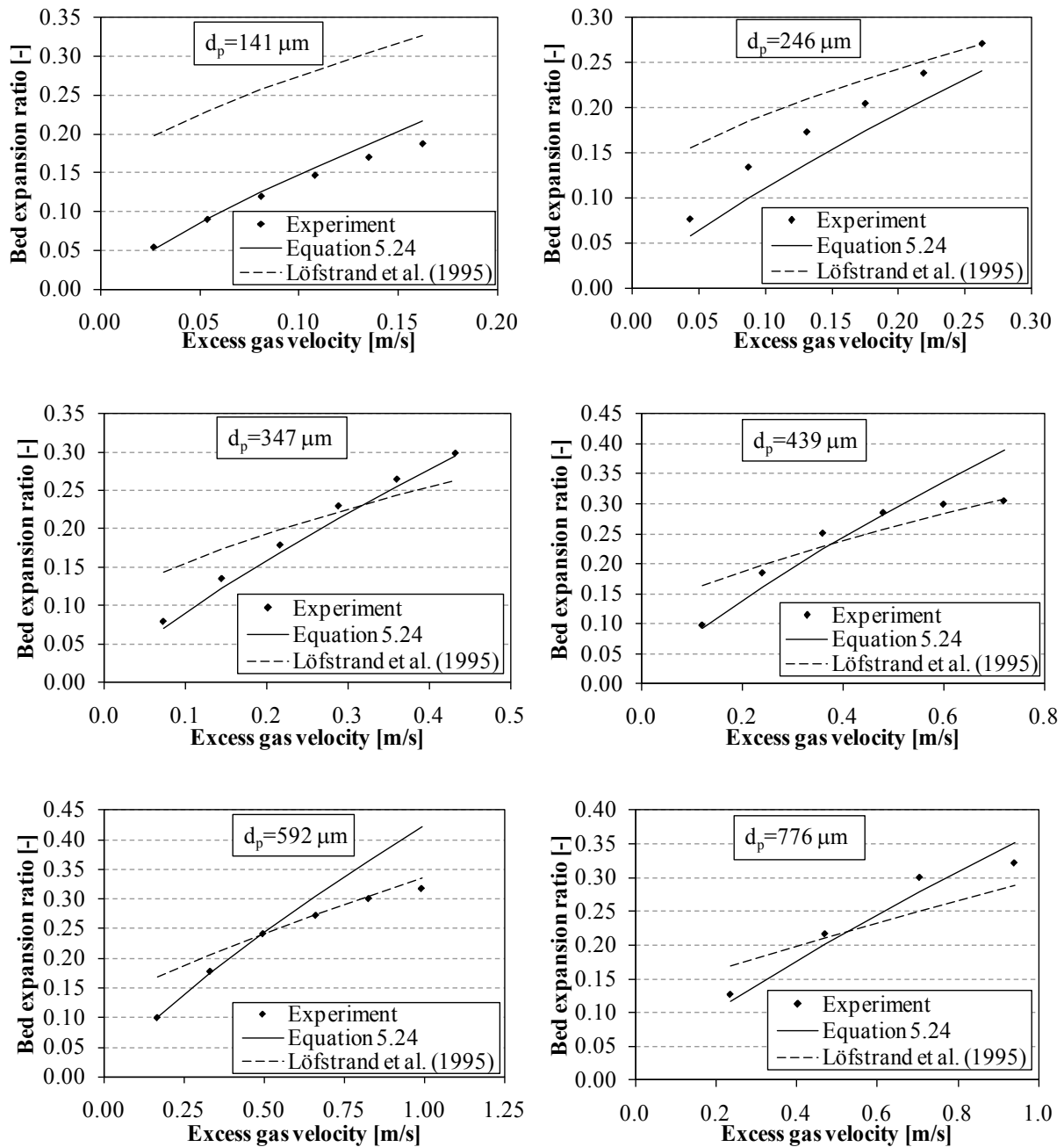


Figure 5.10: Comparison of bed expansion ratio with model predictions from Equation 5.24 and model proposed by Löfstrand et al. (1995) for the bed without immersed tubes (NT) and different particle sizes.

Figure 5.10 shows the comparison between the experimental measurements and model predictions from new model proposed in this work (Equation 5.24) and that of L fstrand et al. (1995) for the bed without immersed tubes (NT). It was found that the model of L fstrand et al. (1995) overpredicted the expansion ratio for the smaller particles as well as lower superficial velocities. The model proposed in this work (Equation 5.24) showed better agreement with the experimental data for wide range of particle size and superficial velocity. In order to validate the proposed model using external data, experimental data published elsewhere in the literature were compared, Figure 5.11. In Figure 5.11a experimental data from Taghipour et al. (2005) is shown along with the model predictions of Equation 5.24 and that of L fstrand et al. (1995). Equation 5.24 showed better prediction than the model of L fstrand et al. (1995) though both underpredicts the expansion ratio. The second set of experimental data is the bed expansion ratio reported by Llop et al. (2000) for a particle size of 213 μm and density of 2650 kg/m^3 as shown in Figure 5.11b. In this case the model showed better agreement than Figure 5.11a. As Geldart (2004) also explained, it should be noted that all correlations for fluidized beds are approximations and are subject to error, so that one should not expect agreement with experimental measurements better than $\pm 30\%$.

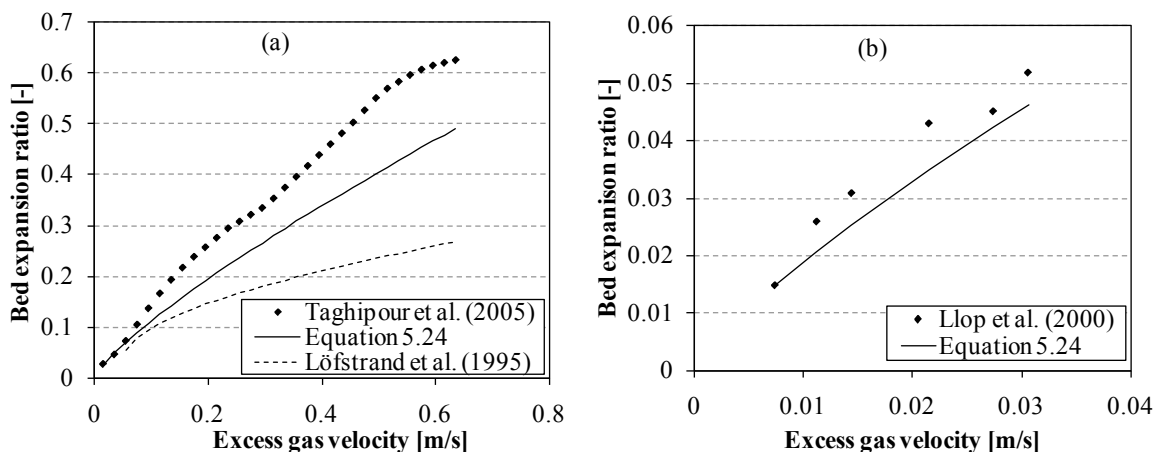


Figure 5.11: Comparison of bed expansion ratio between model predictions and experimental data from literature; (a) Taghipour et al. (2005), (b) Llop et al. (2000).

For the case of fluidized beds with immersed tubes, a comparison between experimental data and model predictions from Equation 5.25 are shown in Figure 5.12 for the dense staggered tube arrangement (S6). The model showed very good agreement with the experimental results. Since the bed expansion ratio is independent of the tube arrangement as shown in Figure 5.9, similar agreement were found for the dense inline tube arrangement (I6) and the results are shown in Appendix B.

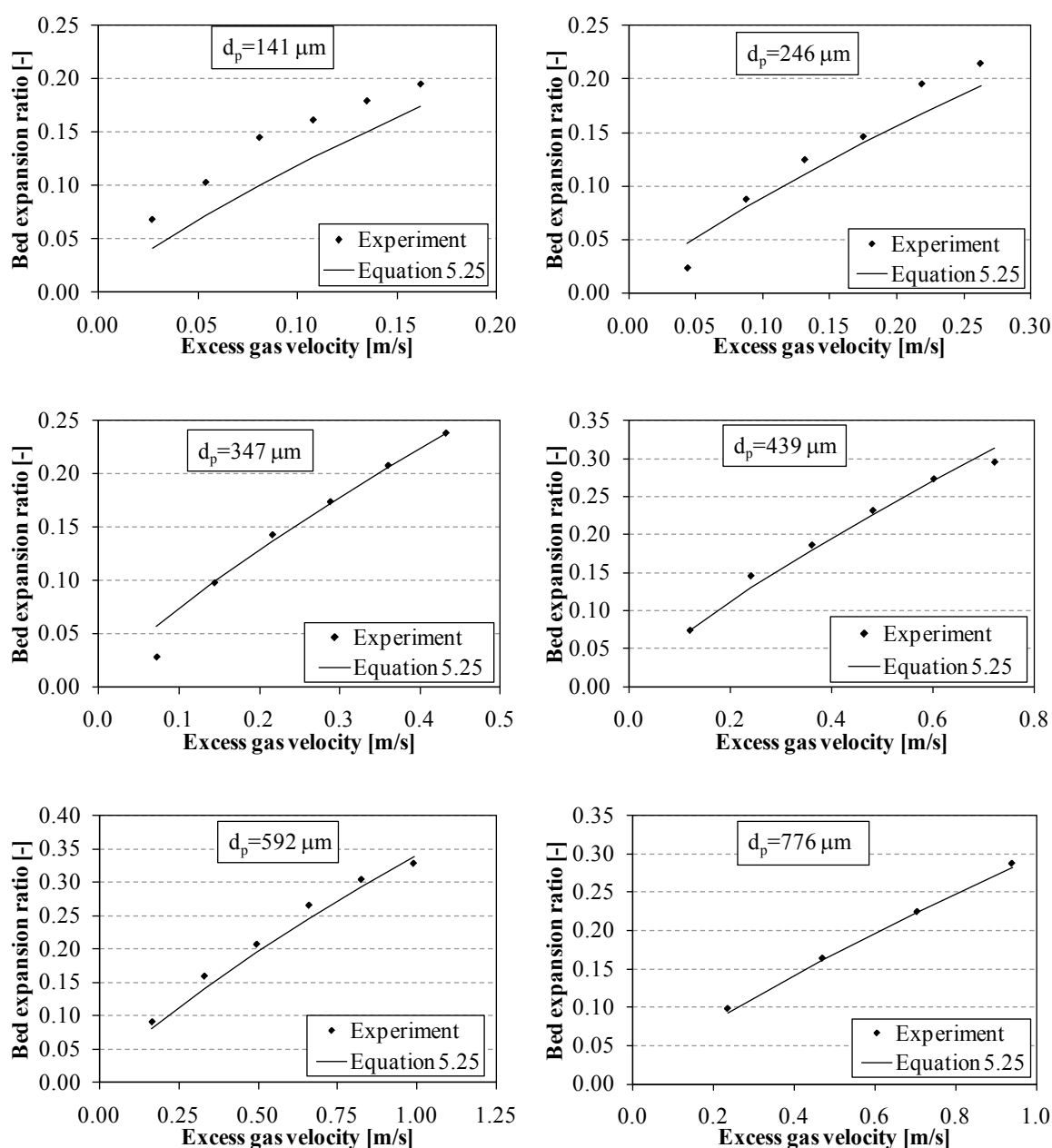


Figure 5.12: Bed expansion ratio for the bed with dense staggered immersed tubes (S6) and different particle sizes: comparison between model prediction and experimental measurements.

5.3 Bubble Properties

In this section, theoretical models were developed for the mean bubble diameter and mean bubble rise velocity as a function of bed height above the distributor for 2D beds without immersed tubes. The new correlations were validated with experimental measurements for different particle sizes and superficial velocities. All experiments were performed using the pseudo-2D bed described in Chapter 4. The minimum fluidization velocity of each particle was determined as

described above and the bed height at minimum fluidization conditions was set at 0.5 m for all cases. To calculate the bubble properties, the automated DIAT was used.

5.3.1 Bubble diameter

As bubbles formed near the distributor and rise in bubbling fluidized beds, they are swept to the center of the bed due to the presence of the of the bed wall. Then they began to grow by coalescence because of increased bubble density at the center and split due to instabilities at the bubble boundary. In beds without internal obstacles, bubbles continuously grow with bed height. A number of theoretical correlations were proposed in the literature to estimate the mean bubble diameter as a function of bed height in 3D tube free beds. Recently Karimipour et al. (2011) evaluated the performance of several of these correlations by calculating the squared difference between the correlation predictions and experimental data available in the open literatures. However, almost all of these correlations were proposed for 3D beds. For 2D beds only few are available in the literature. Lim et al. (1993) used the digital image analysis technique to study bubble behavior in 2D fluidized beds and proposed correlations for bubble diameter based on their experimental data. Their model, shown in Equation 5.30, was in reasonable agreement with the experimental measurements obtained in this work.

$$d_B = \left[\frac{8(U-U_{mf})(2^{3/4}-1)}{\pi\lambda g^{1/2}} h + d_{int}^{3/2} \right]^{2/3} \quad (5.30)$$

Where the initial bubble diameter d_{int} is given by:

$$d_{int} = \left[\frac{8(U-U_{mf})A_0}{\pi\lambda g^{1/2}} \right]^{2/3} \quad (5.31)$$

In Equation 5.30 and 5.31 the proportionality constant, λ , which represents the distance a bubble travels in a stream before coalescing with the adjacent stream to form a bigger bubble, was usually determined from experiments. In the case of a lack of experimental data this proportionality constant is usually assumed to be 2 for 2D beds without internal obstacles (Hull et al., 1999). In this work it was found to increase with superficial velocity and almost independent of the particle size with a mean value of 2. Shen et al. (2004) also used DIAT and proposed another expression by introducing bed thickness as an additional parameter and omitted the proportionality constant, λ . Their model is essentially a simplified form of Equation 5.30 and both provided similar predictions for bubble growth. Comparing with the experimental measurements, both models underpredicted bubble size in lower superficial velocities. In this work, a new model for mean bubble diameter as a function of bed height was proposed based on the experimental data. The model was developed by modifying the well-known and widely used correlation of Darton

et al. (1977). Darton et al. (1977) proposed bubble diameter as a function of bed height for 3D gas-solid fluidized beds and it can be written in a general form as:

$$d_B = K(U - U_{mf})^Q (h + 4\sqrt{A_0})^R g^S \quad (5.32)$$

Where, K, Q, R and S are constants to be determined from experimental measurements. Darton et al. (1977) used these values as 0.54, 0.4, 0.8 and -0.2 respectively. To simplify the analysis the exponent S was kept constant at -1/3 as in previous works in 2D beds (Lim et al., 1993; Shen et al., 2004). Thus the exponent Q was estimated from the slope of the graph showing $\log_{10}(U - U_{mf})$ vs. $\log_{10}d_B$ for different bed heights. Similarly the exponent R was estimated from the slope of the graph showing $\log_{10}(h + 4\sqrt{A_0})$ vs. $\log_{10}d_B$ for different superficial velocities. The average values of Q and R, estimated from these graphs for the different particle sizes studied, were 0.36 and 0.68 respectively, which are close to the values used by Darton et al. (1977). Using these exponents, the value of K for different particle sizes can be determined from the experimental data. Its value was found to vary with particle size with a mean value of 0.76. Since the above values for K, Q, and R are mean values, they did not provide reasonable agreement with the experimental data for all the particle sizes and superficial velocities considered. Moreover, since the experimental data showed some plateaus and inflections, it was necessary to include such behavior of bubble growth in the new model. Thus, some modifications to Equation 5.32 were included. Firstly, instead of a constant value for K a particle size dependent variable was introduced as was observed from the experimental data. Secondly, instead of the bed height h in Equation 5.32, a corrected height, which is a function of the bed height and the height at which the plateaus and inflections starts, was included. With these modifications and taking the values of K, Q, and R determined above as initial values, extensive non-linear regression and data fitting analysis were performed to fine-tune the constants in such a way that the expression could better predict bubble growth for a wide range of superficial velocity and particle sizes. Thus, after some successive approximations and interpolations, the new model for bubble diameter as a function of bed height above the distributor can be written as:

$$d_B = (0.75^{(1-U_{mf})})(U - U_{mf})^{0.5} (h_{corre} + 4\sqrt{A_0})^{3/4} g^{-1/3} \quad (5.33)$$

Where h_{corre} is a corrected height defined by Equation 5.34 and A_0 is area of distributor per orifice. For porous plate distributor $4\sqrt{A_0} = 0.03$ (Lim et al., 1993; Darton et al., 1977).

The corrected bed height, h_{corre} , was introduced instead of the bed height above the distributor in order to account the plateaus and inflections observed on the experimental data and is given by:

$$h_{corre} = \begin{cases} h & \text{if } h \leq h^* \\ h^* + \left[2.52(h - h^*) \left(1 + 3\exp(-U/U_{mf}) \right) \right]^3 & \text{if } h > h^* \end{cases} \quad (5.34)$$

Where h is the bed height above the distributor at which the bubble diameter is measured and h^* is the maximum bubble height defined by Equation 5.35.

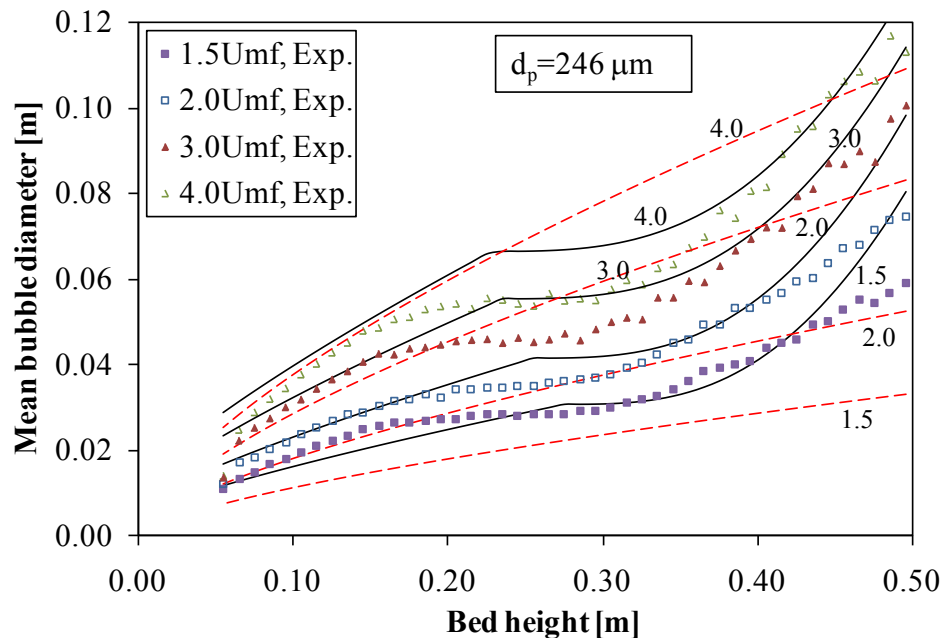


Figure 5.13: Comparison of mean bubble diameter between experiment and model predictions, $U_{mf} = 0.087$ m/s and velocity ratio (U/U_{mf}) as indicated on the respective lines; solid lines-Equation 5.33, and dashed lines-Equation 5.30.

In Figure 5.13 and Figure 5.14 the comparison between experimental measurements and model predictions using Equations 5.30 and 5.33 are shown for two different particle sizes. Generally, both models were in good agreement with the experimental data. The new model showed better prediction of bubble growth as it accounts the plateaus and inflections of the experimental data. The root mean square (RMS) of the relative deviation between the experimental data and model prediction was used to quantify the deviation of the model predictions from the experimental data. The RMS was generally found to increase with superficial velocity for both models and was usually lower for the new model proposed in this work. It was found to be 15, 10, 20 and 19 % for the particle sizes of 246, 347, 439 and 776 μm mean diameter respectively while the model in Equation 5.30 gave a RMS of 20, 19, 25 and 20 % respectively. For beds of Group D powders, the plateaus and inflections slightly disappeared with velocity as shown in Figure 5.14. The reason for this is that bubble splitting and coalescence occurred instantaneously. Since the rise velocity of a bubble is very high, the time delay between splitting and coalescence is very short that the bubble traveled shorter distance to be detected. This can be clearly seen between the different superficial velocities plotted in the figure. For lower superficial velocity ($1.5U_{mf}$), the plateaus and inflections are observed while these disappeared with increasing the superficial velocity ($2U_{mf}$ and $2.5U_{mf}$). In Figure 5.15 and Figure 5.16 additional comparisons of the new

model with experimental data are shown for two additional particle sizes. The proposed model predicted reasonably well the bubble growth as compared with the experiment.

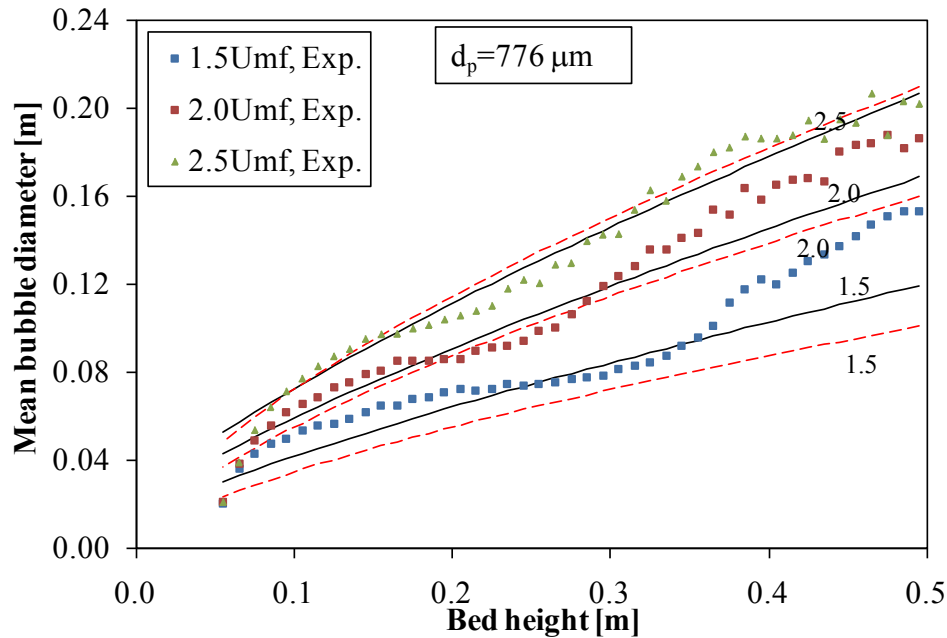


Figure 5.14: Comparison of mean bubble diameter between experiment and model predictions, $U_{mf} = 0.504 \text{ m/s}$ and velocity ratio (U/U_{mf}) as indicated on the respective lines; solid lines-Equation 5.33, and dashed lines-Equation 5.30.

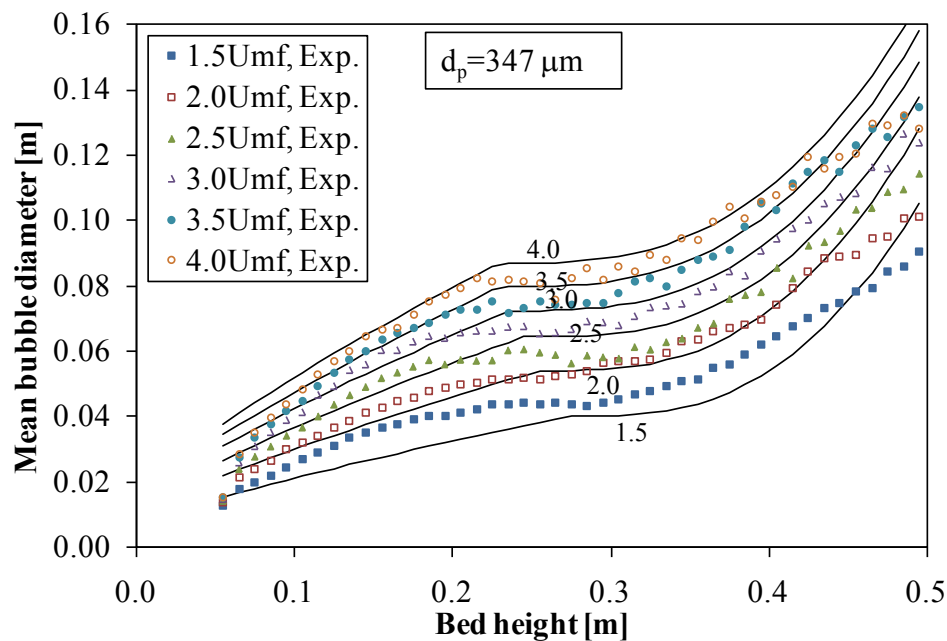


Figure 5.15: Comparison of mean bubble diameter between experiment and model prediction of Equation 5.33; $U_{mf} = 0.144 \text{ m/s}$.

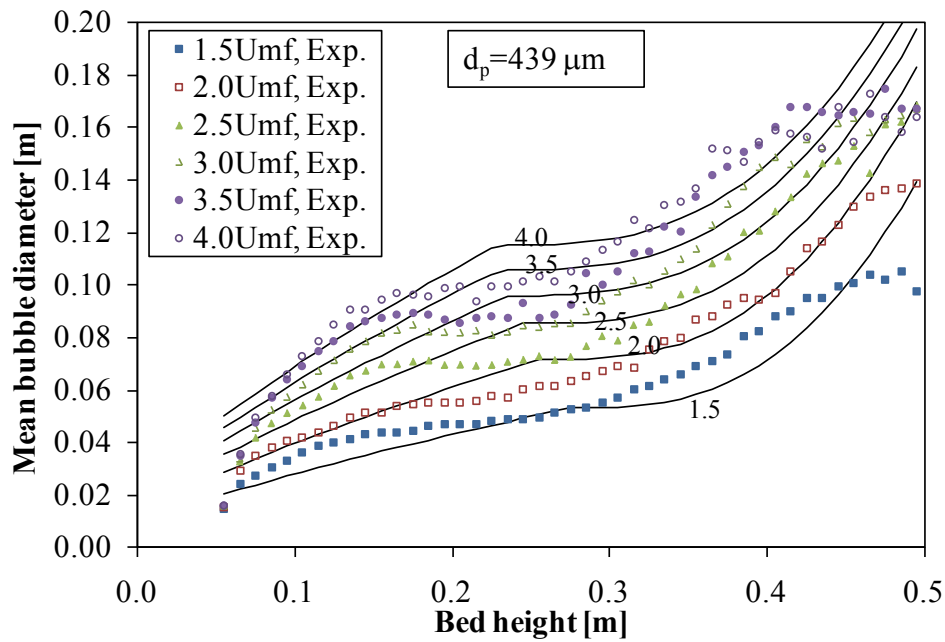


Figure 5.16: Comparison of mean bubble diameter between experiment and model prediction of Equation 5.33; $U_{mf}=0.238$ m/s.

For beds without horizontal tubes, the mean bubble diameter increased to a certain height and then remained constant for a short period before it continued to grow further. This was more pronounced at higher superficial velocities. A closer frame-by-frame analysis of the videos showed the presence of frequent splitting of bigger bubbles at this particular height. Usually these bubbles once again coalesced and moved to the top of the bed. The frequent break-up of larger bubbles at the mid-height of the bed cannot be fully explained yet, but it can be attributed to bubble instability. Clift et al. (1972, 1974) explained that since the roof of a bubble is unstable to the growth of any disturbance of all wavelengths, a curtain of particles is formed due to this disturbance, which eventually descends to the lower part of the bubble and splits it into two smaller ones. The sources of these disturbances have not been clearly mentioned but they could most likely be related to intrusive measurement probes, vibration of the bed, sound waves and the physical structure of the fluidized bed, such as distributor design, bed support and rigidity. Shen et al. (2004) also observed similar trends in bubble growth and introduced a maximum bubble height h^* , whereby bubble diameter could reach a maximum value at a certain height above the air distributor. They concluded that above this height bubbles do not grow further and become unstable and break up. From their experimental results they developed an empirical model to estimate the height h^* :

$$h^* = C \left(1 + 3 \exp(-U/U_{mf}) \right) D_{bed} \quad (5.35)$$

Where C is a coefficient to be experimentally determined and D_{bed} is the bed diameter or bed width in 2D beds. They found the coefficient $C=0.45$. This was found to be slightly higher in this work with a mean value of 0.6 for all particles sizes and superficial velocities studied.

Shen et al. (2004) claimed that the height h^* defined by Equation 5.35 is different from the stable bubble height used by others (Werther, 1978; Horio and Nonaka, 1987). The stable bubble height corresponds to the bed height in which the maximum stable bubble size is reached. The maximum stable bubble size is usually attained in Geldart's group A powders. In these particles bubble growth is characterized by constant splitting and coalescence. At some height above the distributor, a dynamic equilibrium has been achieved between coalescence and splitting and bubbles do not grow further. On the other hand, many agreed that no maximum stable bubble size in beds exists for Geldart's group B and D particles, though van Lare et al. (1997) reported otherwise. In these powders bubble splitting is very rare (Kunii and Levenspiel, 1991) and they grew continuously without reaching their maximum stable size (Davidson and Harrison, 1963). However, from the results of Shen et al. (2004) and van Lare et al. (1997), one can conclude that a bed height does exist whereby continuous growth in bubbles could be halted for a while. This was also observed in this study. As bubbles formed at the distributor, they rose and grew by coalescence until they reached a height at which the bigger bubbles usually split into two smaller ones. These two daughter bubbles were usually seen to coalesce together at a slightly higher height than their split height and further grew with height due to coalescence with other bubbles. Previous researchers (Shen et al., 2004; van Lare et al., 1997) did not report such further coalescence since the maximum bubble height estimated was nearly equal to the bed height at minimum fluidization in their experiments. The model developed for h^* could be associated with the height above the distributor at which bigger bubbles split due to instability and bubbles stopped further growth for a moment. The model predicted this height for our experimental results with a slightly higher value for the coefficient C . Above this height bubbles can further grow by coalescence if the bed height is long enough to allow for further growth and they might never reach their maximum. In this work, further splitting of large bubbles was not observed as the bed was not long enough to allow this. However, from the results it can be deduced that this might occur for longer bed heights.

5.3.2 Bubble rise velocity

Bubble rise velocity was estimated from the ratio of the vertical distance traveled by the centroid of a bubble and the time interval between consecutive time frames. Several correlations are available in the literature for bubble rise velocity in 3D beds and can be expressed by the generalized form of the Davidson and Harrison (1963) model as shown in Equation 5.36.

$$u_B = \psi(U - U_{mf})^E + \varphi(gd_B)^F \quad (5.36)$$

Where ψ and ϕ are empirical coefficients. Different authors have proposed different values depending on their data and bed geometry. For 3D beds Davidson and Harrison (1963) used the values of 1 and 0.71 for ψ and ϕ respectively while Hillgardt and Werther (1986) introduce a particle size and bed diameter dependent variable. Others such as Kunii and Levenspiel (1991) used different expression by including the wall effect in their model. More recently, Karimipour et al. (2011) reviewed some of the models proposed for the rise velocity of bubbles in 3D beds. For 2D beds, Lim et al. (1992, 1993) proposed the values of 1 and 0.4 or 0.5 for ψ and ϕ respectively. The value of 0.5 for ϕ was in better agreement compared to experimental data. Shen et al. (2004) on the other hand proposed a value 0 for ψ and ϕ varied from 0.8-1.0. The exponents E and F are usually taken to be 1 and 0.5 in all of the above proposed models.

In this work both the coefficients ψ and ϕ were found to vary with superficial velocity and particle size. Lim et al. (1992) also reported the variation of ϕ from 0.2 to 1.4. Thus, rigorous non-linear regression and data fitting were performed to correlate the experimental data and the mean bubble rise velocity was reasonably correlated using Equation 5.37 below. The model was found to provide robust predictions for a wide range of superficial velocities and particle sizes in Geldart's group B and D, provided that the minimum fluidization velocity was less than 1 m/s.

$$u_B = 0.91 \left[(U - U_{mf})^{1.25} + (1 - U_{mf})^2 (gd_B)^{3/4} \right] \quad (5.37)$$

The comparison between the predictions from models and experimental measurements are shown in Figure 5.17 to Figure 5.20 for different particle sizes. Comparisons between the new model and that developed by Lim et al. (1992, 1993) are shown in Figure 5.17 and Figure 5.18. The model of Lim et al. (1992, 1993) overpredicted the rise velocity especially for higher superficial velocities and particle sizes while the new model provided better predictions for a wide range of superficial velocity and particle sizes, except for a slight overprediction at the lower part of the beds for higher superficial velocities and bigger particles. The root mean square (RMS) of the relative deviation between experiment and prediction by the new model was found to vary between 15 % for the small particle and 35 % for the larger particle while for the model proposed by Lim et al. (1992) it varied between 20 % for the smaller particle and up to 70 % for the larger particle.

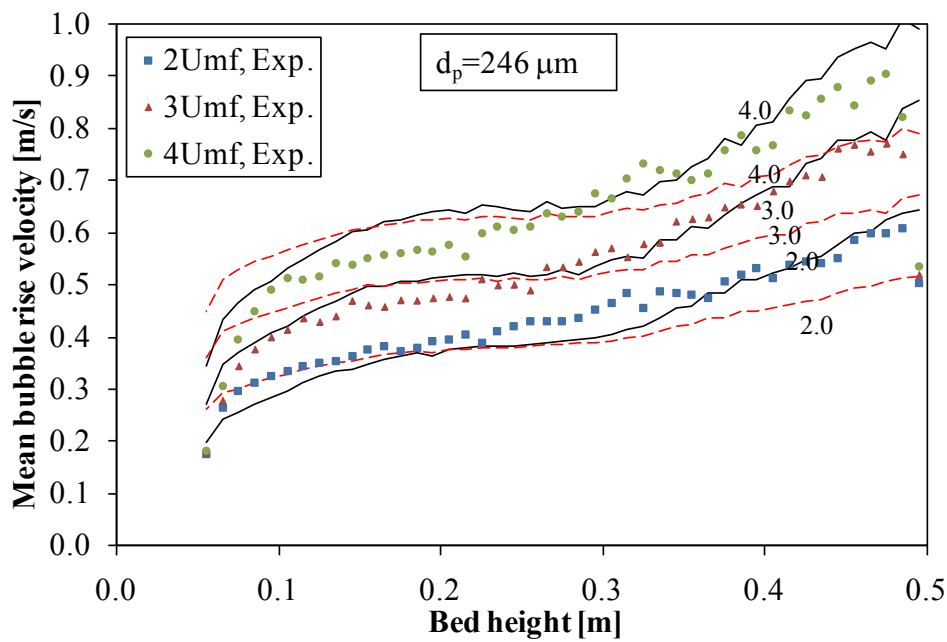


Figure 5.17: Comparison of mean bubble rise velocity between experiment and model predictions, $U_{mf} = 0.087 \text{ m/s}$ and velocity ratio (U/U_{mf}) as indicated on the respective lines; solid lines—Equation 5.37, and dashed lines—model by Lim et al. (1993).

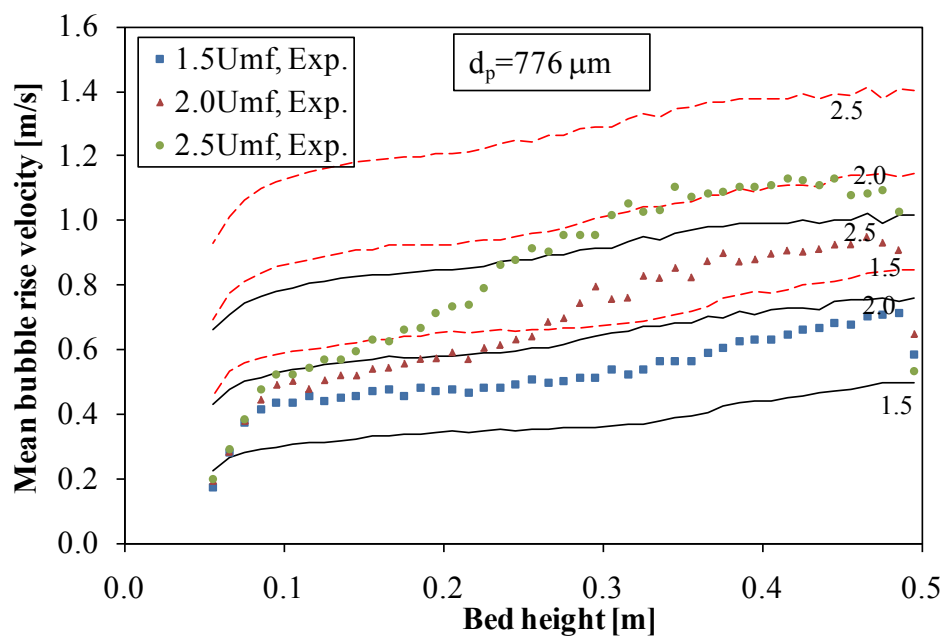


Figure 5.18: Comparison of mean bubble rise velocity between experiment and model predictions, $U_{mf} = 0.504 \text{ m/s}$ and velocity ratio (U/U_{mf}) as indicated on the respective lines; solid lines—Equation 5.37, and dashed lines—model by Lim et al. (1993).

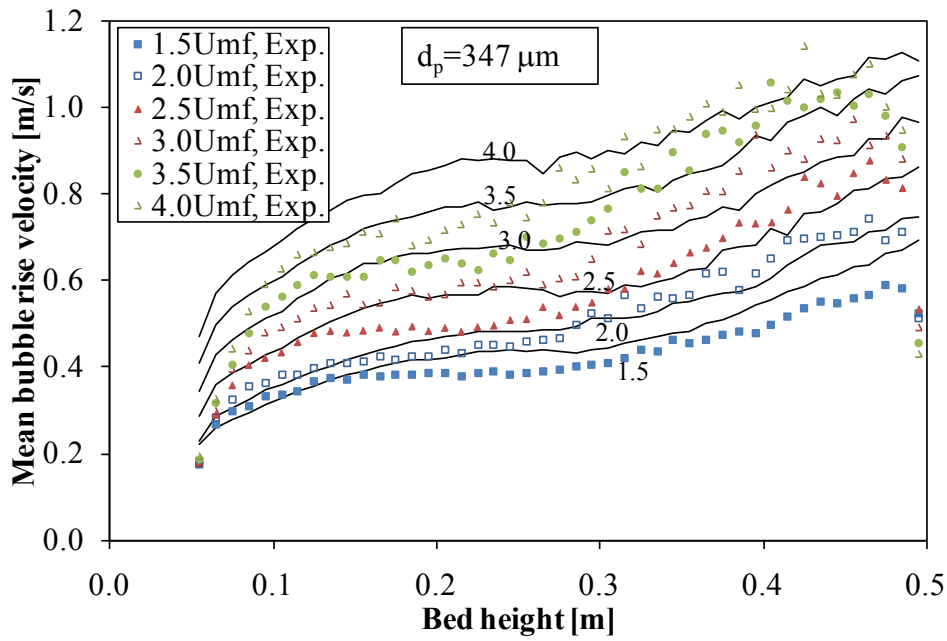


Figure 5.19: Comparison of mean bubble rise velocity with experiment and model prediction of Equation 5.37; $U_{mf}=0.144$ m/s.

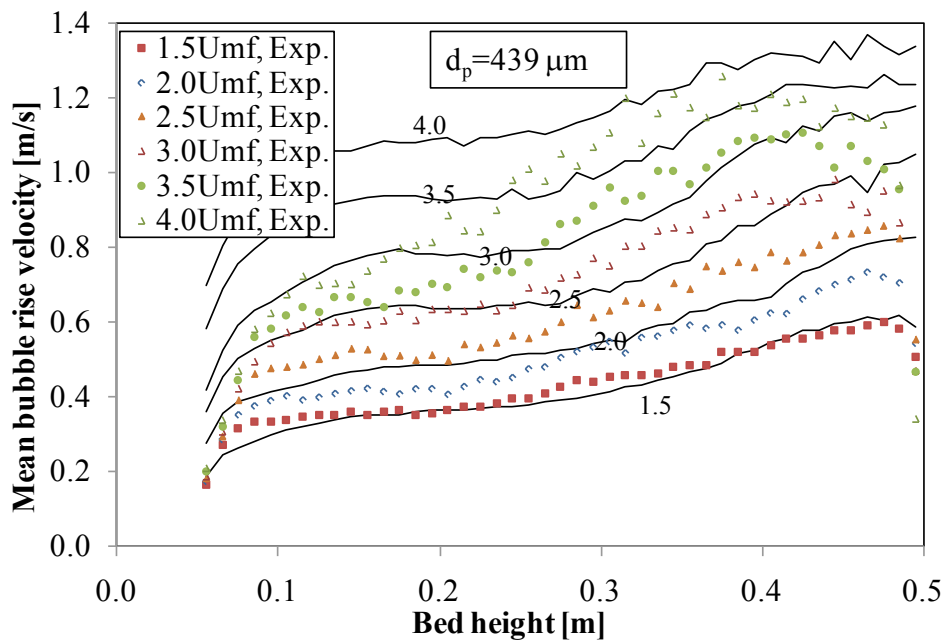


Figure 5.20: Comparison of mean bubble rise velocity with experiment and model prediction of Equation 5.37; $U_{mf}=0.238$ m/s.

6 Experimental Validation of the Two-Fluid Model

Comparison between simulations and experiments is a common way to validate CFD models. Therefore, for the past twenty years a large number of works have been reported in this regard. However, none of the CFD models available is fully validated so far. Especially the validity of the TFM to predict bubble characteristics in the presence of internal obstacles such as dense immersed horizontal tubes is not reported. In this chapter, a detail study of the validation of the TFM with experimental measurements of bubble properties and bed expansion is presented.

6.1 Simulation Parameters

Table 6.1: Summary of physical properties and simulation parameters.

Parameter	Value /Reference
Gas density, kg/m^3	1.2
Gas viscosity, Pa·s	$1.79 \cdot 10^{-5}$
Particle density, kg/m^3	2500
Mean particle diameter, μm	141, 246, 347, 439, 592, 776
Minimum fluidization velocity, U_{mf} , m/s	0.054, 0.087, 0.144, 0.238, 0.333, 0.504
Minimum fluidization solid volume fraction	0.60, 0.62, 0.62, 0.63, 0.63, 0.63
Bed height at minimum fluidization, H_{mf} , m	0.5
Restitution coefficient	0.95
Superficial velocity ratio	$U/U_{mf}=1.5, 2.0, 2.5, 3.0, 3.5, 4.0$
Friction packing limit	0.50, 0.55, 0.60, 0.63, 0.65
Maximum particle packing limit	0.65
Specularity coefficient	0.00, 0.25, 0.50, 0.75, 1.00
Angle of internal friction, $^\circ$	28.5
Time step size, s	$2.5 \cdot 10^{-5}$ and $5 \cdot 10^{-5}$

All dimensions of the beds were similar to the experimental setup except for the 2D simulations where the thickness of the bed is effectively set to zero. For the simulations the commercial CFD code ANSYS FLUENT 12.1 (ANSYS, 2009) was used. Except for the grid sensitivity study discussed in section 6.2 below, for all simulations a uniform quadratic mesh with a size of 5 mm was applied with slight refinement of up to 2 mm near the tube surfaces to capture the higher velocity gradients there. The QUICK and second order upwind scheme were employed for spatial discretization of the continuity and momentum equations respectively and time was discretized using second order implicit. The Phase-Coupled SIMPLE algorithm was used for the pressure-velocity coupling. Detail of the solution procedures and the solver were discussed in

section 3.4 and additional simulation parameters and closure equations used are summarized in Table 6.1 and Table 6.2 respectively.

Table 6.2: Closure equation used in the simulations.

Parameter	Model/Reference
Drag coefficient	Wen and Yu (1966), Syamlal-O'Brien (1989), Gidaspow (1994)
Dissipation of fluctuating energy	Lun et al. (1984)
Granular temperature equation	Algebraic Form (Syamlal et al., 1993)
Solids bulk viscosity	Lun et al. (1984)
Solids shear viscosity	Gidaspow (1994)
Radial distribution function	Ma and Ahmadi (1986)
Solids pressure	Lun et al. (1984)
Frictional shear viscosity	Schaeffer (1987)
Frictional pressure	Johnson et al. (1990)

6.2 Bubble Definition and Averaging Period

For validation of numerical results using experimental measurements either the instantaneous bed characteristics such as pressure fluctuations, bed height fluctuations, voidage fluctuations and distribution, particle velocity distributions or time-averaged properties such as bed height, bed pressure drop, and bubble properties are used. In performing validation studies using time-averaged bubble properties, the length of averaging period is critical, which might significantly influence the simulation results. Another important issue is the discrimination of bubbles from the rest of emulsion phase, i.e. how to define a bubble. The threshold value used to delineate bubbles from the rest of the emulsion phase could also influence the simulation results. These two parameters were investigated in this section and are presented below.

6.2.1 Bubble definition

Bubble properties were calculated from the instantaneous volume fraction contour plots produced during the simulation such as shown in Figure 6.1. The DIAT described in Chapter 3 was used to analyze bubble properties from these volume fraction contours. Unlike to the experimental analysis, bubble discrimination was performed automatically while generating the solid volume fraction contours from the CFD code. The difficulty here lays in identifying the bubble boundary to discriminate the bubble from the rest of the emulsion phase. In the literature, there is no consistent and uniform definition of the bubble boundary with threshold values ranging from 0.15 to 0.30 for the solid volume fraction used. For example, Kuipers and coworkers (Patil et al. 2005b; Kuipers et al. 1992, 1993) used 0.15. Many other researchers such as van Wachem et al. (1998), Gidaspow (1994), Hulme et al. (2005), McKeen and Pugsley (2003), Gera et al. (1998) used 0.20, while Cao et al. (2008) used 0.25. Though some earlier researchers, for exam-

ple Boemer et al. (1998), have concluded that an exact definition of the bubble boundary is not necessary, recently McKeen and Pugsley (2003) and Hulme et al. (2005) have shown otherwise. Figure 6.2 to Figure 6.4 show the comparison of the mean bubble aspect ratio, diameter and rise velocity respectively calculated using different thresholds for bubble boundary for beds without immersed tubes (NT) and with dense staggered tubes (S6). It can be seen that for the investigated bubble boundaries, the mean bubble aspect ratio and mean bubble rise velocity are nearly independent of the threshold value. Utikar and Ranade (2007) also reported similar results for the bubble rise velocity. On the other hand, the mean bubble diameter slightly decreases with increasing the threshold value. The bubble diameter is calculated in-terms of the area equivalent as given by Equation 4.4. Since this area is the sum of the number of pixels inside the area detected as a bubble, any change due to the threshold will alter the diameter accordingly. On the other hand, the bubble rise velocity is calculated as the rate of the vertical translation of the bubble centroid between two consecutive time frames. Thus, the centroid of a bubble is usually independent of the number of pixels or equivalent area detected as a bubble. In general no major influences were observed between the different threshold values thus the threshold value of 0.2 was used for the rest of the simulation results reported in this work.

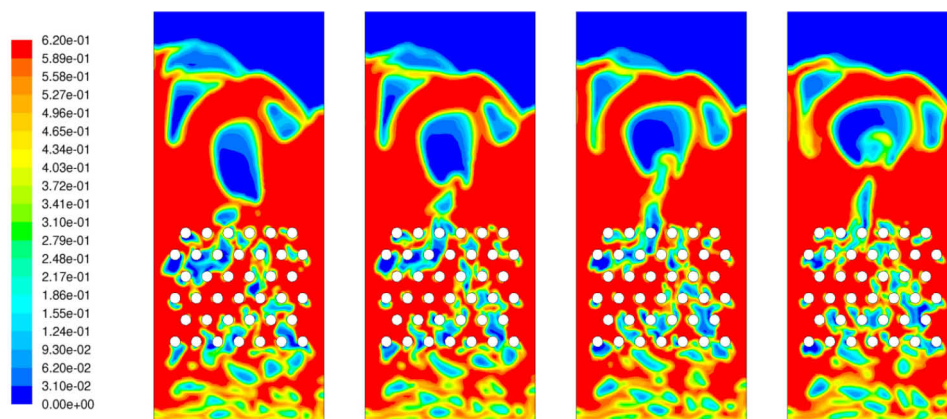


Figure 6.1: Instantaneous solids volume fraction contour for S6 tube arrangement; $\Delta t=0.02$ s.

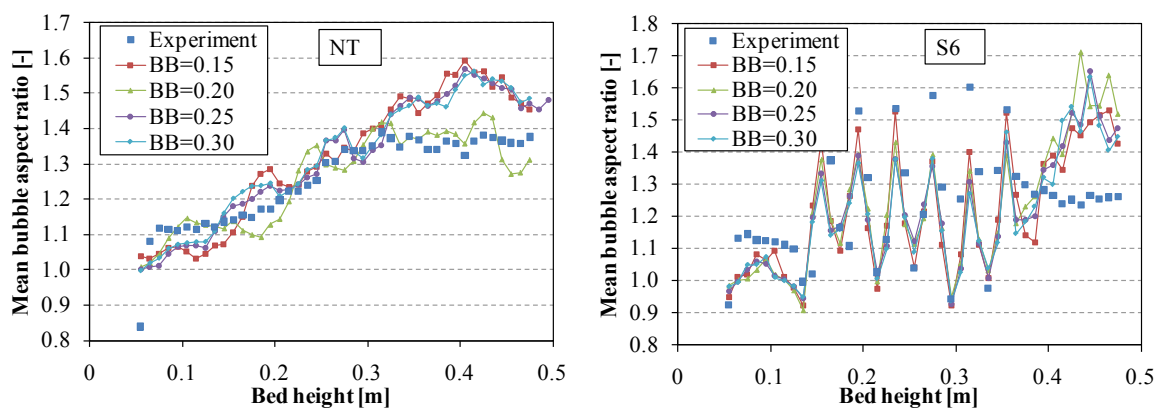


Figure 6.2: Mean bubble aspect ratio for different bubble boundaries (BB); $d_p=246$ μm , $U=2.5U_{mf}$.

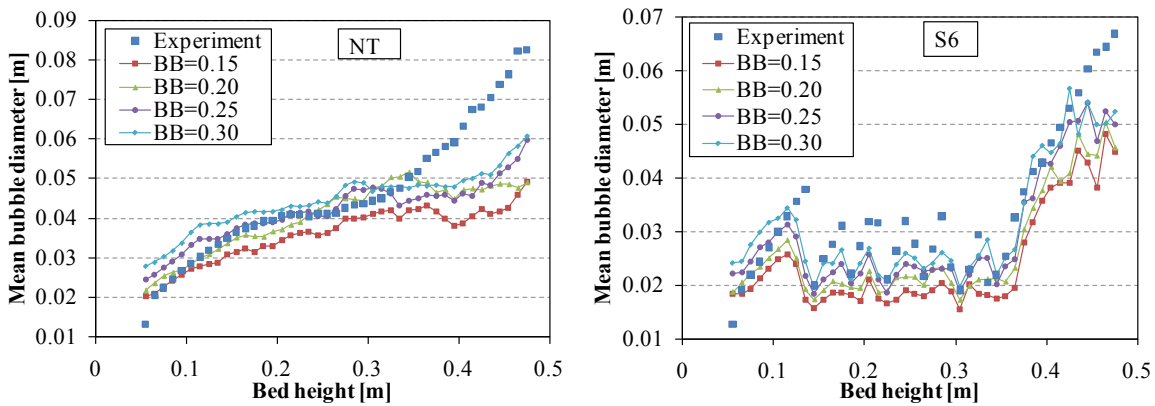


Figure 6.3: Mean bubble diameter for different bubble boundaries (BB); $d_p=246 \mu\text{m}$, $U=2.5U_{mf}$.

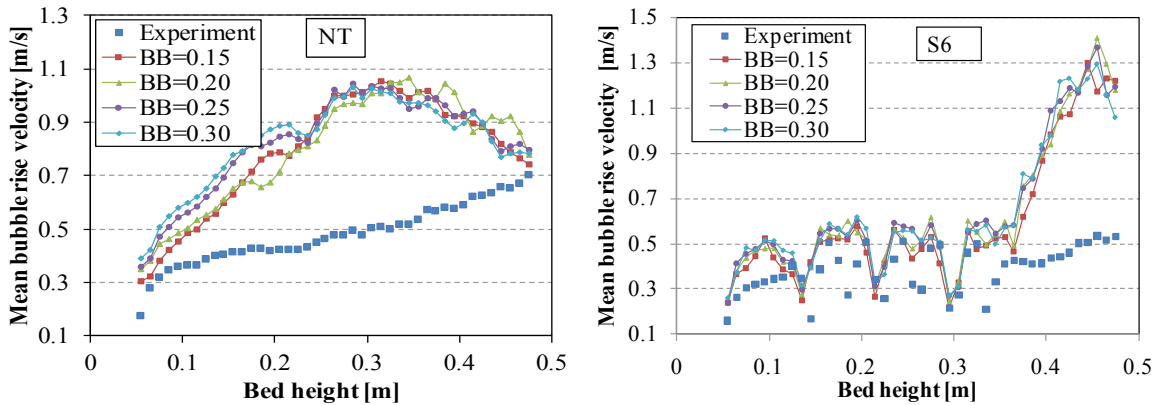


Figure 6.4: Mean bubble rise velocity for different bubble boundaries (BB); $d_p=246 \mu\text{m}$, $U=2.5U_{mf}$.

6.2.2 Averaging period

In analyzing the time-averaged bed properties, the length of the averaging period is an important factor for which it influences the accuracy of the results as well as the computational effort. In experimental studies, the length of averaging time is not of great importance as one can perform tests for quite long time, such as in hours. In contrast, the length of averaging time in numerical simulations is of great concern. At the present status of CFD models for gas-solid multiphase flows and computer power it is impossible to perform simulations for more than few seconds of real flow time for an average laboratory or engineering scale fluidized bed. On the other hand, it is indisputable that the accuracy of the time-averaged bed and bubble characteristics will improve with increasing averaging periods. Therefore, finding an optimum value of the averaging period such that the computational effort is minimized while an acceptable accuracy of the results is achieved is a pressing issue in validating numerical results. Usually researchers choose averaging period mainly based on their computational capacity and simulation time needed. Though this is a natural way to select the averaging time due to computational limitations, many

of them failed to show that their results are at least independent of the short averaging length. Only few have mentioned that they perform sensitivity analysis to investigate the influence of different averaging periods (e.g. Patil et al. 2005b). In the literature, it is possible to find averaging periods ranging from 1 to 18 s (e.g. Gamwo et al., 1999; Taghipour et al., 2005; Patil et al., 2005b; Rong and Horio, 2001; Xie et al., 2008a) which shows the wide difference in treating this value among the researchers. The optimum length of the averaging time may depend on many parameters among them the bed geometry and superficial velocity are of most important and it is difficult to provide a general value for all bed geometries and operating conditions. Nevertheless, it is necessary to ensure that the time-averaged properties are not significantly affected by the length of averaging period for a given bed geometry such that a meaningful validation studies could be achieved. For this purpose, a detail investigation was performed to check the sensitivity of the simulation results to the length of averaging period. The time-averaged bubble properties were studied using wide ranges of averaging periods (1 to 15 s).

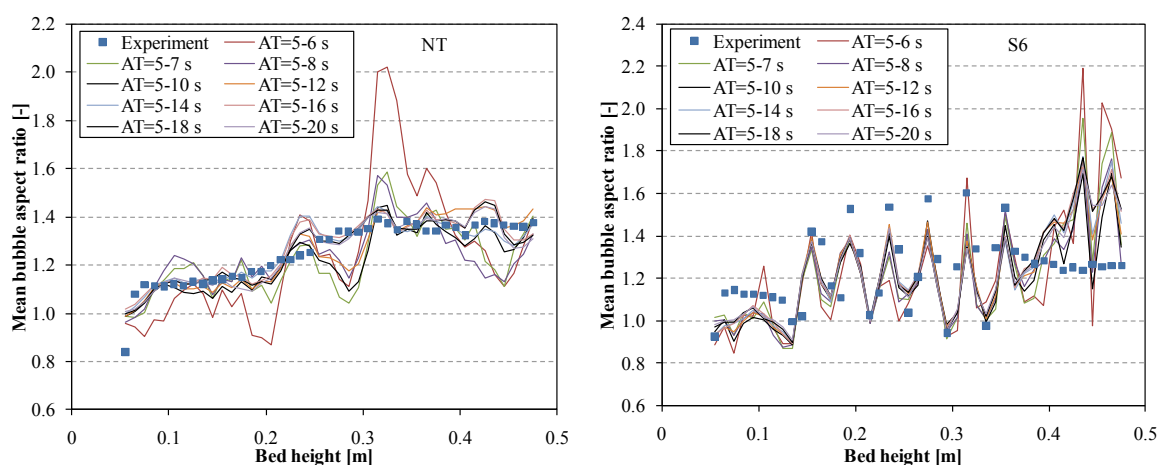


Figure 6.5: Time-averaged bubble aspect ratio for different averaging times (AT); $d_p=246 \mu\text{m}$; $U=2.5U_{mf}$.

Figure 6.5 to Figure 6.7 show the predicted time-averaged bubble properties - aspect ratio, diameter and rise velocity respectively - for different length of averaging periods and comparison with experimental measurements. From the figures, it can be seen that bubble properties are sensitive to the averaging periods within the first few seconds. It was found that after approx. 10 s (i.e 5-15 s) of averaging the mean bubble properties showed no major difference with increase in averaging time. This was observed for both beds with and without immersed tubes thus the length of the averaging time was in depended of the geometry of the bed. Hence, for the presented cases it can be seen that an averaging period of 10 s is satisfactory for analyzing the time-averaged bubble properties. Though increasing the length of the averaging time will improve the simulation results, it also increases the computational effort. From these analyses, though 10 s is satisfactory, taking into account the different superficial velocities and particle sizes investigated as well as the computational facility available an averaging period of 15 s was selected.

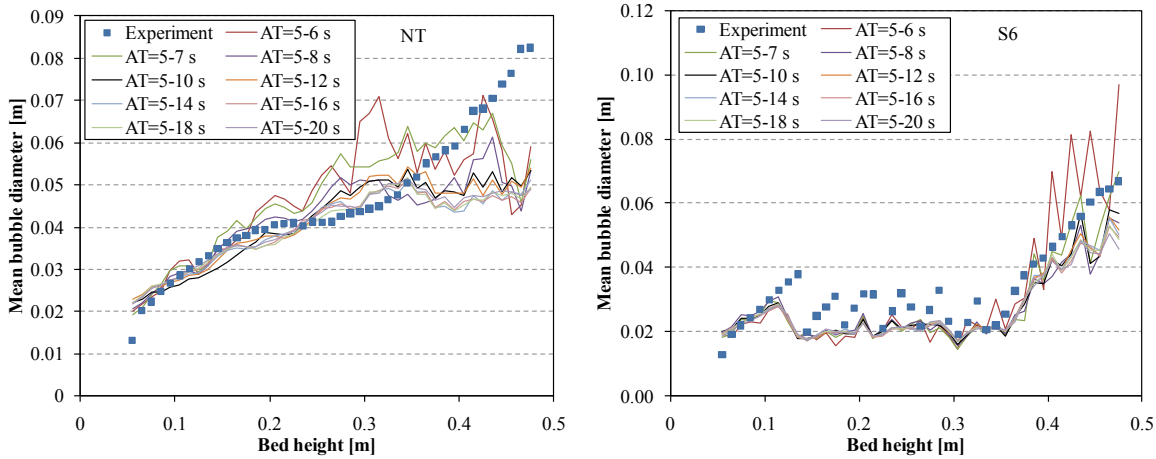


Figure 6.6: Time-averaged bubble diameter for different averaging times (AT); $d_p=246 \mu\text{m}$; $U=2.5U_{mf}$.

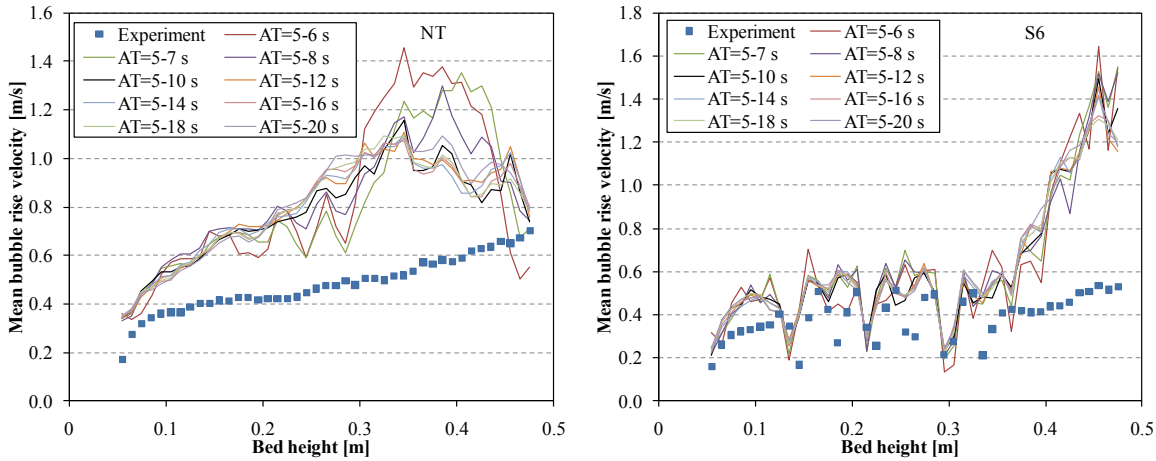


Figure 6.7: Time-averaged bubble rise velocity for different averaging times (AT); $d_p=246 \mu\text{m}$; $U=2.5U_{mf}$.

It should be noted that since the data used in the above analysis are taken from different overlapping intervals, using only the above analysis could lead to insufficient length of averaging period. As the length of the averaging period increased the overlap in data becomes larger, obviously the agreement in output will also be more and more similar. In this case it doesn't mean that the amount of data is sufficient to obtain a good time-average it only means that there are enough overlap to fit the previous set of (bad) data. Therefore, it is necessary to confirm the averaging period by using independent data sets at different time intervals without overlapping. For this purpose, two of the simulations were extended up to 50 s of real flow time. The mean bubble properties during the simulation periods of 5-20 s, 20-35 s and 35-50 s were compared as shown in Figure 6.8 to Figure 6.10. The figures confirmed that the mean bubble properties are independent of the time interval from which they are extracted.

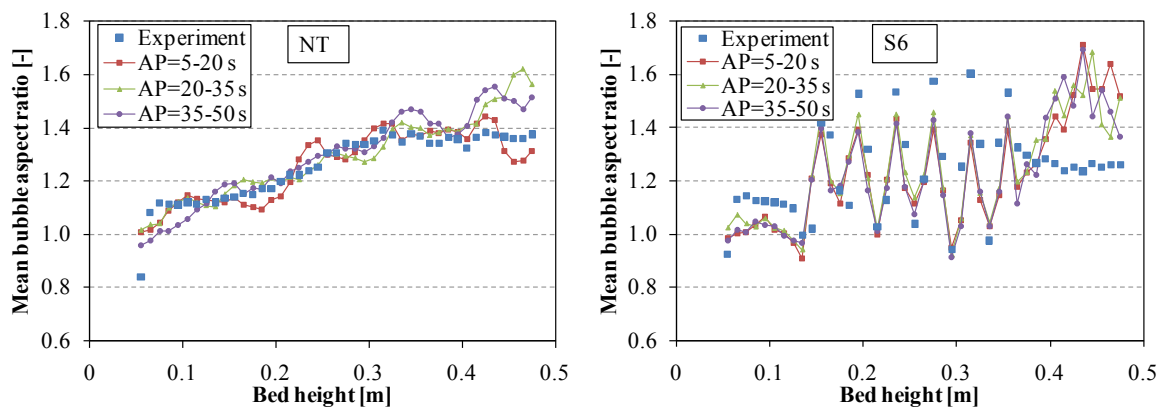


Figure 6.8: Mean bubble aspect ratio for different averaging periods (AP); $d_p=246 \mu\text{m}$; $U=2.5U_{mf}$.

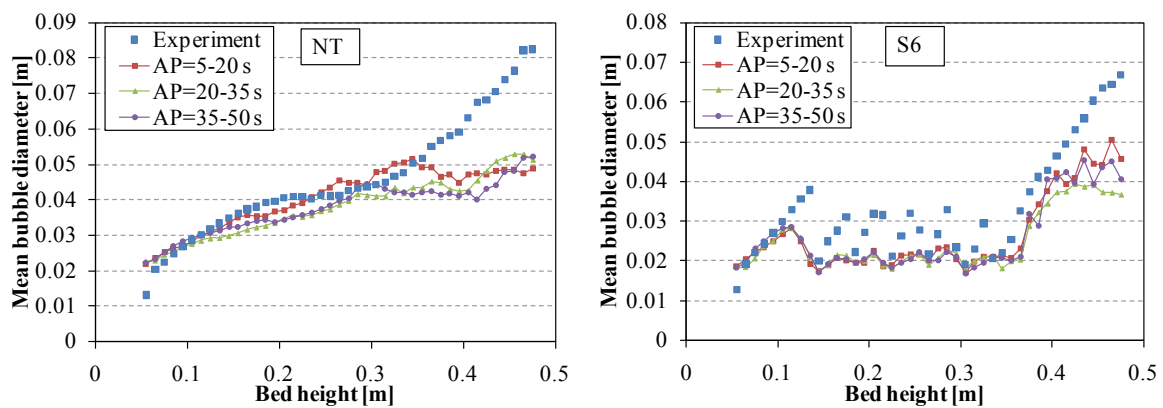


Figure 6.9: Mean bubble diameter for different averaging periods (AP); $d_p=246 \mu\text{m}$; $U=2.5U_{mf}$.

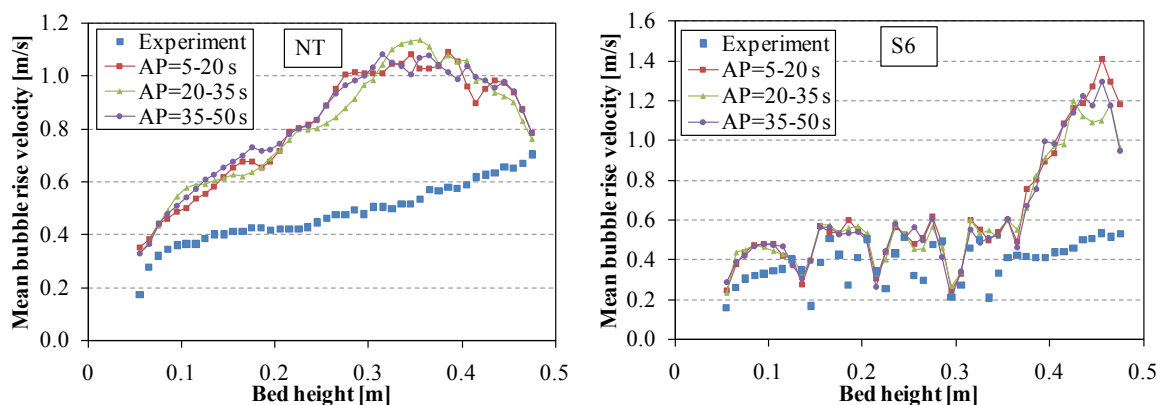


Figure 6.10: Mean bubble rise velocity for different averaging periods (AP); $d_p=246 \mu\text{m}$; $U=2.5U_{mf}$.

Another important aspect that should be considered is the time interval between images. It should be verified that the length of the averaging period is independent of the actual number of

bubbles measured. This is because, if the average lifetime of a bubble in the bed is in the order of 1 s, a small time interval Δt between images means that the same bubble is measured $1/\Delta t$ times. In order to verify this images were extracted using different time intervals (i.e. 1/25 s, 1/50 s, 1/100 s and 1/200 s). The corresponding results of bubble aspect ratio, diameter and rise velocity are shown in Figure 6.11, Figure 6.12 and Figure 6.13 respectively. The results showed that the mean bubble properties are independent of the number of frames per second used.

From all these three different investigations, it can be concluded that an averaging period of 15 s (5-20 s) is sufficient for statistical analysis of time-averaged bubble properties for all particle sizes, superficial velocities and bed geometries presented in this work. Increasing the averaging period will lead to higher computational time without significant improvement in accuracy of the numerical results. Therefore, all simulation results of the mean bubble properties as well as bed expansions and pressured drops presented in this work were averaged over the time interval of 5-20 s.

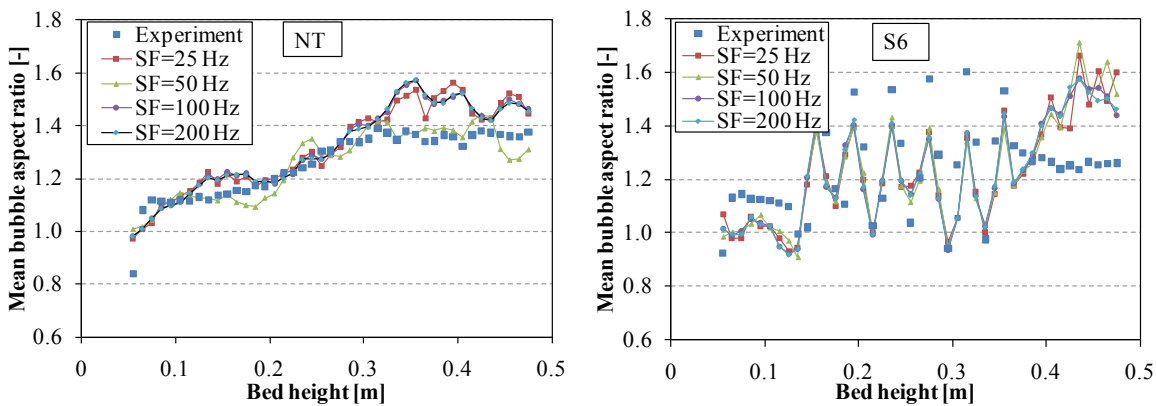


Figure 6.11: Mean bubble aspect ratio for different sampling frequencies (SF); $d_p=246 \mu\text{m}$; $U=2.5U_{mf}$.

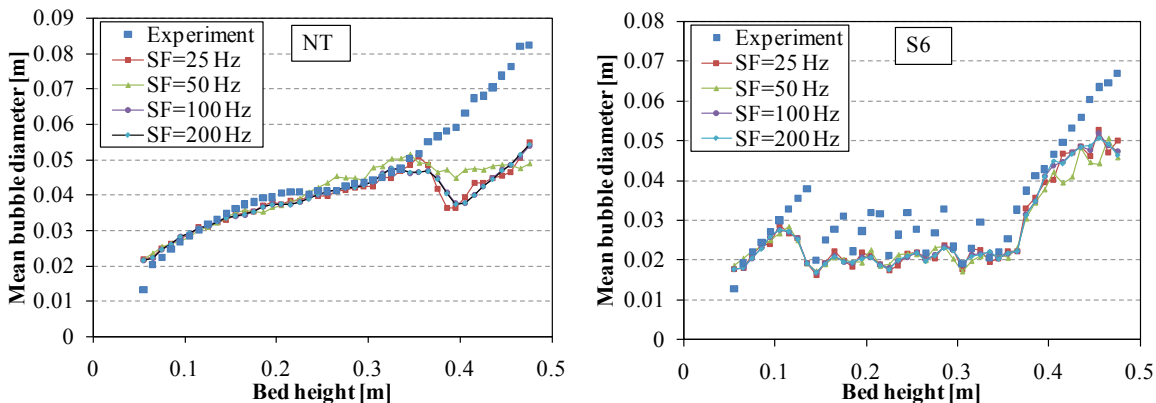


Figure 6.12: Mean bubble diameter for different sampling frequencies (SF); $d_p=246 \mu\text{m}$; $U=2.5U_{mf}$.

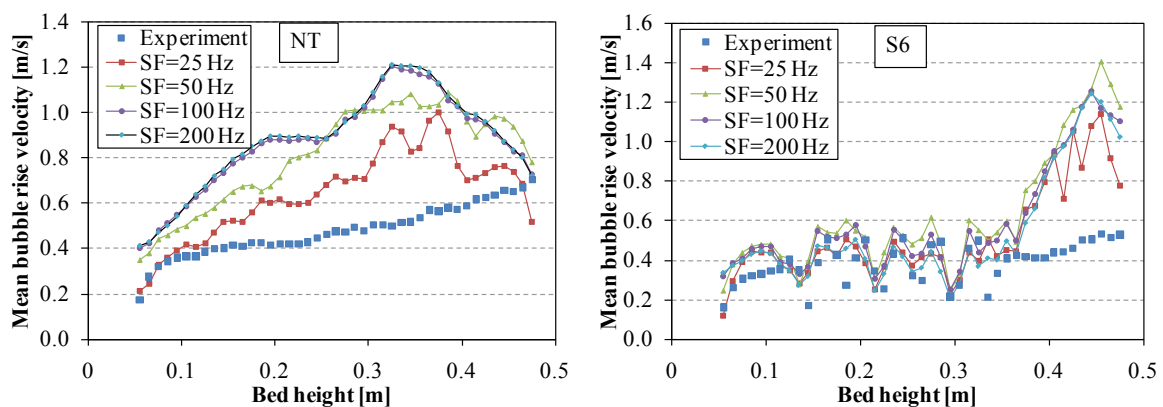


Figure 6.13: Mean bubble rise velocity for different sampling frequencies (SF); $d_p=246 \mu\text{m}$; $U=2.5U_{mf}$.

6.3 Grid Size Dependency

It is common practice to perform grid sensitivity analyses in order to ensure grid independent solution during numerical simulations. However, it is usually difficult to achieve grid independent solution using the TFM as the closure equations from the granular theory do not give grid independent solutions with reasonable grid sizes. Nevertheless, a grid sensitivity analysis was performed at least to ensure the mean bubble properties are not significantly affected by the grid size used and to obtain an optimum between computational effort and accuracy of results.

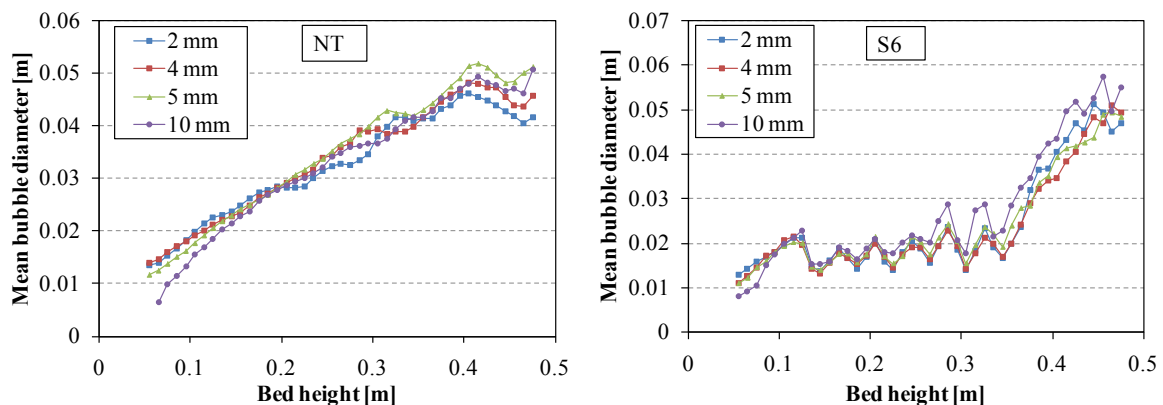


Figure 6.14: Comparison of mean bubble diameter for different grid sizes, $d_p=347 \mu\text{m}$, $U=2U_{mf}$.

The grid size sensitivity analysis was performed using simulations of two bed geometries (NT and S6) with grid sizes ranging from 2 mm to 10 mm. The results are plotted in Figure 6.14 and Figure 6.15 for the mean bubble diameter and mean bubble rise velocity respectively. There are no significant differences of the mean bubble properties predicted with grid sizes of 2, 4 and 5 mm. For the 10 mm grid, however some deviations can be noticed and is more pronounced for the mean bubble rise velocity. No major difference was also observed between the different grid

size in predicting the bed expansion ratio for both the NT and S6 cases. The results indicated that a grid size of 5 mm is sufficient to capture the bed properties and bubble characteristics with acceptable computational effort. This slightly exceeded the suggestion to use a grid size of 10 times the particle diameter to get grid-independent results, as suggested by e.g. Guenther and Syamlal (2001) and Syamlal and O'Brien (2003), but seems to be sufficient for the given cases. Both results were in very good agreement with the findings of Vejahati et al. (2009) and Xie et al. (2008a), who investigated the grid sensitivity based on mean bed voidage for a comparable particle size and fluidized beds without immersed tubes.

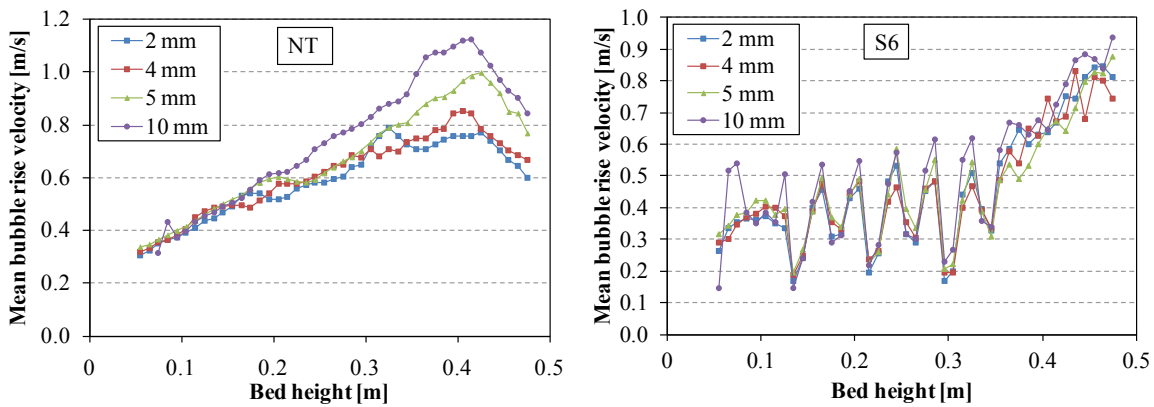


Figure 6.15: Comparison of mean bubble rise velocity for different grid sizes, $d_p=347 \mu\text{m}$, $U=2U_{mf}$.

Table 6.3: Comparison of simulation time for different grid sizes and flow domains.

Domain	Geometry	Grid size [mm]	Number of cells	Simulation time per second of real flow time [h]
2D	NT	2	96000	70
		4	24000	18
		5	15300	12
		10	3840	5
	S6	2	101838	75
		4	27694	27
		5	18469	16
		10	5190	11
3D	NT	4	120000	159
		5	61440	75
	S6	4	145705	219
		5	72924	105

In Table 6.3 the different computational times needed per one second of real flow time is presented for the different grid sizes as well as 2D and 3D simulations. All simulations were performed on a Quad-Core Intel Xeon processor (3 GHz each) workstation and a time step of 2.5×10^{-5} s was used. It can be clearly seen that the simulation time significantly increased as the

grid size reduced. The difference between the NT and S6 can be attributed to the increase in number of cells in S6 as a result of the refinement near the tube surfaces. Therefore, taking into account the computational time needed, a grid size of 5 mm was chosen for the numerical simulations reported in this work.

6.4 Two-and Three-Dimensional Comparison

Generally, all practical gas-solid flows are three-dimensional (3D) in nature and numerical simulations in 3D domains should be performed to validate and study such 3D flows. However, despite improved computational facilities, 3D simulations are still computationally prohibitive even for engineering-scale fluidized beds. Therefore, the majority of simulation studies encountered in the literature are limited to two-dimensional (2D) Cartesian coordinate system to simulate 3D fluidized beds. However, there are no studies proving that 2D computations are sufficient for validation and parametric study of fluidized beds. 2D simulations are most likely to be successful in cases where the flow is presumed to be 2D, that is in cases where the variations in space and time in a given direction of the physical space are negligible compared to the variations encountered in the other directions. This is typically in the case of pseudo-2D beds, which have small depth compared to the height and width. In such cases, the particle motion can be effectively suppressed in the third (depth) direction thus resembling 2D motion of the particles in the axial and radial directions only. Many researchers have applied 2D Cartesian simulations to model such rectangular pseudo-2D beds and found reasonable agreement between model prediction and experimental results. However, such comparisons leave an important difference between the pseudo-2D experimental beds and 2D numerical models. The front and back walls, which are neglected in the numerical model, could have considerable influence on the hydrodynamics of the fluidized beds. In the literature only few have attempted to compare between 2D and 3D simulations and discussed the justification for using 2D simulations for fluidized beds.

Ding and Lyczkowski (1992) were the first to develop 3D hydrodynamic kinetic theory model for fluidized beds. They computed bubble and solids motion in a rectangular fluidized bed and found differences in the time-averaged porosity contour and solids velocity. They emphasized the need to perform 3D simulations for better validation of the CFD models. This was later supported by Cammarata et al. (2003). These authors performed simulations using 2D and 3D domains of a rectangular bed and the results of bubble diameter were compared with the Darton's equation (Darton et al., 1977). The authors found considerable difference of the bubble diameter predicted by the simulations with the 2D simulations predicted smaller bubbles compared to the 3D simulations. They also found that bubble diameter predicted by the 3D simulations were in good agreement with those predicts by the Darton et al. (1977) equation. This is to be expected as the model developed by Darton et al. (1977) is based on experimental measurements from 3D fluidized beds. Peirano et al. (2001) analyzed and compared simulation results of the static (time-averaged bed height and probability density function of the spatial distribution of parti-

cles) and dynamic (power spectra of pressure fluctuations) with experimental measurements. They observed a significant difference between 2D and 3D simulations and concluded that 2D simulations should be used with caution and only for sensitivity analysis whereas 3D simulations are able to reproduce both the statics and the dynamics of the bed. Reuge et al. (2008) performed numerical simulation using 2D and 3D domains for a cylindrical bed and found that the bed expansion ratio and bed height fluctuation predicted by the 3D simulations were much closer to the experimental measurements while the 2D simulations highly overestimated them. The above authors concluded that, although computationally very demanding, 3D simulations should be preferably performed for validating the CFD models except maybe in cases where the flow is by nature 2D such as in case of pseudo-2D beds. They also indicate that 2D simulations could be used to conduct sensitivity analyses. On the other hand, Xie et al. (2008a,b) measured the void fraction and gas and solid velocities and concluded that 2D Cartesian system can be used to successfully simulate and predict a bubbling regime.

Recently Li et al. (2010) performed 2D and 3D simulations of a pseudo-2D bed and compared the results with experimental measurements. They found considerable difference in the bubble rise velocity predicted by the 2D and 3D simulations while the bubble diameter predicted by both domains is generally comparable. In this work, simulations were performed for two different particle sizes and two bed geometries with and without immersed horizontal tubes using 2D and 3D domains and the results of the mean static bed pressure drop, bed expansion, bubble properties were compared with experimental measurements obtained from the pseudo-2D bed.

Table 6.4: Comparison between 2D and 3D simulations for bed pressure drop; $d_p=246 \mu\text{m}$.

Tube arrangement	Superficial velocity	Bed pressure drop [kPa]		
		Experiment	Simulation	
		Pseudo-2D	3D	2D
NT	$2.5U_{mf}$	6.83	7.61	7.53
	$4.0U_{mf}$	7.09	7.66	7.44
S6	$2.5U_{mf}$	6.91	7.35	7.50
	$4.0U_{mf}$	7.00	7.45	7.50

Table 6.4 shows the time-averaged static bed pressure drop predicted by the 2D and 3D simulations and experimental measurements. It can be seen that no major difference of the predicted bed pressure drop was obtained. In Table 6.5 the time-averaged bed expansion ratio are shown with the corresponding experimental measurements. Generally, both simulations overestimated the bed expansion. It can be seen that the 3D simulation predicted lower bed expansion than the 2D. This is consistent with the results of Cammarata et al. (2003) and Reuge et al. (2008). The reason for this is that higher bed fluctuation was observed for the 2D simulation which gave higher expansion of the bed.

Table 6.5: Comparison between 2D and 3D simulations for bed expansion ratio; $d_p=246 \mu\text{m}$.

Tube arrangement	Superficial velocity	Bed expansion ratio, δ		
		Experiment	Simulation	
		Pseudo-2D	3D	2D
NT	$2.5U_{mf}$	0.1729	0.2702	0.2763
	$4.0U_{mf}$	0.2715	0.3453	0.4172
S6	$2.5U_{mf}$	0.1245	0.2899	0.2977
	$4.0U_{mf}$	0.2145	0.3673	0.4689

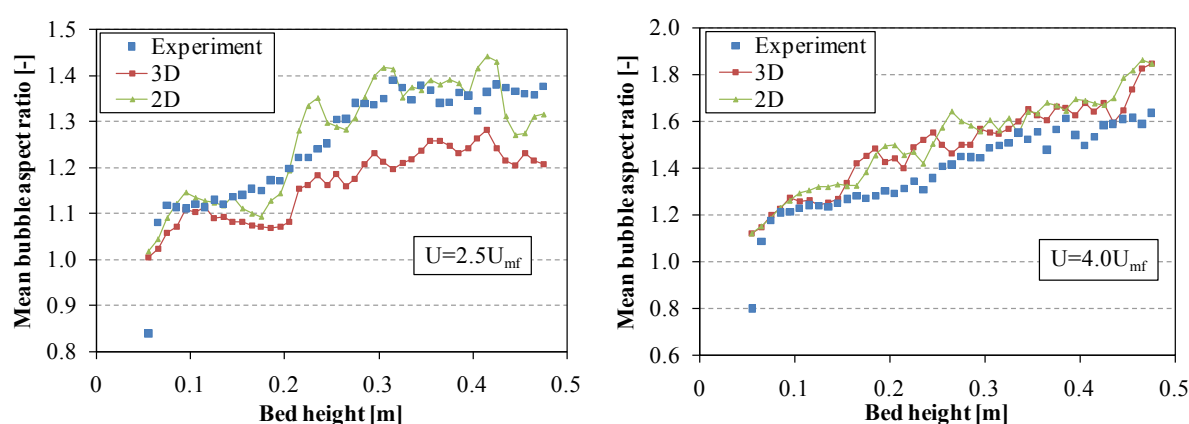
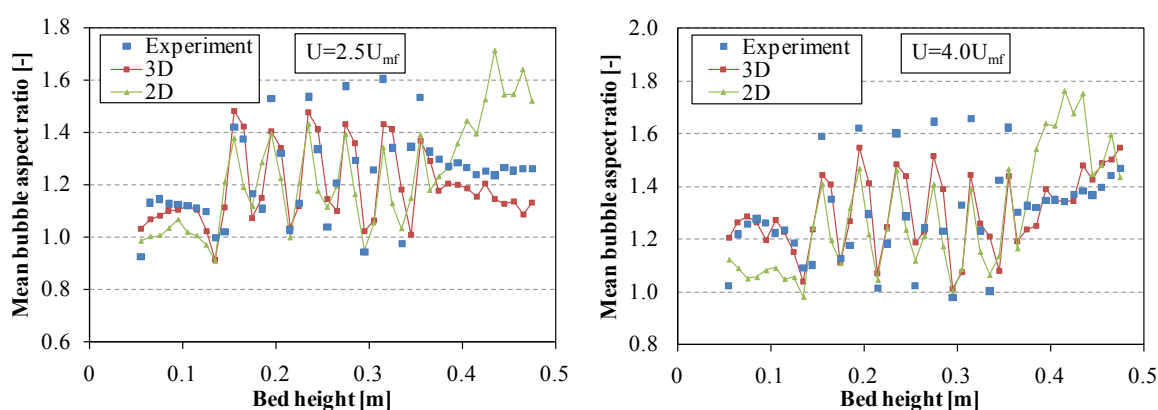
Figure 6.16: Comparison of bubble aspect ratio between 2D and 3D simulations for the bed without tubes (NT), $d_p = 246 \mu\text{m}$.Figure 6.17: Comparison of bubble aspect ratio between 2D and 3D simulations for the bed with dense staggered tubes (S6), $d_p = 246 \mu\text{m}$.

Figure 6.16 and Figure 6.17 show the mean bubble aspect ratio for the NT and S6 beds respectively for different superficial velocities and the particle with mean size of $246 \mu\text{m}$. Generally, both 2D and 3D simulations predicted well compared to the experimental measurements. At

lower superficial velocities, as shown in Figure 6.16 for the NT beds at $2.5U_{mf}$, the 3D simulation underestimated the experimental measurements. The reason cannot be fully explained yet but it could be attributed to the method by which bubbles are detected and measured. For the 3D simulations, bubbles were measured using a plane at the center of the bed. Thus, only bubbles, which are sliced by this central plane, are accounted for. Long bubbles, which are close to the sidewalls, could move undetected. Apart from this, the 3D simulations agreed better with the experimental measurements for both beds with and without immersed tubes. Comparing the bubble aspect ratio in the tube bank region, both the 2D and 3D simulations gave similar results and were in good agreement with the experiment. This showed that in the tube bank region bubble shape is more dictated by the tube bank geometry than the solution domain.

Figure 6.18 to Figure 6.20 illustrate the time-averaged bubble diameter predicted by the 2D and 3D simulations for different bed geometries (NT and S6), particle sizes and superficial velocities. The 3D simulations were in general in better agreement with the experimental measurements. In fact, the 2D simulation predicted reasonably well too in the majority of the bed height. The results obtained from 2D simulations showed greater divergence from the experimental data with increasing bed height and this was more pronounced with increasing superficial velocity, as shown Figure 6.18 at $U=4.0U_{mf}$. Such trend was also reported by Cammarata et al. (2003) who observed underestimation of the mean bubble diameter predicted by 2D simulations compared with correlation. The discrepancy of the 2D simulations was getting worst when the particles size and superficial velocity were further increased. This was thoroughly discussed in section 7.2 with results from different particle sizes and superficial velocities. From these results, it can be seen that the validation of 2D simulations using a pseudo-2D bed for coarser particles and higher superficial velocity should be treated with great cautious. By investigating the time-averaged void fraction and gas and solid velocities, Xie et al. (2008a,b) also arrived at similar conclusion. They concluded that 2D simulations could be successfully used to predict bed hydrodynamics of a bubbling regime. However, caution must be exercised when using 2D simulations for higher fluidization regimes such as the slugging and turbulent regimes.

There is no consistent relationship between bubble diameters predicted by 2D and 3D simulations. For the smaller particle size with NT bed, Figure 6.18, the 2D simulations predicted smaller bubbles than the 3D especially at the upper part of the bed. On the other hand, for bigger particle size and at the lower part of the bed with immersed tubes (S6) the mean bubble diameters predicted by 3D simulations are smaller than the corresponding 2D simulations. Others also reported such inconsistencies. For example, Cammarata et al. (2003) reported that mean bubble diameter predicted by the 2D simulations were much smaller than the corresponding 3D simulations while Li et al. (2010) reported otherwise. These inconsistencies could be partly explained in relation to the methodology used to define bubbles in 3D simulations as explained above. In beds with dense horizontal tubes (S6), both the 2D and 3D simulations predicted similar bubble sizes in the tube bank region. This was also observed in the case of bubble aspect ratio discussed above and it can be concluded that the effect of the three dimensionality was effectively sup-

pressed by the presence of tube banks. Therefore, if a fluidized bed has dense immersed tube banks, the flow dynamics of the bubbles and their characteristics is similar in both 2D and 3D.

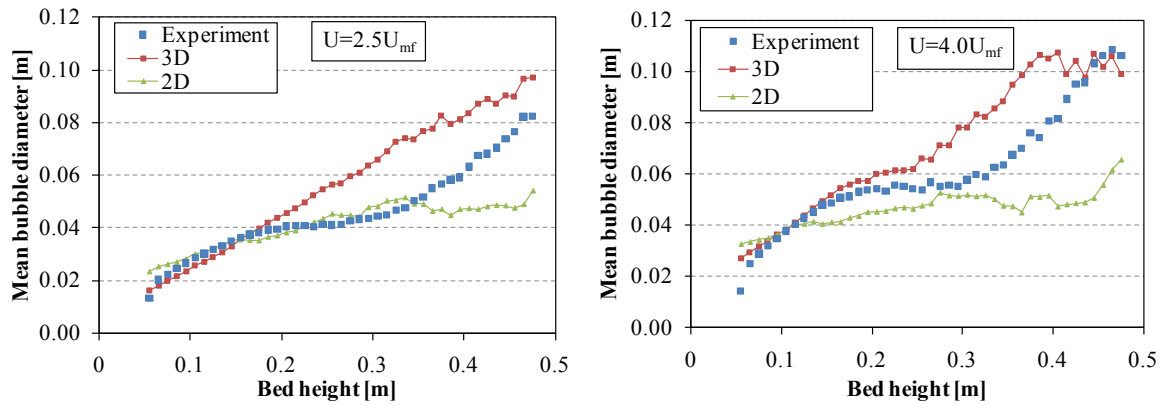


Figure 6.18: Comparison of mean bubble diameter between 2D and 3D simulations for the bed without tubes (NT), $d_p = 246 \mu\text{m}$.

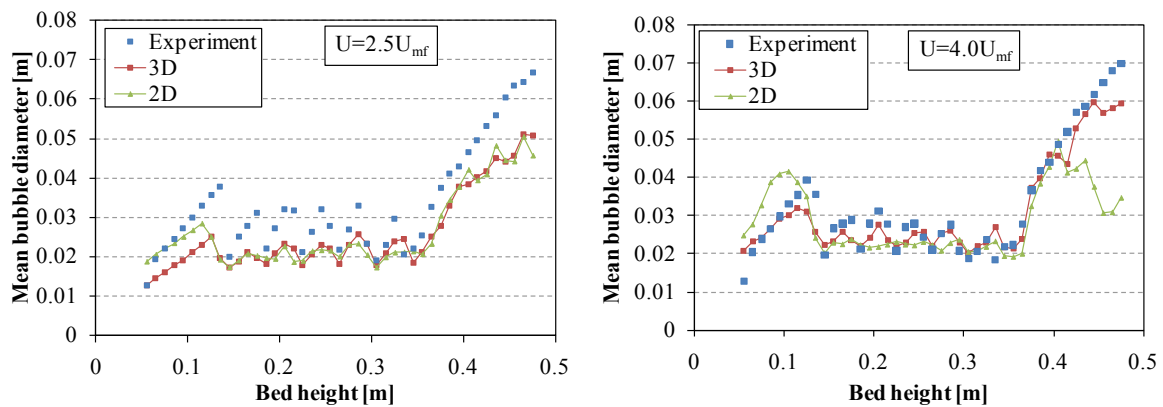


Figure 6.19: Comparison of mean bubble diameter between 2D and 3D simulations for the bed with dense staggered tubes (S6), $d_p = 246 \mu\text{m}$.

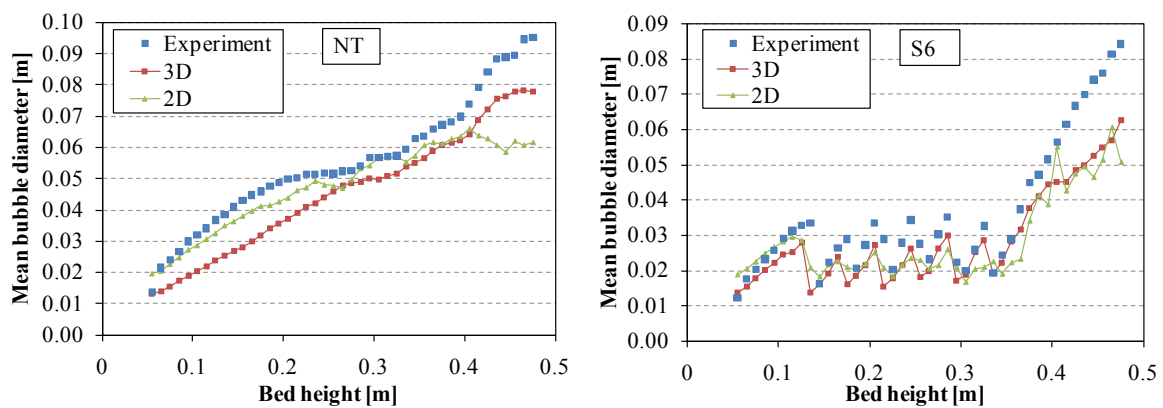


Figure 6.20: Comparison of mean bubble diameter between 2D and 3D simulations, $d_p = 347 \mu\text{m}$, $U=2.0U_{mf}$.

A significant difference between 2D and 3D simulations was observed in predicting the mean bubble rise velocity. Figure 6.21 to Figure 6.24 show the predicted mean bubble rise velocities for different bed geometries, particle sizes and superficial velocities. Generally, the simulation overpredicted the rise velocity for both 2D and 3D simulations with 2D simulations predicted much higher rise velocity than 3D and significantly deviated from the experiment measurements. Figure 6.21 shows the mean bubble rise velocity for NT case and the particle with mean diameter of $246 \mu\text{m}$. It can be seen that the mean rise velocity predicted by the 3D simulations is lower than the 2D simulations in the case of lower superficial velocity ($2.5U_{mf}$) while it is higher for higher superficial velocity ($4.0U_{mf}$). The reason for the higher rise velocity in case of $4.0U_{mf}$ is the large bubbles predicted by 3D. To illustrate this bubble rise velocity as function of bubble diameter is plotted in Figure 6.22.

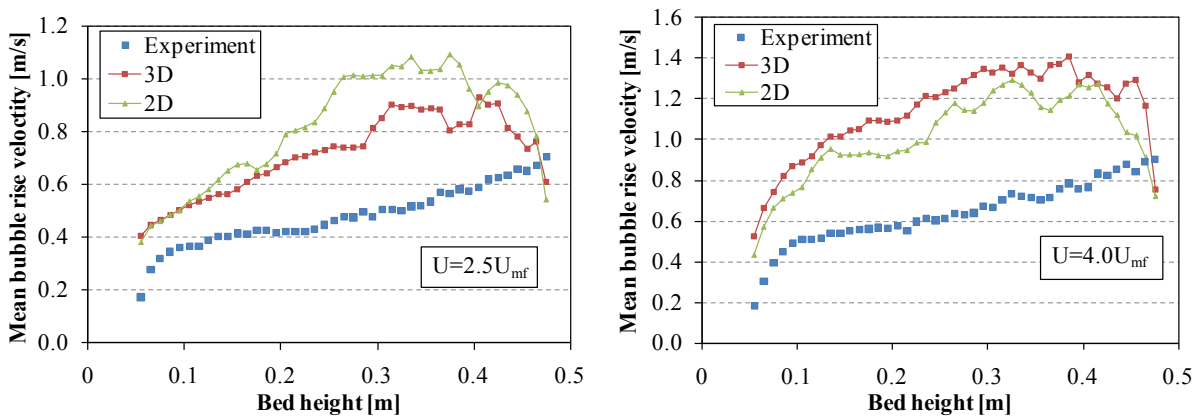


Figure 6.21: Comparison of mean bubble rise velocity between 2D and 3D simulations for the bed without tubes (NT), $d_p = 246 \mu\text{m}$.

As shown in Figure 6.22, it can be clearly seen that for smaller bubbles the 2D simulations predicted slightly lower rise velocities. As the bubbles grow with bed height the rise velocity predicted by the 2D simulations was found to be much higher than the 3D simulations for the same bubble diameter. This was largely attributed to the wall effect. The fluidized bed walls retard the rise of bubbles. It was believed that neglecting the front and back walls in the 2D simulations resulted in higher bubble rise velocities. In the experiment as well as 3D simulations, as a result of small bed thickness, the down flowing particles along the front and back walls increased the drag experienced by the bubbles, thus slowed the bubbles. On the other hand, these walls were neglected in the 2D simulations and bubbles could move freely in the bed without experiencing the drag of down flowing particles as well as the friction of walls. Others also reported similar results, e.g. Kunii and Levenspiel (1991), Krishna et al. (2000) and Li et al. (2010). Particularly Krishna et al. (2000) studied the influence of walls on bubble rise velocity for both gas-liquid and gas-solid systems and they concluded that the rise velocity of single gas bubbles was significantly reduced as the ratio of bubble to bed width increased. Kunii and Levenspiel (1991) reported that the wall effect on the rise velocity become more significant when the ratio of bubble diameter to bed diameter is greater than 0.125. This was similar to the findings of Krishna et

al. (2000). Another important difference between the 2D and 3D simulation of the bubble rise velocity is that, as shown in Figure 6.22, the bubble rise velocity predicted by 2D simulations depends only weakly on the mean bubble size, which is inconsistent with the experimental measurements and theories while the 3D simulations showed similar relationship as that of the experimental data.

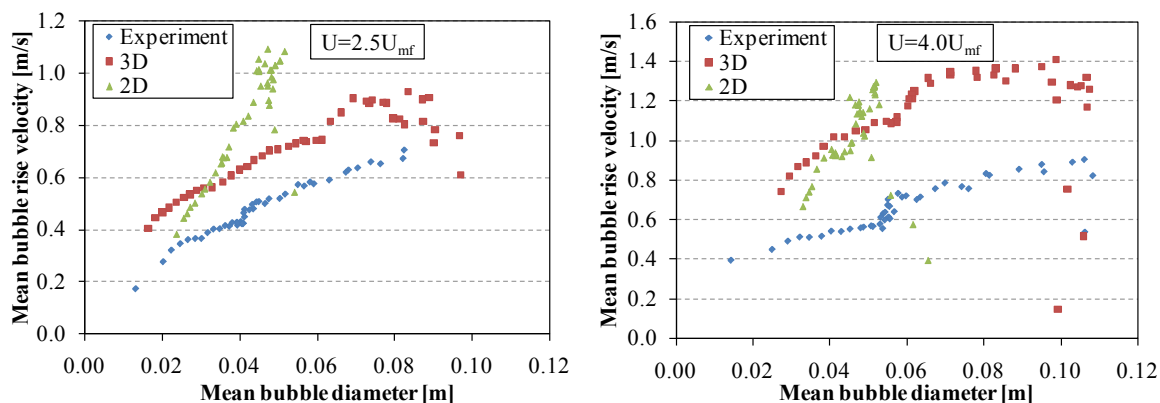


Figure 6.22: Mean bubble rise velocity as a function of bubble diameter for the bed without tubes (NT), $d_p = 246 \mu\text{m}$.

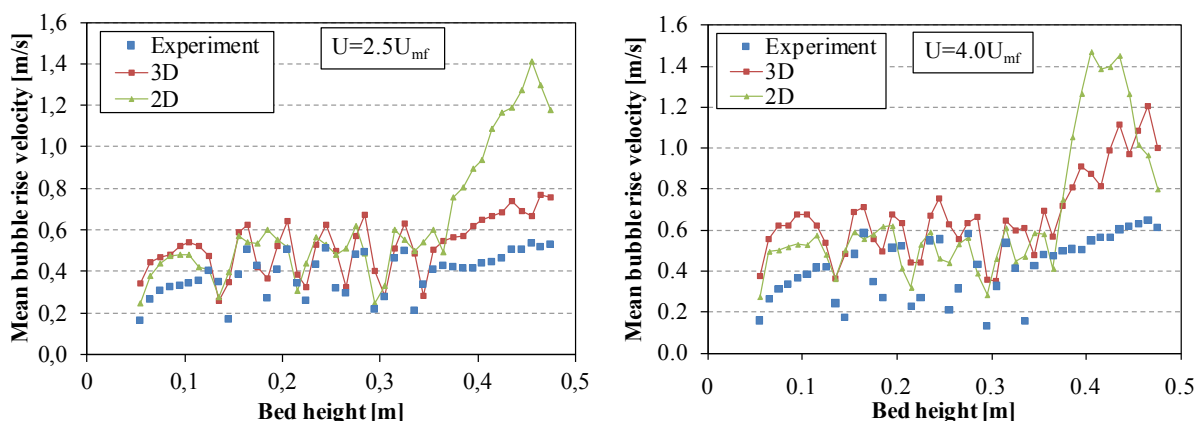


Figure 6.23: Comparison of mean bubble rise velocity between 2D and 3D simulations for the bed with dense staggered tubes (S6); $d_p = 246 \mu\text{m}$.

For beds with immersed horizontal tubes, both the 2D and 3D simulations predicted similar rise velocity in the tube bank region and were in better agreement with the experimental measurements than in the case of NT. Of course in the tube free region of the S6 bed, the rise velocity resembled similar trend as that of NT. Therefore, similar to the bubble shape and bubble diameter, the rise velocity in the tube bank region of fluidized beds with dense tube banks is controlled by the presence and geometry of the tube bundle and nearly independent of the solution domain.

In conclusion, though 2D simulations have certain limitations and are physically different from the 3D flow that exit in practical applications, they can provide quiet satisfactory results com-

pared to experimental observations. Especially when the bed contains dense heat transfer tubes, the bubble flow dynamics predicated by both domains is similar and using 2D simulations could be computationally effective. There is no doubt that 3D simulations are more realistic and should be preferred, but with current, even in the near future, computer capacity these are far from reaching. As shown in Table 6.3, comparing the computational time needed for 2D and 3D simulations, it was found that 3D simulations are 5 to 9 times more expensive than their 2D equivalents. As an example in order to simulate 20 s of real flow time in the 2D domain with a grid size of 5 mm using the no tube geometry 240 h (approx. 10 days) of simulation time were needed while this was increased to 1500 h (approx. 62 days) in the case of 3D simulations. Therefore, as also deduced by Xie et al. (2008a,b) and Cammarata et al. (2003), especially for conducting extensive parametric studies, 2D simulations remain indispensable.

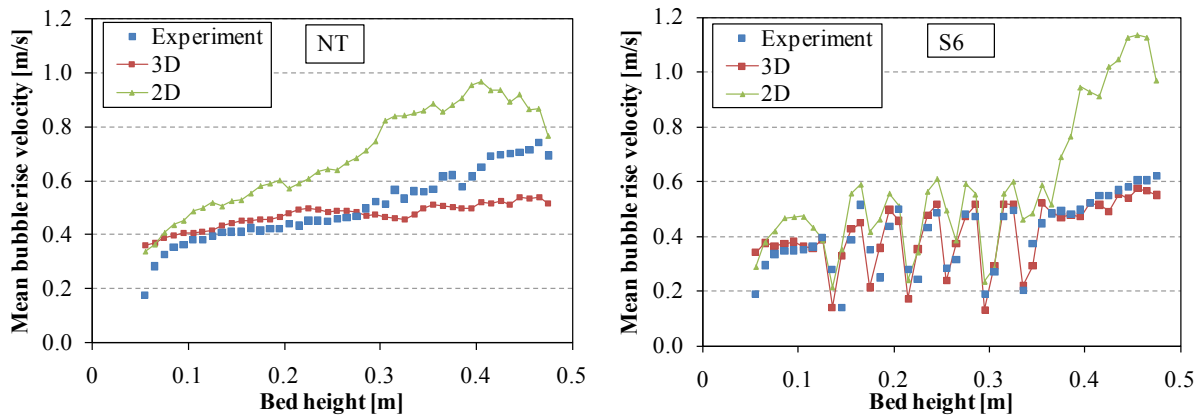


Figure 6.24: Comparison of mean bubble rise velocity between 2D and 3D simulations; $d_p = 347 \mu\text{m}$, $U=2.0U_{mf}$.

6.5 Friction Packing Limit

In the two-fluid model the fictional stresses which arise due to multi-particle contact are simply added to the solid stresses from KTGF when the solid volume fraction exceeds a certain value, $\varepsilon_{s,\min}$, which is termed as the friction packing limit. Several authors have extensively studied different frictional stress models available for gas-solid two-phase flow modeling (see e.g. Patil et al., 2005a,b; Benyahia, 2008; Passalacqua and Marmo, 2009). However, the influence of the minimum solid packing limit at which these frictional stresses should be added to the kinetic contribution has not been adequately reported. Johnson et al. (1990) proposed this value to be 0.5 and many other researchers used the same value without giving explanation. Passalacqua and Marmo (2009) performed sensitivity analysis for friction packing limits of 0.5 and 0.63 with maximum solid packing limit of 0.65. Their comparison was, however, limited to the evolution and growth of a single bubble in fluidized bed with central jet. In this part of the work the influence of friction packing limits, ranging from 0.5 to 0.65, on the bubbling behavior as well as bed expansion were investigated.

Table 6.6: Comparison of bed expansion ratio predicted using different friction packing limits; $d_p=246 \mu\text{m}$, $U=2.5U_{mf}$.

Tube arrangement	Bed expansion ratio, δ					
	Experiment	Simulation				
		Friction packing limits				
		0.50	0.55	0.60	0.63	0.65
NT	0.1729	0.2991	0.2890	0.2763	0.2600	0.2847
S6	0.1245	0.3215	0.3074	0.2977	0.2852	0.3026
I6	0.1360	0.3201	0.3059	0.2999	0.2932	0.3051

Table 6.6 shows the time-averaged bed expansion ratio as predicted using different friction packing limits. It can be seen that the bed expansion ratio decreased as the friction packing limit increased. This can be explained as follows. Lower friction packing limit implies earlier action of the frictional stresses. This leads to reduce the solid volume fraction from reaching higher values the maximum packing limit. Since the initial solid volume fraction, hence the mass of particles, is the same for all cases, lower solid volume fraction means higher bed height. Therefore, with lower friction packing limit the particles are less compact thus the bed height is higher. In the other extreme when friction packing limit is higher the particles are more compact and the bed height will reduced. When the friction packing limit is equal to the maximum solid packing limit (i.e. 0.65), it implies no frictional stresses are applied. In this case different flow structure and solid volume fraction distribution are observed. Though solid volume fractions near to the maximum packing limit are observed, these are only on some locations near the bed walls and the majority of the bed volume showed uniform distribution of solids which give rise to slightly higher bed height.

Figure 6.25 to Figure 6.27 show the predicted bubble aspect ratio, bubble diameter and rise velocity, respectively, as a function of bed height for two bed geometries (NT and S6). Additional results for the I6 tube geometry are given in Appendix C. Generally, with the exception of the friction packing limit of 0.65, which corresponds to no friction case, the value of the friction packing limit has not significant influence on the predicted bubble properties. For the bed without internals (NT) the friction packing limit slightly affected the bubble aspect ratio and diameter. The influence of the friction packing limit was suppressed by the presence of dense immersed tubes in the S6 case. This indicated that bubble properties were largely influenced by the tube bank geometry rather than the friction packing limit. Form the result of the NT bed a friction packing limit of 0.6 gave relatively better agreement with the experimental data. When the friction packing limit is set to 0.65, which is equal to the maximum packing limit, no frictional stresses are applied thus the solid volume fraction approaches to the maximum packing limit. This leads in higher compaction around the bubbles, which prevents gas in-flow and out-flows of the bubbles therefore bubble elongation and growth. As a result, lower aspect ratio and

diameter of the bubble were predicted as compared to the others. On the other hand, lower friction packing limit implies earlier action of the frictional stresses. This leads to reduce the solid volume fraction from reaching the maximum packing limit, hence reduce solid compaction around bubbles. As a result, the gas leakage through the bubble boundary to the emulsion phase increased and thereafter reduced the bubble diameter.

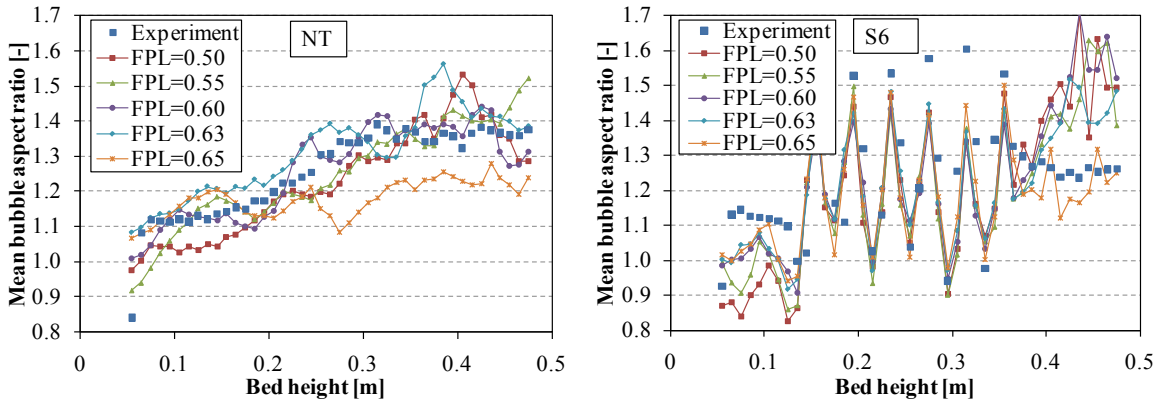


Figure 6.25: Comparison of bubble aspect ratio between experiment and simulation for different friction packing limits (FPL); $d_p=246 \mu\text{m}$, $U=2.5U_{mf}$.

Figure 6.27 shows the mean rise velocity predicted using different friction packing limits. It can be seen that all except for the friction packing limit of 0.65, predicted similar bubble rise velocity with bed height. When the friction packing limit was set to 0.65, due to smaller bubbles and higher drag between the bubbles and emulsion phase which resulted from the high compaction of particles the rise velocity was lower. Comparing between fluidized beds with and without immersed tubes, the presence of tubes had no influence on the choice of the friction packing limit.

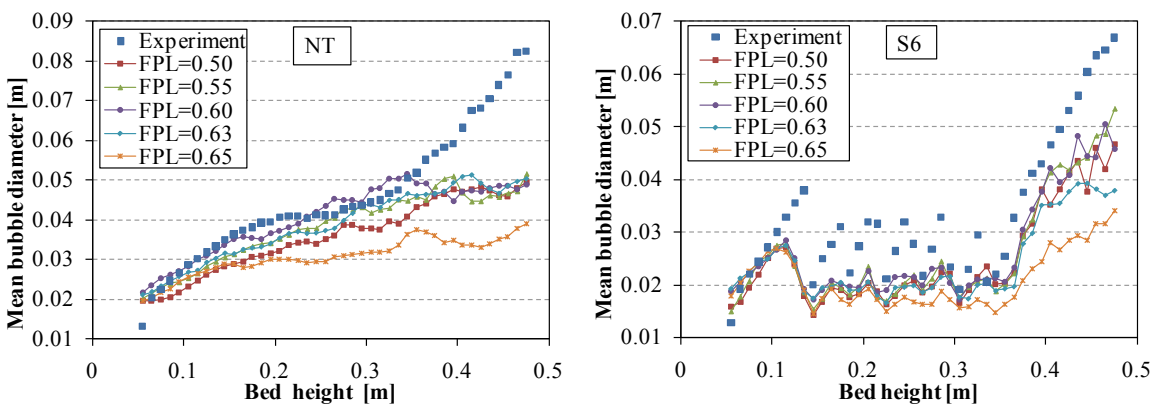


Figure 6.26: Comparison of bubble diameter between experiment and simulation for different friction packing limits (FPL); $d_p=246 \mu\text{m}$, $U=2.5U_{mf}$.

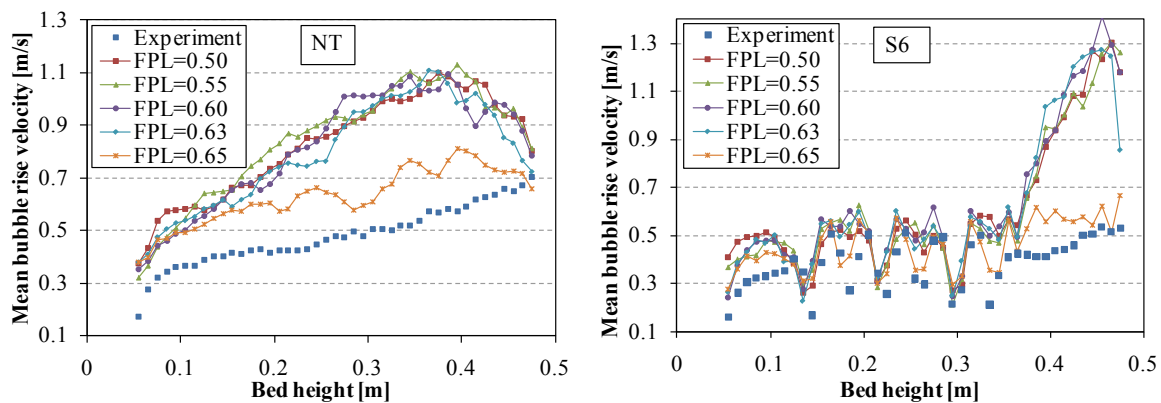


Figure 6.27: Comparison of bubble rise velocity between experiment and simulation for different friction packing limits (FPL); $d_p=246 \mu\text{m}$, $U=2.5U_{mf}$.

6.6 Inter-Phase Momentum Transfer Coefficient

In the TFM the two phases are coupled through interphase momentum transfer, and it is one of the most important and dominant forces in fluidized bed modeling. The drag laws to model the interphase momentum exchange are usually developed empirically and different models have been proposed by many researchers as summarized by Enwald et al. (1996) and recently by Vejahati et al. (2009). Therefore, their applicability and validity to model fluidized bed of specific particle size and flow conditions needs to be evaluated. In this part the bubbling behavior of fluidized beds with and without immersed horizontal tubes were investigated for the three drag models widely used in the literature.

Table 6.7: Comparison of bed expansion ratio predicted using different drag models; $d_p=246 \mu\text{m}$, $U=2.5U_{mf}$.

Tube arrangement	Bed expansion ratio, δ			
	Experiment	Simulation		
		Syamlal and O'Brien	Wen and Yu	Gidaspow
NT	0.1729	0.2181	0.2717	0.2763
S6	0.1245	0.2378	0.2945	0.2977
I6	0.1360	0.2328	0.2998	0.2999

Table 6.7 showed the bed expansion ratio predicted using the three drag models and comparison with the experimental measurements. It can be seen that the drag model of Syamlal and O'Brien (1989) slightly underpredicted the bed expansion compared to the others while both the drag models of Wen and Yu (1966) and Gidaspow (1994) predicted similar bed expansion. Similar

results were reported by van Wachem et al. (2001) and Taghipour et al. (2005). On the other hand, McKeen and Pugsley (2003), Vejahati et al. (2009), Hamzehei et al. (2010) reported that the different drag models showed quantitatively about the same degree of bed expansion.

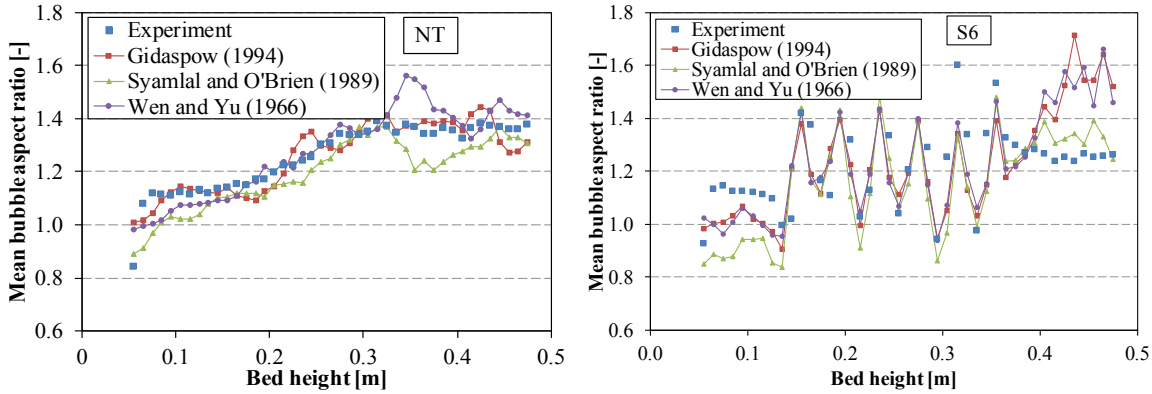


Figure 6.28: Comparison of mean bubble aspect ratio between experiment and simulation using different drag models; $d_p=246 \mu\text{m}$, $U=2.5U_{mf}$.

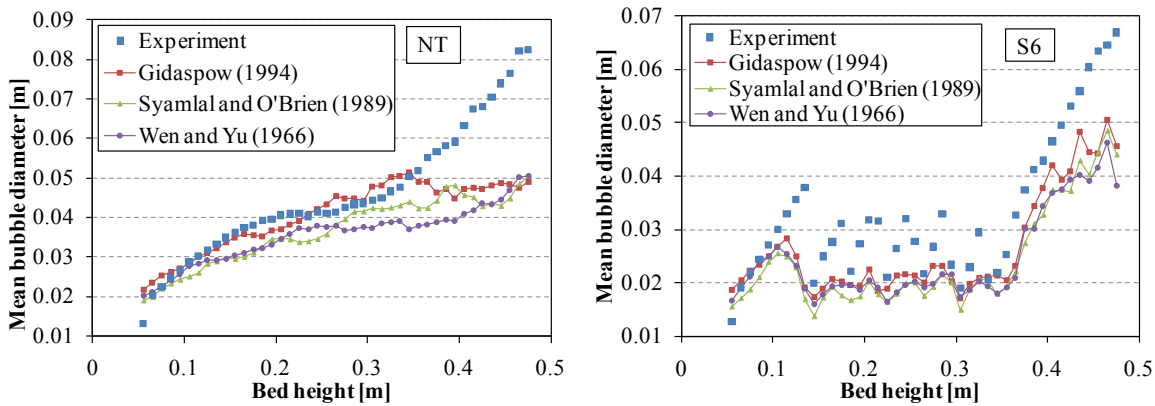


Figure 6.29: Comparison of mean bubble diameter between experiment and simulation using different drag models; $d_p=246 \mu\text{m}$, $U=2.5U_{mf}$.

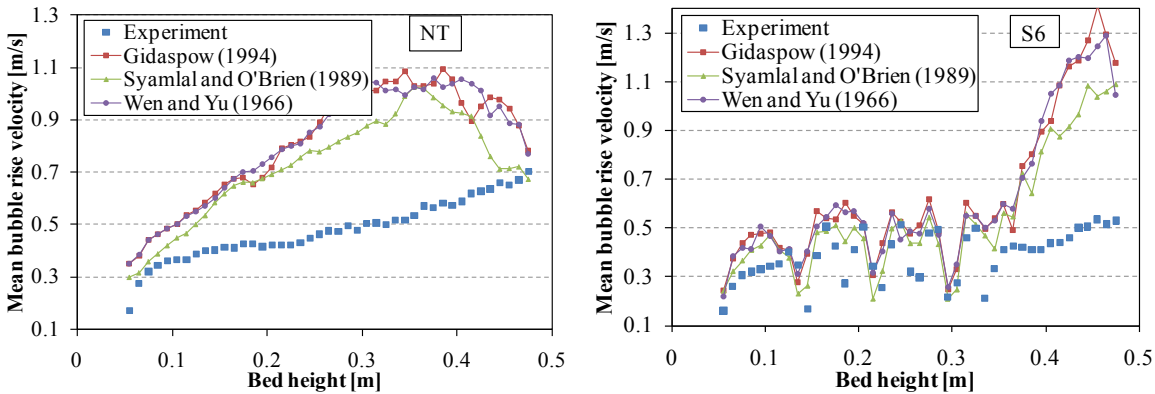


Figure 6.30: Comparison of mean bubble rise velocity between experiment and simulation using different drag models; $d_p=246 \mu\text{m}$, $U=2.5U_{mf}$.

Figure 6.28 shows the mean bubble aspect ratio predicted using the three drag models and comparison with experimental measurements. Generally, similar results can be observed from the three drag models. The Syamlal and O'Brien (1989) drag model predicted lower bubble aspect ratio in the tube free region and the NT case, which indicates relatively circular bubbles. This is consistent with the observation of van Wachem et al. (2001) for single jet entering a minimum fluidized bed. Figure 6.29 shows the mean bubble diameter as a function of bed height for the beds NT and S6. There is no significant difference of bubble properties predicted by the three drag models and all were in good agreement with the experiment. Because the bubble sizes predicted by the different drag models are all close, while the predicted bed expansion of the Syamlal and O'Brien (1989) is lower, it predicted highest solid volume fraction of the dense phase, which resulted in higher solid compaction in the bed. This prevented the bubbles from elongating vertically. Moreover, as shown in Figure 6.30, as a result of higher solid compaction and lower bubble aspect ratio the mean bubble rise velocity predicted by the Syamlal and O'Brien (1989) drag model was slightly lower than the others. Additional results for the I6 tube geometry are given in Appendix C.

6.7 Solid-Wall Boundary Conditions

The solid-wall boundary condition (BC) is an important parameter in CFD modeling of gas solid fluidized beds. The no-, partial- and free-slip solid-wall boundary conditions have been used in numerical simulations of fluidized beds. The partial-slip wall boundary condition proposed by Johnson and Jackson (1987) is most widely used, requiring that, the specularity coefficient and particle wall restitution coefficient be specified. The specularity coefficient is a measurement of the fraction of collisions that transfer momentum to the wall and varies from zero (free-slip condition) to one (no-slip condition). Direct measurement of specularity coefficient is not possible hence different values have been used in numerical simulations. No work has been reported on the influence of solid-wall boundary condition on bubbling behavior of fluidized beds in the presence of immersed obstacles. Thus, the influence of different solid-wall boundary conditions on the characteristics of bubbles for beds with and without immersed horizontal tubes was investigated.

Table 6.8 shows the bed expansion ratio predicted using different solid-wall boundary conditions and comparison with experiment. It can be seen that the bed expansion was lower for the free-slip boundary condition and higher for the no-slip condition. The partial-slip BC predicted between the two extremes with slightly increasing with increasing the specularity coefficient. Since particles are free to slip over the surface of the fluidized bed walls, a high concentration of down flowing solids were predicted by the free-slip BC along the wall of the bed which gave rise to lower bed expansion. The accumulation of solid particles along the bed wall was minimal for the no-slip BC and decreased with increasing specularity coefficient for the partial-slip BC. Compared to the experimental measurements the free-slip predicted better agreement than other

BCs. Others, e.g. Bahramian et al. (2009) who studied the influence of different particle-wall boundary conditions on a conical fluidized bed unit, also reported similar results. These authors reported that the numerical predictions using free-slip/no-friction BC agreed reasonably well with the experimental pressure drop measurements, especially at superficial gas velocities higher than the minimum fluidization velocity. Moreover, the results for simulated mean axial solid velocity showed that the free-slip BC was in better agreement with the experimental data. However, in practical situations the free-slip/no-friction BC is not valid as solid particles dissipated their energy because of collision and friction with the walls. This can be also seen from the result of bubble properties shown below.

Table 6.8: Comparison of bed expansion ratio predicted using different solid-wall boundary conditions; $d_p=246 \mu\text{m}$, $U=2.5U_{mf}$, SC=specularity coefficient.

Tube arrangement	Bed expansion ratio, δ					
	Experiment	Simulation				
		Free-slip	No-slip	Partial-slip		
				SC=0.25	SC=0.50	SC=0.75
NT	0.1729	0.2560	0.2917	0.2564	0.2763	0.2730
S6	0.1245	0.2797	0.3156	0.2864	0.2977	0.2993
I6	0.1360	0.2770	0.3204	-	0.2999	-

Figure 6.31, Figure 6.32 and Figure 6.33 show the simulation results using different solid-wall boundary conditions and comparison with experimental data of mean bubble aspect ratio, diameter and rise velocity respectively. Additional results for the I6 tube geometry are given in Appendix C. In general, the partial-slip boundary condition gave better agreement of bubble shape and diameter compared with the experimental results while all overpredicted the rise velocity. The main reason for higher bubble rise velocity in the simulation was due to the wall effect explained earlier. The free-slip BC predicted elongated (higher aspect ratio) over the entire bed height while the no-slip boundary condition predicted relatively circular bubbles (lower aspect ratio), Figure 6.31. For the free-slip BC, solids are free to move downwards along the walls and a layer of down flowing solids were observed at the wall throughout the bed height leaving the center of the bed relatively void allowing the bubbles to elongate hence, moving faster, Figure 6.33. Since the solids are pushed to the walls of the bed, the solid compactions around the bubbles reduced, as a result the gas flow through the bubble boundary to the emulsion phase increased and thereafter reduce the bubble diameter.

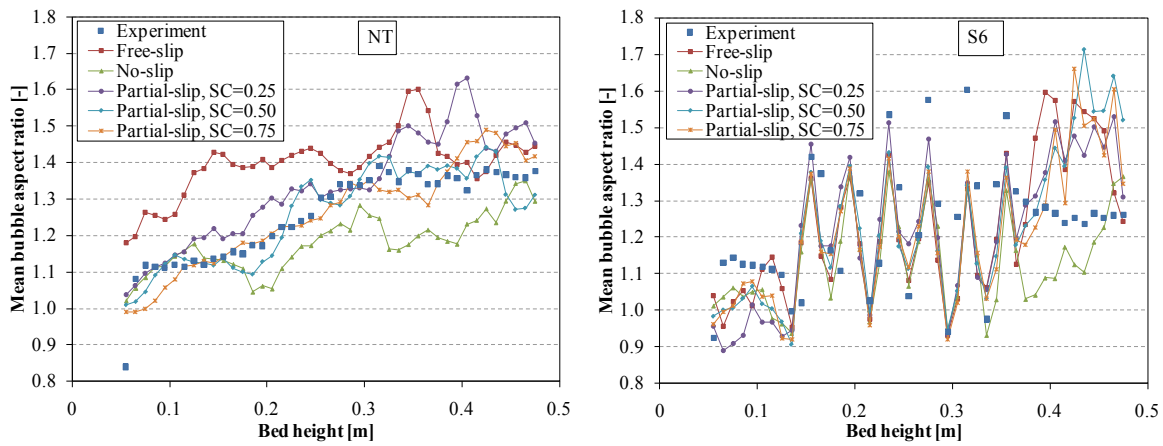


Figure 6.31: Comparison of bubble aspect ratio between experiment and simulation for different solid-wall boundary conditions and specular coefficients (SC); $d_p=246 \mu\text{m}$, $U=2.5U_{mf}$.

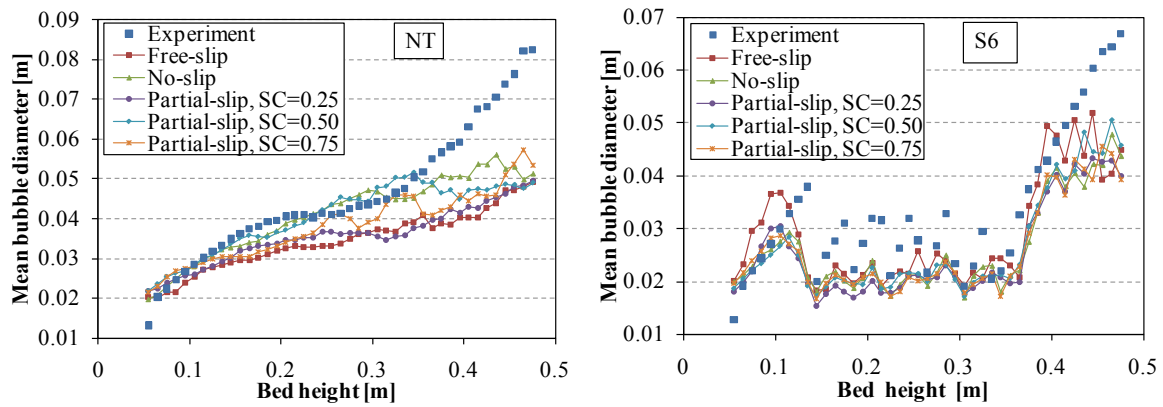


Figure 6.32: Comparison of bubble diameter between experiment and simulation for different solid-wall boundary conditions and specular coefficients (SC); $d_p=246 \mu\text{m}$, $U=2.5U_{mf}$.

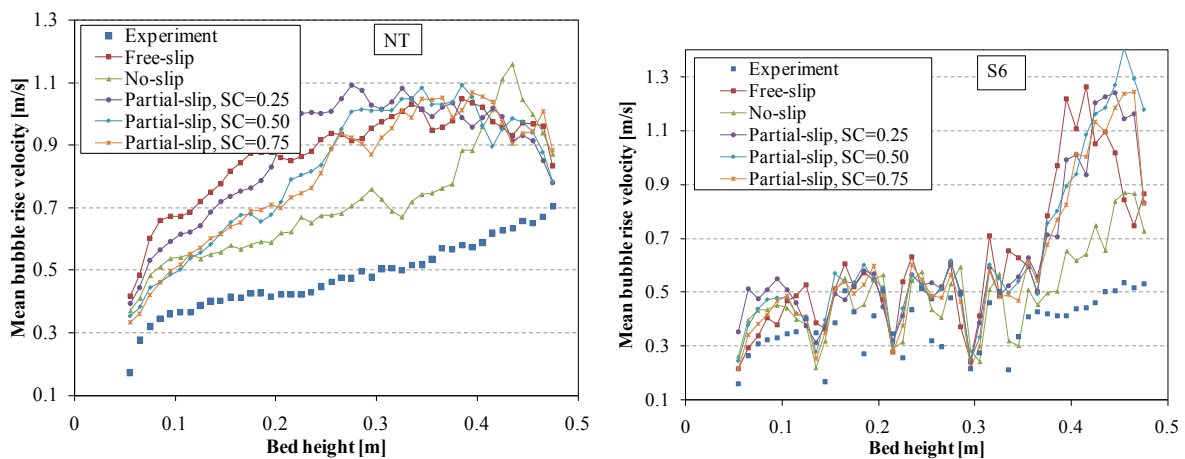


Figure 6.33: Comparison of bubble rise velocity between experiment and simulation for different solid-wall boundary conditions and specular coefficients (SC); $d_p=246 \mu\text{m}$, $U=2.5U_{mf}$.

At the upper part of the beds, the no-slip BC predicted lower bubble aspect ratio and rise velocity compared with other BCs. This is due to higher drag between the particles and bubble. Particles drifted up by the motion of bubbles were pushed side ways to wall of the bed as the bubbles erupted. Since these walls are no-slip for the particulate phase, the particles near the wall did not slip downwards and accumulated at the sidewalls of the bed. This was evident by the higher solid volume fraction that extends to the center of the bed and lower downward velocity particles observed at the upper part of the bed compared with other boundary conditions. Thus, bubble experienced higher drag that eventually prevent bubbles from stretching vertical and reduce their rise velocity. For the partial-slip BC, the choice of specular coefficient showed little influence on the predicted bubble characteristics and were more evident for the bed without immersed tubes. Similar conclusions were reported by Li et al. (2010). If the specular coefficient is lower it tends to the free-slip BC, while higher specular coefficients resembled to the no-slip BC. In this work, the specular coefficient of 0.5 gave better agreement with the experimental data. This value was also frequently used in the literature (Li et al., 2010). Compared the beds with and without immersed tubes, the presence of dense tubes predominated the bubbling characteristics of fluidized beds thus the different boundary conditions considered have little influence in the tube bank region of the bed.

7 Influence of Immersed Horizontal Tube Banks and Mean Particle Size

In many industrial applications, where heat and mass transfer and chemical reaction are important, heat exchanger tubes are usually inserted to enhance the performance of the fluidized beds. However, the influence of these immersed tubes on the bubble hydrodynamics is not yet fully comprehended. Especially numerical studies of fluidized beds with dense immersed horizontal tube banks are not available in the literature. Therefore, in this chapter detail numerical and experimental investigations of the influence of immersed horizontal tube bank geometry and arrangement on bubble hydrodynamics and bed characteristics were presented. Moreover, the influence of mean particle size on bubble hydrodynamics and bed characteristics were discussed.

All the simulations reported on this chapter were performed in 2D domain. From the results of the validation work in Chapter 6, the simulation parameters selected and used in this chapter are summarized in Table 7.1 below.

Table 7.1: Simulation parameters

Parameter	Value/Reference
Gas density, kg/m ³	1.2
Gas viscosity, Pa·s	$1.79 \cdot 10^{-5}$
Particle density, kg/m ³	2500
Mean particle diameter, μm	Table 6.1
Minimum fluidization velocity, U_{mf} , m/s	Table 6.1
Minimum fluidization solid volume fraction	Table 6.1
Bed height at minimum fluidization, H_{mf} , m	0.5
Restitution coefficient	0.95
Superficial velocity ratio, U/U_{mf}	2.0, 3.0, 4.0
Friction packing limit	0.6
Maximum particle packing limit	0.65
Specularity coefficient	0.5
Angle of internal friction, $^{\circ}$	28.5
Time step size, s	$2.5 \cdot 10^{-5}$, $5 \cdot 10^{-5}$
Grid size, mm	5
Drag coefficient	Gidaspow (1994)
Other closure equations	Table 6.2

7.1 Influence of Horizontal Tube Banks

7.1.1 Pressure drop

Figure 7.1 shows the measured and predicted time-averaged static bed pressure drop for two particle sizes and two bed geometries. Additional results with more tube geometries are summarized in Table 7.2. The simulation predicted relatively uniform pressure drop for all bed geometries and superficial velocities. This is to be expected from theoretical principle as the static pressure drop is only a function of the weight of the particles and is independent of the superficial velocity and particle size for monodisperse and smooth particles. The deviations between the predicted static pressure drops is usually less than 200 Pa, which is less than 3 % of the mean static pressured drop for the NT case. On the other hand, experimental measurements showed that the static pressure drop slightly increased with excess gas velocity. Taghipour et al. (2005) also reported similar increase of the bed pressure drop with excess gas velocity and it could be attributed to the slight polydispersity of the particles during the experiment. Smaller particles can agitate within the coarser particles, which is likely to generate additional pressure drop due to attrition phenomena (Donsi et al., 1989). Another reason could be due to friction between particles and wall and in part due to momentum imparted to the rising solids by the fluidizing gas (Clift and Grace, 1985). In addition, experimental measurements showed that the mean static bed pressure drop is higher for the NT case than the S6 and is more pronounced at higher excess gas velocities. Numerical simulations on the other hand predicted similar pressure drop regardless of the bed geometry. The difference between measurement and simulation predictions appeared at lower excess gas velocity and this is more pronounced as the particle size decreased. Apart from these slight differences, the TFM predicted well the static pressure drop for Geldart group B powders. From the results, no major difference was observed between in-line and staggered tube arrangement as well as between dense and sparse tube geometries.

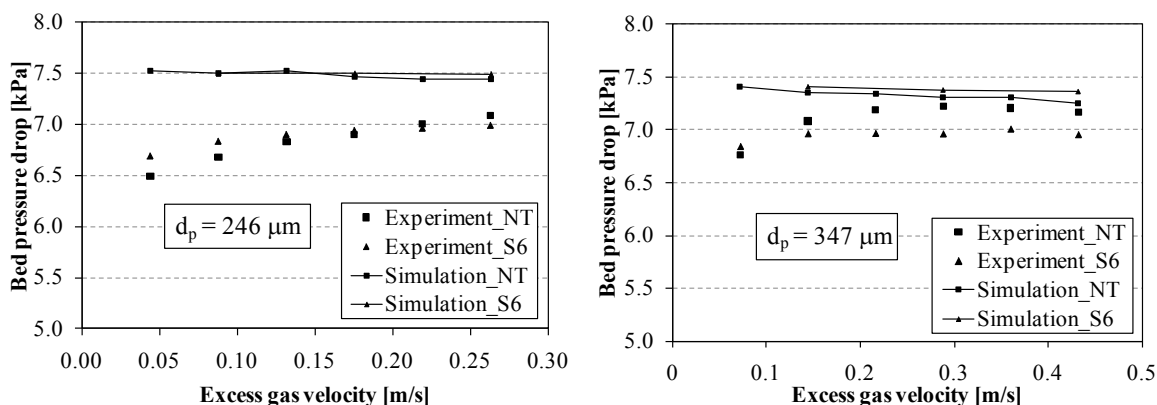


Figure 7.1: Time-averaged bed pressure drop versus excess gas velocity ($U-U_{mf}$).

Table 7.2: Time-averaged bed static pressure drop in kPa.

Mean particle Diameter	Superficial velocity	Experiment					Simulation				
		NT	S6	S3	I6	I3	NT	S6	S3	I6	I3
246 μm	$2U_{mf}$	6.68	6.84	6.32	6.62	6.53	7.349	7.500	7.458	7.470	7.411
	$3U_{mf}$	6.90	6.97	6.65	6.65	6.65	7.310	7.500	7.402	7.454	7.358
	$4U_{mf}$	7.01	6.99	6.84	6.76	6.80	7.254	7.495	7.363	7.416	7.323
347 μm	$2U_{mf}$	7.08	6.97	6.97	6.93	6.87	7.349	7.407	7.325	7.372	7.374
	$3U_{mf}$	7.22	6.97	7.18	7.14	7.11	7.310	7.376	7.237	7.317	7.320
	$4U_{mf}$	7.17	6.96	7.28	7.12	7.26	7.254	7.361	7.207	7.270	7.254

7.1.2 Bed expansion

In general for beds without immersed tubes, bed expansion increases with increase in excess gas velocity ($U-U_{mf}$), because bubbles increase in size and number. As shown in Figure 7.2, both the experimental measurements and numerical simulations showed this well-known increase of bed expansion with increasing superficial velocity. Though the simulation showed qualitatively good agreement, quantitatively it highly overestimated the bed expansion for all bed geometries as compared to the experimental measurement. The deviation became progressive with increasing in excess gas velocity. At higher excess gas velocity, the simulation predicted approx. 30 % greater bed expansion than the respective experimental measurements. For small particles of Geldart's group A powders, McKeen and Pugsley (2003) and Zimmerman and Taghipour (2005) found similar results and they attributed the failure of the TFM to the existence of inter-particle cohesive forces, which results in the formation of clustering and/or aggregating structures in bubbling gas-fluidized beds. However, Wang et al. (2009) suggested that the failure of the TFM in predicting the bed expansion of group A particles is mainly due to the lack of scale resolution. They concluded that the TFM could predict the correct bed expansion, without any artificial modification, provided that a sufficiently fine grid size and small time step is used. In this work at least for group B particles, it was found that the bed expansion hardly depend on the grid size. Therefore, the discrepancy between simulation predictions and experimental measurements could be attributed to the particle size distribution and the drag model. The simulation predicted higher bubbling frequency hence a very high bed fluctuations that resulted from continuous bubble eruptions and consequently bed collapse. In the experiment, such bed fluctuations were minimal. This is due to the polydispersity of the particles that promotes smooth fluidization hence less bed fluctuation.

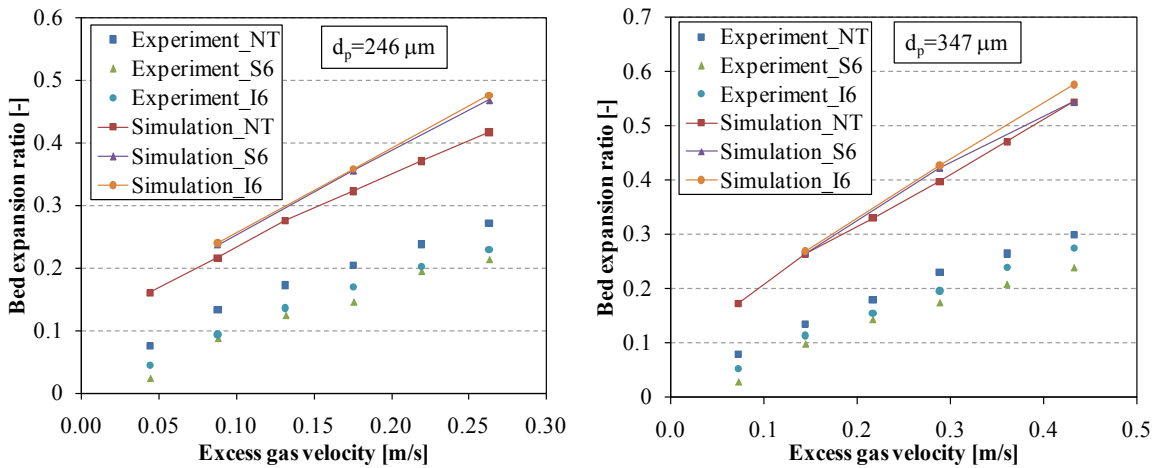


Figure 7.2: Measured and predicted time-averaged bed expansion ratio versus excess gas velocity ($U-U_{mf}$) for different bed geometries.

Comparing the influence of immersed tubes, no significant difference was observed between different tube arrangements and geometries, though it can be seen a slight difference between the dense and sparse tube geometries. Noticeable difference was between the freely bubbling bed and beds with immersed tubes. In this regard both the experimental measurements and numerical simulations showed opposite trends as can be clearly seen for the smaller particle in Figure 7.2. Experimental measurements showed that the bed expansion decreased when horizontal tubes are inserted while simulations showed the other way round. For the experiments, the slight decrease in bed expansion for beds with horizontal tubes is due to the reduction in bubble size as a result of bubble splitting at the tube rows. Thus, smaller bubbles means lower bubble holdup (volume occupied by bubbles) which resulted in lower bed expansion. There are also inconsistent reports from previous researchers in this regard. Glicksman et al. (1991), Wiman and Almstedt (1997) for example reported that tubes in the bed resulted in an increased bed expansion and the greater the number of tubes in the bed, the larger the bed expansion. On the other hand Olsson et al. (1995) observed no significant difference in bed expansion between different tube banks at least at atmospheric pressure.

7.1.3 Bubble properties

In fluidized beds without internal obstacles, coalescence dominates bubble growth. Therefore, it is generally believed that bubbles grow continuously with height above the distributor. Since the rise velocity is proportional to the bubble size, it will increase with bed height as well. On the other hand, for beds with immersed obstacles, the bubbling behavior is quite different from that of fluidized beds without obstacles. In this work, both experimental measurements and simulation results showed that immersed horizontal tubes strongly alter the bubble characteristics such as shape, size and rise velocity. It was observed that tubes increased the rate of bubble splitting. Small bubbles were usually formed at the bottom of the bed. They rose and grew by coalescence

until they reached the first row of the tubes, which then split and further grew by coalescence until they reach the next row of tubes. This continued until the last row of tubes after which large bubbles were formed up to they finally erupted at the surface of the bed. In general, this mechanism was seen to reduce the mean bubble properties such as diameter and rise velocity in the vicinity of the tube bank. Moreover, the shape of the bubbles in the tube bank region is not similar to that of the tube free region. Detail experimental measurements and simulation results of bubble properties for different bed geometries and tube arrangements are discussed below.

7.1.3.1 Bubble shape

Aspect ratio and shape factor are important characteristics of a bubble since they strongly influence the bubble's hydrodynamics. They provide an approximate bubble shape (circularity in 2D). Figure 7.3 and Figure 7.4 show the time-averaged bubble aspect ratios and shape factors respectively for different tube bank geometries from experimental measurements and simulations. For beds without immersed tubes (NT), both the experiment and simulation showed continuous increase of the time-averaged bubble aspect ratio and continuous decrease of the time-averaged bubble shape factor with bed height. This indicates the flattening and vertical stretching of bubbles with increasing bed height. Such vertical elongation of bubbles is mainly due to wall effects and interaction with other bubbles. Comparing the aspect ratio of the NT bed between the simulation prediction and experimental measurement, the wall effect can be clearly seen. During experiment, the bubbles were also influenced by the front and back walls which were absent in the 2D simulation. Thus, the bubbles were stretched in all four directions, which gave rise to lower aspect ratio hence more rounded bubbles. This phenomenon can be also observed in the case of 3D simulations as described in section 6.4. Except at the lower part of the tubes, the aspect ratio is slightly higher than unity for all cases studied, which gave the bubbles a 'kidney' type shape. This indicated that bubbles usually stretched in the direction of their motion. Bubbles elongate vertical more with increasing superficial velocity and this can be clearly seen in Figure 7.5 and Figure 7.6, where the aspect ratio increased and the shape factor decreased with increasing superficial velocity. Therefore, it can be concluded that, for beds without internal obstacles, the bubble shape was nearly circular when the bubble is smaller and flattened, distorted and elongated when the bubble is bigger. Others have also reported similar results (Hatano et al. 1986; Glicksman et al., 1987; Pain et al., 2001b). Hatano et al. (1986) explained that due to higher interaction and an increased coalescence index the number of elongated or distorted bubbles increased with increasing superficial velocity.

In the case of beds with internal obstacles, the aspect ratio and shape factor were found to be strongly dependent on tube geometry rather than bed height. In the tube bank region an alternating rise and fall of the aspect ratio as well as the shape factor were observed. The higher aspect ratios were attained at tube rows while the lowest aspect ratios were attained between the tube rows. These two points corresponds to the lowest and height values of the bubble shape factors respectively. Thus, it can be concluded that bubbles elongated vertically when they passed be-

tween tubes in a row but retained their original shape and became relatively circular when they moved away from the tube rows.

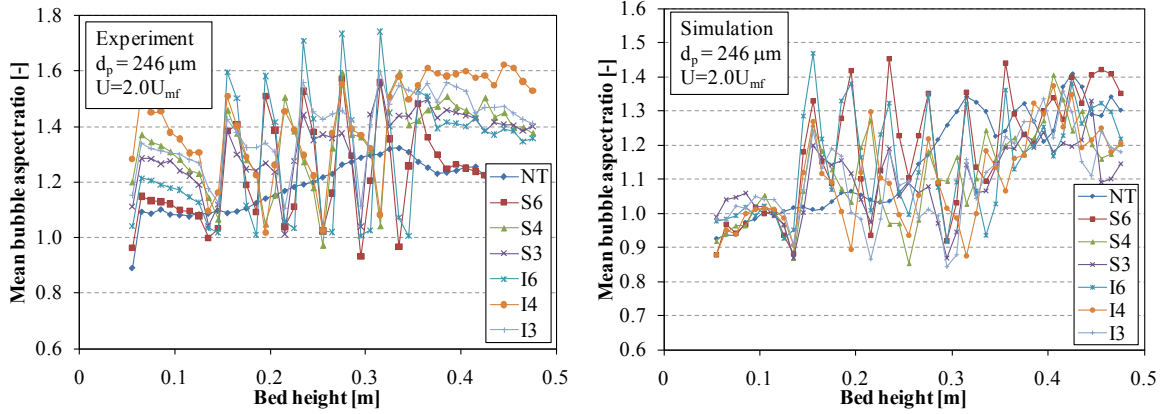


Figure 7.3: Comparison of the mean bubble aspect ratio for different tube bank geometries and arrangements; $d_p=246 \mu\text{m}$, $U=2.0U_{mf}$.

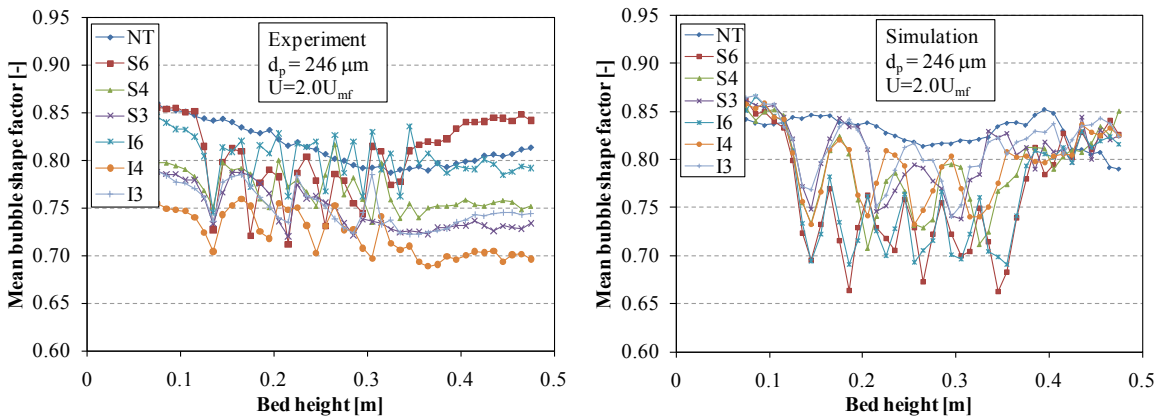


Figure 7.4: Comparison of the mean bubble shape factor for different tube bank geometries and arrangements; $d_p=246 \mu\text{m}$, $U=2.0U_{mf}$.

The elongation of bubbles in the vertical direction could be associated to two possible mechanisms of bubble motion observed. The first mechanism occurred when the horizontal extreme (d_x) of a bubble is greater than the horizontal separation between two tubes in a row. In this case the bubble squeezed or deformed as it passed between the tubes due to the decrease in the area of passage. This resulted in increased vertical extreme (d_y) as the area of the bubble has to be conserved, provided that no splitting or coalescence is taking place during the process. The second mechanism was the stretching of a bubble as it moved over the surface of the tubes. This phenomenon was observed regardless the size of a bubble. When a bubble moved over the surface of a tube, it stretched vertically due to the velocity difference between the bubble surface in contact with the tube and the rest. The surface of the bubble, which was in contact with the

tubes, had lower velocity as compared to the rest part of the bubble. Hence the relative velocity resulted from this velocity difference stretched the bubble in its direction. The reason for the lower velocity of the bubble surface in contact with the tubes could be the friction between the tube surface and the bubble. However, extensive experimental investigations are necessary to verify this conclusion. Below and above the tube bank region the bubble aspect ratio and shape factor show similar trend as in the case of the NT bed.

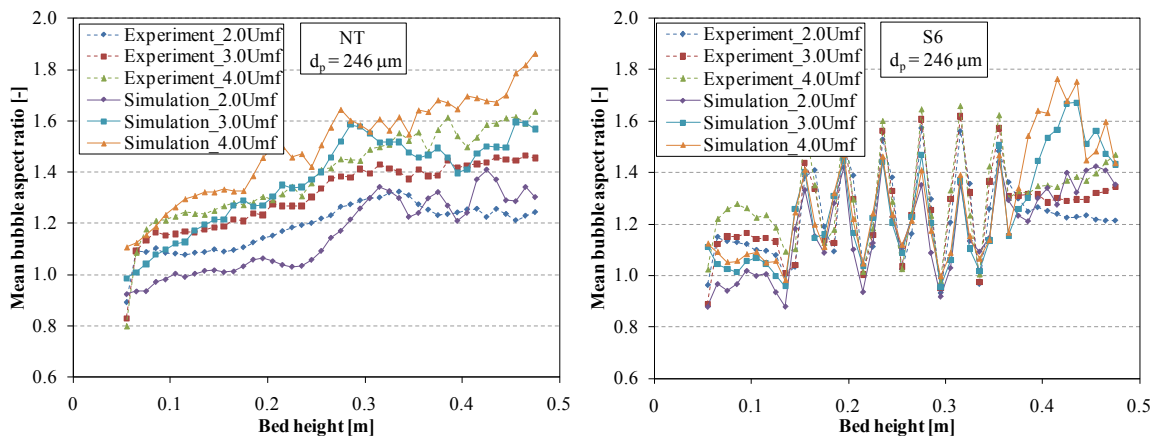


Figure 7.5: Influence of gas superficial velocity on the mean bubble aspect ratio for beds with and without immersed tubes; $d_p=246 \mu\text{m}$.

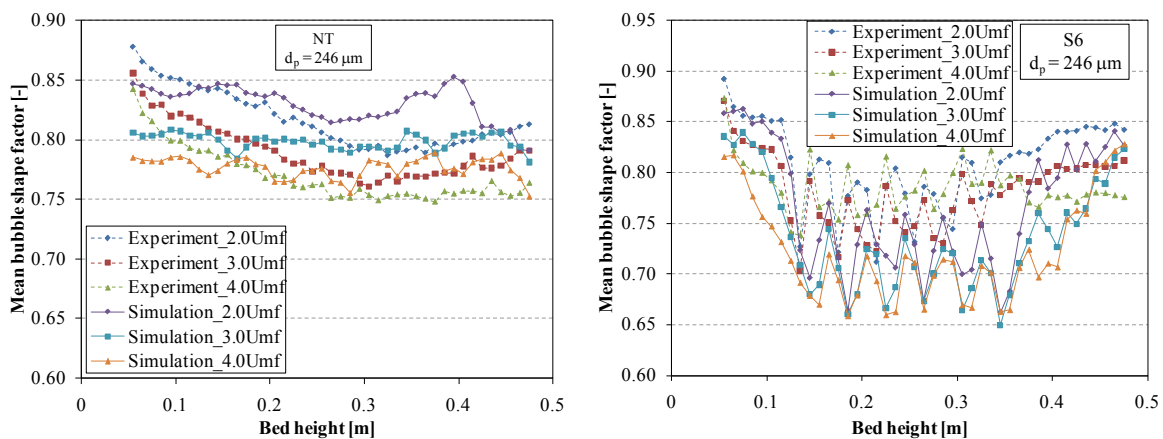


Figure 7.6: Influence of gas superficial velocity on the mean bubble shape factor for beds with and without immersed tubes; $d_p=246 \mu\text{m}$.

Figure 7.7 and Figure 7.8 illustrate comparison between the different tube packing density for both the staggered and in-line arrangements. From the figures, it can be seen that higher bubble shape fluctuation was seen with more dense tubes than the sparse tubes. For dense tube arrangements (i.e., S6 and I6), higher aspect ratio and lower shape factor were observed between the tubes in a row as well as between the rows. This indicated that bubbles were longer in the tube bank region than the corresponding bubbles in the case of S4, I4, S3 and I3 beds. As the

number of tubes decreased, both the vertical and horizontal spacing of the tubes increased which gave larger flow area for the bubbles. Therefore, the bubbles moved without much deformation. On the other hand, as the tube bank is getting denser then the space for the passage of bubble is getting smaller. Thus, bubbles squeezed and elongated more as they passed the tube rows.

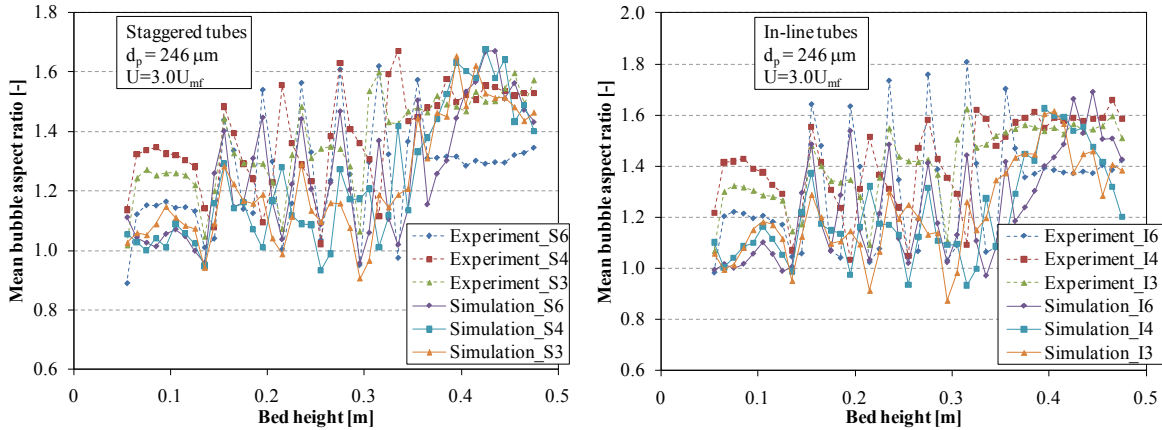


Figure 7.7: Influence of tube packing density on the mean bubble aspect ratio for the staggered and in-line tube arrangements; $d_p=246 \mu\text{m}$, $U=3.0U_{mf}$.

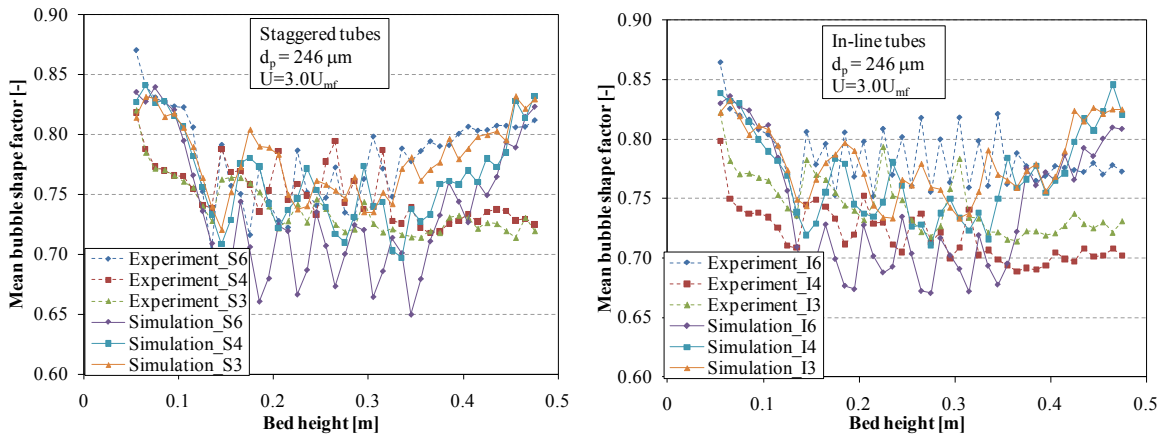


Figure 7.8: Influence of the tube packing density on the mean bubble shape factor for the staggered and in-line tube arrangements; $d_p=246 \mu\text{m}$, $U=3.0U_{mf}$.

To investigate the influence of tube bank arrangement, Figure 7.9 and Figure 7.10 show the time-averaged bubble aspect ratio and shape factor for NT, S6 and I6 beds. The simulation predicted no major differences between staggered and in-line arrangement, whereas the experimental data showed slightly higher aspect ratios for the in-line case at a tube row. Besides this, the simulation showed good agreement with experiment.

In summary, the simulation agreed reasonably well with the experimental measurements in predicting the mean bubble aspect ratio and shaper factor for both beds with and without immersed

tubes at least for Geldart's group B particles. The simulation predicted lower aspect ratio and higher shape factor at the lower part of the bed and lower superficial velocities while it predicted higher aspect ratio for higher superficial velocity and upper part of the bed. This shows that the bubble is more circular when it is smaller and more stretched and distorted when it is bigger. This could be associated with the wall effect discussed in section 6.4. In the tube bank region of the beds, the bubble shape was found to be independent of superficial velocity and particle size.

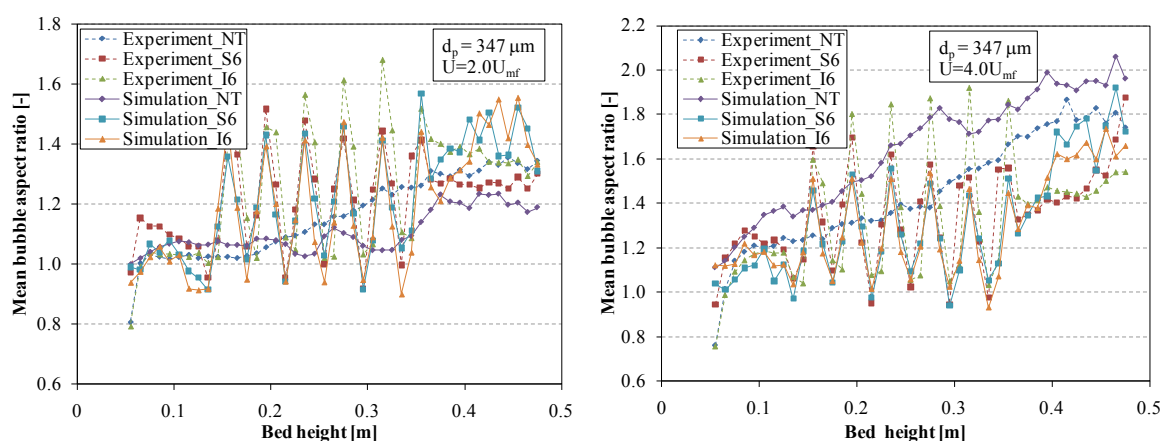


Figure 7.9: Comparison of the mean bubble aspect ratio for the different tube bank arrangements; $d_p=347 \mu\text{m}$, left- $U=2.0U_{mf}$, right- $U=4.0U_{mf}$.

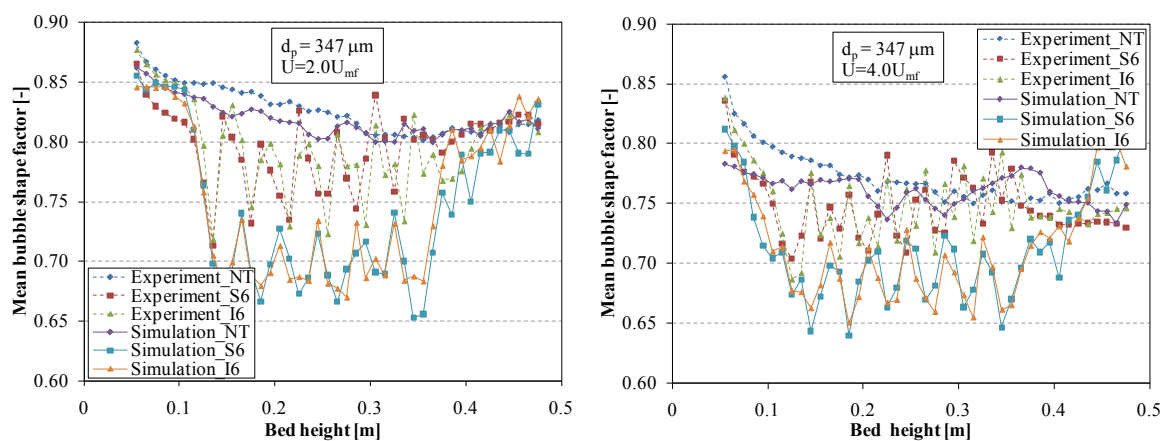


Figure 7.10: Comparison of the mean bubble shape factor for different tube bank arrangements; $d_p=347 \mu\text{m}$, left- $U=2.0U_{mf}$, right- $U=4.0U_{mf}$.

7.1.3.2 Bubble diameter

Bubble size is one of the most important characteristics in determining the hydrodynamics and performance of bubbling fluidized bed reactors. Generally, for beds without internal obstacles, bubble size increases with bed height, particle size and superficial velocity. As bubbles formed

near the distributor and rose in bubbling fluidized beds, they grew due to coalescence and split due to instabilities at the bubble boundary.

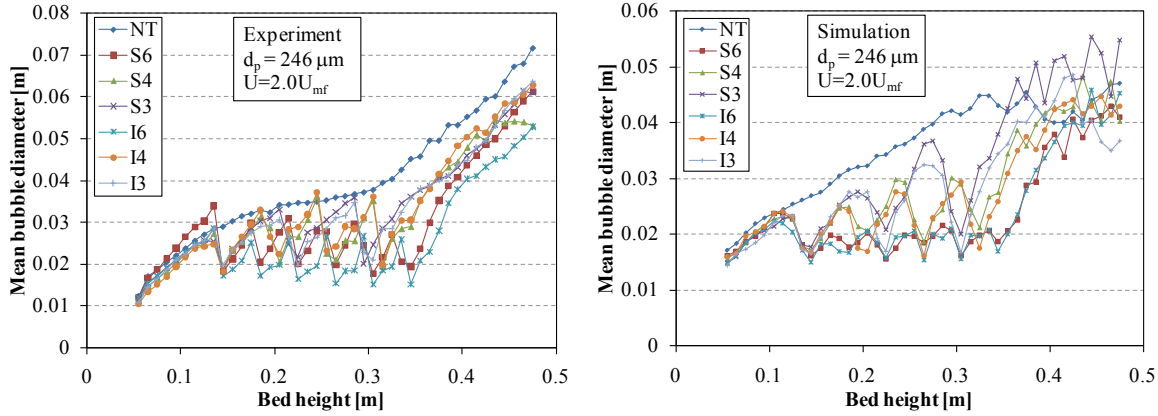


Figure 7.11: Comparison of the mean bubble diameter for different tube bank geometries and arrangements; $d_p=246 \mu\text{m}$, $U=2.0U_{mf}$.

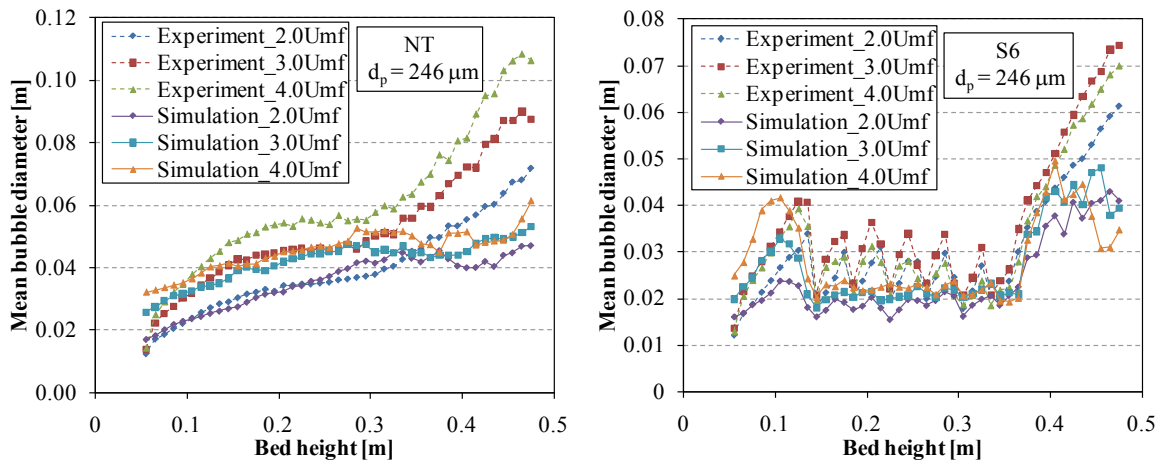


Figure 7.12: Influence of gas superficial velocity on the mean bubble diameter for beds with and without immersed tubes; $d_p=246 \mu\text{m}$.

In freely bubbling bed (NT) coalescence dominates bubble splitting thus bubbles continuously grow with bed height. As shown in Figure 7.11 and Figure 7.12, both experimental measurements and simulation results showed this well established theory of bubble growth in a freely bubbling bed. As explained in Chapter 5, the experimental measurements showed some plateaus and inflections somewhere at mid-way of the bed height. Both the experimental measurements and simulation predictions are in general in reasonable agreement. The discrepancy arises for bigger particles and/or higher superficial velocities where the simulation underestimated the bubble diameter at higher bed heights. This can be clearly seen in Figure 7.13 at superficial velocity of $4.0U_{mf}$ and additional results can be found in Appendix D. In these cases, the simulation predicted no growth of bubbles while experimental measurements showed continuous

growth until the eruption zone. This could be partially attributed to the fluidization regime change and was explained in detail in section 7.2. Apart from this, the TFM is able to reasonably predict bubble growth in a freely bubbling bed for Geldart's group B powders.

For beds with internal obstacles, the presence of immersed horizontal tubes was found to alter the general trends for bubble growth observed in the NT, Figure 7.11 to Figure 7.13. Tubes appear to limit the size of bubbles. The main reasons for the reduction of bubble size in the tube bank region are bubble breakup and local bubble formation at the lower side of the tubes. Generally, for beds with immersed tubes, two different regions can be identified depending on the bubble growth phenomena observed.

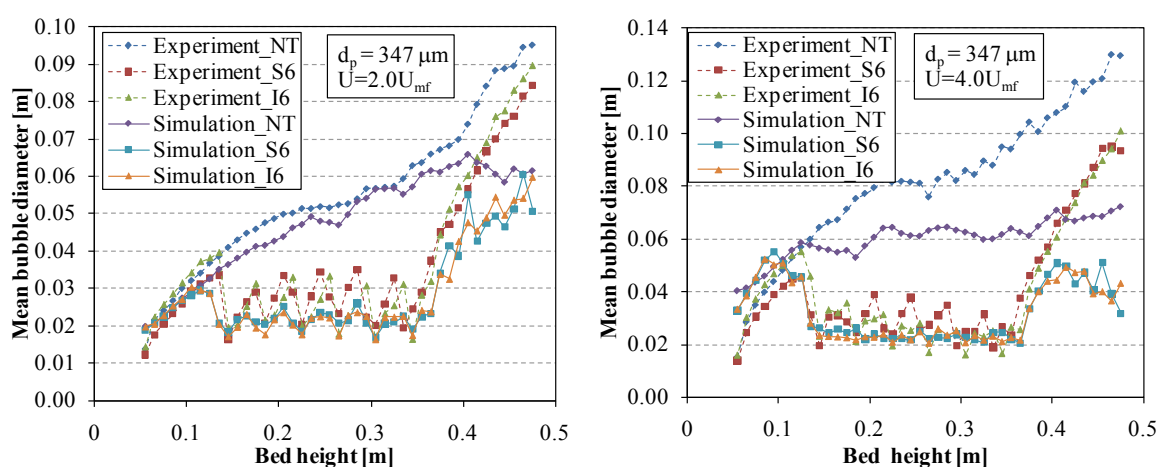


Figure 7.13: Comparison of the mean bubble diameter for different tube bank arrangements; $d_p=347 \mu\text{m}$, left- $U=2.0U_{mf}$, right- $U=4.0U_{mf}$.

The first is the region below and above the tube bank. In this tube free region, bubble growth resembled the case of the bed without immersed tubes (NT), where continuous growth of bubbles was observed. The second region is the tube bank region. In this region the growth of bubbles is characterized by an alternating increase and decrease of bubble diameter that led to a characteristic zig-zag-pattern with its lowest value at the lower half of the tubes equator and its highest value between the two rows (when the bubble leaves the tube row). Immersed horizontal tubes increase the rate of bubble breakup and coalescence thus prevents the formation of rapidly growing bubbles. As a result, the motion and behavior of a bubble upon reaching a horizontal tube is found to be very complex and no uniformity was observed. From visual observation and examination of both the experimental and simulation bubble images, the interaction between bubbles and the tubes can be summarized as follows.

As a bubble approached the bottom of the tube, it begins to flatten and 'wraps' the bottom of the tube. The bubble then moves around the tube and leaves the tube surface at some point above the horizontal. If the bubble is bigger compared to the tube diameter and approaches the tube along its nose, the bubble usually splits into two. If the bubble split into two equivalent daughter

bubbles, they rise up in opposite sides of the tube or recombine above the tube. Sometimes if the bubble is very large it may envelope the tube completely and coalescence starts at the top of the tube before the bubble completes its splitting. If the horizontal extreme of a bubble is greater than twice the pitch size in a row, the bubble may split into three or more daughter bubbles. In another case, if the bubble split into a bigger and smaller, the bigger bubble rise faster over the tube and wraps the tube on side until the top of the tube that pushes the stagnate particles on the top of the tube which results on the raining of the particle to the other bubble and the smaller bubble bursts. On the other hand, large bubbles, which are not destined to the hit the tube directly, tend to distort as they pass the tube while small bubbles usually swerve around the tube.

The second phenomenon that caused smaller mean bubble diameter at the lower side of the tube rows is the presence of local fluidization. It was observed that the regions beneath and adjacent the horizontal tubes are effectively devoid of solid particles while the upper part of the tubes is usually covered with semi-stagnant particles which are periodically replaced with new particles. From the experiments, it was even observed that at velocities lower than the minimum fluidization velocity ($U < U_{mf}$) gas voids at the lower part of the tubes were observed which act as a nucleation sites for bubbles. However, these bubbles were seen to reabsorb in the bed before they reached the freeboard. At gas superficial velocities higher than U_{mf} , both experimental measurements and simulations showed that the lower part of the tubes was usually covered with gas pockets of very low solid concentrations, which eventually led to periodic detachment of bubbles at the equator of the tubes. This resulted in a significant change of the bubble hydrodynamics around the tube bank region. With increasing gas velocity, the bubble frequency at this location also increased. Similar results were also reported by other investigators; e.g., Glass and Harrison, (1964), Loew et al. (1979), Sintai and Whitehead (1985), Bouillard et al. (1989), Pain et al. (2001b), Kim et al. (2003), Schmidt and Renz (2005). However, the mechanism or source of these gas voids or bubbles is not agreeably reported. Sintai and Whitehead (1985) associated the phenomenon as a result of an increase in the vertical component of the gas velocity around the obstacles which eventually leads to local fluidization around the obstacles while Rafailidis et al. (1992) reported this to be due to a decrease in vertical component of the gas velocity. In this work, at least the simulation results showed that the gas velocity was lower at the bottom of the tubes. Rafailidis et al. (1992) explained that particle-free layer act as a low resistance gas path; so that the edge of the layer can be treated to a first approximation as a constant pressure gas surface and gas is drawn towards the tube to form the streams of bubbles which emerge at the sides. Detail discussion on the interaction of a single bubble with a horizontal tube can be found elsewhere in the literature (Clift and Rafailidis, 1993).

The influence of the tubes on bubble breakup and local bubbling can be best seen with the help of the bubble frequency plots shown in Figure 7.14. The figure shows the bubbling frequency as a function of bed height above the distributor. The bubbling frequency is defined here as the total number of bubbles detected per second in a given section of the bed. In the figure large number of bubbles appeared at the lower part of the bed, which shows the formation of small

bubbles at the distributor. The simulation predicted this satisfactorily, though it showed higher bubbling frequency for the lower superficial velocity. For the NT bed, the bubbling frequency continuously decreased with height. Since bubble frequency is proportional to coalescence rate, the results of the NT case confirmed that bubble coalescence dominated than splitting. In this, regard both experiments and simulations showed good agreement. On the other hand, in the tube bank region, bubble splitting dominates as bubbles passed a tube row, which is reflected by the higher bubble frequency, and bubble coalescence dominates as bubbles moved away from the tube row in which the bubble frequency decreased. This give rise to a zig-zag pattern of the mean bubble frequency as a function of bed height. The increased in bubble frequency as bubbles passed a tube row is due to the combined effect of bubble splitting and local bubble formation. Once these bubbles moved away from the tube row they coalesced quickly that led to a drop in the bubbling frequency only until the next row. After the last row, the bubbles coalesced rapidly to form few but large bubbles, which is characterized by the sharp drop in the bubble frequency, Figure 7.14. In the tube bank region, the simulation overestimated the bubbling frequency for the lower superficial velocity ($2.0U_{mf}$) while very good agreement was achieved at higher superficial velocity ($4.0U_{mf}$). Comparing the dense (e.g. S6) and the sparse (S3) tube geometries it can be clearly seen that the bubble frequency is higher in the S6 case than the S3. This is due to higher rate of bubble splitting as well as higher local bubble formation in the S6 case as the result of more horizontal tubes. Both experiment and simulation showed no major difference of bubble frequency for the staggered and in-line tube arrangement. Generally, bubble frequency decreased with increasing height and increased with increasing superficial velocity.

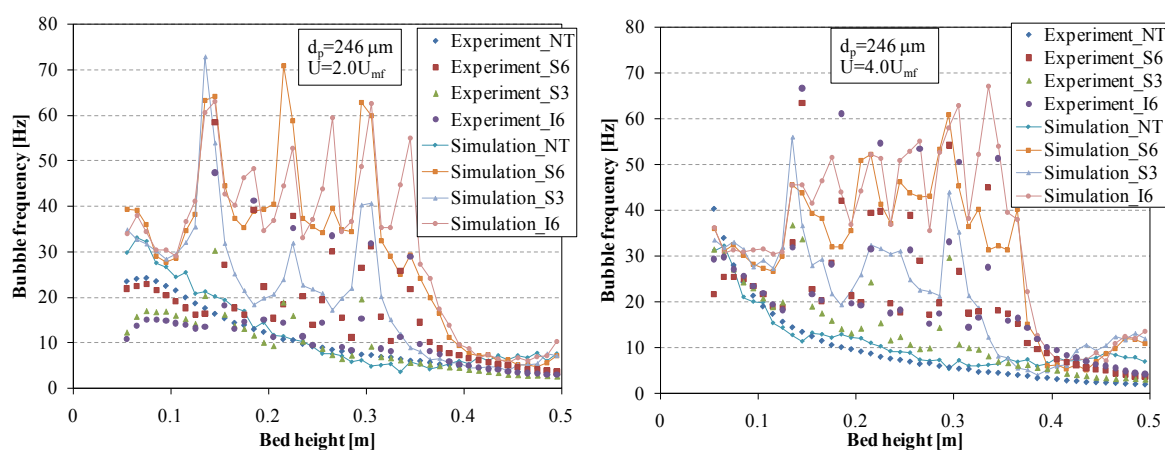


Figure 7.14: Bubble frequency as a function of bed height; $d_p=246 \mu\text{m}$, $U=4.0U_{mf}$.

Furthermore, the influence of superficial velocity was investigated. As shown in Figure 7.12, for the NT bed the bubble size as expected increased with increasing superficial velocity. On the other hand, for the dense tube banks (S6 and I6) both the experiment and simulation showed relatively constant bubble size in the tube bank region, which is nearly equal to the horizontal separation of the tubes in a row. Hence, the mean bubble diameter hardly varies with the superficial velocity. This is consistent with the finding of Glicksman et al. (1987) who concluded that

bubble grow to 1-1.5 times the tube pitch and do not change appreciably with increase in the superficial velocity. Comparing the different tube bank density it can be seen that the more the packing density the higher the bubble splitting and local bubble formation. This led to lower mean bubble diameter. For relatively sparse tube banks, (S3 and I3) bubbles were observed to grow larger between the rows of tubes as there is space until the next row of tubes. This can be clearly seen in Figure 7.15. Therefore, more tubes means higher frequency of bubble splitting, which resulted in lower mean bubble diameter. As the number of tubes is getting fewer, their influence on the bubble growth is getting minimal. This was reported by Olowson (1994) who observed no major difference of bubble and bed characteristics between beds with very few tubes and freely bubbling bed. Regarding different tube arrangement no major difference between the in-line and staggered tube arrangements were observed, see Figure 7.13.

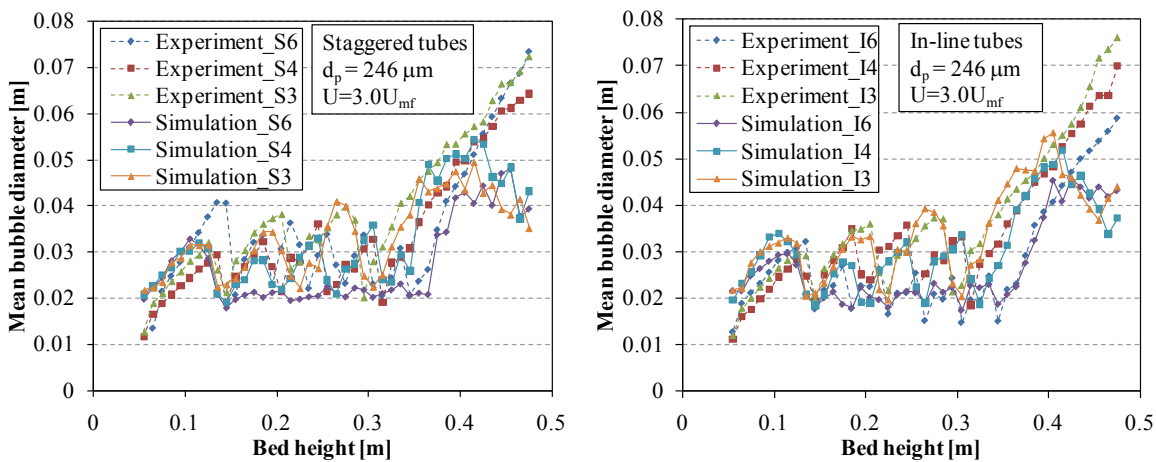


Figure 7.15: Influence of tube packing density on the mean bubble diameter for the staggered and in-line tube arrangements; $d_p=246 \mu\text{m}$, $U=3.0U_{mf}$.

In general, bubble growth in the tube bank region was mainly dictated by tube bank geometry (vertical and horizontal tube spacing) and was nearly independent of bed height and superficial velocity. As a result of frequent splitting and coalescence and local formation of bubbles, the mean bubble diameter in the tube bank region is much less than the mean bubble diameter in the freely bubbling bed for the same particle size and superficial velocity. Additional results are presented in Appendix D.

7.1.3.3 Bubble rise velocity

Small bubbles formed near the distributor rise up in the bed and tend to be drawn near the bed center by the mutual interaction of bubbles and the wall effect (Werther and Molerus, 1973b). This increased the bubble population in the center of the bed, which eventually increased bubble coalescence. This can be clearly seen from the time-averaged solids volume fraction contour of the simulation shown in Figure 7.16. For the NT case it can be seen that the center of the bed has lower solid volume fraction which indicated that higher bubble concentration while the side

walls are permanently covered with higher solid concentration flowing downwards. As a results bubbles coalesced fast to form large bubbles at the center of the bed. For freely bubbling beds, the rise velocity is proportional to bubble diameter, thus it increased with diameter and bed height. This was shown by both the experimental measurement and simulation results.

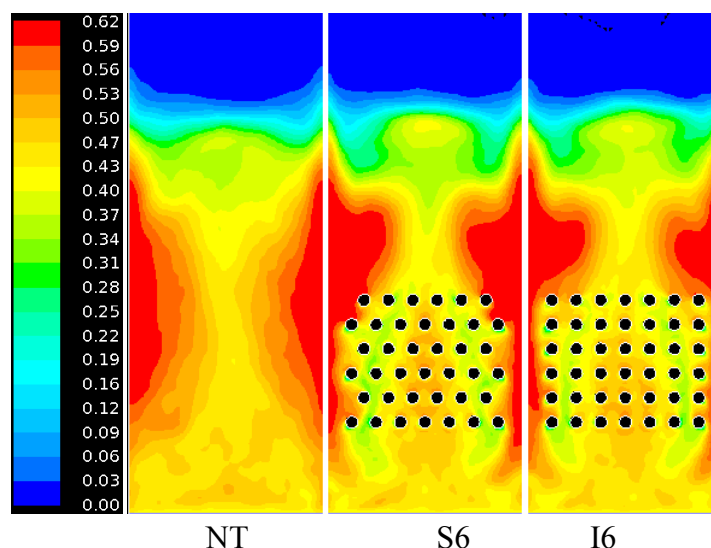


Figure 7.16: Time-averaged solid volume fraction of the NT, S6 and I6 tube geometries; $d_p=246 \mu\text{m}$ and $U=2.5U_{mf}$.

Figure 7.17 and Figure 7.18 illustrate the comparisons between mean bubble rise velocities for beds with and without immersed horizontal tubes. For beds with horizontal tube banks, two different regions can be identified. The first region is the area below and above the tube bank where bubble rise velocity increased with bed height. The second region is the tube bank region, where similar to bubble size the rise velocity is characterized by the zig-zag pattern with its lowest value at the lower half of the tubes equator and its highest value at the upper part of the tube row (when the bubble leaves the tube row). Qualitatively the simulation predicted similar trend compared with the experimental measurements. However, it highly overestimated the rise velocity especially for the NT case and the tube free regions of the beds with tubes. As discussed in section 4.1 this is caused by the missing wall effects in the 2D simulation and wide particle size distribution in experiments. The particles are assumed monodispersed, smooth and spherical in the simulation but the particles in the experiment are polydispersed and it is possible that the particles became less spherical with extensive fluidization because of attrition. If these had been included in the simulation, which is not possible in the TFM, it would have increased the drag on the particles hence slower the bubbles. Inside the tube bank region the simulation showed good agreement with the experimental results. This showed that the relationship between bubble size and rise velocity in the tube bank region is not the same with that of tube free region. From Figure 7.17 especially from the experimental measurements, it can be clearly seen that though the bubble diameter is smaller than the corresponding NT case, the rise velocity is higher than

the corresponding value for the NT bed. Thus for the same bubble diameter the rise velocity is higher in the tube bank region than the tube free region or in the NT case. Therefore, in the tube bank region bubble rise velocity depends not only on the bubble size but also on tube bank.

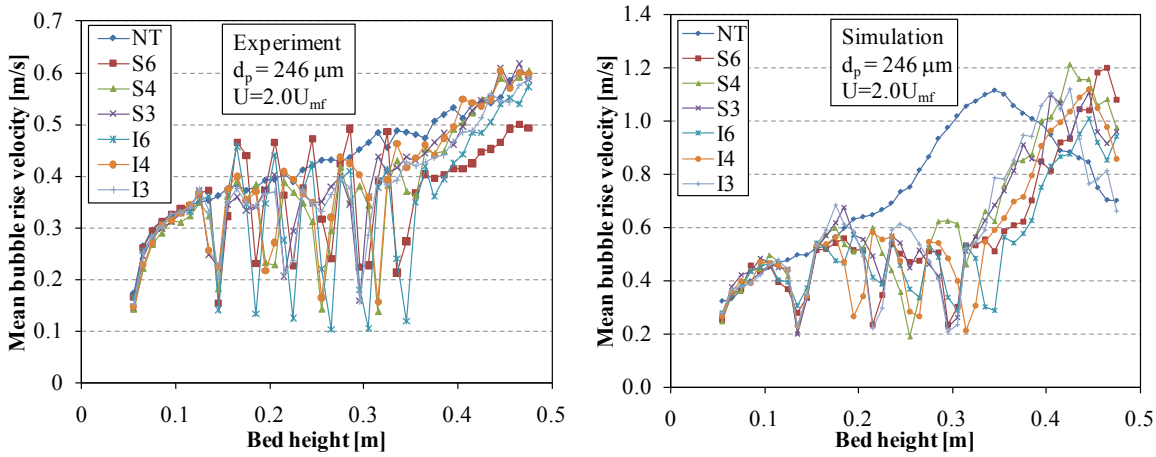


Figure 7.17: Comparison of the mean bubble rise velocity for different tube bank geometries and arrangements; $d_p=246 \mu\text{m}$, $U=2.0U_{mf}$.

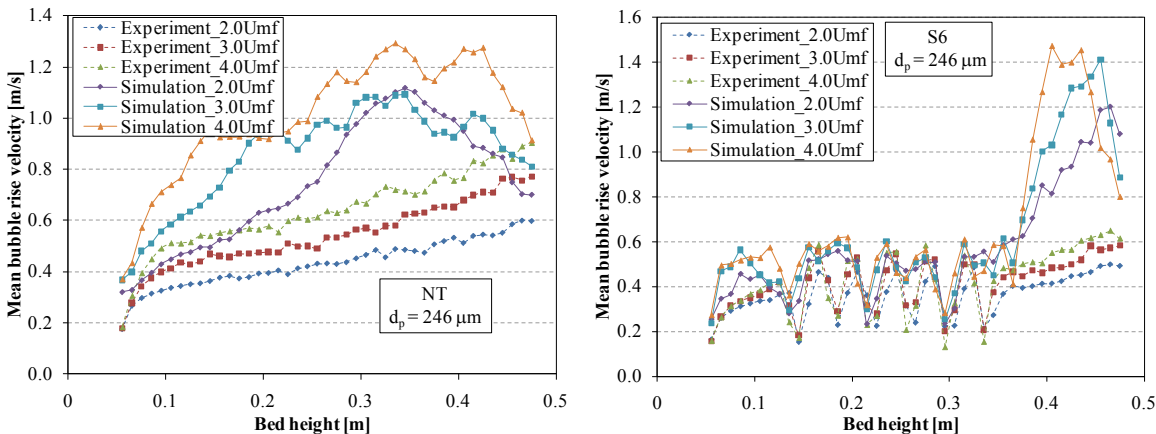


Figure 7.18: Influence of gas superficial velocity on the mean bubble rise velocity for beds with and without immersed tubes; $d_p=246 \mu\text{m}$.

The higher rise velocity was predicted at the upper part of the tube rows as bubbles leave the row. This can be primarily attributed to the elongation of bubbles. As explained in section 7.1.3.1, bubbles elongate vertically as they move through the rows. As a result of the elongation of the bubbles and stretching between the tubes the centroid of the bubbles moved longer distance than it would if it were circular. This caused the centroid of the bubbles to move longer vertically than they usually do. This can also be explained in terms of bubble aspect ratio. Examining the locations of the maxima and minima of the bubble aspect ratio and rise velocity it can be concluded that the higher the aspect ratio the higher the rise velocity and vice-versa. Hatano et al. (1986) have thoroughly analyzed such a relationship for fluidized beds without internals.

They concluded that bubble aspect ratio has a significant influence on bubble velocity and bubbles were classified accordingly into three different types, namely, spherical cap, elongated or accelerated and slug. They reported that the rising velocity coefficient φ in Equation 5.36 had a lower value for the spherical cap and was higher for those that were elongated; e.g., an aspect ratio of 1 gave a rising coefficient of 0.71 and an aspect ratio of 1.5 gave a rising coefficient of 1.7. This was also later supported by Lim et al. (1992). Grace and Harrison (1967) observed from experiments in 2D beds that elliptical-cap and ovary ellipsoidal bubbles rise faster than the corresponding circular-cap and spherical-cap bubbles.

Another reason for the higher rise velocity is the higher coalescence rate occurred when the bubble leave the tube row. When two bubbles are in close proximity during coalescence, the trailing bubble has a substantial increase in rise velocity (Glicksman et al., 1987). Clift and Grace (1985) explained that when two bubbles are centered on a common vertical line rise vertically, the lower bubble accelerates under the influence of the leader so that coalescence occurs when the trailing bubble catch-up the leading bubble. For bubbles not in vertical alignment, the trailing bubble moves towards the lines of rise of the leading bubble, subsequently accelerating vertically to enter the its wake so that coalescence occurred. As shown in Figure 7.16 it is apparent that the bubble flow between rows was mainly concentrated in the spaces between adjacent tubes in a row. Therefore, the presence of tubes reduces the flow cross-sectional area for bubbles, consequently increased bubble-bubble interactions and hence higher coalescence can be expected with the tube bank than if no tubes were present. Yates et al. (1990) and Hull et al. (1999) reported similar results of bubble behavior from experimental measurements.

The reason for the lower mean bubble rise velocity at the lower half of the tubes can be attributed to the hindrance of the tubes to the flow of bubbles and the presence of small semi-stagnant bubbles. It was observed that bubbles slowed down as they approached the tubes. In addition, smaller bubbles were appeared to be semi-stagnant. These small bubbles were the result of the local bubble formation as explained above and bubble splitting into large and small daughters. These small bubbles usually adhere to the tube until they encounter and coalescence with the incoming bubble from below. Sometimes these bubbles were seen to slide along the tube surface and detached when they reached the tube horizontal axis (equator). It was also observed that these bubbles grew by absorbing gas from the emulsion phase without moving which gave a negative displacement of their centroid hence negative rise velocity. This was found to have significant influence on the mean rise velocity of the bubbles.

Figure 7.18 shows the time-averaged bubble rise velocity for different superficial gas velocities. Similar to the bubble diameter, the rise velocity increased with increasing in superficial velocity for the NT case. This is a well-established theory and the simulation showed good qualitative prediction. For beds with dense horizontal tubes (e.g. S6), on the other hand the mean bubble rise velocity was found to be independent of the gas superficial velocity in the tube bank region. This is consistent with the results of the bubble size in section 7.1.3.2 as size and rise

velocity are coupled in a freely bubbling fluidized beds. The simulation results are in good agreement with the experiment in this case. Similar to the NT case larger discrepancies were again mainly seen outside the tube bank region.

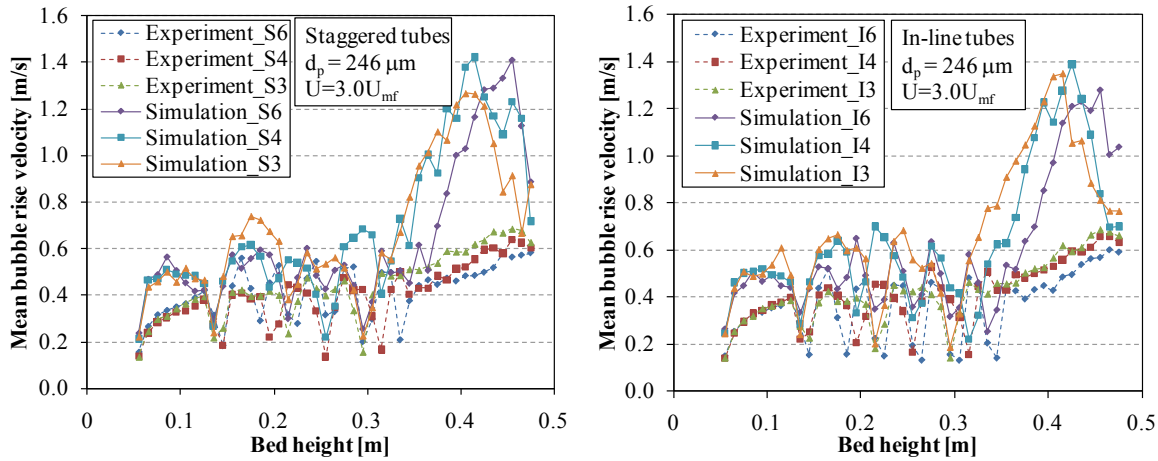


Figure 7.19: Influence of tube packing density on the mean bubble rise velocity for the staggered and in-line tube arrangements; $d_p=246 \mu\text{m}$, $U=3.0U_{mf}$.

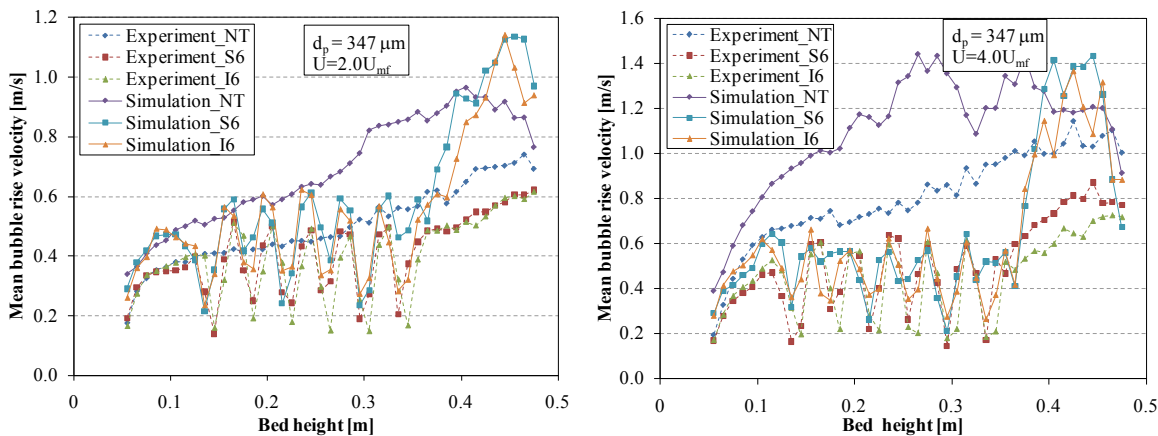


Figure 7.20: Companion of the mean bubble rise velocity for different tube bank arrangements; $d_p=347 \mu\text{m}$, left- $U=2.0U_{mf}$, right- $U=4.0U_{mf}$.

Figure 7.19 shows the influence of the tube packing density on the mean bubble rise velocity. No significant difference was observed between the different tube geometries for both the staggered and in-line cases. This is in contrary to the bubble diameter where bubbles were observed to grow more for the sparse tube geometry than the dense ones. Regarding the tube arrangements, no major difference were observed between staggered and in-line, Figure 7.20. In general, in the tube bank regions of the fluidized beds with immersed tubes bubble the rise velocity is strongly influenced by the presence of tubes. It was found that for Geldart's group B particles the mean rise velocity was almost independent of superficial velocity and tube arrangement.

7.2 Influence of Mean Particle Sizes

7.2.1 Pressure drop

The time-averaged static pressure drop from experimental measurements and simulation predictions are summarized in Table 7.3 below for different mean particle sizes and superficial velocities. As shown in previous results experimental measurement showed an increase in static pressure drop with increasing particle size and superficial velocity. This was mainly attributed to the particle size distribution and was discussed in section 7.1.1 above.

Table 7.3: Time-averaged static bed pressure drop for different mean particle sizes in kPa.

Tube Geometry	Superficial velocity	Experiment Sizes in μm						Simulation Sizes in μm				
		141	246	347	439	592	776	141	246	347	439	592
NT	$2U_{mf}$	6.38	6.48	6.88	6.96	7.29	7.17	7.28	7.51	7.35	7.53	7.51
	$3U_{mf}$	6.42	6.70	7.02	7.11	7.11	5.93	7.27	7.47	7.31	7.41	6.08
	$4U_{mf}$	6.41	6.88	6.97	6.98	7.05	-	7.25	7.44	7.25	5.06	4.78
S6	$2U_{mf}$	6.46	6.64	6.77	7.10	7.09	6.87	7.35	7.50	7.41	7.55	7.51
	$3U_{mf}$	6.49	6.77	6.77	7.04	6.86	6.70	7.38	7.50	7.38	7.55	7.47
	$4U_{mf}$	6.58	6.79	6.76	6.94	6.72	-	7.48	7.50	7.36	7.49	7.24

The simulation predicted almost the same pressure drop regardless of the particle size and superficial velocity with the exception at higher superficial velocities for the bigger particles. As can be seen from Table 7.3, for particles with mean particle size of 439 μm and 592 μm at superficial velocities greater than $3U_{mf}$, the static bed pressure drop drastically decreased. Such unexpected results were seen also for the bed expansion and bubble properties. It was found that the simulation predicted different flow regime at higher superficial velocities. In fact, similar trend can be seen from the experimental measurements as well. For example for the particle size of 592 μm , the mean static bed pressure drop decreased from 7.29 kPa at $2U_{mf}$ to 7.05 kPa when the superficial velocity is increased to $4U_{mf}$. For the particle with mean size of 776 μm , the static pressure drop decreased from 7.17 kPa to 5.93 kPa as the superficial velocity increased from $2U_{mf}$ to $3U_{mf}$. This is in contrary to the fact that the static bed pressure drop should remain constant once the particles are fluidized as discussed in Chapter 5. It should be noted that experiments with superficial velocities higher than $3U_{mf}$ for the particle with mean size of 776 μm and higher than $4U_{mf}$ for the other two coarser particles were not possible due to the limitation of the experimental test rig. As a result, it not clear if increasing the superficial velocity beyond these

values could result in further decrease in pressure drop and bed expansion similar to the simulation. Nevertheless, from the trend it can be expected to happen at higher superficial velocities.

Figure 7.21 illustrates simulation results of the time-averaged static bed pressure drop profile as a function of bed height for two different particles. It can be seen that the static pressure drop is linear with bed height for all velocity ranges for the smaller particle as well as lower superficial velocity ($2U_{mf}$) for the bigger particle. This is consistent with the well-established theory that the static pressure drop decreases linearly with increasing bed height for fixed, homogenous and bubbling beds. For the coarser particles, the static pressure drop decreased and deviated from the linear relationship with bed height as the superficial velocity is increased to $3U_{mf}$ and became non-linear as the superficial is further increased to $4U_{mf}$. On the other hand, the experimental measurements showed this linear relationship for all particle sizes and superficial velocities within the investigated ranges. However, the fact that experimental measurements also showed somehow a decrease in static bed height, it can be confirmed that a fluidization regime change may have occurred. The difference between the simulation and experimental measurements is that the simulation predicted this regime change earlier than the experiments. A possible reason for this discrepancy is discussed below together with the bubble properties. Apart from this, the simulation predicted reasonably well the static bed pressure drop for the bubbling regime of Geldart's group B particles.

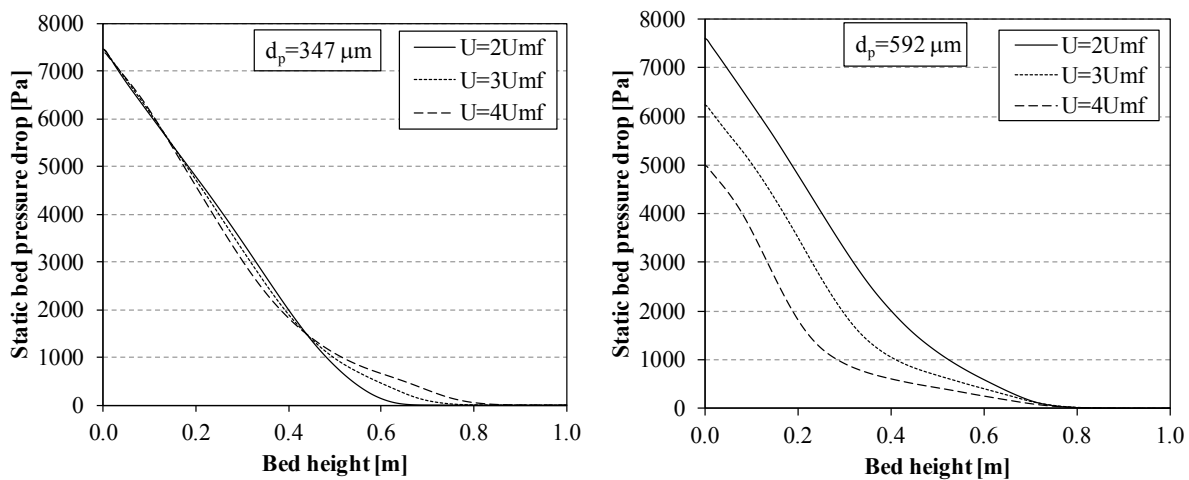


Figure 7.21: Static bed pressure drop profile predicted by numerical simulations.

7.2.2 Bed expansion

Comparison of the bed expansion ratio for different particles sizes are shown in Figure 7.22 and Figure 7.23 for the NT and S6 cases respectively. In General, though for comparable particle sizes the bed expansion ratio was nearly independent of the particle size, it can be concluded that the bed expansion increased with particle size at the same gas superficial velocity ratio (U/U_{mf}).

For example, experimental measurements showed that the bed expansion ratios of the particles with mean size of 246 μm and 346 μm are similar. The particles with mean size of 439 μm and 592 μm also showed similar expansion. These trends were also seen from the numerical simulations and were independent of the presence of tubes. For beds without immersed tubes, Wiman and Almstedt (1998) observed no significant influence of the particle size on the bed expansion ratio at the same excess gas velocity ($U-U_{mf}$) which is partly seen in this work as well. These authors concluded that at the same excess gas velocity, the bed exhibits similar hydrodynamic behavior for different particle sizes.

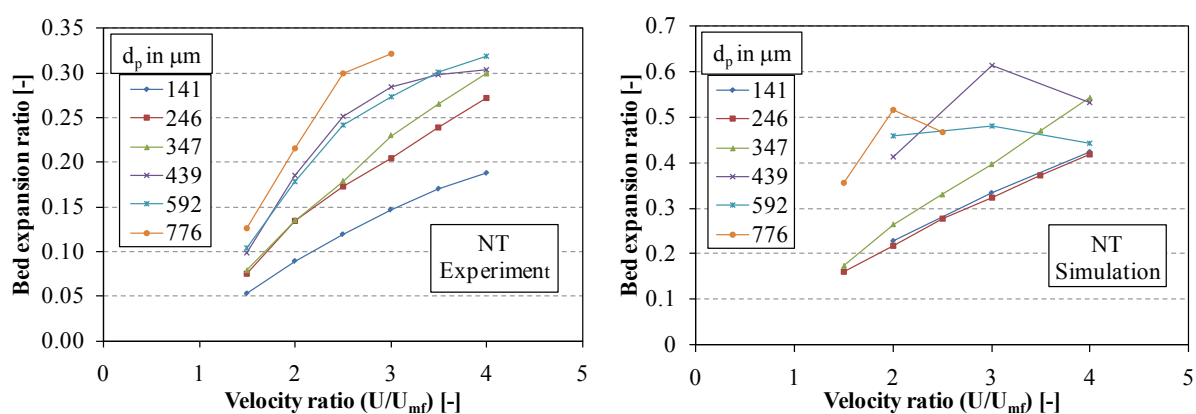


Figure 7.22: Bed expansion for different particle sizes and fluidized bed without tubes (NT); experimental measurement (left), numerical prediction (right).

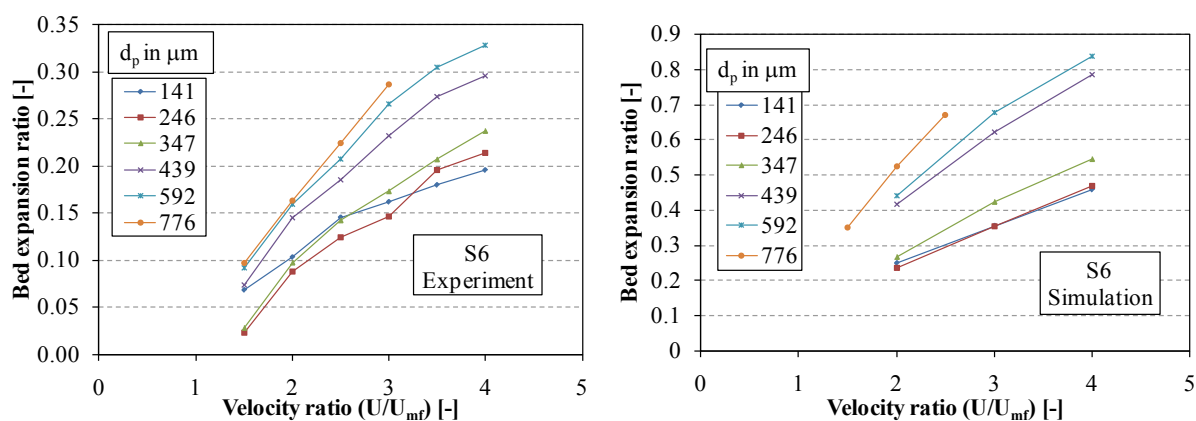


Figure 7.23: Bed expansion for different particle sizes and fluidized bed with dense staggered tubes (S6); experimental measurement (left), numerical prediction (right).

Qualitatively the simulation showed the well-known increase in the bed expansion with increasing in excess gas velocity, except for coarser particles at higher superficial velocities, which is discussed below. However, quantitatively it overestimated the bed expansion compared to the experimental measurements. The reason could be due to the particle size distribution and 2D simulations. The particles in the simulation were assumed monodispersed, smooth and spherical,

while the actual particles in the experiment are polydispersed and probably non-spherical due to intensive fluidization. Thus, the presence of fine particles in the experiment increases the interparticle friction such as cohesive forces. This resulted in higher resistance to expansion in the experiment. McKeen and Pugsley (2003) explained that due to the lack of the TFM to incorporate the prevailing cohesive force for Geldart's group A powders, it highly overestimated the bed expansion. Though the particles used in this work are all Geldart's group B and D whose cohesiveness is usually neglected, the presence of fines could raise the cohesiveness of the particle system. For the fines particle used in this work (141 μm) for example, the simulation predicted the same expansion as the particle with mean sizes of 246 μm while experimental measurements showed significant differences for the NT case. This can be associated to presence of cohesive forces due to the presence of fine particles as explained by McKeen and Pugsley (2003). For the S6 case the bed expansion ratio was higher for this particle than the NT case while the simulation predicted similar trend between the NT and S6. This is another proof for the presence of cohesive force. The presence of tubes helped to break the interparticle force and reduce the cohesiveness of the particles hence promoting smooth fluidization and higher bed expansion.

Previous researchers concluded that the bed expansion decreases with increasing particle size (Johnson et al., 1991; Al-Zahrani and Daous, 1996; Hepbasli, 1998). While others such as Glicksman and Yule (1991), Wiman and Almstedt (1998) concluded that particle size has a modest or no major influence on the bed expansion at the same excess gas velocity. The problem with the above researchers is that, they used the same excess gas velocity ($U-U_{mf}$) to compare the expansion for different particle sizes. Since the minimum fluidization velocity increased with particle size, the fluidization quality hence bubbling behavior of two particles with the same excess gas velocity is different and incomparable. As an example, let's consider the smallest (141 μm) and biggest (776 μm) particles used in this work with minimum fluidization velocity of 0.054 m/s and 0.467 m/s respectively and an excess gas velocity of 0.2 m/s. This gives a superficial velocity of 0.254 for the smallest particle size, which is greater than $4U_{mf}$. In this case, the bed was in vigorous bubbling regime with large bubbles and high bed expansion. On the other hand, the same excess gas velocity gives a superficial velocity of 0.667 m/s for the bigger particle, which is only less than $1.5U_{mf}$. In this case, the bed is slightly fluidized with small bubbles and hardly any expansion. At the same excess gas velocity, the bubble density is lower for the bigger particles, which give rise to higher bed density than the smaller particles. Therefore, it is obvious from the concept of fluidization that the bed expansion is lower as the particle size increases at the same excess gas velocity. It is believed that reasonable comparison of the bed expansion and other bed properties could be achieved if the comparison among different particle sizes is based on dimensionless velocity such as the velocity ratio (U/U_{mf}). Therefore, in this work the comparisons of bed properties and bubble characteristics were performed as a function of this velocity ratio. At the same superficial velocity ratio (U/U_{mf}), Hilal and Gunn (2002) showed that the bed density drastically reduced as the particle size increased. This is due to large bubbles for the bigger particles, which eventually increased the bed expansion ratio.

The simulation reasonably predicted the bed expansion ratio except at higher superficial velocities for the coarser particles where the simulation showed a decrease in the bed expansion ratio. This discrepancy is related to the decrease in pressure drop shown above and should be explained together. In fact, at high superficial velocity the experimental measurements also showed that the bed expansion became less influenced by the increase in gas velocity, Figure 7.22. Perhaps further increase could lead to a decrease in the bed expansion. However, as explained in the previous section further increase in superficial velocity was not possible due to the limitation of test rig. Nevertheless, the simulation predicted different flow and bubble dynamics as the superficial velocity increased. The reason for this discrepancy cannot be fully explained yet, but it can be partially attributed to the 2D approximation of the simulation and poor account of the gas-particle as well as particle-particle interaction in the TFM. Additional reason, which was found to influence to some extent the measured expansion ratio was the experimental measurement technique used.

As described in Chapter 4, the experimental measurements were performed using the DIAT where, images of the bed were captured by a video camera. Since the objective of this work is to investigate the bubbling behavior of fluidized bed in the presence of horizontal tubes, it was necessary to capture images of the bed section that covers the distributor outlet to the freeboard region slightly higher than the minimum fluidization bed height. Efforts were made to include the expanded bed height at all superficial velocities; unfortunately, the expansion of the bigger particles at higher superficial velocities was higher than the video can focus without significant loss of resolution for the main part of the bed. Therefore, it was decided to enhance the resolution of the main part of the bed and lose the expanded bed height. Thus, as the bed expanded then collapsed due to the bursting of large bubbles (slugs) the code could not correctly delineate the bed boundary in some frames and hence underestimated the expanded bed height.

7.2.3 Bubble properties

From the results of static pressure drop and bed expansion ratio presented above it can be concluded that the simulation predicted different flow regime compared with the experimental observations at higher superficial velocities for the coarser particles. This was also revealed from the results of bubble properties presented below. Therefore, it was deemed necessary to discuss this discrepancy before presenting the results of bubble characteristics.

From the discussions in the previous sections, it was seen that the simulation predicted fast moving bubbles. As the superficial velocity increased, bubble coalescence increased hence resulted in formation of large bubbles. This shows that the bed is transformed into a slugging regime. In fact slugging was also occurred in the experiment. Generally, slugging occurs in small diameter beds and if the following three conditions are fulfilled (Clift and Grace, 1985); 1) The maximum bubble size is greater than 0.6 times the diameter of the bed; 2) the superficial gas velocity is sufficiently high; 3) the bed is sufficiently deep. Geldart (1986) combined conditions 2 and 3

into a criterion for slug flow and the minimum superficial velocity, U_{ms} , at which slug flow will occur for a given gas-solid system is given by:

$$U_{ms} = U_{mf} + 0.07\sqrt{gD_{bed}} + 0.16(1.3D_{bed}^{0.175} - H_{mf})^2 \quad (7.1)$$

Where, D_{bed} is the diameter of the bed, in this case the bed width.

Using this equation, the theoretical minimum slugging velocities for the particles are shown in Table 7.4. From the table it can be seen that for the last three coarser particles slugging may occur for superficial velocities above $2U_{mf}$. Glicksman et al. (1987) reported that adjacent bubbles compete their coalescence faster in a large particle bed than do in a small-particle bed. As a result, slugging is predominant in large particles of relatively small-diameter fluidized beds (Lim et al., 1995). Since the superficial velocities used in this work are much higher than the theoretical minimum slugging velocity, the bed is more likely in the slugging regime instead of bubbling for the three coarser particles. This was also observed for the experiments. The discrepancy between the simulation predictions and experimental measurements is that the simulation showed a relatively early transition of fluidization regime from bubbling to slugging. At even higher superficial velocities it showed different regime than the typical slugging observed in the experiments. In fact, the mean bubble size is bigger for the experimental measurements than the simulation predictions, which could contradict this. However, due to the higher rise velocity predicted by the simulation the bubbles formed a chain of large bubbles that stretched along the bed height. This is clearly seen in Figure 7.24 as higher voidage at the center of the bed. The experiments on the other hand, though the bubbles are bigger they rose in a periodic and were followed with dense emulsion phase that is typical of slugging bed. It should be also noted that in a slugging regime the static bed pressure drop and bed expansion increased (Clift and Grace, 1985), which is different from what the simulations have predicted. Hence, from the results of the simulation it can be presumed that the simulation showed a fluidization regime different from the slugging one.

Table 7.4: Theoretical minimum slugging velocity for different mean particle sizes.

Particle size [μm]	Minimum fluidization velocity, U_{mf} [m/s]	Minimum slugging velocity, U_{ms} [m/s]	Ratio, U_{ms}/U_{mf}
141	0.054	0.229	4.20
246	0.087	0.262	3.01
347	0.144	0.319	2.22
439	0.238	0.413	1.74
592	0.333	0.508	1.53
776	0.504	0.679	1.35

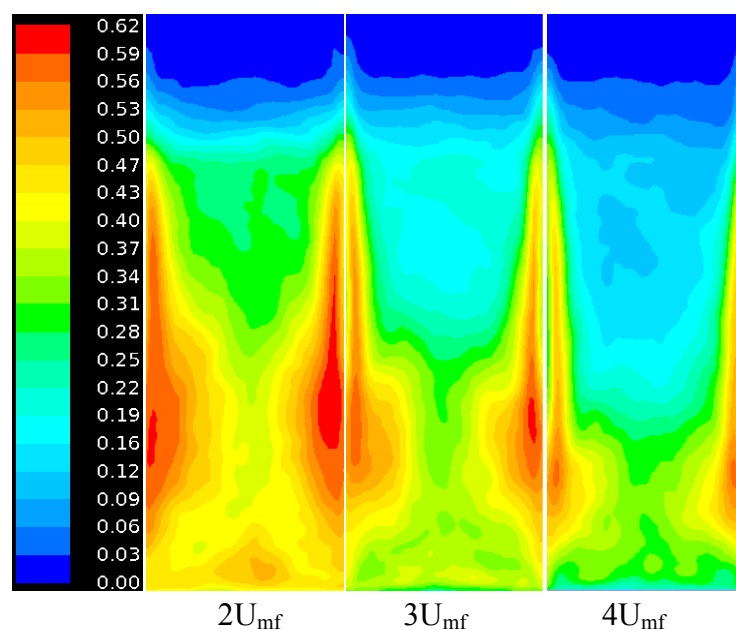


Figure 7.24: Time-averaged solids volume fraction contours; $d_p=592 \mu\text{m}$.

Beyond the slugging regime, a turbulent regime should prevail. However, it is not clear if a turbulent fluidization does occur though its main characteristics can be observed, such as a diffused bed surface, turbulent motion of solids clusters, and voids of irregular shapes. Transition from bubbling to turbulent is gradual and spans a range of gas velocities, which depend on the properties of gas and solids and on equipment scale (Yerushalmi and Avidan, 1985). This transition is not well understood and defined especially for coarser particles of Geldart's group D and many explained different reasons for the onset of turbulent fluidization. (See e.g., Yerushalmi and Avidan, 1985; Chehbouni et al., 1994; Bi et al., 1995). They explained differently, but all agreed that the onset of turbulent flow is when large bubbles (slugs) start to breakup into small bubbles and interstitial gas that result in significant change in bubbling behavior of the bed.

In this work, breakup of the slugs were observed, see section 7.2.3.2, but further coalescence were occurred in contrary to the typical turbulent regime. From this observation, it can be deduced that the beds are not in a fully turbulent regime and as explained above they are not in slugging regime either. Staub and Canada (1978) found that for large particles the transition to turbulent flow occurred well below the terminal velocity of particles. They also observed that the transition is gradual and the progression is from bubbly to a mixture of bubbly slug, to a mixture of turbulent slug, and finally to turbulent flow. This was later supported by Andreux et al. (2005). They showed that an appreciable changes in the hydrodynamics appeared well below the transition velocity from bubbling to turbulent determined based on pressure fluctuations. Thus, as it was also seen in this work there is an intermediate fluidization regime between slugging and turbulent for coarse particles. It should be also noted that the coarser particles ($592 \mu\text{m}$, and $776 \mu\text{m}$) used in this work are on the B/D boundary and D respectively based on the

Geldart's powder classification (Geldart, 1973). The fact that these particles are spoutable, they tend to spout, due to the bubble chains (slugs) extended from the lower bed to the upper surface, instead of prevailing the turbulent regime as in the case of group A and B particles. Therefore, the fluidization regime observed from the simulations is a combination of slugging and spouting bed, hence slug driven spouted bed, while the experiments showed still a pure slugging regime. This regime has certain similar characteristics as the turbulent regime but also differs from the turbulent regime reported for Geldart's A and B powders. The reason for the decrease in pressure drop and bed expansion is therefore due to spouting behavior of the bed. As can be seen from Figure 7.24, the center of the bed is permanently occupied by large slugs and the particles are pushed to the sidewalls. As a result, the wall partially supports the particles, which results in a decrease in pressure drop. Since the bed expansion is estimated by tracing the bed surface, the high voidage at the center of the bed during high gas velocity led to lower expansion.

Nevertheless, from the results for the bed characteristics such as bed pressure drop and bed expansion as well as bubble characteristics, it can be concluded that the TFM failed to reasonably predict the hydrodynamics of fluidized beds of coarse group B and group D particles at higher superficial velocities. The reason could be due to the 2D approximation and poor account of the gas-particle and particle-particle interactions. It was discussed in section 6.4 that the bubbling behavior predicted by 2D simulations deviates from experimental measurements for a pseudo-2D fluidized beds at higher superficial velocities. As presented in the section with increasing in mean particle size the deviation became more. This is because as the bubble size increased the effect of the wall became more pronounced.

Another important issue that could lead to the discrepancy is the modeling capability of the TFM. Though the TFM is the only realistic CFD model for engineering scale fluidized beds, it has certain inherent limitations that are crucial for the accuracy of the results. Two of the most important but weakly accounted by the TFM are the gas-solid and particle-particle interaction models. The gas-solid drag force is the only accelerating force acting on the particles and bubble size is mainly determined by the drag exerted on the particles by the gas. Therefore, accurate prediction of this drag force is crucial in CFD simulations. The original drag laws such as those by Gidaspow (1994), which is also used in this work, are usually obtained from pressure drop measurements in fixed, smoothly fluidized or settling beds where the particles have no relative motion. For the motion of particles clouds, however, it has been found that the volume fraction of the particles phase as well as their mutual interaction have subtle influence on the drag force. Therefore, if it is to be extended to freely moving particles, the particle volume fraction and the random fluctuation velocity of individual particles should be considered (Zhang and Reese, 2003). For bubbling bed, the drag law does not seem to be an important problem as was discussed in section 6.6. However, at higher superficial gas velocity where slugging or turbulent regime prevails their accuracy should be well studied. For example modelers of fluidized bed riser employed a correction factor for the drag law to account the heterogeneous structures existed in the riser such clustering (Yang et al., 2004). This heterogeneity arose from the sharp

differences between the dense and dilute regions, which resembled to the flow structure observed in this work, Figure 7.24. Therefore, validity of the standard drag models at higher gas superficial velocities should be critically evaluated.

The particle-particle interaction is another issue to consider in the TFM. Because the concept of particles has disappeared in the TFM, one can only include indirectly the effect of particle-particle interactions, via an effective solids' pressure and an effective solids shear and bulk viscosities for which closures should be used. Gera et al. (1998) compared bubble properties predicted by the TFM and DPM and found that the bubble formation, motion and eruption predicted by the DPM were in better agreement with their own experimental observations. They attributed the failure of the TFM to the key parameters defining the particle-particle interactions especially the particles pressure. It can be deduced that if the inter-particle friction is neglected or assumed to small in the TFM then one would expect an unrealistically elongated bubbles (Gera et al. 1998). This was what was observed in this work, see Figure 7.27. On another account, Goldschmidt et al. (2001) also showed the importance of the particle-particle interaction in the TFM simulation by investigating different particle-particle coefficient of restitutions.

7.2.3.1 Bubble shape

Figure 7.25 and Figure 7.26 show the bubble aspect ratio and shape factor respectively for different particle sizes and two bed geometries (NT and S6) for a gas superficial velocity of $2.0U_{mf}$. It can be seen that experimental measurements showed a moderate increase in aspect ratio and decrease in shape factor as a function of bed height. As explained above, this showed that bubbles have a 'kidney' type shape with slightly elongating vertically as they moved through the bed. It can also be seen that, for freely bubbling bed (NT case), the bubble elongated vertically with increase in mean particle size. On the other hand, the simulation showed similar bubble shape at least for the smaller particles, but it predicted very long bubbles for the bigger particles. This is more pronounced at higher superficial velocity as shown in Figure 7.27. In this figure even the particle with mean diameter of $439 \mu\text{m}$ showed elongated bubbles, which was not seen at the lower superficial velocity of $2U_{mf}$, see Figure 7.25. Experimental measurements also showed elongated bubbles at higher superficial velocity for the coarser particles as shown in Figure 7.27. For group D particles large spherical bubbles are formed immediately after the minimum fluidization velocity is exceeded. These bubbles coalesced quickly to form large bubbles (slugs) that span over the bed height. This resulted in a very large vertical extreme (d_y) than the horizontal extreme (d_x) hence high aspect ratio. The discrepancy between simulation results and experimental measurements are discussed above.

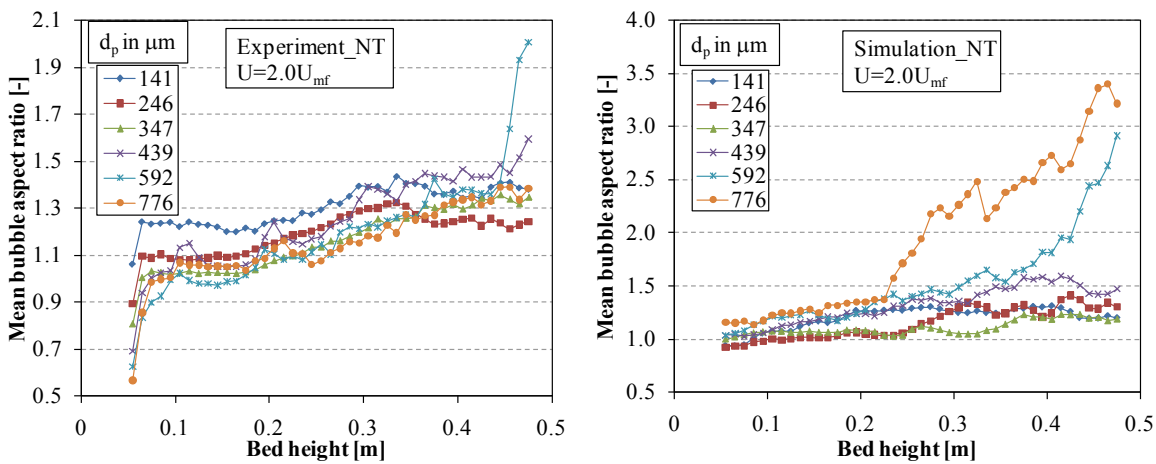


Figure 7.25: Comparison of the mean bubble aspect ratio for different mean particle sizes for NT; $U=2.0U_{mf}$.

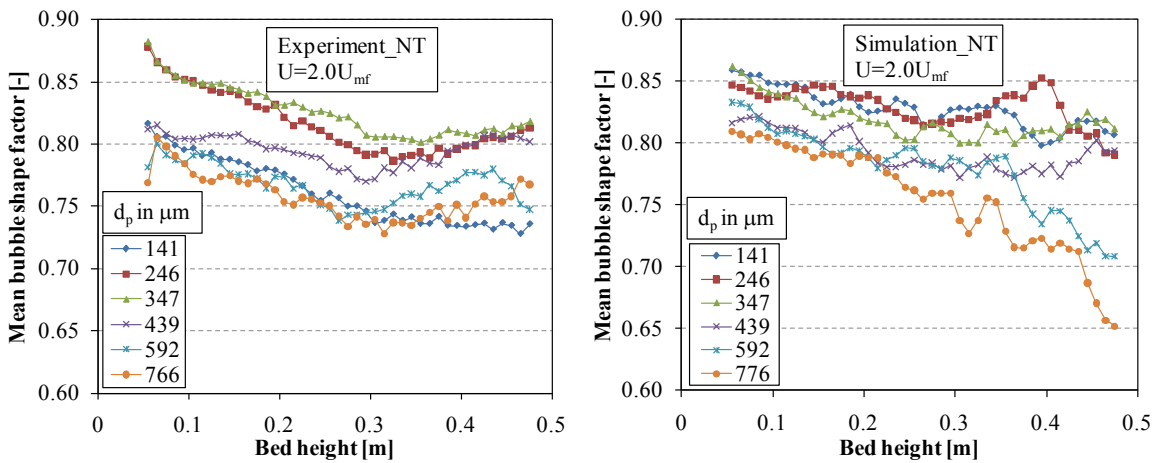


Figure 7.26: Comparison of the mean bubble shape factor for different mean particle sizes for NT; $U=2.0U_{mf}$.

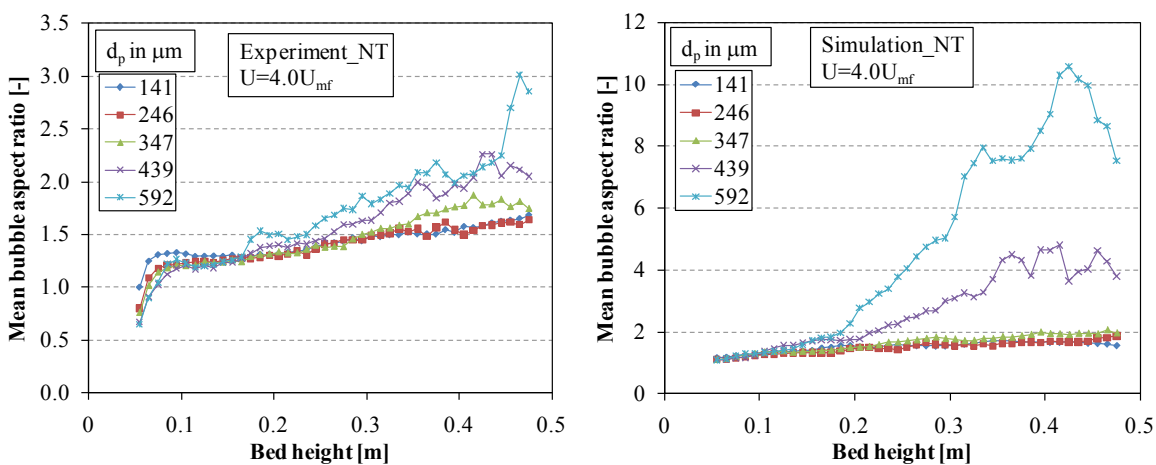


Figure 7.27: Comparison of the mean bubble aspect ratio for different mean particle sizes for NT; $U=4.0U_{mf}$.

Figure 7.28 and Figure 7.29 show the time-averaged bubble aspect ratio and shape factor respectively for the S6 case. Unlike the NT case, the bubble shape was found to be independent of the particle size. Both experimental measurements and numerical simulations showed similar trend and they were in very good agreement. This is consistent with the discussion in section 7.1. The presence of tubes prevents the formation of large bubbles and their shape is mainly dictated by the tube geometry rather the particle size. In general, the discrepancy observed in the NT case was not observed for the S6. This indicated that the presence of tubes reduced bed slugging by suppressing the formation of large bubbles or slugs.

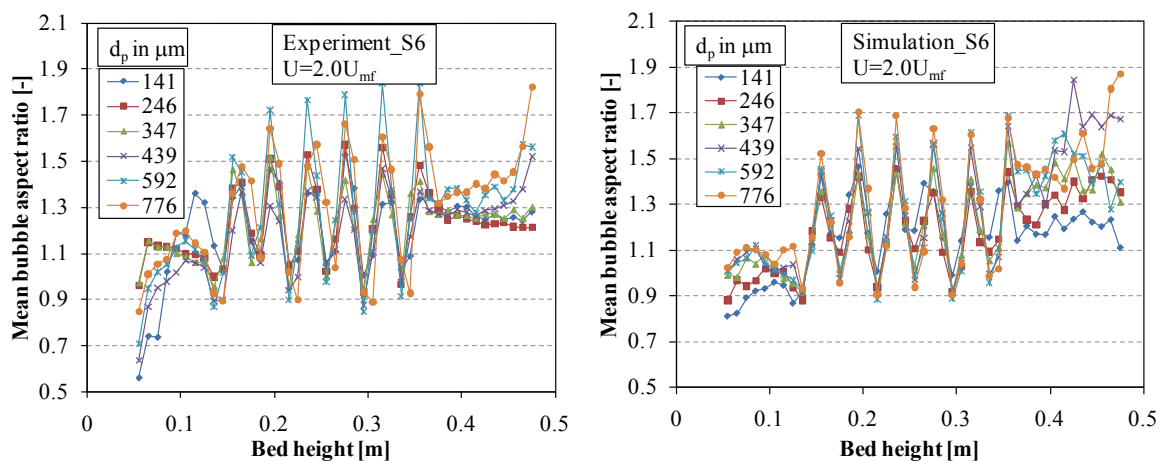


Figure 7.28: Comparison of the mean bubble aspect ratio for different mean particle sizes for S6; $U=2.0U_{mf}$.

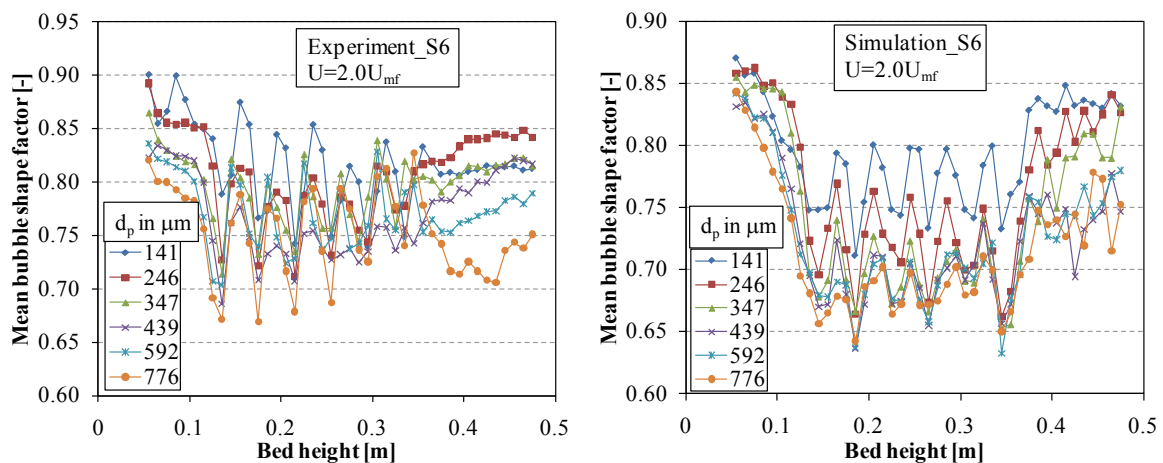


Figure 7.29: Comparison of the mean bubble shape factor for different mean particle sizes for S6; $U=2.0U_{mf}$.

7.2.3.2 Bubble size

Figure 7.30 shows the comparison of the mean bubble diameter for different particle sizes at a gas superficial velocity of $2.0U_{mf}$. It can be seen that experimental measurements showed continuous growth of bubbles with bed height for all particle size. In addition, bubble size increased with increasing in mean particle size at the same superficial gas velocity ratio (U/U_{mf}). Though the simulation predicted similar trend of bubble growth, the bubble diameter for the last three bigger particles (439, 592 and 776 μm) is nearly the same for the majority of bed height. This showed that bubble growth is independent of the particle size. At higher superficial velocity for the coarser particles, the mean particle size and increased superficial velocity have little or no influence on the bubbling characteristic of the bed. This is clearly seen at $2.0U_{mf}$ (Figure 7.30) from simulation results and at $4.0U_{mf}$ (Figure 7.31) for the experimental measurements. As explained above the difference for the change in bubbling behavior at different fluidization velocity is that the simulation predicted regime transition earlier than the experiment. This can be more clearly seen in Figure 7.31 where the simulation predicted different bubble growth for the two coarser particles that indicated a transition to slugging-spouting regime while the experiment showed still a slugging regime.

In the slugging regime, bubbles formed at the distributor coalesced quickly slightly higher than the distributor to form the slug. The slugs then grew as it rises along the bed height. The growth of the slugs is predominated by the absorption of gas from the emulsion phase rather than coalescence. This is consistent with the general theory of bubble growth in coarse powders of Geldart's group D (Geldart, 1986). This can be illustrated with the help of Figure 7.32, which shows the bubbling frequency for different particle size as a function of bed height at $4.0U_{mf}$. From the figure, it can be seen that for the smaller particles both the simulation and experiment showed a continuous decrease in the bubbling frequency as the bubbles moved along the bed. Since bubbling frequency is proportional to bubble coalescence, this showed that bubbles continuously coalesced as they moved along the bed. The sharp drop in bubble frequency at the lower of the bed height shows a higher rate of bubble coalescence. After certain height the number of bubbles decreased drastically, hence the coalescence rate also decreased. For the coarser particles on the other hand, both the simulation and experiment showed different trends of bubble coalescence. Experimental measurements showed practically similar trend to the smaller particles, though in this case the bubbling frequency became unchanged at the higher part of the bed (approx. above 0.35 m). This shows that the slugging regime prevails. The simulation on the other hand predicted the formation of bigger bubbles at the distributor and quickly coalesced to form the slugs after few centimeters above the distributor. Thus, the bubbling frequency became practically unchanged, Figure 7.32. Therefore, from the above discussion, bubble growth was not predominated by coalescence as the bubbling frequency is practically constant. The reason then is bubbles grow by absorbing gas from the emulsion phase.

From Figure 7.31 it can be seen that at a bed height of approx. 0.20 m above the distributor, the simulation predicted a decrease in bubble diameter, which also corresponds to the slight increase in bubble frequency, Figure 7.32. This shows the breakup of the slugs at this particular height. This cannot be fully explained but could be due to the size and shape of bubbles formed at the distributor. At higher superficial velocities, bubbles were formed as large horizontal voids near the distributor, which eventually split after they moved few centimeters. The formation of bubbles was also one major difference between the experiments and simulations. While the experiments showed uniform bubble formation at the distributor regardless of the particle size and superficial velocity, the simulation predicted quiet different bubble formation with the initial bubbles drastically increased with increasing in superficial velocity. This could be also another reason for the discrepancy in fluidization regime observed between the two techniques.

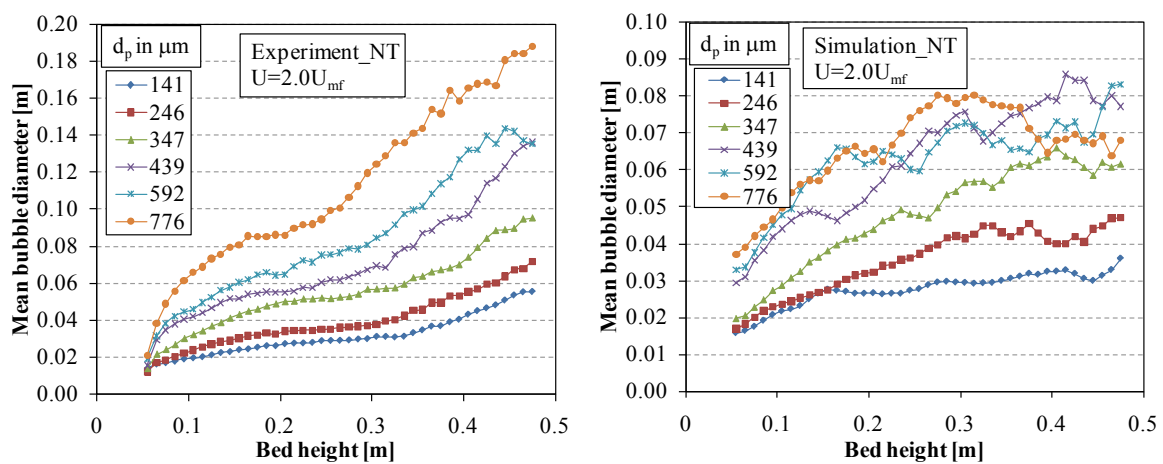


Figure 7.30: Comparison of the mean bubble diameter for different mean particle sizes for NT; $U=2.0U_{mf}$.

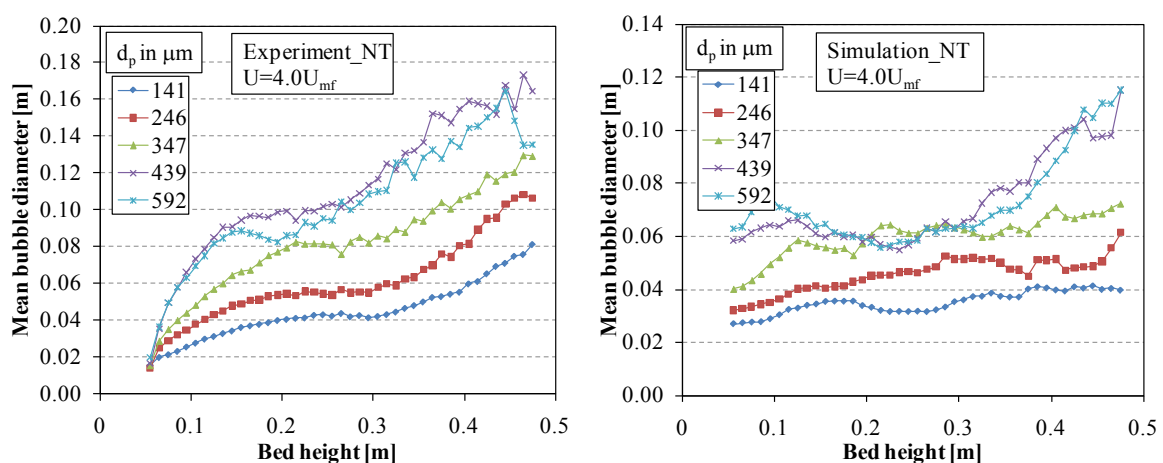


Figure 7.31: Comparison of the mean bubble diameter for different mean particle sizes for NT; $U=4.0U_{mf}$.

From both simulation and experimental measurements, the influence of particle size on the bubbling behavior can be summarized in two classes. For particle in Geldart's group B, the mean bubble size increased both with mean particle size and with superficial velocity. On the other hand, for coarser particles of Geldart's group D and on the boundary of B/D, the particle size dependency of bubble size is observed only at lower superficial velocities where the bed is fully in a bubbling regime. At higher superficial velocities where bubbles grew very fast to form slugs, the influence of the mean particle size as well as superficial velocity on bubble growth became minimal. In this case the growth of slugs is mainly due to gas leakage from the emulsion phase and controlled by the bed width.

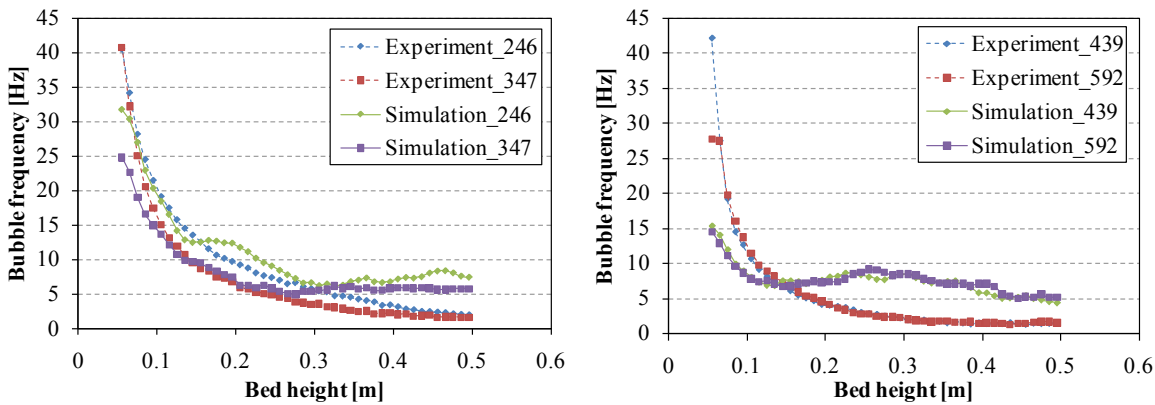


Figure 7.32: Comparison of bubble frequency for different mean particle sizes; $U=4.0U_{mf}$.

Figure 7.33 shows the mean bubble diameter for the S6 case. From the figures, it can be concluded that for beds with immersed tubes bubble growth is mainly controlled by the geometry of the tube bank and is nearly independent of the particle size. The presence of tubes promote bubble breakup hence prevent the formation of slugs. As a result the simulations were in very good agreement with the experimental measurements qualitatively as well as quantitatively.

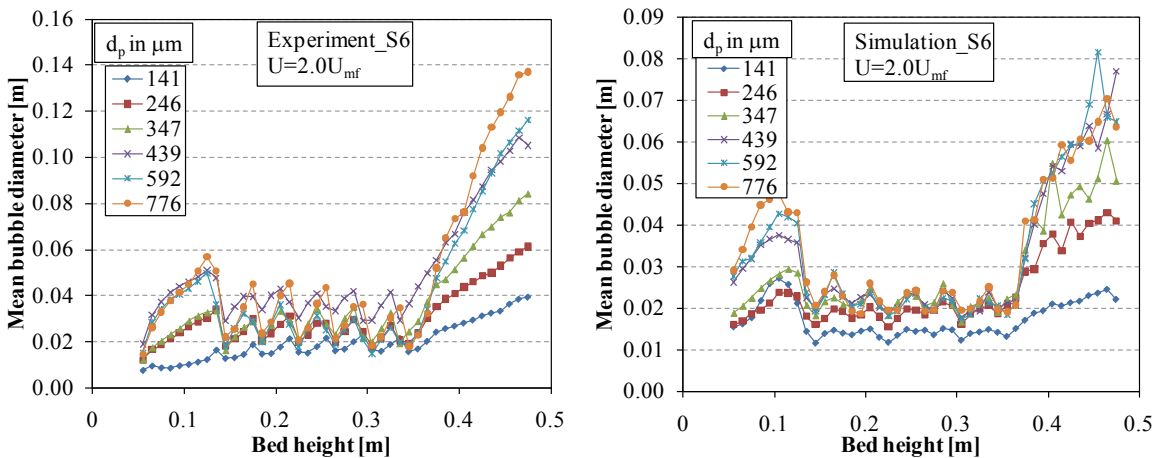


Figure 7.33: Comparison of the mean bubble diameter for different mean particle sizes for S6; $U=2.0U_{mf}$.

7.2.3.3 Bubble rise velocity

Figure 7.34 and Figure 7.35 show the mean bubble rise velocities for different particles sizes for the NT case at different superficial velocities. The plots showed qualitatively similar trend as the bubble diameter at least for the experimental measurements. This is to be expected as the rise velocity is a function of bubble diameter in a freely bubbling bed. As explained in the previous sections the simulation overestimated the rise velocity for all particle sizes. It also predicted no major difference between the coarser particles, which more pronounced at higher superficial velocity, $4.0U_{mf}$. The simulation showed a relatively constant rise velocity at higher superficial velocity for the coarser particles, which shows the prevailing regime change. This is also shown slightly at the upper part of the bed in the experimental results. At higher superficial velocity the influence of particle size became minimal as the rise velocity of slugs is mainly controlled by the walls of the bed. This is observed for both numerical and experimental results, Figure 7.35.

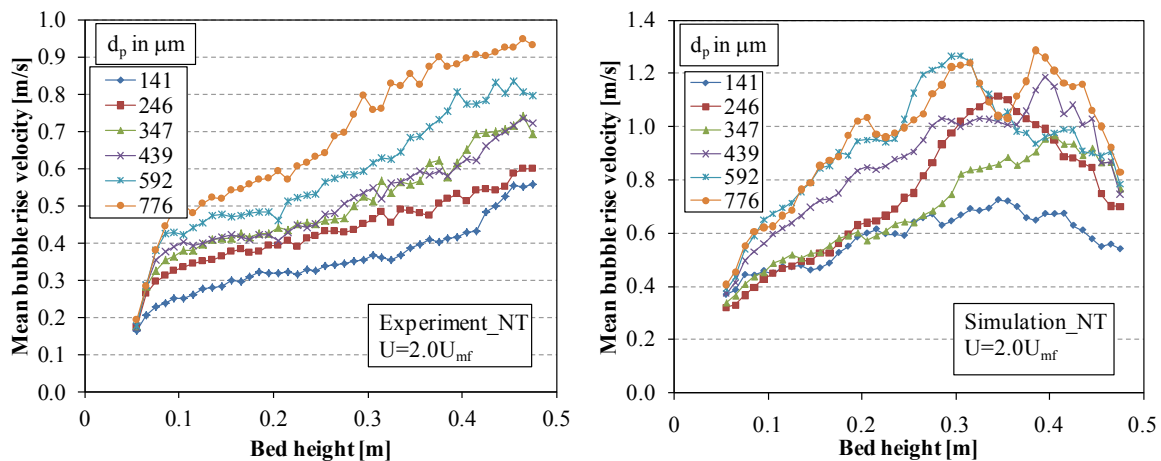


Figure 7.34: Comparison of the mean bubble rise velocity for different mean particle sizes for NT; $U=2.0U_{mf}$.

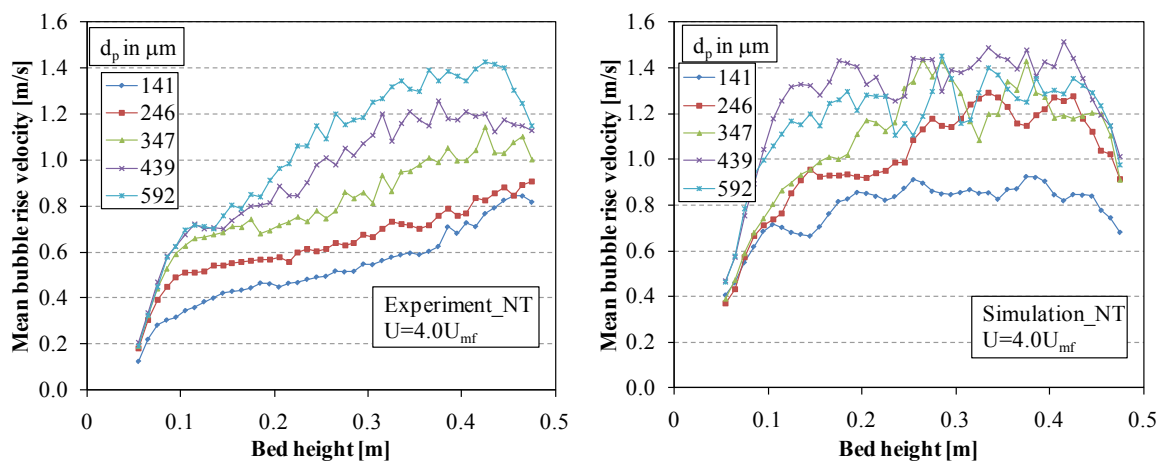


Figure 7.35: Comparison of the mean bubble rise velocity for different mean particle sizes for NT; $U=4.0U_{mf}$.

In Figure 7.36 the mean bubble rise velocities for different particle sizes are plotted for the bed with dense staggered arrangement, S6. Again similar to the bubble diameter, the rise velocity is independent of the particle size in the tube bank region. The simulation also shows similar trend and were in good agreement though it predicted higher rise velocity in the tube free regions compared to experimental measurements. Additional results can be found in Appendix D.

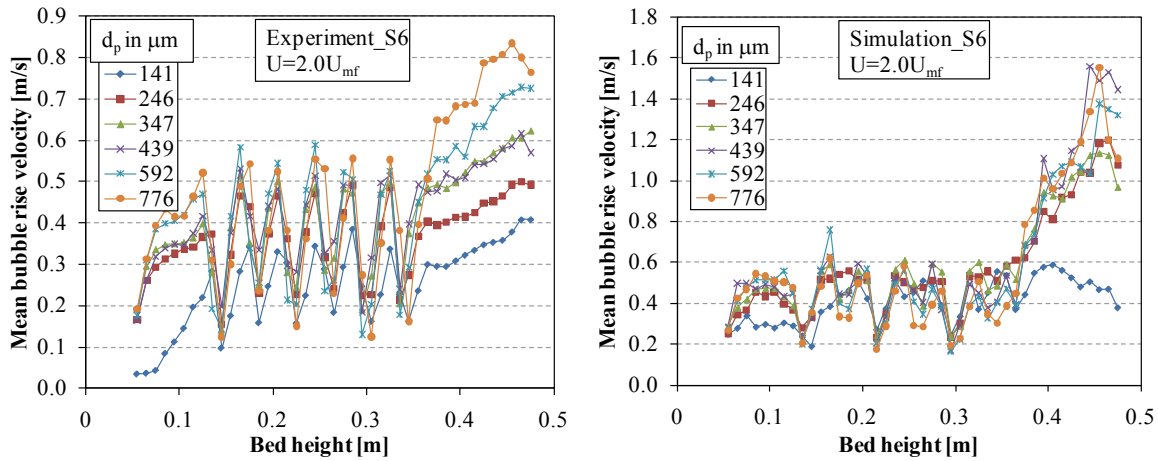


Figure 7.36: Comparison of the mean bubble rise velocity for different mean particle sizes for S6; $U=2.0U_{mf}$.

8 Conclusions and Future Work

8.1 Conclusions

The main objective of this research work was to investigate the behavior of bubbles in bubbling gas-solid fluidized beds with and without immersed horizontal tubes. The influence of tube bank geometry and arrangements, and particle size on bubble hydrodynamics and the macroscopic bed properties (pressure drop and bed expansion) were thoroughly investigated.

In this research work both experimental and numerical techniques were employed. For the experimental studies, a novel digital image analysis technique (DIAT) was developed and implemented for the analysis of bed expansion and bubble behavior in pseudo-two-dimensional gas-solid fluidized beds with and without immersed tubes. An in-house software was developed to fully automate the procedure of image acquisition and data processing. The DIAT was able to analyze both video outputs from experimental measurements and images of volume fraction contours from numerical simulations. Results obtained using the DIAT were validated with manual calculations, well-known theories and correlations available in the literature. The technique was found to successfully predict bubble characteristics such as bubble aspect ratio, shape factor, bubble diameter and rise velocity for beds with and without dense horizontal tube banks. Detail description of the experimental facility and the procedures of the DIAT development along with the validation of the technique were presented in Chapter 4.

In Chapter 5, based on the experimental results new theoretical correlations for mean bubble diameter and rise velocity as a function of bed height above the distributor were proposed for 2D fluidized beds without immersed tubes. The calculated bubble properties using these new models were in reasonable agreement with the experimental measurements. The models were capable of accounting the inflections and plateaus observed from experiments that resulted in better predictions of the bubble properties than previous models such as those from Lim et al. (1993). In addition, theoretical models were developed for the bed expansion ratio for fluidized beds with and without immersed tubes. The models agreed well with experimental measurements obtained using the DIAT.

For the numerical studies, the Eulerian-Eulerian Two-Fluid Model (TFM) with closure equation based on the Kinetic Theory of Granular Flow (KTGF) was employed. This model is widely used in the fluidization research since it is the only realistic method for modeling dense gas-solid fluidized beds at the current computational facilities. However, its quantitative validation with experimental measurements for different bed geometries and operating conditions is still not fully established. Therefore, in Chapter 6 detail validation of the model with experimental measurements of pressure drop, bed expansion and bubble properties were presented. For this particu-

lar study, the particle size and superficial velocity were kept constant. From the validation results presented the following can be concluded:

- The TFM is capable of predicting the main bubble characteristics such as bubble aspect ratio, diameter and rise velocity with and without immersed tubes for Geldart's group B particles. Except for the bubble rise velocity for which the simulation overestimated it, the calculated bubble properties as well as bed pressure drop and bed expansion were in general in reasonable agreement with the experimental data;
- For validation of CFD models using time-averaged results, the length of the averaging period was found to significantly influence the simulation results in the first few seconds of averaging time. Therefore, for a given bed geometry and operating conditions it is deemed necessary to perform sensitivity analysis at least to ensure that the time-averaged properties are independent of the length of the averaging period with acceptable computational effort;
- No significant differences of bubble properties were observed between the different threshold values used to define the bubble boundary;
- For the studied bed geometries, a grid size ranging from 2 mm to 5 mm showed no major differences in the predicated bubble properties and bed expansion while the computation time increased linearly with the number of cells;
- Comparing 2D and 3D simulation results, 2D simulations predicted smaller but faster bubbles. Significant deviations were observed at the upper part of the bed where the 2D simulations underpredicted the bubble diameter compared with the experimental measurements and 3D simulations. This was more pronounced at higher superficial velocity. Due to absence of the front and back walls the bubble rise velocity predicted by 2D simulations were higher compared to the corresponding 3D simulations and experimental data;
- In general, 3D simulations are preferable than 2D simulations and were in better agreement with the experimental measurements. However, they are computationally expensive (5-9 times more than 2D). Provided that the bed is operated in a bubbling regime, 2D simulations can be successfully used for parametric study and sensitivity analysis for engineering scale gas-solid fluidized beds;
- For beds with horizontal tubes, 2D and 3D simulations predict quiet similar results in the tube bank region and were both in very good agreement with experimental data. This showed that the presence of tubes suppressed the influence of the walls neglected in 2D simulations;
- Except for a friction packing limit of 0.65 in the no tube case, which corresponds to the maximum solid packing limit, the choice of the friction packing limit had little influence on bubble behavior in fluidized beds with and without immersed horizontal tubes;
- The three drag models studied here showed no major difference in the predicted bubble properties for both beds with and without immersed horizontal tubes;
- In beds without horizontal tubes, bubble properties showed greater sensitivity to the choice of solid-wall boundary conditions with the partial-slip boundary condition in bet-

ter agreement with experimental results. For the partial-slip boundary condition, the choice of specular coefficient had little influence on the predicted bubble properties;

- In general, the different modeling parameters studied in this work had negligible influence on the bubbling behavior of fluidized bed with dense immersed horizontal tubes. Their influence was relatively significant for freely bubbling beds. In fluidized beds with dense immersed tubes, bubbling behavior is controlled by the tube bank geometry.

In Chapter 7, detail investigations of the influence of different tube bank geometries and arrangements as well as mean particle size on the fluidized bed hydrodynamics were presented. For a bubbling bed, both experimental measurements and numerical simulations showed that inserting horizontal tube banks had either no or marginal influence on the static bed pressure drop and bed expansion. Numerical simulations predicted constant bed pressure drop for the majority of particle sizes and superficial velocities studied in this work, while experimental measurements showed an increase in bed pressure drop with particle size and superficial velocity. This was mainly attributed to the particle size distribution in the experiments while in the simulation monodispered, smooth and spherical particles were assumed. A major discrepancy between the numerical predictions and experimental measurements occurred at higher superficial velocities for the coarser particles in the no tube bed. In these cases the simulation predicted a sharp drop in the static bed pressure drop while the experimental measurements showed consistent increase in pressure drop with superficial velocity. In fact, it was also observed from experimental measurements that the static bed pressure drop slightly decreased at higher superficial velocities; however, this was not in the same degree as that of the numerical predictions. Similar discrepancies were observed for the bed expansion as well. The reason for these discrepancies was attributed to a different fluidization regime observed during simulation. The simulation showed a chain of large bubbles (slugs) which extend from the lower bed section to the bed surfacing. This led to a regime somewhat a combination of slugging and spouting hence was defined as slugging-spouting regime in this work. Therefore, due to the spouting behavior of the bed, the sidewalls partially supported the particles, which give to a drop in static pressure drop. In addition, since the center of the bed is usually free of particles, the measured bed height is lower that resulted in lower bed expansion ratio. The reason for the change to such complex regime of a combination of slugging and spouting during simulation while the experiments showed still pure slugging regime could be attributed to the wall effect and particle distribution. In addition, the poor account of the TFM for the gas-particle and particle-particle interactions could have significant influence in these regards. However, extensive study is required to verify this.

Results of bubble properties showed that for freely bubbling fluidized beds bubble size as well as rise velocities were found in general to increase with bed height, superficial velocity and mean particle size. Bubbles were observed to have generally a 'kidney' type shape. They were found to be flattened and vertically stretched with increase in their size. The simulation was in reasonable agreement with the experimental measurements in predicting the different bubble

characteristics at least when the bed is in bubbling regime. For beds with immersed horizontal tubes on the other hand, the bubble hydrodynamics were strongly influenced and controlled by the geometry of the immersed tubes. The presence of horizontal tubes was seen to be the main cause of bubble breakup. Tubes appeared to prevent rapidly growing bubbles hence limit the mean bubble diameter and rise velocity in the vicinity of the tube banks. Small bubbles formed at the bottom of the bed rose and grew by coalescence. As a bubble approached the bottom of the tube, it begins to flatten and 'wraps' the bottom of the tube. If the bubble is bigger compared to the tube diameter and approaches the tube along its nose, the bubble usually splits into two. Bubbles were also observed to split into three or more daughter bubble usually if the horizontal extreme of a bubble is greater than twice the pitch size in a row. If the bubble split into a bigger and smaller, the bigger bubble rise faster over the tube and wraps the tube on side until the top of the tube. On the other hand, large bubbles, which are not destined to hit the tube directly, tend to distort as they pass the tube while small bubbles usually swerve around the tube. Thus, in the tube bank region bubble behavior is mainly characterized by the frequent splitting and coalescence, which eventually resulted in limiting their growth and velocity. Moreover, the shape of the bubbles were highly distorted which resulted in higher aspect ratio.

Another important difference observed between freely bubbling beds and beds with horizontal tubes which was also found to significantly influence the fluidization behavior in the tube bank region was local bubble formation at the lower side of the tubes. From both experiments and simulations it was observed that the regions beneath and adjacent the horizontal tubes are effectively devoid of solid particles which act as nucleation sites for bubbles. Such local fluidization and local bubbling were observed even at superficial velocities lower than the minimum fluidization velocity during experiments, though the bubbles were usually reabsorbed by the bed before they reached the bed surface. Since these bubbles are very small and usually semi-stagnant or slowly swerve around the tubes, they significantly reduced the mean bubble diameter and rise velocity.

As a result of the above mentioned phenomena the bubbling behavior of gas-solid fluidized beds with horizontal tubes is dictated by the geometry of the tube bank rather than superficial velocity and/or particle size. At least for the dense tube geometries studied in this work the mean bubble properties in the tube bank region were found to be nearly independent of superficial velocity, particle size and bed height. In these cases the mean bubble diameter in the tube bank region is restricted to the space between the tubes and it does not appreciably grow with bed height as well as superficial velocity. For the sparse tube banks the bigger vertical spacing between rows allowed further growth of bubbles thus the mean bubble diameter were found to be larger and more circular compared to bubbles in the dense tube bank cases. However, even for such sparse tubes the influence of horizontal tubes on bubble properties was very strong. For intermediate tube geometries the estimated bubble properties were usually between the dense and sparse ones.

Concerning the tube arrangement (in-line and staggered) both experimental measurements and numerical simulations showed no major difference of bubble properties as well as bed expansion for all tube bank geometries. Hence, the choice could lie on the influence of other hydrodynamic properties such as gas and solid distribution and heat transfer characteristics. It is believed that staggered tubes promote lateral mixing of solids better than the in-line arrangements because they destruct the continuous axial movements of solids.

Similar to the bed pressure drop and bed expansion, major discrepancies between experimental measurements and numerical results of bubble properties were seen for the freely bubbling bed at higher superficial velocities of the coarser particles. As explained above the simulation predicted a very complex flow regime in these cases where bubbles can no longer be regarded as either bubbles or slugs. As observed from the simulation, these are large voids extended from the lower bed section to the bed surface that resulted in non-physical bubble aspect ratios. The reason for such unrealistically long bubbles was discussed in Chapter 7. In general the CFD TFM is capable of predicting the macroscopic fluidized bed hydrodynamics such as pressure drop, bed expansion and bubble properties of Geldart's group B and D particles operated in a bubbling regime. It was found in this work that the validity of the model at fluidization regimes beyond the bubbling (such as slugging and turbulent) especially for coarser particles at higher superficial velocities is doubtful. The application of the model in such cases should be done with great caution.

Nevertheless, since the objective of this research work is to investigate bubble hydrodynamics in bubbling gas-solid fluidized bed which are applicable in lignite drying, the failure of the TFM for higher fluidization regime is not of great concern. In lignite drying application, the particles have low density (1000 kg/m^3) and particle size distribution of 0 to 2 mm, which could practically lies in Geldart's group B powders or even group A powders depending on the percentage of fines. Moreover, the drying process is operated at low excess gas velocity to prevent entrainment of the fine particles. Therefore, fluidization of lignite drying is preformed entirely in the bubbling regime. Moreover, it was shown that the TFM predicted well the bed hydrodynamics in the presence of dense immersed tubes regardless of the particle size. Thus, in applications such as lignite drying where very dense heat transfer tube are present, the TFM can be reasonably applied for predictions of the fluidized bed hydrodynamics.

8.2 Recommendations for Future Work

The author recommends that future research work on the hydrodynamics of gas-solid fluidized bed with immersed horizontal tubes and applicable for lignite drying should include:

- Extended experimental studies of bubble behavior using 3D and pseudo-2D beds. The aim of which would be to investigate the influence of the bed thickness on the bubbling

behavior;

- An extended experimental studies to investigate the influence of particle size distribution on bubble behavior using mono-sized and mixtures of two or more mono-sized powders;
- Experimental studies of the bubbling behavior of lignite powders;
- An extended study of the influence of particle-particle frictional stresses on the bubble behaviour;
- Extend the TFM model in order to take into account multisize particle flows;
- Extend the TFM model in order to take into account the cohesive forces of fine particles;
- An extended study using additional drag models to find a drag model that could be suitable for wide range of particle sizes and superficial velocities;
- Detail investigation of the influence of tube arrangements on solid distribution and mixing;
- Detail investigation of the motion of bubbles and solids around immersed tubes.

9 Bibliography

- Agarwal, P.K., Hull, A.S., Lim, K.S., 1979. *Digital image analysis techniques for the study of bubbling fluidized beds*. In: J. Chaouki (Ed.), *Non-invasive monitoring of multiphase flows*, Elsevier, Amsterdam, pp. 407-454.
- Al-Zahrani, A.A., Daous, M.A., 1996. *Bed expansion and averaged bubble rise velocity in a gas-solid fluidized bed*. *Powder Technology* 87, 255-257.
- Almstedt, A.E., Zakkay, V., 1990. *An investigation of fluidized bed scaling capacitance probe measurements in a pressurized bed combustor and a cold model bed*. *Chemical Engineering Science* 45, 1071-1078.
- Almuttahir, A., Taghipour, F., 2008. *Computational fluid dynamics for a circulating fluidized bed under various fluidization conditions*. *Chemical Engineering Science* 63, 1696-1709.
- Anderson, T.B., Jackson, R., 1967. *A Fluid Mechanical Description of Fluidized Beds Equations of Motion*. *Industrial & Engineering Chemistry Fundamentals* 6, 527-539.
- Andreux, R., Gauthier, T., Chaouki, J., Simonin, O., 2005. *New description of fluidization regimes*. *AIChE Journal* 51, 1125-1130.
- ANSYS, Inc., 2009. *Eulerian Model Theory*. ANSYS FLUENT 12.0 Theory Guide, Chapter 16.5, Lebanon.
- Asegehegn T.W., Schreiber, M., Krautz H.J., 2011. *Numerical study of bubbling gas-solid fluidized beds hydrodynamics: Influence of immersed horizontal tubes and data analysis*. *International Journal of Chemical Reactor Engineering* 9, A16.
- Bahramian, A., Kalbasi, M., Olazar, M., 2009. *Influence of boundary conditions on CFD simulation of gas-particle hydrodynamics in a conical fluidized bed unit*. *International Journal of Chemical Reactor Engineering* 7, A60.
- Bai, B., Gheorghiu, S., van Ommen, J.R., Nijenhuis, J., Coppens, M.-O., 2005. *Characterization of the void size distribution in fluidized beds using statistics of pressure fluctuations*. *Powder Technology* 160, 81-92.
- Benyahia, S., 2008. *Validation study of two continuum granular frictional flow theories*. *Industrial & Engineering Chemistry Research* 47, 8926-8932.

- Benyahia, S., Arastoopour, H., Knowlton, T.M., Massah, H., 2000. *Simulation of particles and gas flow behavior in the riser section of a circulating fluidized bed using the kinetic theory approach for the particulate phase*. Powder Technology 112, 24-33.
- Bi, H.T., Grace, J.R., Lim, K.S., 1995. *Transition from bubbling to turbulent fluidization*. Industrial & Engineering Chemistry Research 34, 4003-4008.
- BMWi, Bundesministerium für Wirtschaft und Technologie; Bundesministerium für Umwelt, Naturschutz und Reaktorsicherheit, Eds. *Energieversorgung für Deutschland-Statusbericht für den Energiegipfel am 3*; Berlin, 2006.
- BDEW, Bundesverband der Energie- und Wasserwirtschaft. *Burrto-Stromerzeugung nach Energieträgern*. 2020. (Press release)
- Boemer, A., Qi, H., Renz U., 1997. *Eulerian simulation of bubble formation at a jet in a two-dimensional fluidized bed*. International Journal of Multiphase Flow 23, 927-944.
- Boemer, A., Qi, H., Renz U., 1998. *Verification of Eulerian Simulation of Spontaneous Bubble Formation in a Fluidized Bed*. Chemical Engineering Science 53, 1835-1846.
- Bouillard, J.X., Lyczkowski, R.W., Gidaspow D., 1989. *Porosity distributions in a fluidized bed with an immersed obstacle*. AIChE Journal 35, 908-922.
- Busciglio, A., Vella, G., Micale, G., Rizzuti, L., 2008. *Analysis of the bubbling behavior of 2D gas solid fluidized beds Part I. digital image analysis technique*. Chemical Engineering Journal 140, 398-413.
- Busciglio, A., Vella, G., Micale, G., Rizzuti, L., 2009. *Analysis of the bubbling behavior of 2D gas solid fluidized beds: Part II. Comparison between experiments and numerical simulations via digital image analysis technique*. Chemical Engineering Journal 148, 145-163.
- Busciglio, A., Vella, G., Micale, G., Rizzuti, L., 2010. *Experimental analysis of bubble size distributions in 2D gas fluidized beds*. Chemical Engineering Science 65, 4782-4791.
- Buyevich, Y.A., Yates, J.G., Cheesman, D.J, Wu, K.T., 1995. *A model for the distribution for voidage around bubbles in a fluidized bed*. Chemical Engineering Science 50, 3155-3161.

- Caicedo, G.R., Marques, J.J.P., Ruiz, M.G., Soler, J.G., 2003. *A study on the behavior of bubbles of a 2D gas-solid fluidized bed using digital image analysis*. Chemical Engineering and Processing 42, 9-14.
- Cammarata, L., Lettieri, P., Micale, G.D., Colman, D., 2003. *2D and 3D simulations of bubbling fluidized beds using Eulerian-Eulerian models*. International Journal of Chemical Reactor Engineering 1, A48.
- Cao, J., Cheng, Z., Fang, Y., Jing, H., Huang J., Wang, Y., 2008. *Simulation and experimental studies on fluidization properties in a pressurized jetting fluidized bed*. Powder Technology 183, 127-132.
- Carnahan, N.F., Starling, K.E., 1969. *Equations of state for non-attracting rigid spheres*. Journal of Chemical Physics 51, 635-636.
- Chandran, A.N., Rao, S.S, Varma, Y.B.G., 1990. *Fluidized bed drying of solids*. AIChE Journal 36, 29-38.
- Chaouki, J., Larachi, F., Dudukovic, M.P., 1997. *Noninvasive Tomographic and velocimetric monitoring of multiphase flows*. Industrial & Engineering Chemistry Research 36, 4476-4503.
- Chaouki, J., 1997. *Non-Invasive Monitoring of Multiphase Flows*. Elsevier, Amsterdam.
- Chaplin, G., Pugsley, T., 2005. *Application of electrical capacitance tomography to the fluidized bed drying of pharmaceutical granule*. Chemical Engineering Science 60, 7022 - 7033.
- Chapman, S., Cowling, T.G., 1970. *The Mathematical Theory of Non-Uniform Gases*. Cambridge University Press, Cambridge.
- Chehbouni, A., Chaouki, J., Guy, C., Klvana, D., 1994. *Characterization of the flow transition between bubbling and turbulent fluidization*. Industrial & Engineering Chemistry Research 33, 1889-1896.
- Chen, X.Z., Shi, D.P., Gao, X., Luo, Z.H., 2011. *A fundamental CFD study of the gas-solid flow field in fluidized bed polymerization reactors*. Powder Technology 205, 276-288.
- Cheremisinoff, N.P., 1986. *Review of experimental methods for studying the hydrodynamics of gas-solid fluidized beds*. Industrial & Engineering Chemistry. Process Design. And Development 25, 329-351.

- Chiesa, M., Mathiesen, V., Melheim, J.A., Halvorsen, B., 2005. *Numerical simulation of particulate flow by the Eulerian-Lagrangian and the Eulerian-Eulerian approach with application to a fluidized bed*. Computers and Chemical Engineering 29, 291-304.
- Clark, N.N., McKenzie, E.A., Gautam, M., 1991. *Differential pressure measurements in a slugging fluidized bed*. Powder Technology 67, 187-199.
- Clark, N.N., Liu, W., Turton, R., 1996. *Data interpretation techniques for inferring bubble size distribution from probe signals in fluidized systems*. Powder Technology 88, 179-188.
- Clift, R., Grace, J.R., 1985. *Continuous bubbling and slugging*. In: Davidson, J.F., Clift, R., Harrison D., (Eds), Fluidization, second ed., Academic Press Inc. London.
- Clift, R., Grace, J. R., 1972. *The mechanism of bubble break-up in fluidized beds*. Chemical Engineering Science 27, 2309-2310.
- Clift, R., Grace, J.R., Weber, M.E., 1974. *Stability of bubbles in fluidized beds*. Industrial & Engineering. Chemistry. Fundamentals 13, 45-51.
- Clift, R., Rafailidis, S., 1993. *Interparticle stress, fluid pressure, and bubble motion in gas-fluidized beds*. Chemical Engineering Science 48, 1575-1582.
- Crowe, C., Sommerfeld, M., Tsuji, Y. 1998. *Multiphase Flows with Droplets and Particles*. CRC Press LLC.
- Darton, R.C., LaNeuze, R.D., Davidson, J.F., Harrison, D., 1977. *Bubble growth due to coalescence in fluidized beds*. Transactions of the Institution Chemical Engineering 55, 274-280.
- Das Sharma, S.K., Mohan, R., 2003. *Numerical study of the influence of horizontal tube banks on the hydrodynamics of a dense gas-solid bubbling fluidized bed*. International Journal of Chemical Reactor Engineering 1, A26.
- Davidson, J. F. 1961. *Discussion following symposium on fluidization*. Transactions of the Institution Chemical Engineering 39, 230-232.
- Davidson, J.F., Harrison, D., 1963. *Fluidized Particles*. Cambridge Univ. Press, New York, 1963.
- Deen, N.G., van Sint Annaland, M., van der Hoef, M.A., Kuipers, J.A.M., 2007. *Review of discrete particle modeling of fluidized beds*. Chemical Engineering Science 62, 28-44.

- Deen, N.G., Godlieb, W., Gorter, S., Kuipers, J.A.M., 2010. *An electrical capacitance tomography study of pressurized fluidized beds*. ECI Conference on The 13th International Conference on Fluidization - New Paradigm in Fluidization Engineering Hotel Hyundai, Gyeong-ju, Korea
- Ding, J., Gidaspow, D., 1990. *A bubbling fluidization model using kinetic theory of granular flow*. AIChE Journal 36, 523-538.
- Ding, J., Lyczkowski, R.W., 1992. *Three-dimensional kinetic theory modeling of hydrodynamics and erosion in fluidized beds*. Powder Technology 73, 127-138.
- Donsi, G., Ferrari, G., Formisani, B., 1989. *Expansion behavior of confined fluidized beds of fine particles*. The Canadian Journal of Chemical Engineering 67, 185-190.
- Du, W., Bao, X., Xu, J., Wei, W., 2006. *Computational fluid dynamics (CFD) modeling of spouted bed: Influence of frictional stress, maximum packing limit and coefficient of restitution of particles*. Chemical Engineering Science 61, 4558-4570.
- Dyakowski, T., Edwards, R.B., Xie, C.G., Williams, R.A., 1997. *Application of capacitance tomography to gas–solid flows*. Chemical Engineering Science 52, 2099–2110.
- Enwald, H., Peirano, E., Almstedt, A.E., 1996. *Eulerian two-phase flow theory applied to fluidization*. International Journal of Multiphase Flow 22, suppl. 21-66.
- Ergun, S., 1952. *Fluid flow through packed columns*. Chemical. Engineering Progress. 48, 89-94.
- Foerster, S.F., Louge, M.Y., Chang, H., Allia, K., 1994. *Measurements of the collision properties of small spheres*. Physics of Fluids 6, 1108-1115.
- Franka, N.P., Heindel, T.J., 2009. *Local time-averaged gas holdup in a fluidized bed with side air injection using X-ray computed tomography*. Powder Technology 193, 69-78.
- Gamwo, I.K., Soong, Y., Lyczkowski, R.W., 1999. *Numerical simulation and experimental validation of solids flows in a bubbling fluidized bed*. Powder Technology 103, 117-129.
- Gao, W.M., Kong, L.X., Hodgson, P.D., 2007. *Computational simulation of gas flow and heat transfer near an immersed object in fluidized beds*. Advances in Engineering Software 38, 826-834.
- Geldart, D., 1973. *Types of gas fluidization*. Powder Technology 7, 285-292.

- Geldart, D., 1986. *Gas Fluidization Technology*. John Wiley & Sons Ltd, Chichester.
- Geldart D., 2004. *Expansion of gas fluidized beds*. Industrial & Engineering Chemistry Research 43, 5802-5809.
- Geldart, D., Kelsey, J.R. 1972. *The use of capacitance probes in gas fluidized beds*. Powder Technology 6, 45-50.
- Gelderbloom, S.J., Gidaspow, D., Lyczkowski, R.W., 2003. *CFD simulation of bubbling/collapsing fluidized beds for three Geldart groups*. AIChE Journal 49, 844-858.
- Gera, D., Gautam, M., Tsuji, Y., Kawaguchi, T., Tanaka, T., 1998. *Computer simulation of bubbles in large-particle fluidized beds*. Powder Technology 98, 38-47.
- Gidaspow, D., 1994. *Multiphase Flow and Fluidization: Continuum and kinetic theory descriptions*. Academic Press, Boston.
- Gidaspow, D., Ettehadieh, B., 1983. *Fluidization in two-dimensional beds with a jet. 2. hydrodynamic modeling*. Industrial & Engineering Chemistry Fundamentals 22, 193-201.
- Glass D.H., Harrison D., 1964. *Flow patterns near a solid obstacle in fluidized bed*. Chemical Engineering Science 19, 1001-1002.
- Glicksman, L.R., Lord, W.K., Sakagami, M., 1987. *Bubble properties in large-particle fluidized beds*. Chemical Engineering Science 42, 479-491.
- Glicksman, L.R., Yule, T., Dyrness, A., 1991. *Prediction of the expansion of fluidized beds containing tubes*. Chemical Engineering Science 46, 1561-1571.
- Goldschmidt, M.J.V., Link, J.M., Mellema, S., Kuipers, J.A.M., 2003. *Digital image analysis measurements of bed expansion and segregation dynamics in dense gas fluidized beds*. Powder Technology 138, 135-159.
- Goldschmidt, M., Kuipers, J.A.M., van Swaaij, W.P.M., 2001. *Hydrodynamic modeling of dense gas-fluidized beds using the kinetic theory of granular flow: effect of coefficient of restitution on bed dynamics*. Chemical Engineering Science 56, 571-578.
- Goldschmidt, M. J. V., Beetstra, R., Kuipers, J. A. M., 2002. *Hydrodynamic modeling of dense gas-fluidized beds: Comparison of the kinetic theory of granular flow with 3D hard-sphere discrete particle simulations*. Chemical Engineering Science 57, 2059- 2075.

- Goldschmidt, M. J. V., Beetstra, R., Kuipers, J. A. M., 2004. *Hydrodynamic modeling of dense gas-fluidized beds: Comparison and validation of the 3D discrete particle and continuum models*. Powder Technology 142, 23-47.
- Goldsmith, W., 1960. *Impact: The Theory and Physical Behavior of Colliding Solids*. Richard Clay and Co. Ltd., London.
- Grace, J.R., Baeyens, J., 1986. *Instrumentation and experimental techniques*. In D. Geldart (Ed.), Gas Fluidization Technology, John Wiley & Sons, Chichester.
- Guenther, C., Syamlal, M., 2001. *The effect of numerical diffusion on simulation of isolated bubbles in a gas-solid fluidized bed*. Powder Technology 116, 142-154.
- Gunn, D.J., Al-Doori, H.H., 1985. *The measurement of bubble flows in fluidized beds by electrical probe*. International Journal of Multiphase Flow 11, 535-551.
- Gustavsson, M., Almstedt, A.E., 2000. *Numerical simulation of fluid dynamics in fluidized beds with horizontal heat exchanger tubes*. Chemical Engineering Science 55, 857-866.
- Halow, J.S., 1979. *Electrical capacitance imaging of fluidized bed*. In: J. Chaouki (Ed.), Non-Invasive Monitoring of Multiphase Flows, Elsevier, Amsterdam.
- Halow, J.S., Nicoletti, P., 1992. *Observations of fluidized bed coalescence using capacitance imaging*. Powder Technology 69, 255-277.
- Halow, J.S, Fasching, G.E, Nicoletti P., Spenik J.L, 1993. *Observations of a fluidized bed using capacitance imaging*. Chemical Engineering Science 48, 643-659.
- Hamzehei, M., Rahimzadeh, H., Ahmadi, G., 2010. *Computational and experimental study of heat transfer and hydrodynamics in a 2D gas-solid fluidized bed reactor*. Industrial & Engineering Chemistry Research 49, 5110-5121.
- Hamzehei, M., Rahimzadeh, H., 2009. *Experimental and numerical study of hydrodynamics with heat transfer in a gas-solid fluidized bed reactor at different particle sizes*. Industrial & Engineering Chemistry Research 48, 3177-3186.
- Hatano, H., Khattab, I.A.H., Nakamura, K., Ishida, M., 1986. *Spatiotemporal measurement of bubble properties in free-bubbling fluidized beds*. Journal of Chemical Engineering Japan 19, 425-430.

- Hatano, H., Ishida, M., 1981. *The entrainment of solid particles from gas-solid fluidized bed*. Journal of Chemical Engineering of Japan 14, 306-311.
- He, Y., Zhan, W., Zhao, Y., Lu, H., Schlaberg, I., 2009. *Prediction on immersed tubes erosion using two-fluid model in a bubbling fluidized bed*. Chemical Engineering Science 64, 3072-3082.
- He, Z., Wu, B., Chandrasekaran, B., Bellehumeur, C., Kantzas, A., 2007. *X-ray fluoroscopy measurements and CFD simulation of hydrodynamics in a two dimensional gas-solids fluidized bed*. ECI Conference on the 12th International Conference on Fluidization - New Horizons in Fluidization Engineering Vancouver, Canada.
- Hepbasli, A., 1998. *Estimation of bed expansion in a freely-bubbling three-dimensional gas-fluidized bed*. International Journal of Energy Research 22, 1365-1380.
- Hilal, N., Gunn, D.J., 2002. *Solids hold up in gas fluidized beds*. Chemical Engineering and Processing 41, 373-379.
- Hillgardt, K., Werther, J., 1986. *Local bubble gas hold-up and expansion of gas/solid fluidized beds*. German Chemical Engineering 9, 215-221.
- Hoehne, O.; Lechner, S.; Schreiber, M.; Krautz, H.J. 2010. *Drying of lignite in a pressurized steam fluidized bed – Theory and Experimentation*. Drying Technology 28, 5-19.
- Hoffmann, A.C. and Yates, J.G., 1986, *Experimental observations of fluidized beds at elevated pressures*. Chemical Engineering Communications 41, 133-149.
- Hoomans, B.P.B., Kuipers, J.A.M., Briels, W.J., van Swaaij, W.P.M., 1996. *Discrete particle simulation of bubble and slug formation in a two-dimensional gas-fluidized bed: A hard-sphere approach*. Chemical Engineering Science 51, 99-118.
- Hoomans, B.P.B. 2000. *Granular Dynamics of Gas-Solid Two-Phase Flows*, PhD Thesis, University of Twente, Netherlands.
- Horio, M., Nonaka, A., 1987. *A generalized bubble diameter correlation for gas-solid fluidized beds*. AIChE Journal 33, 1865-1872.
- Hrenya, C.M., Sinclair, J.L., 1997. *Effect of particle-phase turbulence in gas-solid flows*. AIChE Journal 43, 853-869.

- Huilin, L., Yurong, H., Wentie, L., Ding, J., Gidaspow, D., Bouillard, J., 2004. *Computer simulations of gas-solid flow in spouted beds using kinetic-frictional stress model of granular flow*. Chemical Engineering Science 59, 865-878.
- Hull, A.S., Chen, Z., Fritz, J.W., Agarwal, P.K., 1999. *Influence of horizontal tube banks on the behavior of bubbling fluidized beds: 1. bubble hydrodynamics*. Powder Technology 103, 230-242.
- Hull, A.S., Chen, Z., Agarwal, P.K., 2000. *Influence of horizontal tube banks on the behavior of bubbling fluidized beds: 2. mixing of solids*. Powder Technology 111, 192-199.
- Hulme, I., Kantzas, A., 2004. *Determination of bubble diameter and axial velocity for a polyethylene fluidized bed using X-ray fluoroscopy*. Powder Technology 147, 20-33.
- Hulme, I., Clavelle, E., van der Lee, L., Kantzas, A., 2005. *CFD modeling and validation of bubble properties for a bubbling fluidized bed*. Industrial & Engineering Chemistry Research 44, 4254-4266.
- Ishii, M., 1975. *Thermo-Fluid Dynamic Theory of Two-Phase Flow*. Eyrolles, Paris
- Ishida, M., Shirai, T., 1980. *Measurement of the velocity and direction of flow of solid particles in a fluidized bed*. Powder Technology 27, 1-6.
- Jackson, R., 1963. *The mechanics of fluidized beds I. The stability of the state of uniform fluidization*. Transactions of the Institution Chemical Engineering 41, 13-28.
- Jackson, R., 1997. *Locally averaged equations of motion for a mixture of identical spherical particles and a Newtonian fluid*. Chemical Engineering Science 52, 2457-2469.
- Jenkins, J.T., Savage, S.B., 1983. *A Theory for the rapid flow of identical, smooth, nearly elastic, spherical particles*. Journal of Fluid Mechanics 130, 187-202.
- Johnsson, F., Andersson, S., Lecker, B., 1991. *Expansion of freely bubbling fluidized bed*. Powder Technology 68, 117-123.
- Johansson, K., van Wachem, B.G.M., Almstedt, A.E., 2006. *Experimental validation of CFD models for fluidized beds: Influence of particle stress models, gas phase compressibility and air inflow models*. Chemical Engineering Science 61, 1705-1717.

- Johansson, K., Norling, R., Almstedt, A.E., Johnsson, F., Nylund, A., 2004. *Hydrodynamics and steel tube wastage in a fluidized bed at elevated temperature*. Chemical Engineering Science 59, 31-40.
- Johnson, P.C., Nott, P., Jackson, R., 1990. *Frictional-collisional equations of motion for particulate flows and their application to chutes*. Journal of Fluid Mechanics 210, 501-535.
- Johnson, P.C., Jackson, R., 1987. *Frictional-collisional constitutive relations for granular materials, with application to plane shearing*. Journal of Fluid Mechanics 176, 67-93.
- Johnsson, H., Johnsson, F., 2001. *Measurements of local solids volume-fraction in fluidized bed boilers*. Powder Technology 115, 13-26.
- Kaart, S., Schouten, J., van den Bleek, C., 1999. *Improving conversion and selectivity of catalytic reactions in bubbling gas-solid fluidized bed reactors by control of the nonlinear bubble dynamics*. Catalysis Today 48, 185-194.
- Kai, T., Misawa, M., Takahashi, T., Tiseanu, I., Ichikawa, N., Takada, N., 2000. *Application of fast X-ray CT scanner to visualization of bubbles in fluidized bed*. Journal of Chemical Engineering of Japan 33, 906-909.
- Kai, T., Misawa, M., Takahashi, T., Tiseanu, I., Ichikawa, N., 2005. *Observation of 3-D structure of bubbles in a fluidized catalyst bed*. The Canadian Journal of Chemical Engineering 83, 113-118.
- Kantzas, A., 1994. *Computation of holdups in fluidized and trickle beds by computer-assisted tomography*. A.I.Ch.E. Journal 40, 1254-1261.
- Kantzas, A., Wright, I., Bhargava, A., Li, F., Hamilton, K., 2001. *Measurement of hydrodynamic data of gas-phase polymerization reactors using non-intrusive methods*. Catalysis Today 64, 189-203.
- Karimipour, S., Pugsley, T., 2011. *A critical evaluation of literature correlations for predicting bubble size and velocity in gas-solid fluidized beds*. Powder Technology 205, 1-14.
- Karthikeyan, M., 2008. *Minimization of moisture readsorption in dried coal samples*. Drying Technology 26, 948-955.
- Karthikeyan, M.; Zhonghua, W.; Mujumdar, A.S., 2009. *Low-rank coal drying technologies - current status and new developments*. Drying Technology 27, 403-405.

- Kawaguchi, T., Tanaka, T. and Tsuji, Y., 1998. *Numerical simulation of two-dimensional fluidized beds using the discrete element method (comparison between the two and three dimensional models)*. Powder Technology 96, 129-138.
- Kim, S.W., Ahn, J.Y., Kim, S.D., Lee, D.H., 2003. *Heat transfer and bubble characteristics in a fluidized bed with immersed horizontal tube bundle*. International Journal of Heat and Mass Transfer 46, 399-409.
- Klutz, H.-J., Klöcker, K.-J., Lambertz, J., 1996. *Das WTA-Verfahren als Vortrocknungsstufe für moderne Kraftwerkskonzepte auf Basis Braunkohle*. VGB Kraftwerkstechnik 76, Nr.3.
- Klutz, H.-J., 2008. *Theoretische und experimentelle Untersuchungen zur Entwicklung eines Wirbelschichttrockners für Braunkohle*. Dissertation, TU Hamburg-Harburg.
- Klutz, H.-J., Moser, C., Block, D., 2010. *Stand der Entwicklung der Wirbelschicht-Trocknung mit interner Abwärmenutzung (WTA) für Braunkohle bei der RWE AG*. Kraftwerkstechnik, Dresden.
- Krishna, R., van Baten, J.M., Urseanu, M.I., Ellenberger, J., 2000. *Rise velocity of single circular-cap bubbles in two-dimensional beds of powders and liquids*. Chemical Engineering and Processing 39, 433-440.
- Kuipers, J.A.M., van Swaaij, W.P.M., 1998. *Computational fluid dynamics applied to chemical reaction engineering*. Advances in Chemical engineering 24, 227-328.
- Kuipers, J.A.M., van Duin K.J., van Beckum, F.P.H., van Swaaij, W.P.M., 1992. *A numerical model of gas-fluidized beds*. Chemical Engineering Science 47, 1913-1924.
- Kuipers, J.A.M., van Duin K.J., van Beckum, F.P.H., van Swaaij, W.P.M., 1993. *Computer simulation of the hydrodynamics of a two-dimensional gas-fluidized bed*. Computers & Chemical Engineering 17, 839-858.
- Kumar, S.B., Dudukovic, M.P., 1997. *Computer assisted gamma and X-ray tomography: applications to multiphase flow systems*, in: J. Chaouki, F. Larachi, Dudukovic, M.P., (Eds.), Non-Invasive Monitoring of Multiphase Flows, Elsevier, New York.
- Kunii, D., Levenspiel, O., 1991. *Fluidization Engineering*, 2nd ed., Butterworth-Heineman, Boston.

- Laverman, J.A., Roghair, I., van Sint Annaland, M., Kuipers, H., 2008. *Investigation into the hydrodynamics of gas–solid fluidized beds using particle image velocimetry coupled with digital image analysis*. The Canadian Journal of Chemical Engineering 86, 523-535.
- Lechner, S., Höhne, O., Krautz, H.J., 2009. *Pressurized steam fluidized bed drying (PSFBD) of lignite: constructional and process optimization at the BTU test facility and experimental results*. Proceedings of the XII Polish Drying Symposium, Lodz, Poland, September 14-16, pp. 734-741.
- Leidich, F.U., Britenfelder, R., Mandel, H., Krautz, J., Gniazdowski, M., 2005. *Development of a Lignite-Fired Power Plant Concept with Integrated Pressurized Fluidized Bed Drying and Fuel Cells*. International Journal of Energy Technology and Policy 2, 39-49.
- Leithner, R., 2002. *zukünftige Entwicklungen in der Braunkohlen- Kraftwerkstechnik*. BWK 54, Nr. 12, 64-70.
- Li, T., Grace, J.R., Bi, X., 2010. *Study of wall boundary condition in numerical simulations of bubbling fluidized beds*. Powder Technology 203, 447-457.
- Lim, C.N., Gilbertson, M.A., Harrison, A.J.L., 2006. *Measurement and simulation of bubbling fluidized beds*. Powder Technology 170, 167-177.
- Lim, C.N., Gilbertson, M.A., Harrison, A.J.L., 2007. *Bubble distribution and behavior in bubbling fluidized beds*. Chemical Engineering Science 62, 56-69.
- Lim, K.S., Agarwal, P.K., O'Neill, B.K., 1990. *Experimental and modeling of bubble parameters in a two-dimensional gas-fluidized bed using imaging analysis*. Powder Technology 60, 159-171.
- Lim, K.S., Agarwal, P.K., 1990. *Conversion of pierced lengths measured at a probe to bubble size measures: an assessment of the geometrical probability approach and bubble shape models*. Powder Technology 63, 205-219.
- Lim, K.S., Agarwal, P.K., 1992. *Bubble velocity in fluidized beds: the effect of non-vertical bubble rise on its measurements using submersible probes and its relationship with bubble size*. Powder Technology 69, 239-248.
- Lim, K.S., Gururajan, V.S., Agarwal, P.K., 1993. *Mixing of homogenous solids in bubbling fluidized beds: theoretical modeling and experimental investigation using digital image analysis*. Chemical Engineering Science 48, 2251-2265.

- Lim, K.S., Zhu, J. X., Grace J.R., 1995. *Hydrodynamics of gas-solid fluidization*. International Journal of Multiphase Flow 21, Suppl. 141-193.
- Lindborg, H., Lysberg, M., Jakobsen, H.A., 2007. *Practical validation of the two-fluid model applied to dense gas–solid flows in fluidized beds*. Chemical Engineering Science 62, 5854-5869.
- Liu, J., Grace, J.R., Bi, X., 2003. *Novel multifunctional optical-fiber probe: I. development and validation*. AIChE Journal 49, 1405-1420.
- Liu, M., Zhang, Y., Bi, H., Grace, J.R., Zhu, Y., 2010. Non-intrusive determination of bubble size in a gas–solid fluidized bed: An evaluation. Chemical Engineering Science 65, 3485-3493.
- Llop, M.F., Casal, J., Arnaldos, J., 2000. *Expansion of gas-solid fluidized beds at pressure and high temperature*. Powder Technology 107, 212-225.
- Loew, O., Shmutter, B. Resnick, W., 1979. *Particle and bubble behavior and velocities in a large-particle fluidized bed with immersed obstacles*. Powder Technology 22, 45-57.
- Löfstrand, H., Almstedt, A.E., Andersson, S., 1995. *Dimensionless expansion model for bubbling fluidized beds with and without internal heat exchanger tubes*. Chemical Engineering Science 50, 245-253.
- Lun, C.K.K., Savage, S.B., Jeffrey, D.J., Chepuruiy, N., 1984. *Kinetic theories for granular flow: Inelastic particles in couette flow and slightly inelastic particles in a general flow field*. Journal of Fluid Mechanics 140, 223-256.
- Lun, C.K.K., Savage, S.B., 1986. *The effects of an impact velocity dependent coefficient of restitution on stresses developed by sheared granular materials*. Acta Mechanica 63, 15-44.
- Lyczkowski, R.W., Bouillard, J.X., Gamwo, I.K., Torpey, M.R., Montrone, E.D., 2010. *Experimental and CFD analyses of bubble parameters in a variable-thickness fluidized bed*. Industrial & Engineering Chemistry Research 49, 5166-5173.
- Lyczkowski, R.W., Bouillard, J.X., Berry, G.F., 1987. *Erosion calculations in a two-dimensional fluidized bed*. In: Proceedings of the 9th International Conference on Fluidized Bed Combustion, Boston, pp. 697-706.

- Lyczkowski, R.W., Folga, S., Chang, S.L., Bouillard, J.X., Wang, C.S., Berry, G.F., Gidaspow, D., 1989. *State-of-the-art computation of dynamics and erosion in fluidized bed tube banks*. In: Proceedings of the 10th International Conference on Fluidized Bed Combustion, San Francisco, pp. 465-478.
- Ma, D., Ahmadi, G., 1986. *An equation of state for dense rigid sphere gases*. Journal of Chemical Physics 84, 3449-3450.
- Mainland, M.E., Welty, J.R., 1995. *Use of optical probes to characterize bubble behavior in gas-solid fluidized beds*. AIChE Journal 41, 223-228.
- Makkawi, Y.T., Wright, P.C., 2004. *Tomographic analysis of dry and semi-wet bed fluidization: the effect of small liquid loading and particle size on the bubbling behavior*. Chemical Engineering Science 59, 201-213.
- Makkawi, Y., Ocone, R., 2007. *Integration of ECT measurements with hydrodynamic modeling of conventional gas-solid bubbling bed*. Chemical Engineering Science 62, 4304-4315.
- Makkawi, Y., Duncan, J., McAndrew, M., Ocone, R., 2007. *Drying of Moist Solid Particulate in a Bubbling Fluidized Bed*. ECI Conference on the 12th International Conference on Fluidization - New Horizons in Fluidization Engineering Vancouver, Canada
- Martin, J., Höhne, O., Lechner, S., Krautz, H.J., Jentsch, N., 2007. *Druckaufgeladene Dampfwirbelschicht-Trocknung (DDWT) von Braunkohlen: Von den Betriebsergebnissen des Versuchstrockners (0.5 t/h) zur Konzeptentwicklung der Großtechnischen Versuchsanlage (GTVA, 70 t/h)*. 39. Kraftwerkstechnischen Kolloquium, Dresden.
- Matsuura, A., Fan, L.S., 1984. *Distribution of bubble properties in gas-liquid-solid fluidized bed*. AIChE Journal 30, 894-903.
- McKeen, T., Pugsley, T., 2003. *Simulation and experimental validation of a freely bubbling bed of FCC catalyst*. Powder Technology 129, 139-152.
- Mudde, R.F., Schulte, H.B.M., van den Akker, H.E.A., 1994. *Analysis of a bubbling 2-D gas-fluidized bed using image processing*. Powder Technology 81, 149-159.
- Mudde, R.F., 2010. *Time-resolved X-ray tomography of a fluidized bed*. Powder Technology 199, 55-59.

- Mujumdar, A.S., 2006. *Handbook of Industrial Drying*. Taylor and Francis Group, LLC.
- Murray, J.D., 1965. *On the mathematics of fluidization Part I. Fundamental equations and wave propagation*. Journal of Fluid Mechanics 21, 465-493.
- Neri, A., Gidaspow, D., 2000. *Riser hydrodynamics: Simulation using kinetic theory*. AIChE Journal 46, 52-67.
- Nieuwland, J.J., van Sint Annaland M., Kuipers, J.A.M., van Swaaij, W.P.M., 1996. *Hydrodynamic modeling of gas/particle flows in riser reactors*. AIChE Journal 42, 1569-1582.
- Olowson, P.A., 1994. *Influence of pressure and fluidization velocity on the hydrodynamics of a fluidized bed containing horizontal tubes*. Chemical Engineering Science 49, 2437-2446.
- Olsson, S.E., Wiman, J., Almstedt, A.E., 1995. *Hydrodynamics of a pressurized fluidized bed with horizontal tubes: influence of pressure, fluidization velocity and tube-bank geometry*. Chemical Engineering Science 50, 581-592.
- Olowson, P.A. and Almstedt, A.E., 1990. *Influence of pressure and fluidization velocity on the bubble behavior and gas flow distribution in a fluidized bed*. Chemical Engineering Science 45, 1733-1741.
- Olowson, P.A., Almstedt, A.E. 1992. *Hydrodynamics of a bubbling fluidized bed: influence of pressure and fluidization velocity in terms of drag force*. Chemical Engineering Science 47, 357-366.
- Olsson, S.E., Almstedt, A.E., 1995. *Local instantaneous and time-averaged heat transfer in a pressurized fluidized bed with horizontal tubes: Influence of pressure, fluidization velocity and tube-bank geometry*. Chemical Engineering Science 50, 3231-3245.
- Orr, C., Jr., 1966. *Particulate Technology*. Macmillan, New York.
- Ouyang, J., Li, J., 1999. *Discrete simulation of heterogeneous structure and dynamic behavior in gas-solid fluidization*. Chemical Engineering Science 54, 5427-5440.
- Owoyemi, O., Lettieri, P., 2005. *Experimental validation of Eulerian-Eulerian simulations of Rutile industrial powders*. Industrial & Engineering Chemistry Research 44, 9996-10004.
- Pain, C.C., Mansoorzadeh, S., de Oliveira, C.R.E., Goddard, A.J.H., 2001a. *Numerical modeling of gas-solid fluidized beds using the two-fluid model*. International Journal for Numerical Methods in Fluids 36, 91-124.

- Pain, C.C., Mansoorzadeh, S., de Oliveira, C.R.E., 2001b. *A Study of bubbling and slugging fluidized beds using the two-fluid granular temperature model*. International Journal of Multiphase Flow 27, 527-551.
- Pain, C.C., Mansoorzadeh, S., Gomes, J.L.M., de Oliveira, C.R.E., 2002. *A numerical investigation of bubbling gas-solid fluidized bed dynamics in 2D geometries*. Powder Technology 128, 56-77.
- Park, A.-H., Bi, H., Grace, J.R., 2002. *Reduction of electrostatic charges in gas–solid fluidized beds*. Chemical Engineering Science 57, 153-162.
- Passalacqua, A., Marmo, L., 2009. *A critical comparison of frictional stress models applied to the simulation of bubbling fluidized beds*. Chemical Engineering Science 160, 2795-2806.
- Patankar, S.V., 1980. *Numerical Heat Transfer and Fluid Flow*. Taylor & Francis.
- Patil, D.J., van Sint Annaland, M., Kuipers, J.A.M., 2005a. *Critical comparison of hydrodynamic models for gas-solid fluidized beds - Part I: Bubbling gas-solid fluidized beds operated with a jet*. Chemical Engineering Science 60, 57-72.
- Patil, D.J., van Sint Annaland, M., Kuipers, J.A.M., 2005b. *Critical comparison of hydrodynamic models for gas-solid fluidized beds - Part II: Freely bubbling gas-solid fluidized beds*. Chemical Engineering Science 60, 73-84.
- Peirano, E., Delloume, V., Leckner, B., 2001. *Two- or three-dimensional simulations of turbulent gas-solid flows applied to fluidization*. Chemical Engineering Science 56, 4787-4799.
- Pikon, J.; Mujumdar, A.S., 2006. *Drying of coal*. In *Handbook of industrial drying*, 3rd Ed.; Mujumdar, A.S., Ed.; Taylor and Francis Group, LLC, CRC Press; Boca Raton, Florida, pp. 993-1016.
- Pita, J.A., Sundaresan, S., 1991. *Gas-solid flow in vertical tubes*. AIChE Journal 37, 1009-1018.
- Potter, O.E., Beeby, C.J., Fernando, W.J.N., Ho, P., 1983. *Drying brown coal in steam-heated, steam-fluidized beds*. Drying Technology 2, 219- 234.
- Potter, O.E , Guang, Li Xi , Georgakopoulos, S., Ming, M.Q., 1990. *Some design aspects of steam-fluidized steam heated dryers*. Drying Technology 8, 25-39.

- Prieto, J.J., García, M., Ramos G., Guardiola, J., 2003. *Evolution of the Population of Bubbles in 2D Fluidized Beds*. The Canadian Journal of Chemical Engineering 81, 1232- 1238.
- Pugsley, T, Tanfara, H., Malcus, S., Cui, H., Chaouki, J., Winters C., 2003. *Verification of fluidized bed electrical capacitance tomography measurements with a fiber optic probe*. Chemical Engineering Science 58, 3923-3934.
- Rafailidis, S.V., Clift, R., Addis, E.J., Bagshaw, W., Cheesman, D.J., Yates, J.G., 1992. *The effect of horizontal tubes on bubble motion*. In Fluidization VII, Potter, O.E., Nicklin, D.J.,(Eds), Engineering Foundation New York.
- Ramayya, A. V., Venkateshan, S.P., Kolar, A. K., 1996. *Estimation of bubble parameters from differential pressure measurements in gas-fluidized beds*. Powder Technology 87, 113-126.
- Ramayya, A. V., Venkateshan, S.P., Kolar, A. K., 1998. *Bubble detection with horizontal pressure gradient measurements in gas-fluidized beds*. Powder Technology 97, 77-84.
- Reay, D., 1986. *Fluid bed drying* In Gas Fluidization Technology, Geldart (Ed) John Wiley & Sons Ltd., Chichester.
- Reuge, N., Cadoret, L., Coufort-Saudejaud, C., Pannala, S., Syamlal, M., Caussat, B., 2008. *Multifluid Eulerian modeling of dense gas-solid fluidized bed hydrodynamics: Influence of the dissipation parameters*. Chemical Engineering Science 63, 5540-5551.
- Rong D., Horio M., 2001. *Behavior of particles and bubbles around immersed tubes in a fluidized bed at high temperature and pressure: a DEM simulation*. International Journal of Multiphase Flow 27, 89-105.
- Rowe, P.N, MacGillivray, H.J., Cheesman, D.J., 1979. *Gas discharge from an orifice into a gas fluidized bed*. Transactions of the Institution Chemical Engineering 57, 194-199.
- Rowe, P.N, Masson, H, 1981. *Interaction of bubbles with probes in gas fluidized beds*. Transactions of the Institution Chemical Engineering 59, 177-185.
- Rowe, P.N., Partridge, B.A. 1965. *An X-ray study of bubbles in fluidized beds*. Transactions of the Institution Chemical Engineering 43, 157-165.
- Safoniuk, M., Grace, J.R., Lim K-S., 2002. *Bubble characteristics of a scaled-down three-phase fluidized bed*. The Canadian Journal of Chemical Engineering 80, 177-185.

- Samuelsberg, A., Hjertager, B.H., *Computational modeling of gas/particle flow in a riser*. AIChE Journal 42, 1536-1546.
- Santana, D., Macias-Machin, A., 2000. *Local bubble-size distribution in fluidized beds*. AIChE Journal. 46, 1340-1347.
- Schaeffer, D.G., 1987. *Instability in the evolution equations describing incompressible granular flow*. Journal of Differential Equations 66, 19-50.
- Schmidt, A., Renz, U., 2005. *Numerical prediction of heat transfer in fluidized beds by a kinetic theory of granular flows. International*. Journal of Thermal Science 39, 871-885.
- Schmidt, A., Renz, U., 2005. *Numerical prediction of heat transfer between a bubbling fluidized bed and an immersed tube bundle*. Heat Mass Transfer 41, 257-270.
- Schweitzer, J.-M., Bayle, J., Gauthier, T., 2001. *Local gas hold-up measurements in fluidized bed and slurry bubble column*. Chemical Engineering Science 56, 1103–1110.
- Shen, L., Johnsson, F., Leckner, B., 2004. *Digital image analysis of hydrodynamics two-dimensional bubbling fluidized beds*. Chemical Engineering Science 59, 2607-2617.
- Shuyan, W., Xiang, L., Huilin, L., Long, Y., Dan, S., Yurong, H., Yonglong, D., 2009. *Numerical simulations of flow behavior of gas and particles in spouted beds using frictional-kinetic stresses model*. Powder Technology 196, 184-193.
- Simons, S.J.R., 1995. *Imaging techniques for fluidized bed systems: A review*. Chemical Engineering Journal 56, 83-93.
- Sinclair, J.L., Jackson, R., 1989. *Gas-particle flow in a vertical pipe with particle-particle interactions*. AIChE Journal 35, 1473-1486.
- Sitnai, O., Whitehead, A.B., 1985. *Immersed tubes and other internals*, in: Davidson, J.F., Clift, R., Harrison, D. (Eds.), Fluidization, 2nd Edition, Academic Press, London, pp. 473-493.
- Sitnai, O., 1982. *Utilization of the pressure differential records from gas fluidized beds with internals for bubble parameters determination*. Chemical Engineering Science 37, 1059-1066.
- Sobrinho, C., Acosta-Iborra, A., Santana, D., de Vega, M., 2009. *Bubble characteristics in a bubbling fluidized bed with a rotating distributor*. International Journal of Multiphase Flow 35, 970–976.

- Soo, S.L., 1967. *Fluid Mechanics of Multiphase Systems*, Blaisdell Publishing Co., Waltham, MA.
- Staub, F.W., Canada, G.S., 1978. *Effect of tube bank and gas density on flow behavior and heat transfer in fluidized beds*, Fluidization, Eds, Xavier, A.M., Davidson J.F., Cambridge University Press, pp. 339-344.
- Syamlal, M., O'Brien, T.J., 1989. *Computer simulation of bubbles in a fluidized bed*. AIChE Symposium Series 85, 22-31.
- Syamlal, M., Rogers, W., O'Brien, T.J., 1993. *MFIX Documentation: Theory guide*. National Technical Information Service, DOE/METC-94/1004, Springfield.
- Syamlal, M.; O'Brien, T. J. 2003. *Fluid dynamic simulation of O₃ decomposition in bubbling fluidized bed*. AIChE Journal 49, 2793-2801.
- Taghipour, F., Ellis, N., Wong, C., 2005. *Experimental and computational study of gas-solid fluidized bed hydrodynamics*. Chemical Engineering Science 60, 6857-6867.
- Toomey, R.D., Johnstone, H.F., 1952. *Gaseous fluidization of solid particles*. Chemical Engineering Progress 48, 220-226.
- Tsuji, Y., Kawaguchi, T., and Tanaka, T., 1992. *Lagrangian numerical simulation of plug flow of cohesionless particle in a horizontal pipe*. Powder Technology 71, 239-250.
- Tsuji, Y., Kawaguchi, T., and Tanaka, T., 1993. *Discrete particle simulation of two-dimensional fluidized bed*, Powder Technology 77, 79-87.
- Tsuo, Y., Gidaspow, D., 1990. *Computation of flow patterns in circulating fluidized beds*. AIChE Journal 36, 885-896.
- Utikar, R.P., Ranade, V.V., 2007. *Single jet fluidized bed: Experiments and CFD simulations with glass and polypropylene particles*. Chemical Engineering Science 62, 167-183.
- van der Hoef, M.A., van Sint Annaland, M., Deen, N.G., Kuipers, J.A.M., 2008. *Numerical simulation of dense gas-solid fluidized beds: A multiscale modeling strategy*. Annual Review of Fluid Mechanics 40, 47-70.
- van der Lee, L., Chandrasekaran, B., Hulme, I., Kantzas, A., 2005. *A non-invasive hydrodynamic study of gas-solid fluidized bed of linear low density polyethylene*. The Canadian Journal of Chemical Engineering 83, 119-126.

- van der Schaaf, J., Schouten, J.C., Johnson, F., van den Bleek, C.M., 2002. *Non-intrusive determination of bubble and slug length scales in fluidized beds by decomposition of the power spectral density of pressure time series*. International Journal of Multiphase Flow 28, 865-880.
- van Lare, C.E.J., Piepers, H.W., Schoonderbeek, J.N., Thoenes, D., 1997. *Investigation on bubble characteristics in a gas fluidized bed*. Chemical Engineering Science 52, 829-841.
- van Ommen, J.R., Mudde, R.F., 2008. *Measuring the gas-solids distribution in fluidized beds - A review*. International Journal of Chemical Reactor Engineering 6, R3.
- van Wachem, B.G.M., Schouten, J.C., Krishna, R., van den Bleek, C.M., 1998. *Eulerian simulation of bubbling behaviour in gas-solid fluidized beds*. Computers and Chemical Engineering 22, suppl. 1, S299-S306.
- van Wachem, B.G.M., Schouten, J.C., Krishna, R., van den Bleek, C.M., 1999. *Validation of the Eulerian simulated dynamic behaviour of gas-solid fluidized beds*. Chemical Engineering Science 54, 2141-2149.
- van Wachem, B.G.M., Schouten, J.C., van den Bleek, C.M., Krishna, R., Sinclair J.L., 2001. *Comparative analysis of CFD models of dense gas-solid systems*. AIChE Journal 47, 1035-1051.
- van Wachem, B.G.M., Almstedt, A.E., Methods for multiphase computational fluid dynamics. Chemical Engineering Journal 96, 81-98.
- Vasquez, S.A., Ivanov, V.A., 2000. *A phase coupled method for solving multiphase problems on unstructured meshes*. ASME FEDSM'00: ASME 2000 Fluid Engineering Division Summer Meeting.
- Vejahati, F., Mahinpey, N., Ellis, N., Nikoo, M.B., 2009. *CFD simulation of gas-solid bubbling fluidized bed: A new method for adjusting drag law*. The Canadian Journal of Chemical Engineering 87, 19-30.
- Viswanathan, K., Rao, D.S., 1984. *Measurement of bubble size in fluidized beds*. Industrial & Engineering Chemistry Process Design and Development 23, 573- 576.
- Wang, S.J., Dyakowski, T., Xie, C.G., Williams, R.A., Beck, M.S., 1995. *Real time capacitance imaging of bubble formation at the distributor of a fluidized bed*. The Chemical Engineering Journal, 56 95-100.

- Wang, J., van der Hoef, M.A., Kuipers, J.A.M., 2009. *Why the two-fluid model fails to predict the bed expansion characteristics of Geldart A particles in gas-solid fluidized beds: A tentative answer*. Chemical Engineering Science 64, 622-625.
- Weiss, J.M., Maruszewski, J.P., Smith, W.A., 1999. *Implicit solution of preconditioned Navier-Stokes equation using Algebraic Multigrid*. AIAA Journal 37, 29-36.
- Wen, C.Y., Yu, Y.H., 1966. *Mechanics of fluidization*. Chemical Engineering Progress Symposium Series 62, 100-111.
- Werther, J., 1999. *Measurement techniques in fluidized beds*. Powder Technology 102, 15-36.
- Werther, J., 1978. *Mathematische Modellierung von Wirbelschichtreaktoren*. Chemie-Ingenieur Technik 50, 850-860.
- Werther, J., Molerus, O., 1973. *The local structure of gas fluidized beds: I. A statistically based measuring system*. International Journal of Multiphase Flow 1, 103-122.
- Werther, J., Molerus, O., 1973. *The local structure of gas fluidized beds: II. The spatial distribution of bubbles*. International Journal of Multiphase Flow 1, 123-138.
- White, R.B., 2005. *Using Electrical Capacitance Tomography to Investigate Gas Solid Contacting*. The Canadian Journal of Chemical Engineering 83, 64-67.
- Wick, W., Kallmeyer, D., 1997. *Entwicklungsschritte zum trocken braunkohlebefeuerten Kraftwerk*. VGB Kraftwerkstechnik 77, 300-303.
- Wilson, W.J.; Walsh, D.; Irvin, W., 1997. *Overview of low rank coal drying*. Coal Preparation 18, 1-15.
- Wiman, J., Almstedt, A.E., 1997. *Hydrodynamics, erosion and heat transfer in a pressurized fluidized bed: Influence of pressure, fluidization velocity, particle size and tube bank geometry*. Chemical Engineering Science 52, 2677-2695.
- Wiman, J., Almstedt, A.E. 1998. *Influence of pressure, fluidization velocity and particle size on the hydrodynamics of a freely bubbling fluidized bed*. Chemical Engineering Science 53, 2167-2176.
- Wu, B., Yu, G., Bellehumeur, C, Kantzas, A., 2007a. *Dynamic flow behavior measurements in gas-solid fluidized beds using different non-intrusive techniques and polyethylene powder*. Flow Measurement and Instrumentation 18, 197-203.

- Wu, B., Shepperson, J., van der Lee, L., Bellehumeur, C., Kantzas, A., 2007b. *Hydrodynamics of Gas-Solids Bubbling Fluidized Beds Using Polyethylene Resin*. ECI Conference on the 12th International Conference on Fluidization - New Horizons in Fluidization Engineering Vancouver, Canada
- Xie, N., Battaglia, F., Pannala, S., 2008a. *Effects of using two- versus three-dimensional computational modeling of fluidized beds: Part I, hydrodynamics*. Powder Technology 182, 1-13.
- Xie, N., Battaglia, F., Pannala, S., 2008b. *Effects of using two- versus three-dimensional computational modeling of fluidized beds: Part II, budget analysis*. Powder Technology 182, 14-24.
- Xu, B.H., and Yu, A.B., 1997. *Numerical simulation of the gas-solid flow in a fluidized bed by combining discrete particle method with computational fluid dynamics*. Chemical Engineering Science. 52, 2785-2809.
- Yang, N., Wang, W., Ge, W., Wang, L., Li, J., 2004. *Simulation of heterogeneous structure in a circulating fluidized bed riser by combining the two-fluid model with the EMMS approach*, Industrial & Engineering Chemistry Research 43, 5548-5561.
- Yang, W.C., Chitester, D.C., Kronsoky, R.M., Keairns, D.L., 1985. *A generalized methodology for estimating minimum fluidization velocity at elevated pressure and temperature*. AIChE Journal 31, 1086-1092.
- Yates, J.G., Ruiz-Martinez, R.S., 1987. *Interaction between horizontal tubes and gas bubbles in a fluidized bed*. Chemical Engineering Communications 62, 67-78.
- Yates, J.G., Cheesman, D.J., Sergeev, Y.A., 1994. *Experimental observations of voidage distribution around bubbles in a fluidized bed*. Chemical Engineering Science 49, 1885-1895.
- Yates, J.G., Simons, S.J.R., 1994. *Experimental methods in fluidization research*. International Journal of Multiphase Flow 20, Suppl. 297-330.
- Yates, J.G., Ruiz-Martinez, R.S., Cheesman, D.J., 1990. *Prediction of size in a fluidized bed containing horizontal tubes*. Chemical Engineering Science 45, 1105-1111.
- Yerushalmi, J., Avidan, A., 1985. *High velocity fluidization*. In Davidson, J.F., Clift, R., Harrison, D. (Eds), Fluidization, 2nd Edition, Academic press, London.

-
- Yurong, H., Huilin, L., Qiaoqun, S., Lidan, Y., Yunhua, Z., Gidaspow, D., Bouillard, J., 2004. *Hydrodynamics of gas-solid flow around immersed tubes in bubbling fluidized beds*. Powder Technology 145, 88-105.
- Zarabi, T., Kantzas, A., 1998. *Predictions on bubble and solids movement in laboratory polyethylene fluid bed as visualized by X-ray computer assisted tomography (CAT) scanning*. The Canadian Journal of Chemical Engineering 76, 853-865.
- Zhang, Y., Reese J., 2003. *The drag force in two-fluid models of gas-solid flows*. Chemical Engineering Science 58, 1641-1644.
- Zhu, H.P., Zhou, Z.Y., Yang, R.Y., Yu, A.B., 2008. *Discrete particle simulation of particulate systems: A review of major applications and findings*. Chemical Engineering Science 63, 5728-5770.
- Zimmermann S., Taghipour, F., 2005. *CFD modeling of the hydrodynamics and reaction kinetics of FCC fluidized beds reactors*. Industrial & Engineering Chemistry Research 44, 9818-9827.

Appendices

Appendix A: Particle size distribution and mean particle size

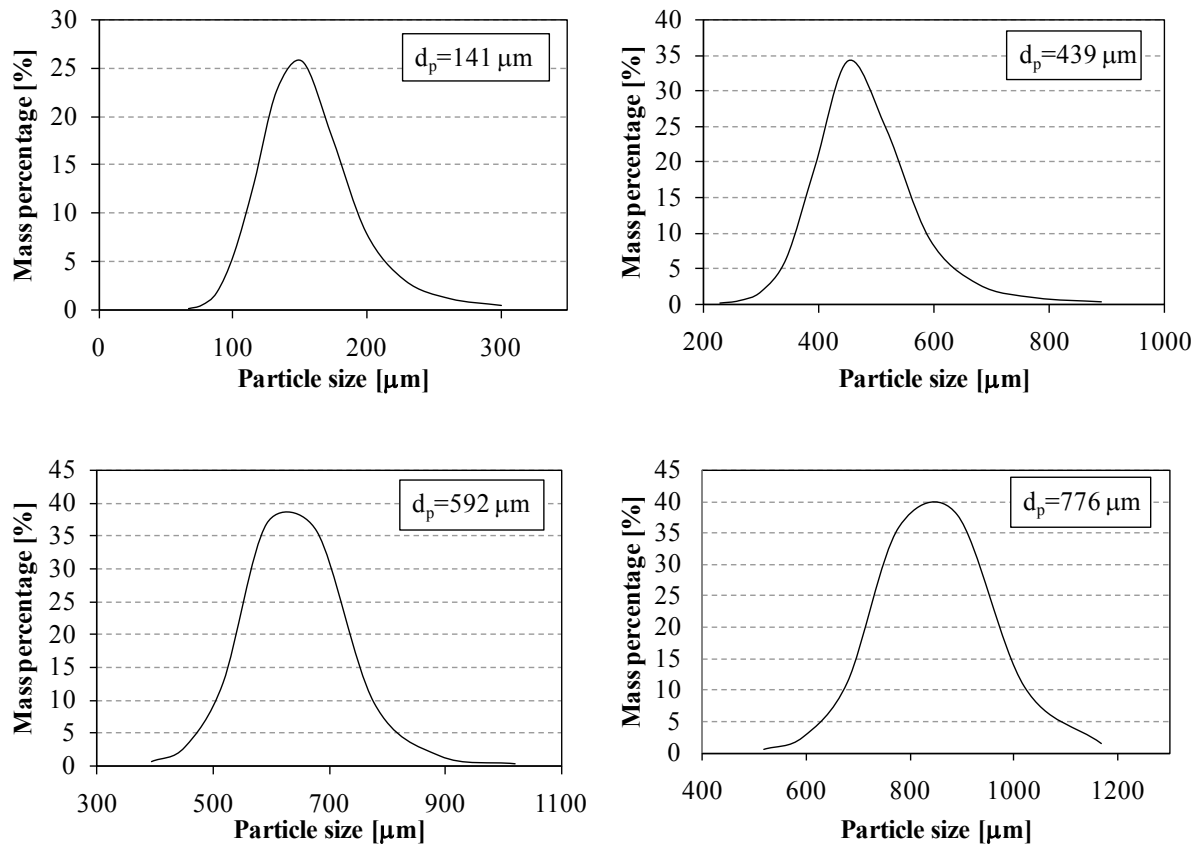


Figure A.1: Particle size distribution

Appendix B: Bed expansion ratio for the I6 case and comparison with Equation 5.25

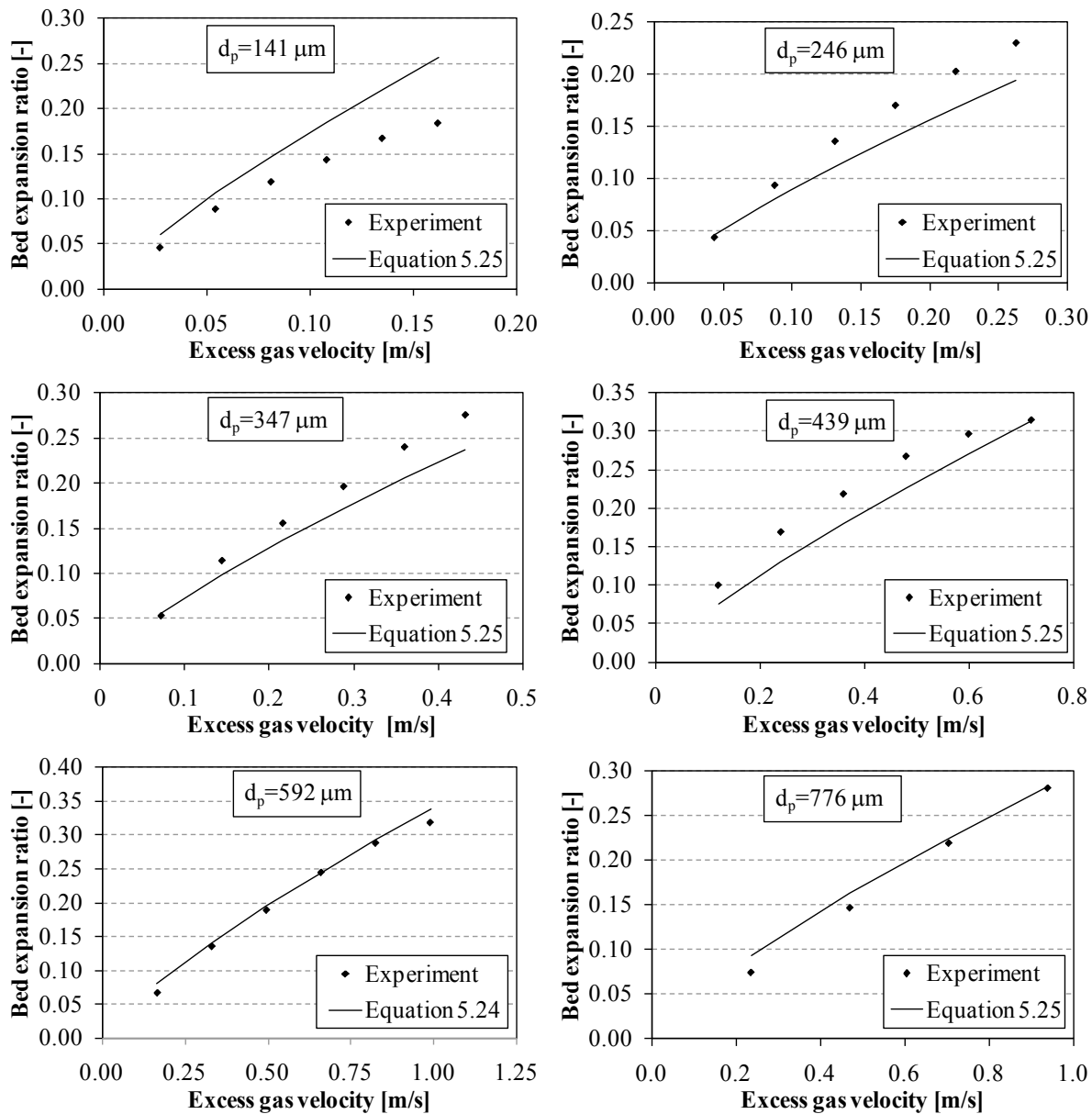


Figure B.1: Comparison of bed expansion ratio for the I6 case with model prediction of Equation 5.25.

Appendix C: Simulation results for the I6 case for validation of the TFM

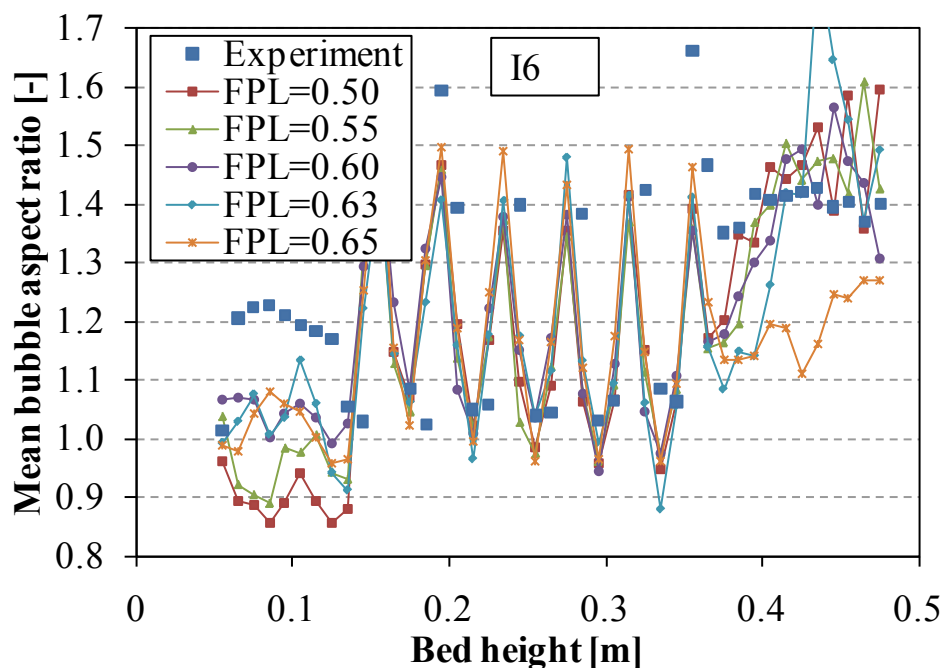


Figure C1: Comparison of mean bubble aspect ratio using different friction packing limits (FPL).

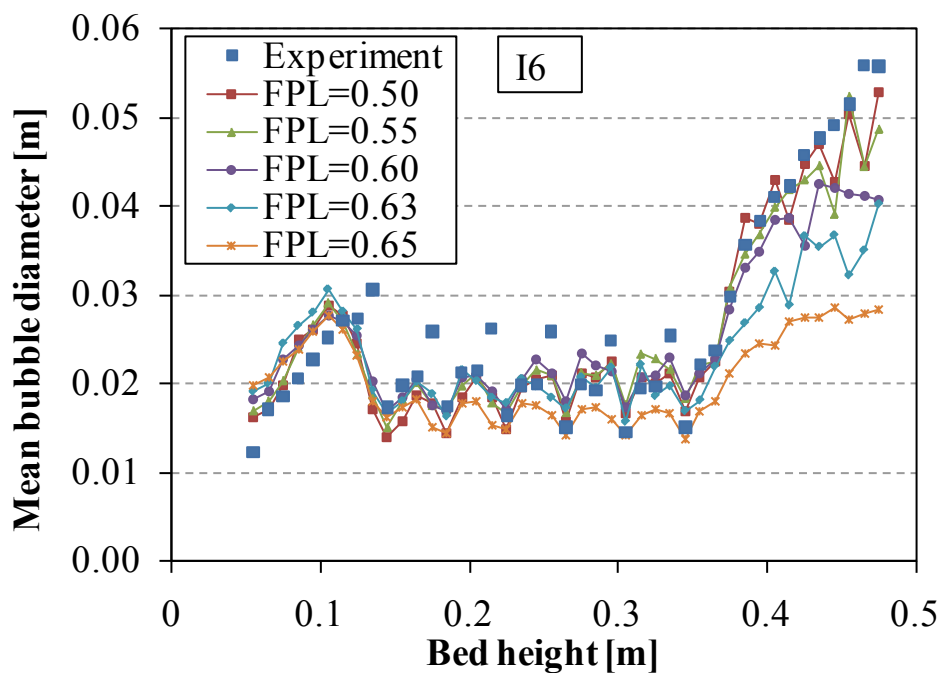


Figure C2: Comparison of mean bubble diameter using different friction packing limits (FPL).

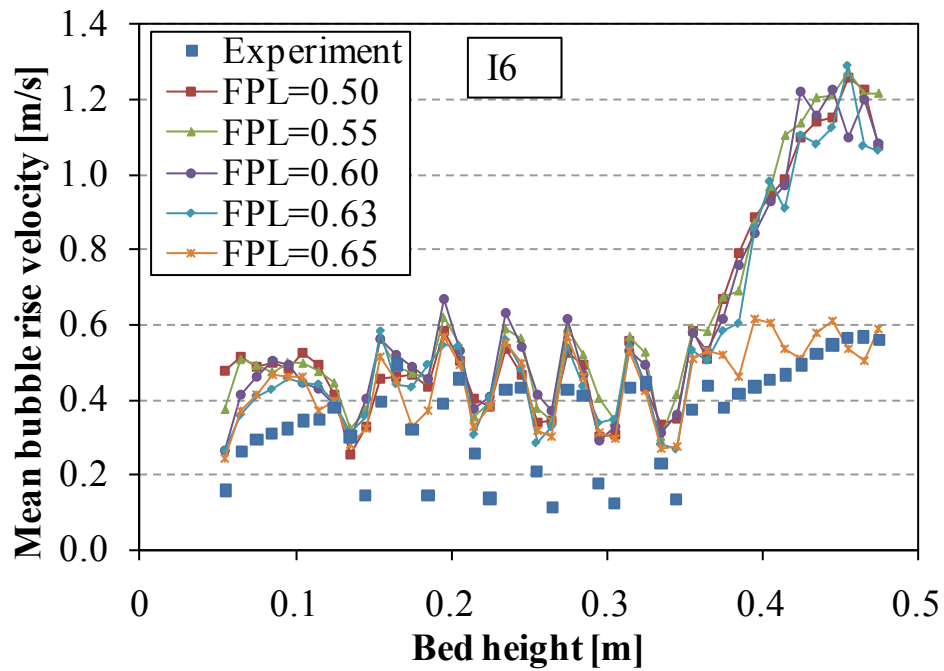


Figure C3: Comparison of mean bubble rise velocity using different friction packing limits (FPL).

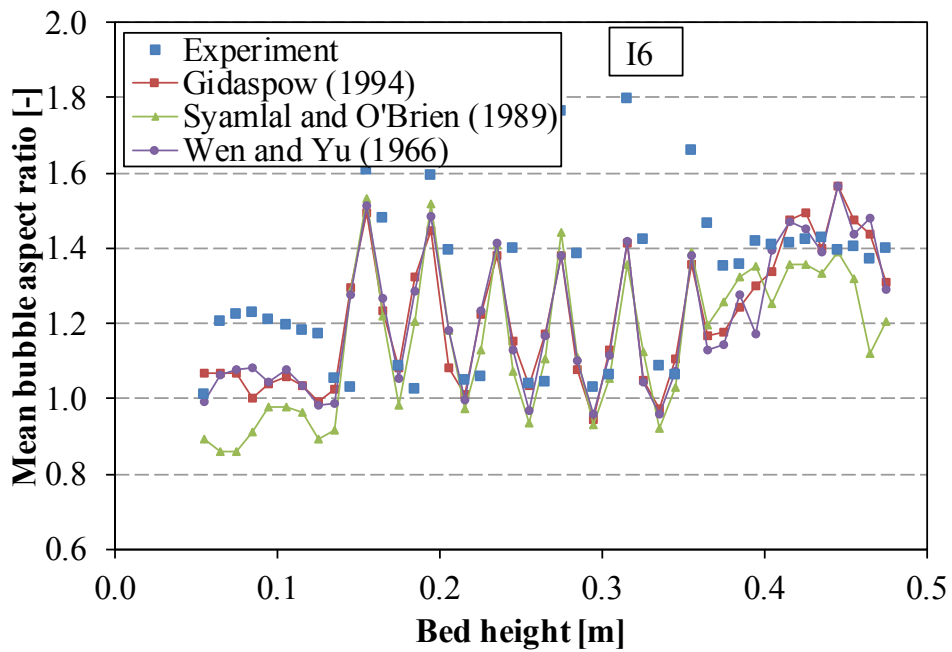


Figure C4: Comparison of mean bubble aspect ratio using different drag models.

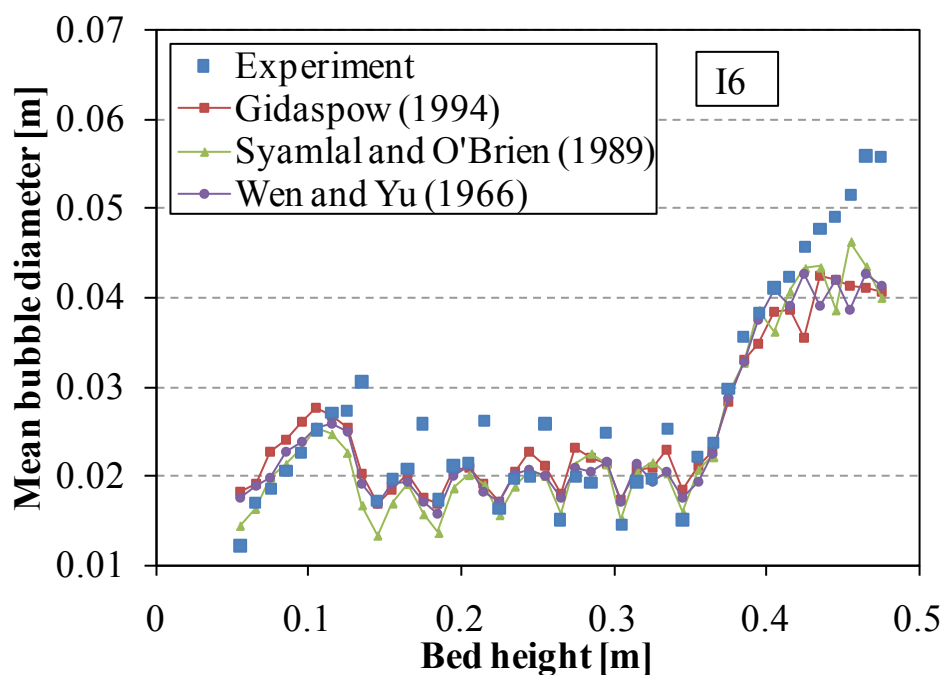


Figure C5: Comparison of mean bubble diameter using different drag models.

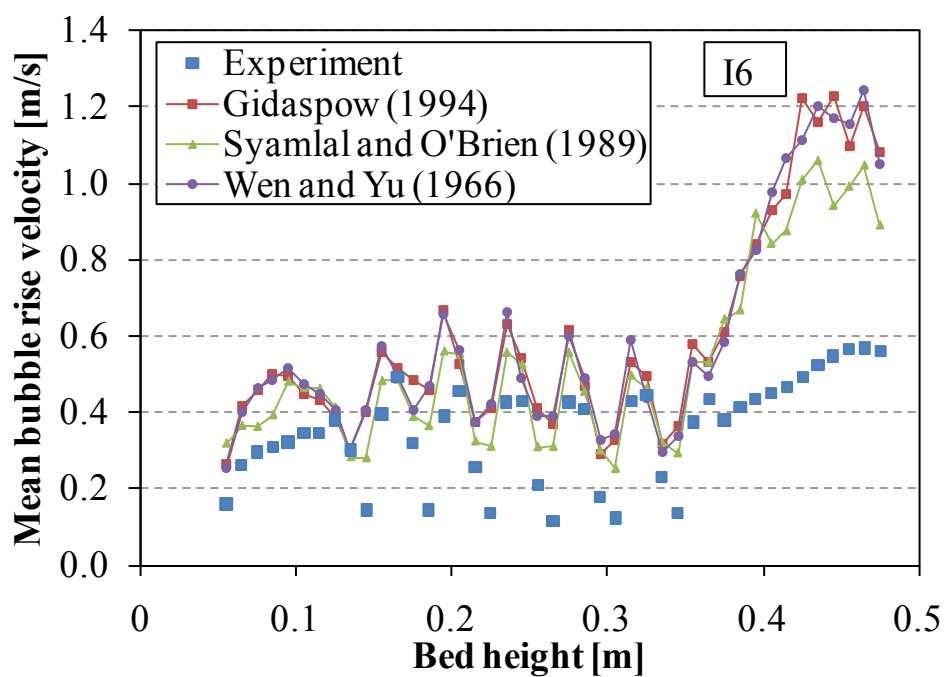


Figure C6: Comparison of mean bubble rise velocity using different drag models.

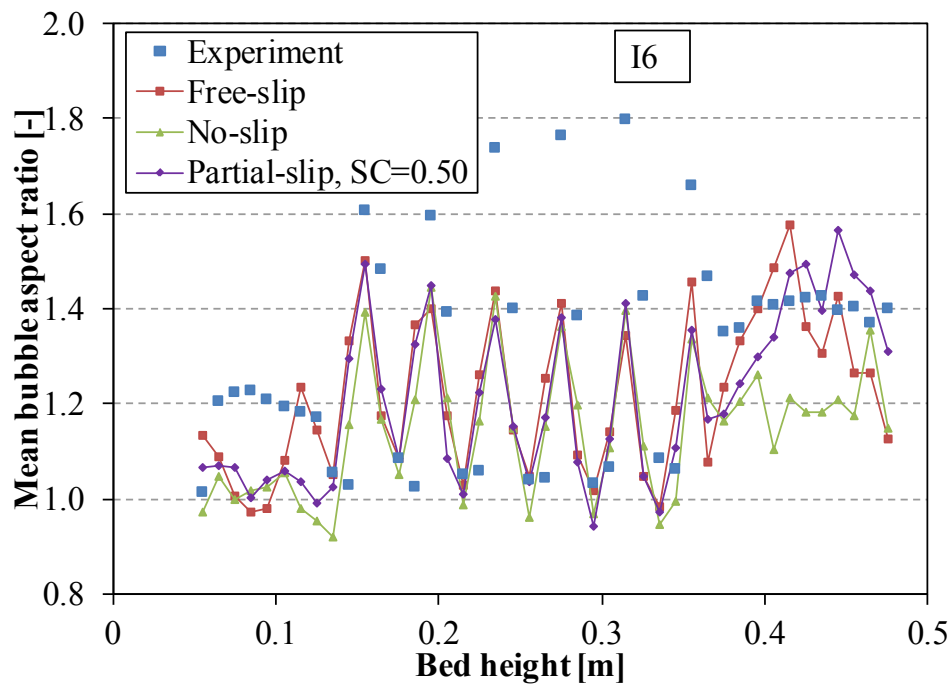


Figure C7: Comparison of mean bubble aspect ratio using different solid-wall boundary conditions.

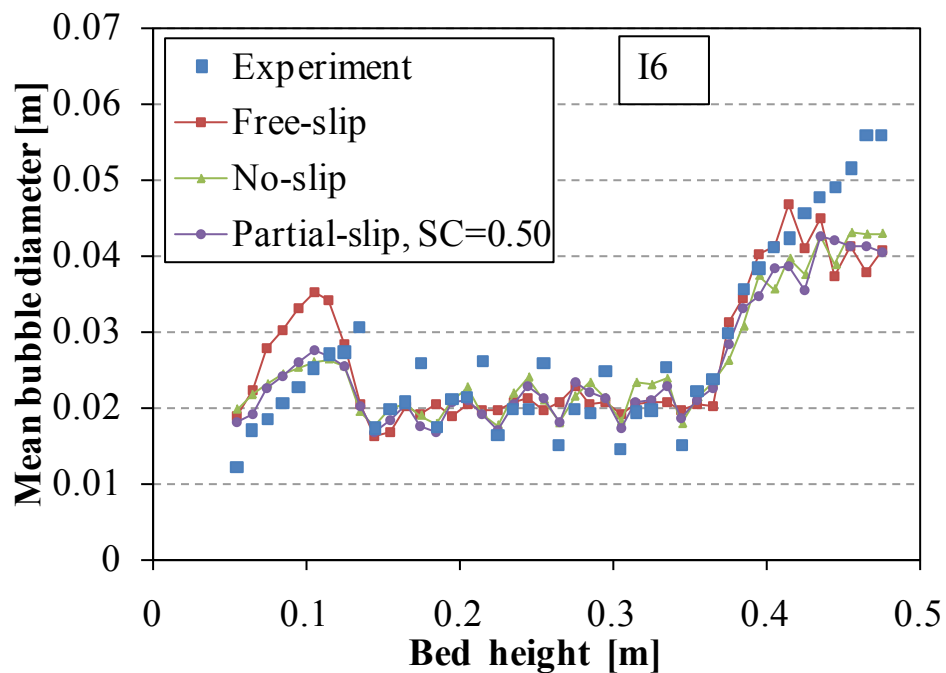


Figure C8: Comparison of mean bubble diameter using different solid-wall boundary conditions.

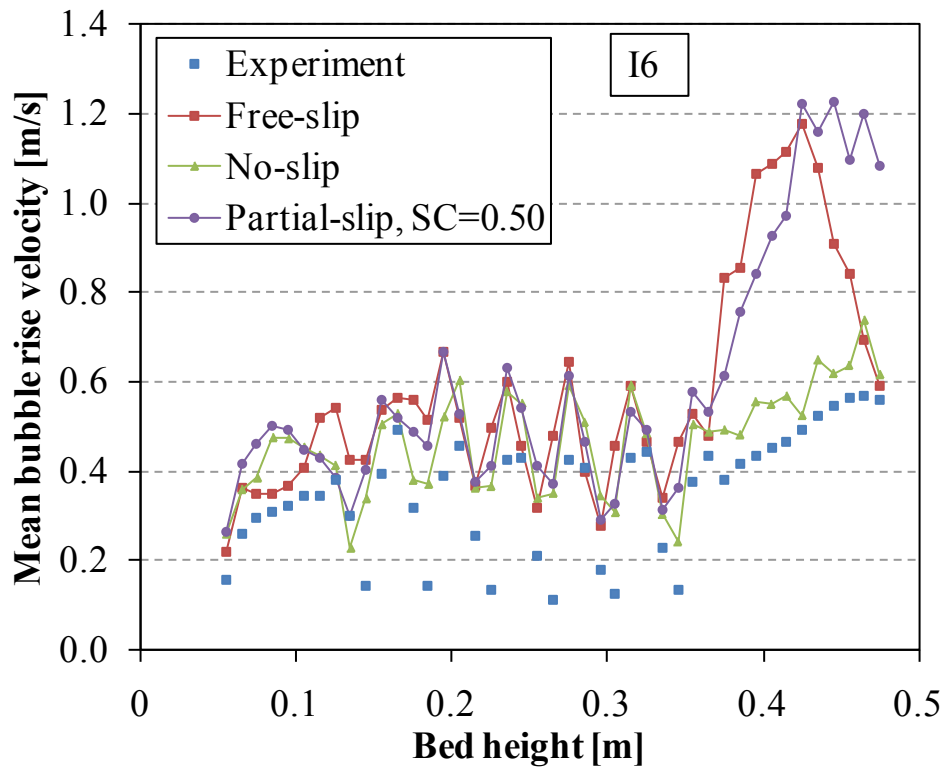
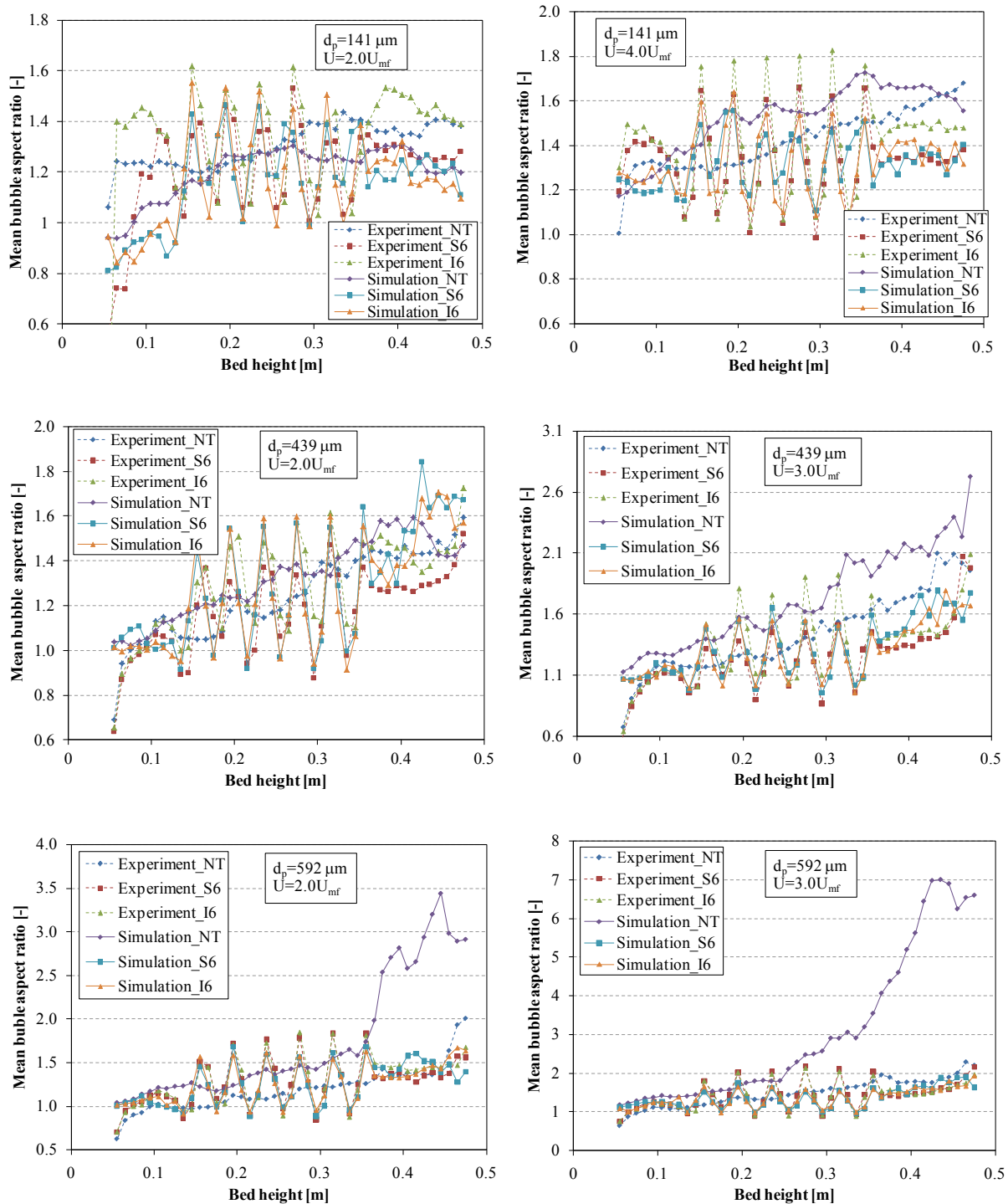
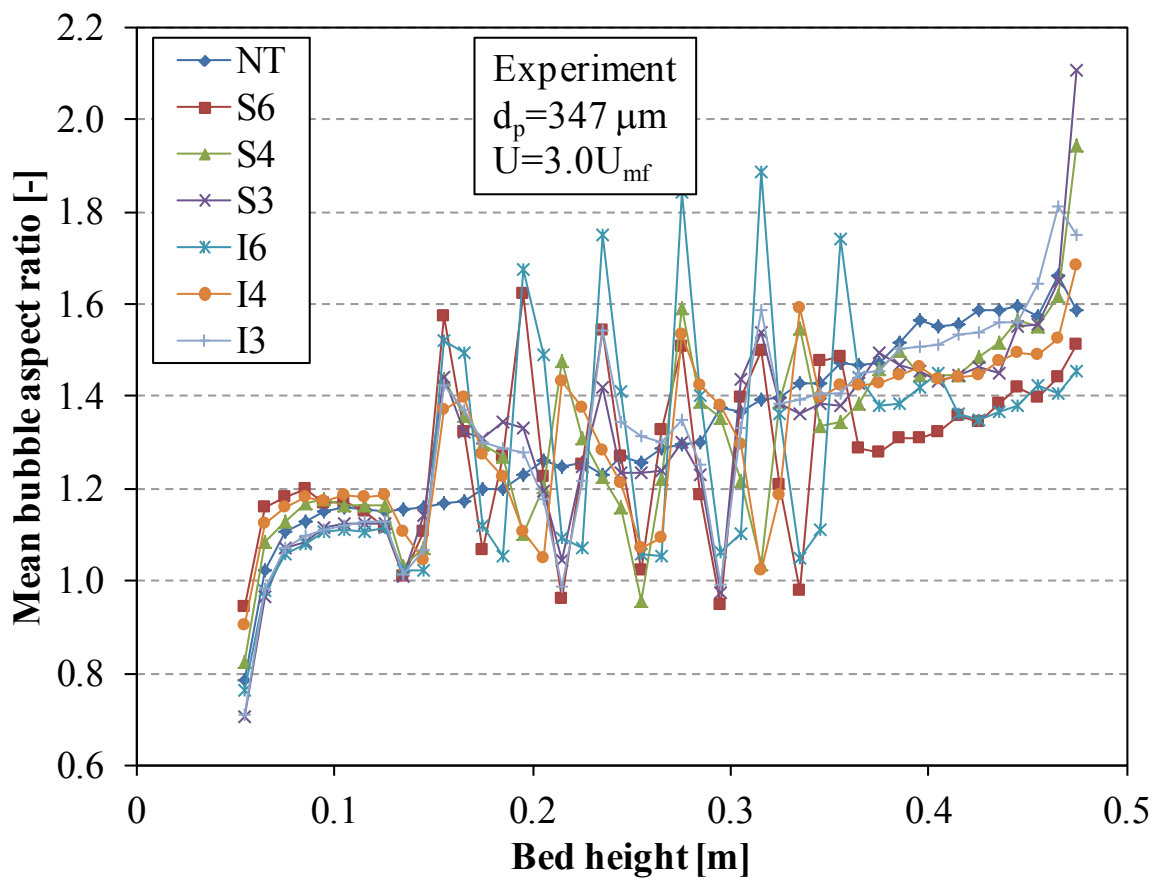
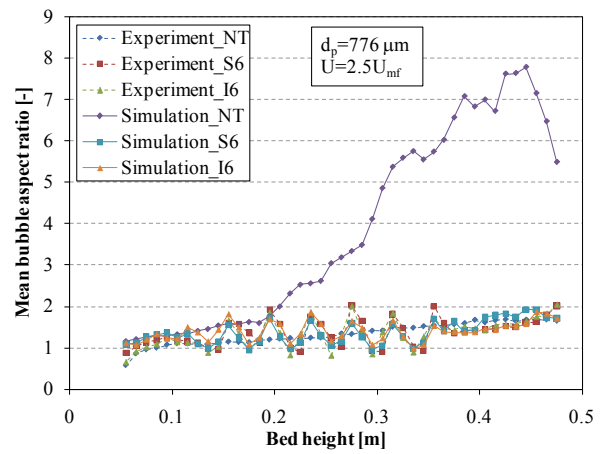
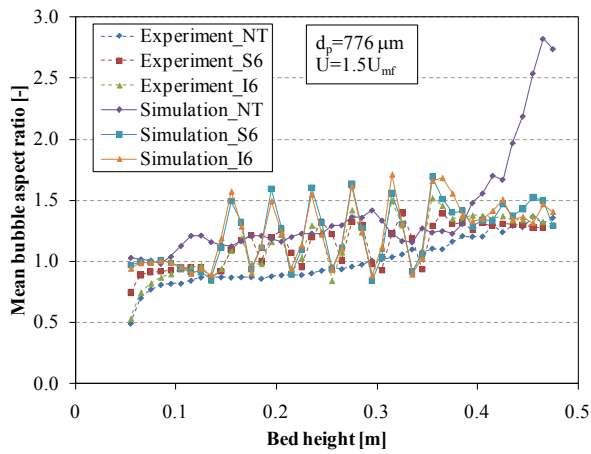


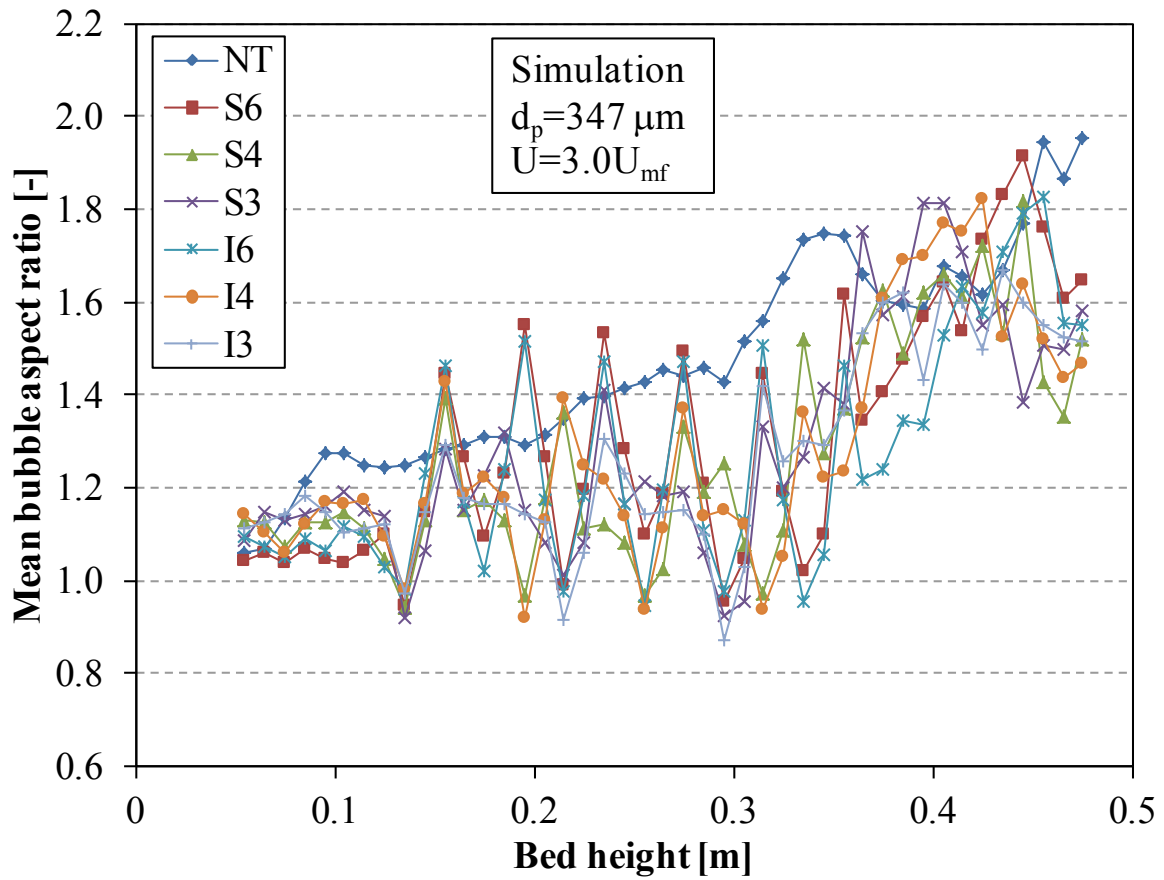
Figure C9: Comparison of mean bubble rise velocity different solid-wall boundary conditions.

Appendix D: Bubble properties for different particle sizes and bed geometries

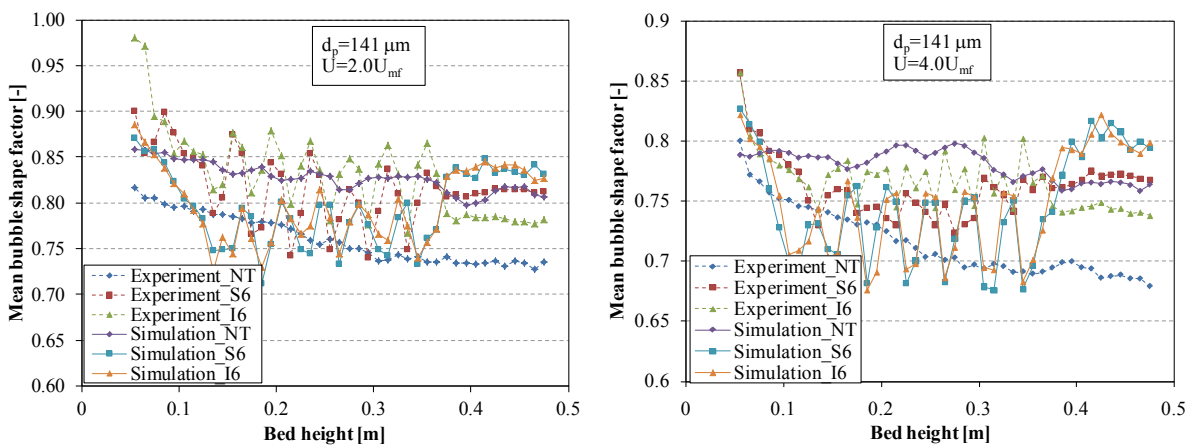
D1. Figures of bubble aspect ratio for different particle sizes and bed geometries

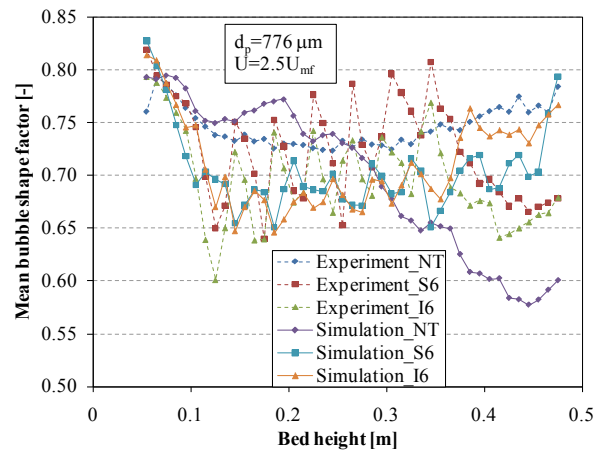
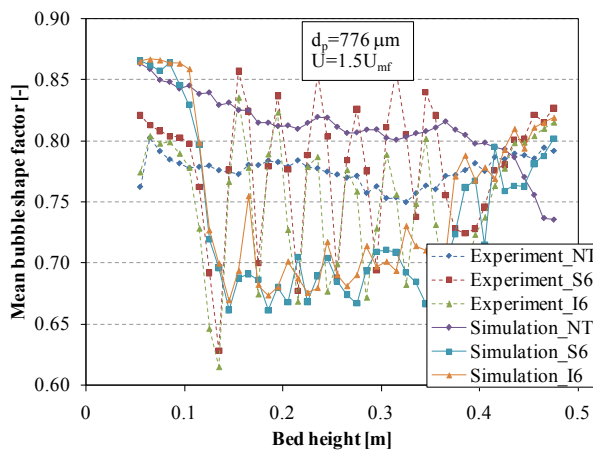
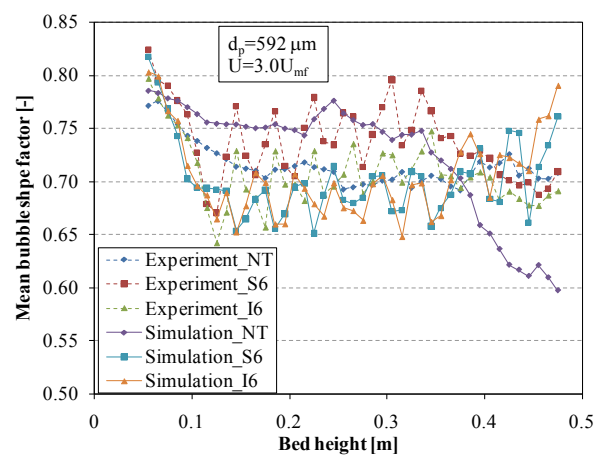
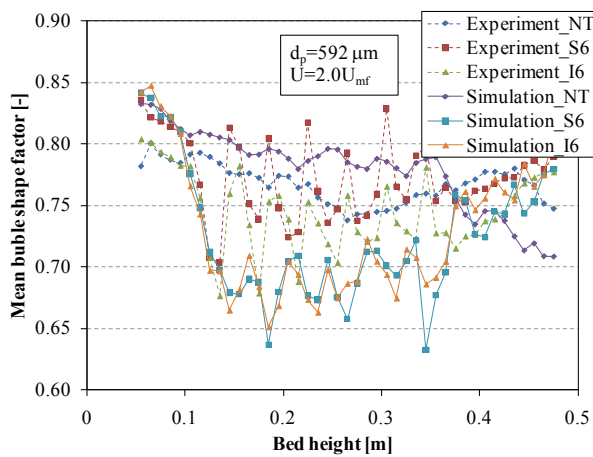
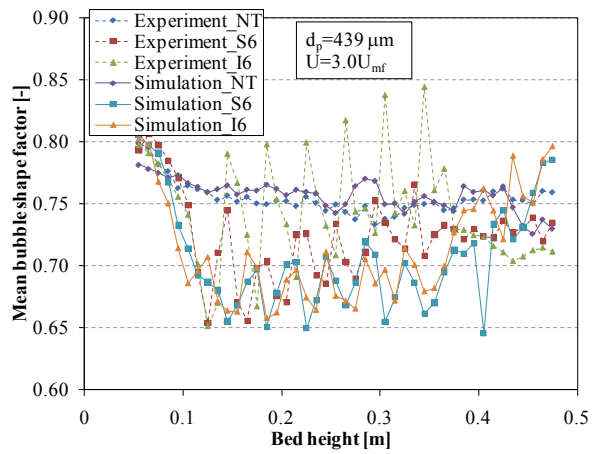
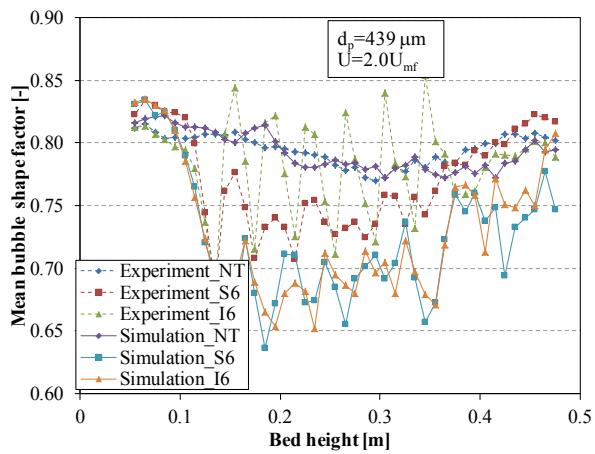


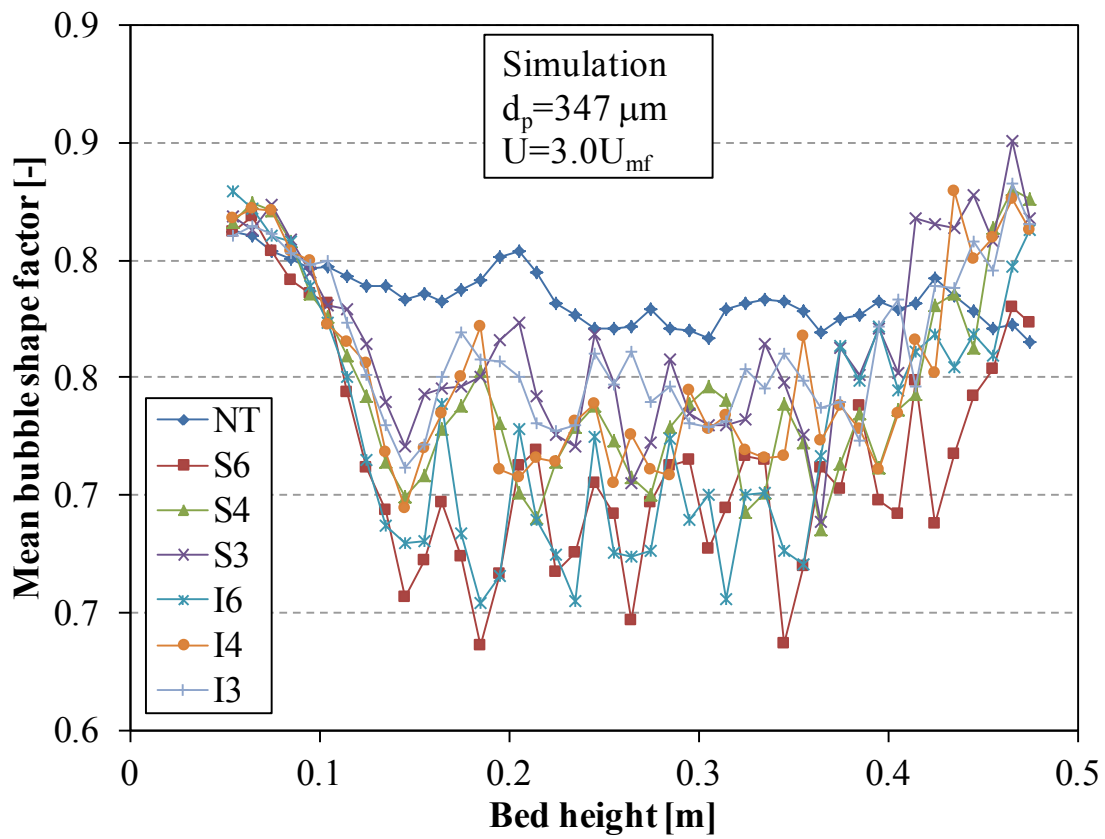
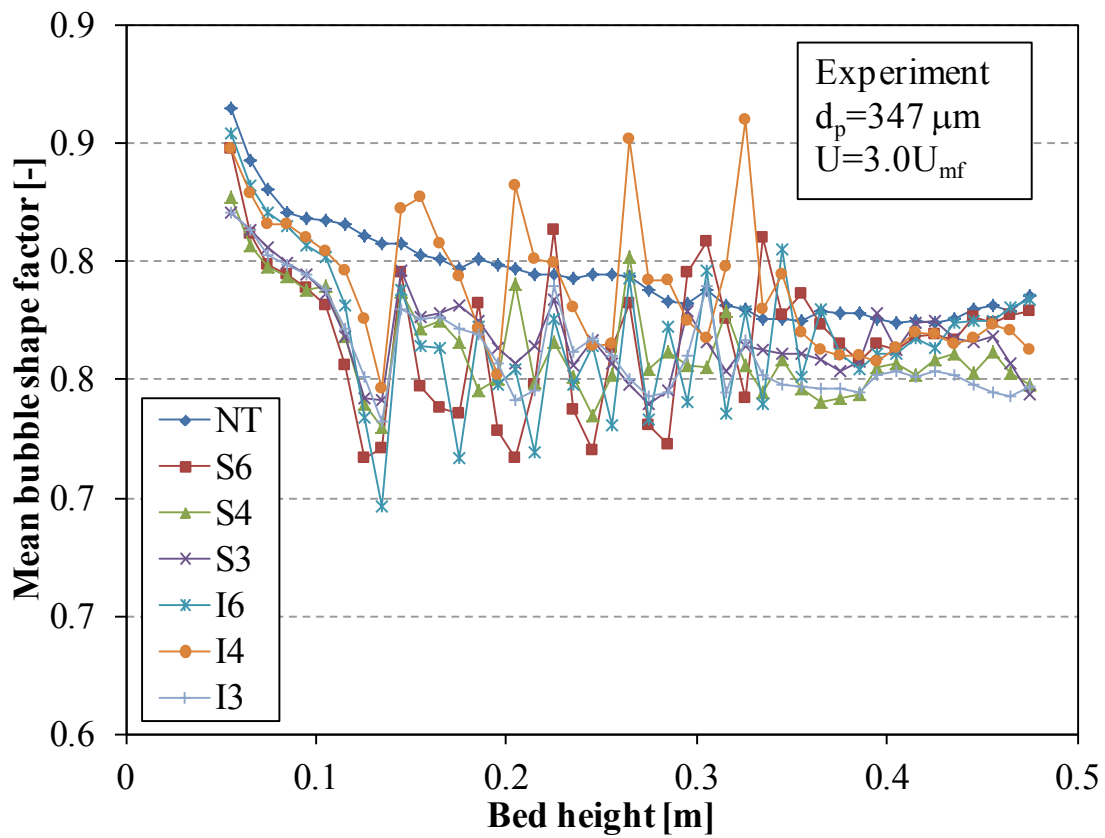




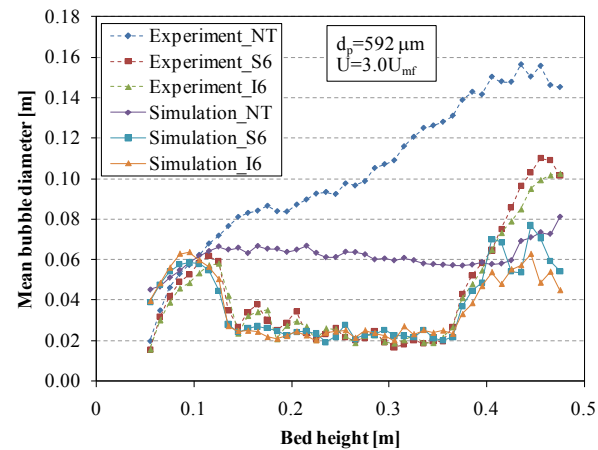
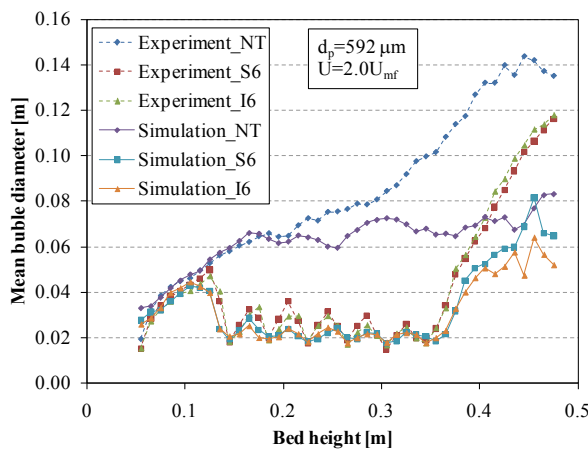
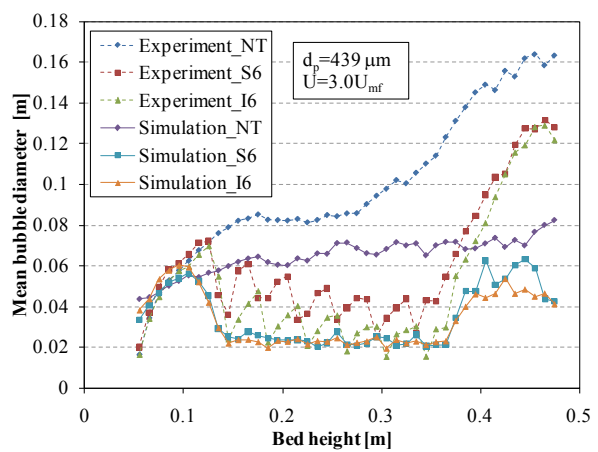
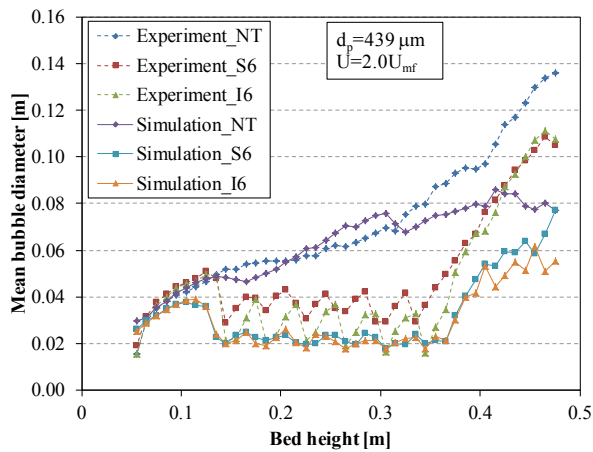
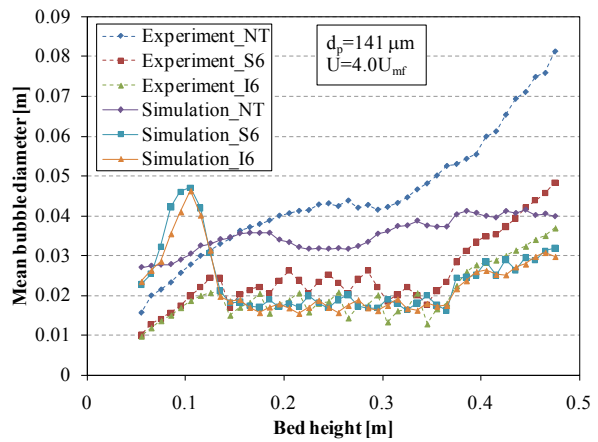
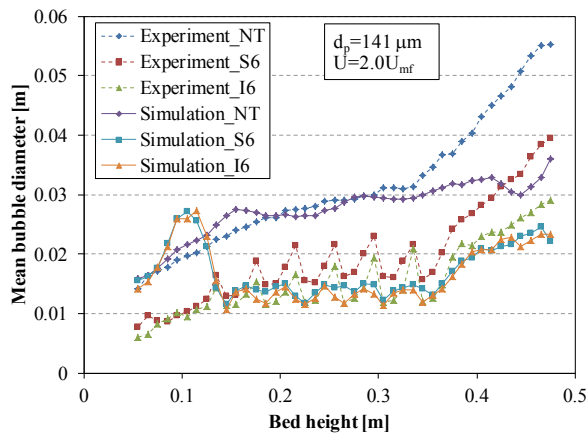
D2. Figures of mean bubble shape factor for different particle sizes and bed geometries

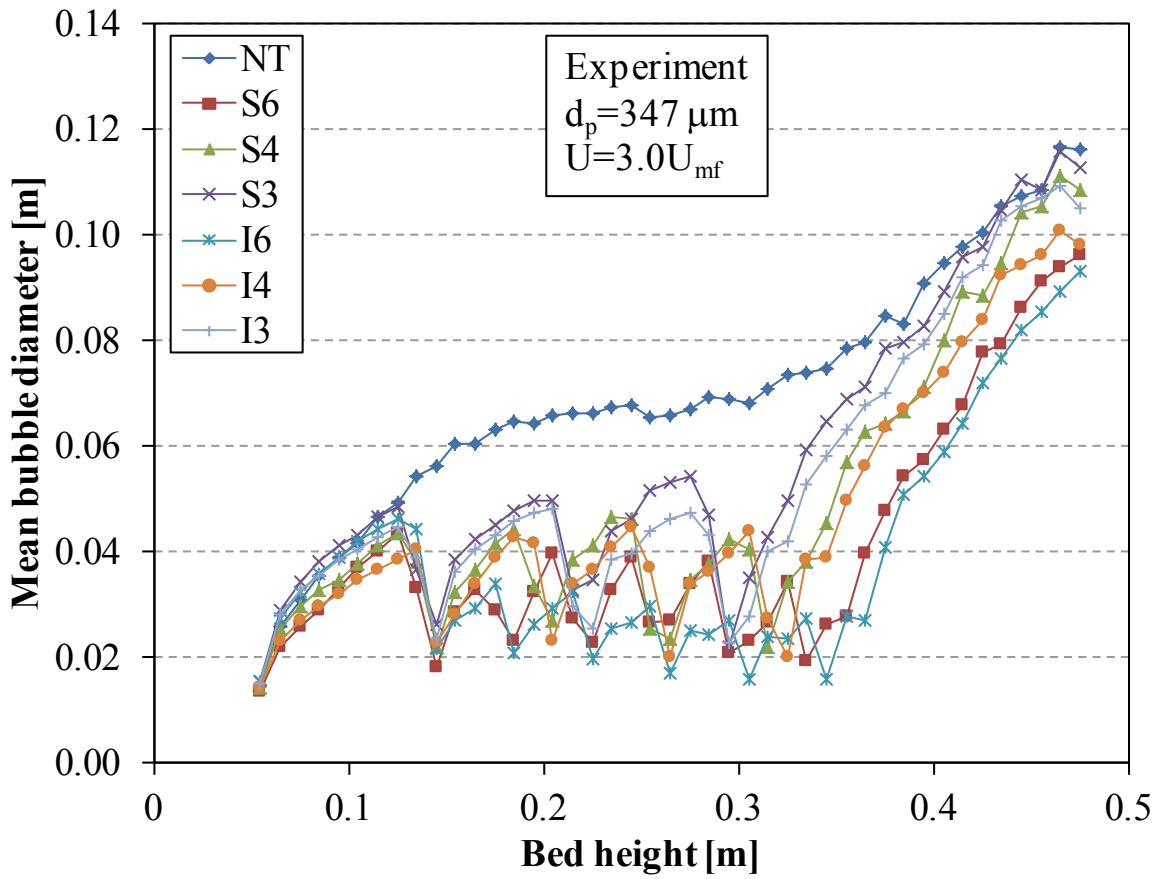
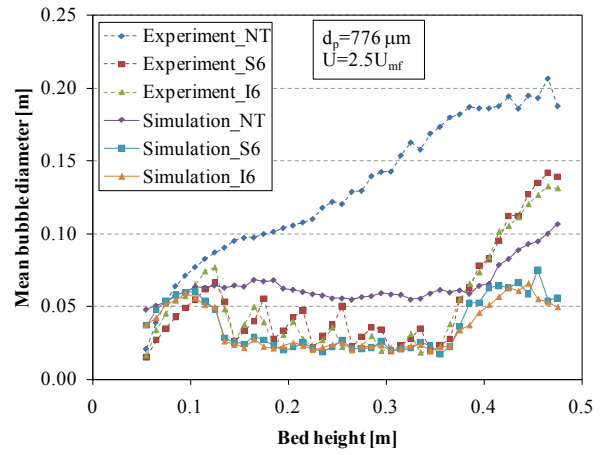
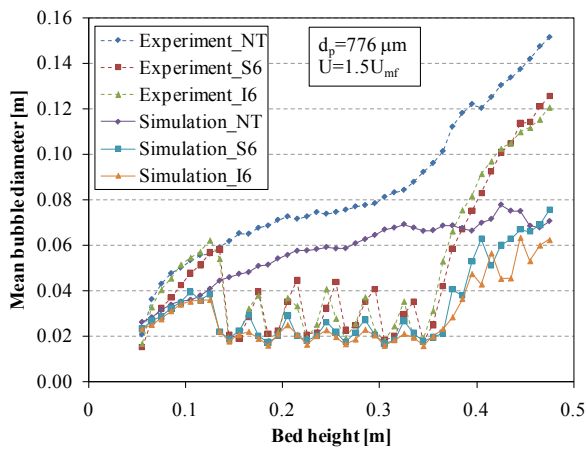


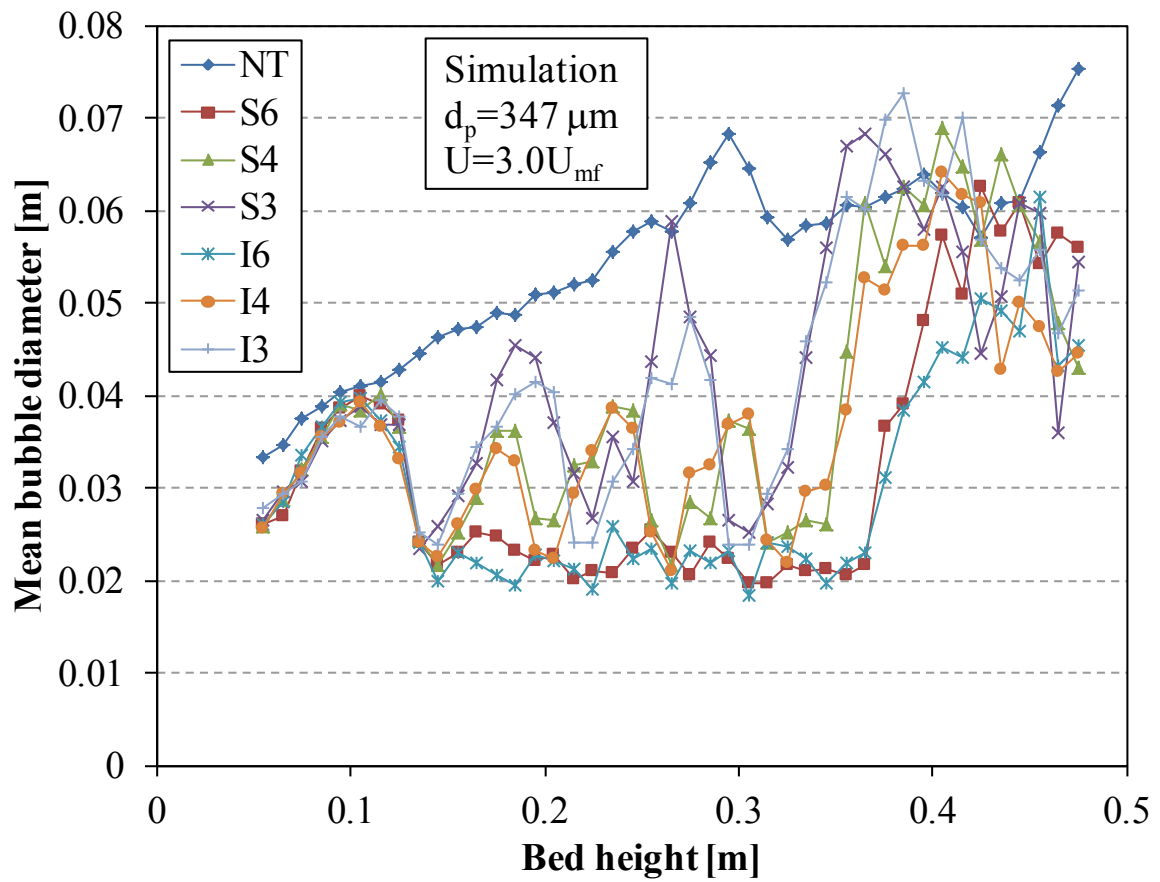




D3. Figures of mean bubble diameter for different particle sizes and bed geometries







D4. Figures of mean bubble rise velocity for different particle sizes and bed geometries

